Dissertation

# Multi-Black-Hole Configurations as Models for Inhomogeneous Cosmologies

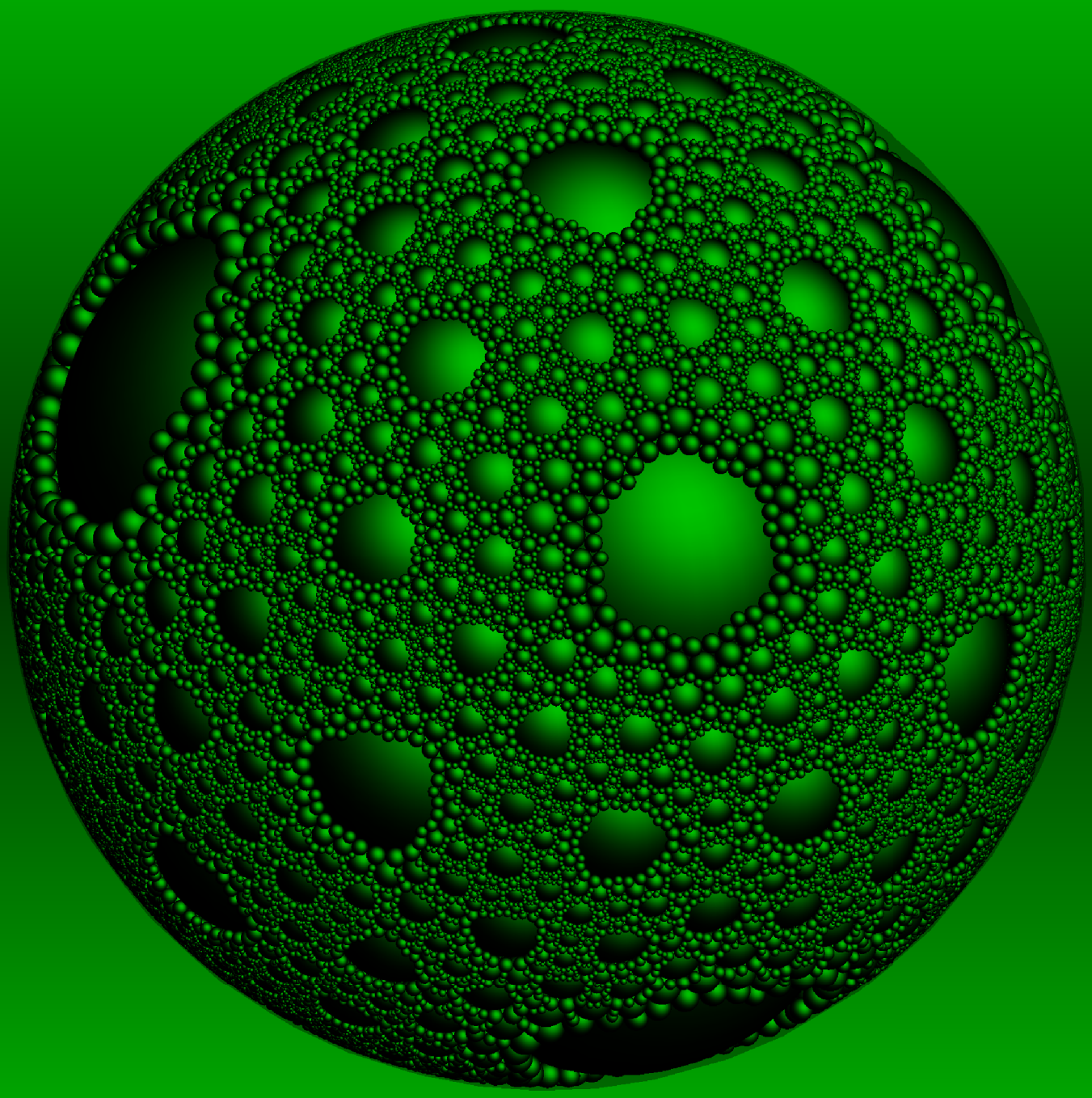

Michael Fennen

2017

# Multi-Black-Hole Configurations as Models for Inhomogeneous Cosmologies

## Dissertation

zur Erlangung des Grades

## Doktor der Naturwissenschaften
### - Doctor rerum naturalium -

am Fachbereich 1 (Physik und Elektrotechnik)
der Universität Bremen

Vorgelegt am 08. März 2017

von

**M. Sc. Michael Fennen**

geboren am 11. August 1988 in Löningen

**Gutachter:**

Prof. Dr. Domenico Giulini

Prof. Dr. Dominik Schwarz

**Kolloquium:**

09. Mai 2017

„Wir dürfen das Weltall nicht einengen, um es den Grenzen unseres Vorstellungsvermögens anzupassen, wie der Mensch es bisher zu tun pflegte. Wir müssen vielmehr unser Wissen ausdehnen, so dass es das Bild des Weltalls zu fassen vermag.“

*Sir Francis von Verulam Bacon (1561 - 1626),*
*englischer Philosoph, Essayist und Staatsmann,*
*entwarf die Methodologie der Wissenschaften*

**Cover image:** The image on the cover shows an Apollonian sphere packing of 1 424 789 tangent spheres inside a big sphere. About 94.2 % of the outer sphere is filled. The construction of the packing on the cover based on a tetrahedron configuration is described in appendix A. The Apollonian sphere packings serve as models for inhomogeneous cosmological spacetimes. Each cap contains a black hole at its centre. The mass of a black hole is determined by the size of its sphere.

# Abstract

On the largest scales, the Universe is homogeneous and isotropic, whereas on smaller scales, various structures immediately begin to emerge. The transition from an inhomogeneous spacetime to the homogeneous and isotropic Friedmann universe is not sufficiently understood yet. Modern cosmology rests on the hypothesis that the ΛCDM-model applies and, indeed, this model is very successful. On the other hand, as the precision of observations steadily increases, it is more than likely that inhomogeneities will no longer be negligible in the future. For this reason, the study of inhomogeneous cosmological models is reasonable.

In this thesis, we consider the question which Friedmann universe is the best fit to a particular given inhomogeneous spacetime, which is known as the 'fitting problem'. We consider models in which matter is replaced by a discrete configuration of black holes, that is, we concentrate on vacuum solutions to Einstein's equations. Since the full system of the field equations is too complicated to find an exact time-dependent solution for the whole spacetime, we restrict ourselves to approximative models as well as solutions to the initial value problem. In the former case, we reconsider Swiss-cheese and Lindquist-Wheeler models. In both models, the spacetime around a mass is described by the Schwarzschild metric. In the latter case, we determine the spatial metric of a space-like hypersurface. We limit our attention to time-symmetric initial data characterised by the vanishing of the extrinsic curvature. In this case, we are able to find a solution for an arbitrary number of black holes using the conformal method.

Clearly, it is not reasonable to assume that every configuration of black holes leads to a spacetime which may be approximated well by a Friedmann solution. Such an approximation should be possible if the masses are distributed somehow uniformly. The aim of this thesis is to clarify this statement and to provide criteria which allow quantitative statements about the degree of uniformity. We determine the parameters of the fitted dust universe, in particular the scale factor. Our considerations are supported by several example configurations. In particular, we provide a new method based on Lie sphere geometry to construct various configurations with a high degree of uniformity in a surprisingly simple fashion.

Moreover, we provide a generalisation to an approximative inhomogeneous model given by Lindquist and Wheeler. In this case, it is possible to determine the parameters of the fitted Friedmann universe even if we do not know the exact solution. Under certain conditions, this model becomes similar to a Swiss-cheese model, allowing us to formulate first expectations on the time evolution, which is otherwise mostly disregarded within the framework of this thesis.

# Zusammenfassung

Auf den größten Skalen erscheint das Universum homogen und isotrop. Auf kleineren Skalen sind dagegen unmittelbar verschiedenste Strukturen zu erkennen. Der Übergang von einer inhomogenen Raumzeit zu einer Beschreibung durch ein homogenes und isotropes Friedmann-Universum ist noch nicht hinreichend verstanden. In der Kosmologie wird lediglich angenommen, dass das ΛCDM-Modell die richtige Beschreibung sei. Tatsächlich ist dieses Modell äußerst erfolgreich. Aufgrund der stetigen Verbesserung der Messgenauigkeit ist jedoch anzunehmen, dass mögliche Effekte durch Inhomogenitäten auf die Messungen in Zukunft nicht mehr zu vernachlässigen sind. Aus diesem Grund erscheint es angebracht, inhomogene kosmologische Modelle zu untersuchen.

Diese Arbeit beschäftigt sich mit der Frage, welches das beste Friedmann-Universum ist, um eine gegebene inhomogene Raumzeit zu approximieren. Dies ist auch als „Fitting-Problem“ bekannt. Wir ersetzen die Materie durch eine diskrete Verteilung von Schwarzen Löchern, was bedeutet, dass wir Vakuumlösungen der Einstein-Gleichungen betrachten. Da die Feldgleichungen zu kompliziert sind, um eine zeitabhängige Lösung für die gesamte Raumzeit zu finden, beschränken wir uns approximative Modelle und auf Lösungen des Anfangswertproblems. Im ersten Fall beschäftigen wir uns mit den sogenannten „Swiss-cheese“- und Linquist-Wheeler-Modellen, bei denen die Raumzeit in der Umgebung einer Masse durch die Schwarzschild-Metrik beschrieben wird. Im zweiten Fall bestimmen wir die Metrik einer raumartigen Hyperfläche. Dabei beschränken wir uns auf zeitsymmetrische Hyperflächen, die durch das Verschwinden der äußeren Krümmung charakterisiert sind. In diesem Fall können wir mit Hilfe der konformen Methode eine Lösung für eine beliebige Anzahl von schwarzen Löchern finden.

Es ist sicherlich davon auszugehen, dass nicht jede Verteilung von schwarzen Löchern zu einer Raumzeit führen wird, die sich gut durch eine Friedmann-Universum annähern lässt. Dazu sollten die Massen einigermaßen gleichmäßig verteilt. Das Ziel dieser Arbeit ist es, diese Aussage zu spezifizieren und ein entsprechendes Kriterium anzugeben, durch das der Grad der Gleichmäßigkeit quantitativ beurteilt werden kann. Weiterhin sollen die Parameter der Approximation bestimmt werden, womit vor allem der Skalenfaktor gemeint ist. Unsere Ergebnisse werden durch die Betrachtung von verschiedenen Beispielkonfigurationen unterstützt. Insbesondere präsentieren wir ein neues, auf Lie-Sphären-Geometrie basierendes Verfahren, das es erlaubt auf einfachste Weise unterschiedlichste Konfigurationen mit einem hohen Grad an Gleichmäßigkeit zu erzeugen.

Wir beschäftigen uns ebenfalls mit der Verallgemeinerung einer Approximation inhomogener Raumzeiten, die von Lindquist und Wheeler entwickelt wurde. Dies erlaubt uns die Parameter eines Friedmann-Universums zu bestimmen, falls wir die exakte Lösung nicht kennen. Unter bestimmten Bedingungen ähnelt dieses Modell einem „Swiss-Cheese“-Modell, was es uns erlaubt, erste Vermutungen zur Zeitentwicklung aufzustellen, die ansonsten im Rahmen dieser Arbeit in den Hintergrund rückt.

# Contents

# List of Figures

# List of Tables

# Notation

### General

| | |
|---|---|
| $G = c = 1$ | Geometric units such that [length] = [time] = [mass] |
| $\boldsymbol{\partial}_\alpha$ | Basis vector fields |
| $\boldsymbol{e}_\alpha$ | Orthonormal basis vector fields |
| $\mathbf{d}x^\alpha$ | Basis 1-form fields dual to $\boldsymbol{\partial}_\alpha$ |
| $\mathbf{d}x^2 \equiv \mathbf{d}x \otimes \mathbf{d}x$ | |
| $\boldsymbol{\theta}^\alpha$ | Orthonormal basis 1-form fields dual to $\boldsymbol{e}_\alpha$ |
| $S^\alpha{}_\beta$ | Components of a tensor |
| $\boldsymbol{\Phi}^\alpha{}_\beta$ | Tensor-valued $p$-form |
| $\boldsymbol{x}^\perp = \{\boldsymbol{y} \in \mathcal{M} : \boldsymbol{g}(\boldsymbol{x}, \boldsymbol{y}) = 0\}$ | Orthogonal complement |
| $\boldsymbol{u}^\flat = \boldsymbol{g}(\boldsymbol{u}, \cdot\,)$ | Associated 1-form field to a vector field $\boldsymbol{u}$ |
| $\mathbf{d}\Omega^2 = \mathbf{d}\vartheta^2 + \sin^2\vartheta\,\mathbf{d}\varphi^2$ | Spherical surface element |
| $\nabla, \nabla[g]$ | Covariant derivative with respect to the metric $\boldsymbol{g}$ |
| $\Delta$ | Laplace operator |
| $\boldsymbol{d}$ | Exterior derivative |
| $\boldsymbol{D}$ | Covariant exterior derivative |

### Indices

| | |
|---|---|
| $\alpha, \beta, \dots \in \{(0,)\,1, 2, \dots\}$ | General component indices with respect to any frame (Riemannian or Lorentzian) in arbitrary dimensions |
| $\mu, \nu, \dots \in \{0, 1, 2, 3\}$ | Lorentzian components indices |
| $a, b, \dots \in \{1, 2, 3\}$ | Riemannian components indices |
| $i, j, \dots \in \{1, 2, 3\}$ | Indices with respect to a conformal basis in the conformal method |
| $A, B, \dots \in \{1, 2, 3, \dots\}$ | Indices counting different objects not components |

### Metric spaces

| | |
|---|---|
| $\mathcal{M}$ | Lorentzian spacetime with metric $\boldsymbol{g}$ of signature $(-,+,+,+)$ |
| $\boldsymbol{x}, \boldsymbol{y} \in \Gamma\mathrm{T}\mathcal{M}$ | $\boldsymbol{g}(\boldsymbol{x}, \boldsymbol{y}) = g_{\mu\nu} x^\mu y^\nu$ |
| $\boldsymbol{\alpha}, \boldsymbol{\beta} \in \Gamma\mathrm{T}^*\mathcal{M}$ | $\boldsymbol{g}^{-1}(\boldsymbol{\alpha}, \boldsymbol{\beta}) = g^{\mu\nu} \alpha_\mu \beta_\nu$ |
| $\mathbb{R}^{n,m}$ | Real vector space of dimension $(n+m)$ with metric signature $(\underbrace{-, \dots, -}_{n \text{ times}}, \underbrace{+, \dots, +}_{m \text{ times}})$ |

| | |
|---|---|
| $\boldsymbol{X} \in \mathcal{M} \subset \mathbb{R}^{n,m}$ | Space-like vectors on a hypersurface in $\mathbb{R}^{n,m}$ |
| $\mathbb{R}^n \equiv \mathbb{R}^{0,n}$ | Riemannian flat space with metric $\boldsymbol{\delta}$ |
| $\boldsymbol{E}_n \in \mathbb{R}^n$ | unit vector in $\mathbb{R}^n$ |
| $\boldsymbol{x}, \boldsymbol{y} \in \mathbb{R}^n$ | $\boldsymbol{x} \cdot \boldsymbol{y} = \sum_{\alpha=1}^n x_\alpha y_\alpha$<br>$\|\boldsymbol{x}\|_n^2 = \boldsymbol{x} \cdot \boldsymbol{x} = \boldsymbol{x}^2$ |
| $\mathbb{R}^{1,n}$ | Minkowski space with metric $\boldsymbol{\eta}$ |
| $\boldsymbol{\xi}, \boldsymbol{\omega} \in \mathbb{R}^{1,n}$ | $\langle \boldsymbol{\xi}, \boldsymbol{\omega} \rangle = -\xi_0\omega_0 + \sum_{\alpha=1}^n \xi_\alpha\omega_\alpha \geq 0$ |
| $\boldsymbol{X}, \boldsymbol{Y} \in \mathbb{R}^{1,n}$ | $\langle \boldsymbol{X}, \boldsymbol{Y} \rangle = -X_0Y_0 + \sum_{\alpha=1}^n X_\alpha Y_\alpha < 0$<br>$\|\boldsymbol{X}\|_{\mathrm{M}}^2 = \langle \boldsymbol{X}, \boldsymbol{X} \rangle$ |
| $\mathbb{R}^{1,n,1}$ | Flat space with signature $(-,+,\ldots,+,-)$ |
| $\boldsymbol{\Xi}, \boldsymbol{\Omega} \in \mathbb{R}^{1,n,1}$ | $\langle\langle \boldsymbol{\Xi}, \boldsymbol{\Omega} \rangle\rangle = -\Xi_0\Omega_0 + \sum_{\alpha=1}^n \Xi_\alpha\Omega_\alpha - \Xi_{n+1}\Omega_{n+1}$ |
| $S^n = \left\{ \boldsymbol{X} \in \mathbb{R}^{n+1} : \|\boldsymbol{X}\|_n^2 = 1 \right\}$ | Hypersphere with positive constant curvature and Riemannian metric |
| $\boldsymbol{E}_{n+1} = (\sin\chi\, \boldsymbol{E}_n, \cos\chi)$ | Unit vector parametrising $S^n$ |
| $H_2^n = \left\{ \boldsymbol{X} \in \mathbb{R}^{1,n} : \|\boldsymbol{X}\|_{\mathrm{M}}^2 = -1 \right\}$ | Two-sheeted hyperboloid with negative constant curvature and Riemannian metric |
| $\boldsymbol{E}_{\mathrm{M}} = (\pm\cosh u, \sinh u\, \boldsymbol{E}_n)$ | unit vector parametrising $H_2^n$ |
| $H_1^n = \left\{ \boldsymbol{\xi} \in \mathbb{R}^{1,n} : \langle \boldsymbol{\xi}, \boldsymbol{\xi} \rangle = 1 \right\}$ | One-sheeted hyperboloid with positive constant curvature and Lorentzian metric |
| $\mathbb{P}(\mathbb{R}^{n,m}) = (\mathbb{R}^{n,m} \setminus \{\boldsymbol{0}\}) / \sim$ | Projective space |

### Often used tensors

| | |
|---|---|
| $\boldsymbol{g}$ | Metric of a Riemannian or Lorentzian space |
| $\boldsymbol{\eta}$ | Minkowski metric, mostly $\eta_{\alpha\beta} = \mathrm{diag}\,(-1,1,\ldots,1)$, on spacetime $\eta_{\mu\nu} = \mathrm{diag}\,(-1,1,1,1)$ |
| $\boldsymbol{\delta}$ | Flat metric with $\delta_{\alpha\beta} = (1,\ldots,1)$ |
| $\boldsymbol{h} = \mathbf{d}\chi^2 + \sin^2\chi\, \mathbf{d}\Omega^2$ | Round metric of $S^3$ |
| $\boldsymbol{\omega}^\mu{}_\nu$ | Connection 1-forms |
| $\boldsymbol{\Omega}^\mu{}_\nu$ | Curvature 2-forms |
| $\boldsymbol{R}[g]$ | Ricci tensor with respect to the metric $\boldsymbol{g}$ |
| $\mathcal{R}[g]$ | Ricci scalar with respect to the metric $\boldsymbol{g}$ |
| $\boldsymbol{n}$ | Normal vector field |
| $\boldsymbol{K}$ | Extrinsic curvature |
| $\mathcal{K}$ | Trace of the extrinsic curvature |
| $\alpha$ | Lapse function |
| $\boldsymbol{\beta}$ | Shift vector field |
| $\boldsymbol{N}$ | Evolution vector field |
| $\Psi$ | Conformal factor |

# 1 Introduction

*The Universe is homogeneous and isotropic on the largest scales for an observer comoving with the cosmic matter.* This is the cosmological principle and usually the starting point in cosmology, the theory of the dynamics and structure of the Universe[1]. Assuming that general relativity is the correct theory of gravity on cosmological scales, this leads to the very successful standard model of cosmology, the *ΛCDM-model*, which depends only on six free parameters[2]: four describing the homogeneous background and two describing scalar perturbations. Although the cosmological principle is a quite crude approximation to the complex nature of the whole Universe, it provides a good explanation for most observations to high accuracy. Open questions concern for example the nature of dark energy.

The homogeneity and isotropy assumptions are supported by observations. In 1964, Penzias and Wilson stumbled upon unexpected microwave radiation coming to Earth with the same intensity from all directions. Nowadays, we know that this is the cosmic microwave background (CMB) with a thermal black body spectrum at a temperature of 2.725 K. The CMB is a relic from the time when the Universe became transparent about 380 000 years after the Big Bang. A simulation of their measurement results is presented in fig. 1.1 showing high evidence for isotropy.

In contrast, homogeneity is more difficult to justify since we can only make observations on our past null cone rather than on a constant-time slice. Of course, it is natural to assume that we are at no special point in space, but there are also hints from number counting of galaxies that the Universe is actually statistically homogeneous, see fig. 1.2.

However, the cosmological principle is only justified on the largest scales. On smaller scales the Universe is very inhomogeneous: There are localised matter distributions in an almost empty space, as the image in fig. 1.3 shows. Several structures vary strongly over all scales: We may start in our Solar System with the planets orbiting the central Sun. The Sun and billions of other stars form our galaxy, the Milky Way. On larger scales the galaxies form clusters. These clusters form superclusters which are part of the cosmic web. The largest structures, separated by huge voids, have an extension of about a billion light-years which is about a hundredth to a tenth of the size of the visible Universe. This is shown in fig. 1.4. It is just about this scale ($\gtrsim 300\,\mathrm{Mpc}$)[3] where the Universe starts to appear statistically homogeneous.

The largest known cosmic structure is the Hercules–Corona Borealis Great Wall with an extension of about 2 Gpc to 3 Gpc with redshift values between 1.6 and 2.1, discovered in 2013 [HHB14]. Actually, structures like the Hercules–Corona Borealis Great Wall are too big to be compatible with the cosmological principle; for example Yadav, Bagla and

[1] The term 'Universe' always refers to our Universe, whereas 'universe' refers to a general solution of the Friedmann equations.

[2] Physical baryon density parameter, physical dark matter parameter, Hubble constant, scalar spectral index, curvature fluctuation amplitude, optical depth at reionisation.

[3] $1\,\mathrm{Mpc} = 3.262 \times 10^6\,\mathrm{ly} \approx 3.086 \times 10^{19}\,\mathrm{km}$. The distance between the Milky Way and the Andromeda galaxy is 0.792 Mpc.

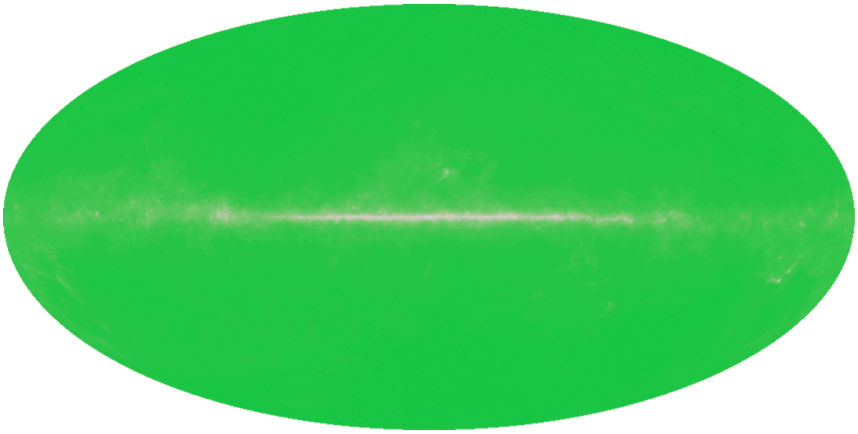

Credit [1]: NASA/WMAP Science Team

**Figure 1.1:** 'A view of the sky as would have been seen by the microwave receiver of Penzias and Wilson, if it could have surveyed the whole sky. This is a simulated image.' [NAS] The light structures are due to foreground effects mainly in the Milky Way.

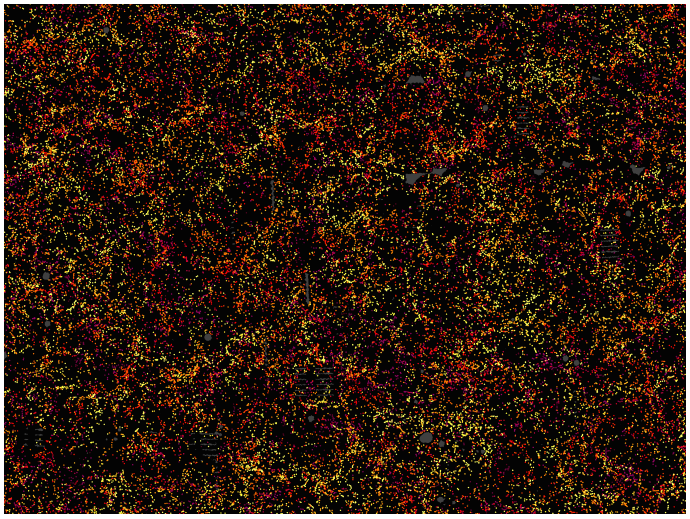

Credit [2]: D. Eisenstein and the SDSS-III collaboration

**Figure 1.2:** 'This is one slice through the map of the large-scale structure of the Universe from the Sloan Digital Sky Survey and its Baryon Oscillation Spectroscopic Survey. Each dot in this picture indicates the position of a galaxy 6 billion years into the past. The image covers about 1/20th of the sky, a slice of the Universe 6 billion light-years wide, 4.5 billion light-years high, and 500 million light-years thick. Color indicates distance from Earth, ranging from yellow on the near side of the slice to purple on the far side. Galaxies are highly clustered, revealing superclusters and voids whose presence is seeded in the first fraction of a second after the Big Bang. This image contains 48,741 galaxies, about 3% of the full survey dataset. Grey patches are small regions without survey data.' [ES16]

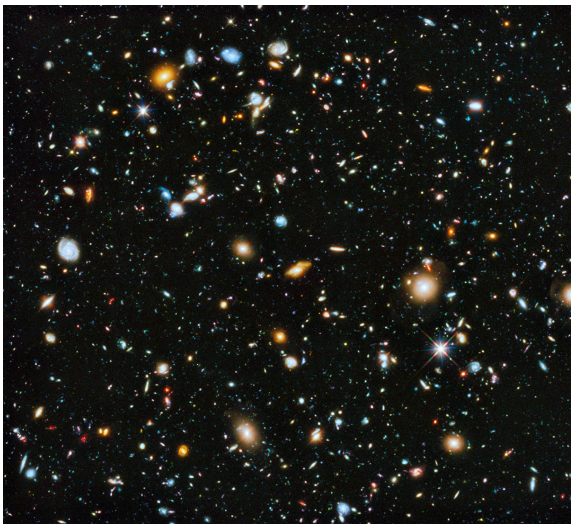

Credit [3]: NASA, ESA, H. Teplitz and M. Rafelski (IPAC/Caltech), A. Koekemoer (STScI), R. Windhorst (Arizona State University), and Z. Levay (STScI)

**Figure 1.3:** 'The Hubble Ultra Deep Field 2014 image is a composite of separate exposures taken in 2002 to 2012 with Hubble's Advanced Camera for Surveys and Wide Field Camera 3. Astronomers previously studied the Hubble Ultra Deep Field (HUDF) in visible and near-infrared light in a series of images captured from 2003 to 2009. The HUDF shows a small section of space in the southern-hemisphere constellation Fornax. Now, using ultraviolet light, astronomers have combined the full range of colors available to Hubble, stretching all the way from ultraviolet to near-infrared light. The resulting image – made from 841 orbits of telescope viewing time – contains approximately 10,000 galaxies, extending back in time to within a few hundred million years of the big bang.' [NAS14]

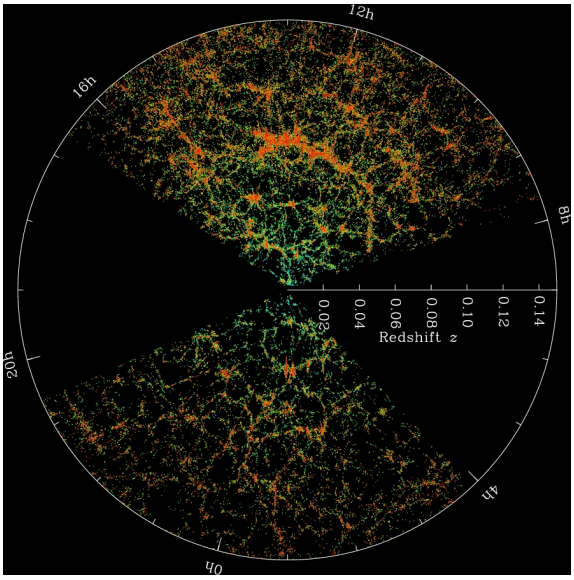


Credit [4]: Sloan Digital Sky Survey

**Figure 1.4:** 'The SDSS's map of the Universe. Each dot is a galaxy; the color bar shows the local density.' [Slo13]

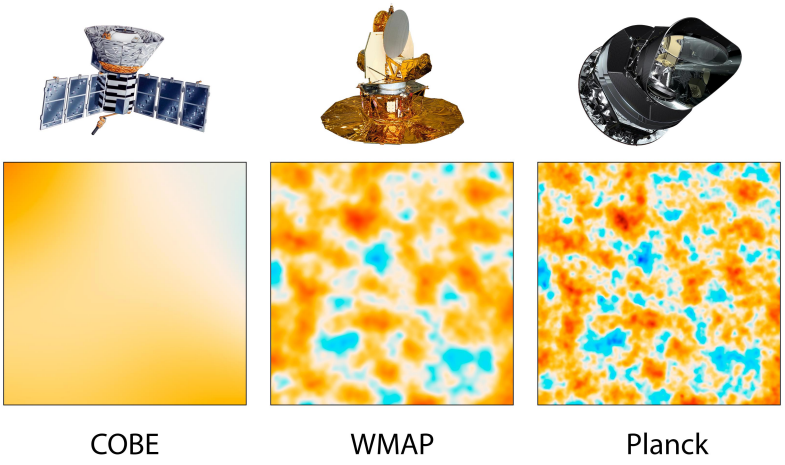


Credit [5]: NASA/JPL-Caltech/ESA

**Figure 1.5:** 'The three panels show 10-square-degree patches of all-sky maps created by space-based missions capable of detecting the cosmic microwave background. The first spacecraft, launched in 1989, is NASA's Cosmic Background Explorer, or COBE (left panel). Two of COBE's principal scientists earned the Nobel Prize in Physics in 2006 for the mission's evidence supporting the big bang theory, and for its demonstration that tiny variations in the ancient light reveal information about the state of the universe. These variations, called anisotropies, came into sharper focus with NASA's next-generation spacecraft, the Wilkinson Microwave Anisotropy Probe, or WMAP (middle panel). This mission, launched in 2001, found strong evidence for inflation, the very early epoch in our universe when it expanded dramatically in size, and measured basic traits of our universe better than ever before. The most advanced satellite yet of this type is Planck, a European Space Agency mission with significant NASA contributions. Planck, launched in 2009, images the sky with more than 2.5 times greater resolution than WMAP, revealing patterns in the ancient cosmic light as small as one-twelfth of a degree on the sky. Planck has created the sharpest all-sky map ever made of the universe's cosmic microwave background, precisely fine-tuning what we know about the universe.' [NAS13]

Khandai [YBK10] suggest a maximum scale of 260 Mpc for structures. Therefore first doubts on the validity of the cosmological principle arise.

It is quite astonishing that a simple model like the ΛCDM-model is able to provide such a good description for the large-scale structure and the dynamics of the Universe. However, the cosmological principle can only be a first approximation to describe the Universe on cosmic scales. As the precision of observations steadily increases, it is more than likely that effects due to inhomogeneities will no longer be negligible in the future. Hence, more realistic models should take the inhomogeneities on smaller scales into account. It seems that first inconsistencies with measurements already occur [Buc+16]

A good example for the increasing precision is provided by the measurement of the temperature variations of the CMB showing the deviation from isotropy in the CMB. The improvement of the angular resolution of the satellite missions COBE, WMAP and recently Planck is illustrated in fig. 1.5. The Planck satellite provided an angular resolution of about 10 arc minutes and a sensitivity of 10 µK; see [Pla+16] for an overview of the results of the Planck mission.

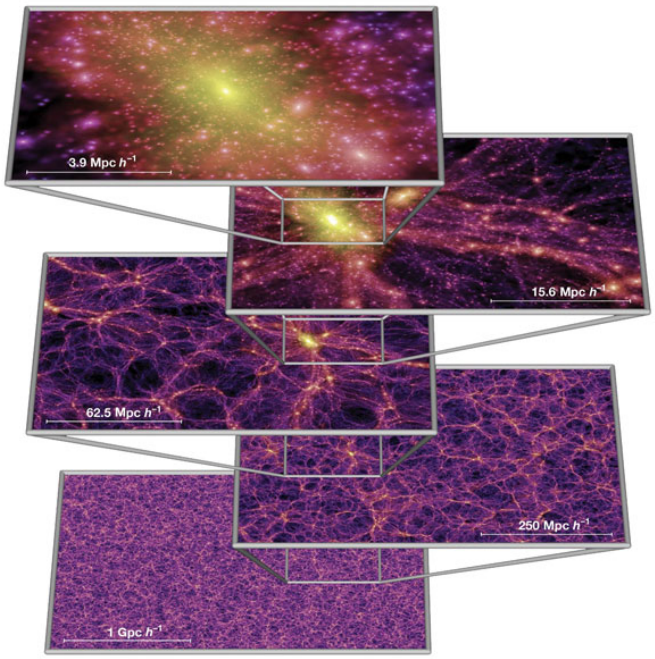


Credit [6]: Reprinted by permission from Macmillan Publishers Ltd
Nature 435, 629-636, 2 June 2005 (doi: 10.1038/nature03597)

**Figure 1.6:** 'The high-resolution simulation described here — dubbed the Millennium Simulation because of its size — was carried out by the Virgo Consortium, a collaboration of British, German, Canadian and US astrophysicists. It follows $N = 2,160^3 \cong 1.0078 \cdot 10^{10}$ particles from redshift $z = 127$ to the present in a cubic region 500 $h^{-1}$ Mpc on a side, where $1+z$ is the expansion factor of the Universe relative to the present and $h$ is Hubble's constant in units of 100 km s$^{-1}$ Mpc$^{-1}$. [...] Each individual image shows the projected dark matter density field in a slab of thickness 15 $h^{-1}$ Mpc (sliced from the periodic simulation volume at an angle chosen to avoid replicating structures in the lower two images), colour-coded by density and local dark matter velocity dispersion. The zoom sequence displays consecutive enlargements by factors of four, centred on one of the many galaxy cluster haloes present in the simulation.' [Spr+05].

We have physical intuition for what it means to smooth out a matter distribution. However in order to improve the ΛCDM-model, it is necessary to understand how the homogeneity assumption is justified from a mathematical point of view. It is still an open question how the transition from the inhomogeneous lower-scale structure to the homogeneous and isotropic large-scale structure has to be performed mathematically.

The general treatment in cosmology to include inhomogeneities is the application of perturbation theory assuming that the Universe is approximated well by a FLRW spacetime implementing the cosmological principle and that the inhomogeneities can be treated as small perturbations. A similar ansatz are $N$-body simulations like the Millennium Run [Spr+05], see also fig. 1.6. In this case, it is assumed that matter can be treated non-relativistically in a Newtonian approximation on a given cosmological background. Both approaches lead to results well-supported by observations.

These approaches are not really satisfactory from our point of view because they follow

more a top-down path using a cosmological FLRW spacetime in the background. This procedure may provide a good description for the structure formation assuming that the Universe was quite homogeneous in the beginning. However, it does not explain if the Friedmann solution is still a good approximation for the inhomogeneous Universe nowadays or if the deviations are already too big. For this problem a bottom-up approach, in which we start with an inhomogeneous spacetime and somehow arrive at a homogeneous universe by an averaging process, seems to be more reasonable.

There are three major approaches to this problem:

(i) The study of exact inhomogeneous cosmological solutions to Einstein's equations,

(ii) the construction of inhomogeneous models for discrete matter distributions,

(iii) the development of averaging methods.

In the first case, one considers a special class of exact solutions to Einstein's equation, called *inhomogeneous cosmological models*. These are non-static and non-vacuum solutions which reduce to a FLRW metric in a certain limit. In these spacetimes, the matter is typically modelled as an inhomogeneous fluid.

Many classes of such solutions are collected in the book *Inhomogeneous Cosmological Models* of Krasiński [Kra06] and in the subsequent article [BCK11] with recent developments. The most prominent and best-studied families are given by the Lemaître-Tolman-Bondi models [Lem33; Tol34; Bon47] and the Szekeres models [Sze75]. As exact perturbations of cosmological FLRW spacetimes, they allow the study of the influence of inhomogeneities on the large-scale behaviour. They can also be used to test the results from averaging procedures.

In view of the structure of our Universe, it is preferable to have models with a discrete matter distribution in vacuum. However, it is not simple to solve Einstein's equations without any symmetry assumptions. For this reason, one usually concentrates on approximative models. The most prominent example is provided by the Swiss-cheese models [ES45; Sch54]. These models are based upon Friedmann dust universes in which some regions are replaced by a Schwarzschild spacetime ensuring that the mass of the black hole equals the mass of removed dust. This way we obtain a spacetime containing static regions unaffected by the cosmological expansion while the global behaviour is still that of a FLRW spacetime. However, the Friedmann-like global behaviour is still achieved by construction.

A model which does not assume a Friedmann universe a priori was developed by Lindquist and Wheeler [LW57]. They approximated the regions around masses by overlapping Schwarzschild spacetimes. The Friedmann-like global behaviour arises from the movement of the boundaries of the Schwarzschild regions. Lindquist and Wheeler considered a spherical universe with black holes placed at the vertices of the 4-dimensional Platonic solids. Later the Lindquist-Wheeler models were generalised to regular lattices in flat space [CF09a; CF09b; Liu15; LW16; Yoo+12; YON13; YO14].

Another way of approximation is given by a perturbative approach to Einstein's equations. In this case, one makes an expansion of the metric and solves Einstein's equations iteratively. In the simplest case, one considers black holes on a regular lattice so that one has to solve the vacuum equations [Cli11; BL12; BL13].

For a given solution to Einstein's equations, it is in general not obvious, if at all possible, to decide which FLRW spacetime is the best fit describing the behaviour on cosmological

scales. This problem is known as the *fitting problem* [Ell84; ES87; Cla+11]. Standard cosmology rests on the hypothesis that our Universe is approximated best by a FLRW spacetime without providing a mathematical explanation. A possible derivation may be given by some kind of averaging scheme as applied successfully in fluid dynamics, macroscopic electrodynamics and solid state physics. The naive approach is to adapt the methods of these theories to general relativity. The idea is to smear out several matter properties of discrete particles to a continuous analogue over a certain volume beyond the particle scale; for example, the mass is replaced by the mass density. In the second step, the equations of motion are reformulated for these continuous variables.

However, this procedure is problematic in cosmology for several reasons. The scale on which the Universe starts to appear homogeneous ($\gtrsim 100\,\mathrm{Mpc}$) is just beneath the cosmic scales (size of the Universe $\approx 28\,\mathrm{Gpc}$ at redshift $z = 0$). Hence, a typical averaging region should have a diameter of about 100 Mpc. Usually, the averaging scale should be small compared to the size of the system but also large in comparison to the particle size. This is the case in fluid dynamics but not in cosmology. To illustrate this further, consider the galaxy content in a typical averaging region: There are about $10^{11}$ galaxies in the observable Universe implying that there are about $10^4$ galaxies in a typical averaging volume. This is still quite grained, as we also see in fig. 1.2. Hence, the question arises if a continuum approximation is really justified. Furthermore, as discussed above, there still exist structures on these scales, creating further doubt if a homogeneous fluid is the best description for matter on cosmic scales.

Maybe more problematic is the fact that there is no reasonable covariant averaging scheme which can be applied to tensors. In the usual averaging procedure, a scalar $\phi$ is integrated over a certain region $\mathcal{V}$ and the result is divided by the volume of this region. Hence, the average is given by

$$\langle\phi\rangle = \frac{1}{\operatorname{vol}\mathcal{V}} \int_{\mathcal{V}} \phi \,\mathrm{d}\mathcal{V}. \tag{1.1}$$

This is unproblematic for scalars and, in the case of global linear transformations like the Galilei transformations in Newtonian mechanics and Lorentz transformations in special-relativistic dynamics and electrodynamics, also for tensors.

This is not true any more if we are working with general diffeomorphism-invariant tensors as they appear in general relativity. In this case, the result of an averaging is usually no tensor, that is, the averaged tensors do not transform correctly under coordinate transformations. The most popular averaging schemes appearing in the literature are Buchert's spatial averaging [Buc00; Buc01] and Zalaletdinov's 'Macroscopic Gravity' [Zal92; Zal93; MZ97; Zal08]. Buchert considers in his works only averages of scalar objects like the expansion $\theta$ over spatial slices. In contrast, Zalaletdinov proposed a covariant averaging scheme so that the averaged metric is still a metric. But a new problem arises: The averaged Riemann curvature tensor is not the one of the averaged metric resulting in further ambiguities.

Further problems are whether we average with respect to the exact metric or to some background metric. The averaging region may be a four-dimensional volume in the spacetime, the past light cone of cosmic observes or a part of a three-dimensional space-like slice. In the latter case we have the additional problem how to slice the spacetime, which is closely related to the definition of a cosmic observer in an arbitrary spacetime.

Assuming that there exists some kind of averaging procedure, there are further problems regarding the dynamics. In contrast to fluid dynamics (without friction) or macroscopic electrodynamics, Einstein's field equations are non-linear. For this reason we expect that, in general, the time evolution does not commute with the averaging procedure. This means that the averaged Einstein tensor $\langle \boldsymbol{G} \rangle$ differs from the Einstein tensor $\boldsymbol{G}[\langle \boldsymbol{g} \rangle]$ formed by the averaged metric $\langle \boldsymbol{g} \rangle$. For this reason an additional source term $\boldsymbol{\mathcal{T}}$ may appear in Einstein's field equations for the averaged metric representing the effects of averaging

$$G[\langle g \rangle]_{\mu\nu} + \Lambda \langle g \rangle_{\mu\nu} = 8\pi \langle T \rangle_{\mu\nu} + \mathcal{T}_{\mu\nu} \,. \tag{1.2}$$

This additional effect is usually referred to as *backreaction*, that is, the influence from smaller scales to the large ones. It has been suggested that the cosmological constant term is due to backreaction so that there is no dark energy, for example see [Kol11]. For some general reviews on averaging and backreaction see Buchert [Buc08], Ellis [Ell11] and Räsänen [Räs11].

The structure of the Universe may also influence the light propagation because the Weyl and the Ricci part of the Riemann curvature tensor cause different lensing effects on null congruences. While the Ricci part tends to focus light, the Weyl part tends to shear and rotate light. In vacuum solution, the Ricci part vanishes identically, so that the light propagation is governed by the Weyl part. In contrast, in cosmological spacetimes, the Ricci part, determined by the energy-momentum tensor of a fluid through Einstein's equations, becomes important. It is possible that the data have been misinterpreted because the influence of inhomogeneities on the propagation has not been taken into account. This may be another explanation for dark energy. Since all our observations of the Universe are based on optical measurements, it is important to study light propagation in the models discussed above; here we can only mention a few examples [CFO12; FDU13; LRS13; BS14; LR15; Ben+16]. After the recent first measurement of gravitational waves [Abb+16b; Abb+16a], cosmological observations with gravitational wave detectors may be possible in the future. Hence, the effects on gravitational waves need to be studied in the future.

There have been many discussions in the literature if backreaction effects exist and if they are negligible or not. In particular, we want to mention the recent controversy between Green and Wald [GW14; GW15; GW16] on the one side and many prominent cosmologists on the other side [Buc+15]. The former ones claimed to have proven that there are no other backreaction effects than negligible radiation effects which was doubted by the latter group. There are many articles in the literature supporting either view. However, the results often depend on the properties of the considered models or on the generalisation of observables to inhomogeneous spacetimes. Often there are several possible definitions for an observable which coincide in Friedmann universes but differ in inhomogeneous spacetimes. In this context, it is important to note that the validity of Einstein's field equations for the averaged geometry is assumed. This may be false and the theory of general relativity may not be applicable any more. So we may say that a final answer cannot be given yet.

Our approach to gain further insights into this topic is the study of exact solutions to Einstein's field equations. Nowadays, our Universe is mainly dominated by dust; radiation is already negligible and dark energy will become dominant in the future. For this reason, we concentrate on spacetimes containing many discrete masses of common matter only. The cosmological constant and radiation are neglected.

The discrete matter distribution is replaced by black holes because we expect that all kinds of matter should behave similarly if we are far enough away, that is, on the largest

scales. The real structure of the masses should only be important if we are interested in the local dynamics. This means that we are assuming that on cosmological scales it is not important if we are considering a galaxy with its complex structure, a cloud of dust or a even simpler a black hole. This is similar to the interior solution of a Schwarzschild spacetime. In this case, we are not able to decide from local measurements in the exterior region what kind of matter is located in the centre. The outer region of any spherical symmetric mass distribution is given by the Schwarzschild spacetime. According to this, we expect that it should be possible to approximate the spacetime of an isolated mass distribution by a black hole. Actually, this step involves some averaging procedure to replace an object with a complicated structure by a simpler one. Due to the difficulties of averaging discussed above, we simply assume that a black hole is a good approximation for isolated massive objects without providing a mathematical justification. This leads to another fitting problem: What is the correct mass of a black hole fitted to the galaxy? As discussed by Korzyński [Kor15], the mass of a multi-scale structure is strongly influenced by the distribution of the masses. However, this problem will not be discussed in this thesis.

The advantage of black holes over other localised matter distributions is that are the simplest solutions to Einstein's equations describing a massive object. Black holes are solutions to the vacuum equations so that we do not have to deal with any matter equations. This simplifies the problem a lot. However, the full system of Einstein's equations is hard to solve even in the vacuum case. There are several solutions known for single black holes. For example the static, spherically symmetric Schwarzschild black hole or the Kerr spacetime of a rotating black hole. However, there are no known time-dependent solutions describing two or more black holes. The two-body problem in general relativity can only be treated approximatively by numerical methods or post-Newtonian expansions. For this reason, we divide the problem into two steps. Instead of solving the full system, we consider the initial value problem and determine only the initial data for a multi-black-hole configuration. In this case, exact solutions can be found. The next step would be the evolution of this data but in this thesis, we concentrate on the first step.

In the four-dimensional covariant formulation of electrodynamics, Maxwell's equations are given by $\mathbf{d}\boldsymbol{F} = 0$ and $\mathbf{d}{*}\boldsymbol{F} = 4\pi * \boldsymbol{J}$, where $\boldsymbol{F}$ is the electromagnetic field strength and $\boldsymbol{J}$ the 4-current. Applying a 3+1 split of spacetime, we obtain Maxwell's equations in their well-known form

$$\nabla \cdot \boldsymbol{E} = 4\pi\rho, \qquad \nabla \cdot \boldsymbol{B} = 0, \tag{1.3a}$$

$$\nabla \times \boldsymbol{E} = -\partial_t \boldsymbol{B}, \qquad \nabla \times \boldsymbol{B} = 4\pi \boldsymbol{j} + \partial_t \boldsymbol{B}. \tag{1.3b}$$

The second line are the evolution equations for the electric and magnetic field, whereas the equations in the first line constrain the initial data. Similarly, Einstein's equations can be decomposed into constraint and evolution equations. The three-dimensional time-dependent fields in General Relativity are the spatial metric $\bar{\boldsymbol{g}}$ and the extrinsic curvature $\bar{\boldsymbol{K}}$. These fields cannot be chosen freely but they are restricted by the Hamiltonian and momentum constraints.

In order to simplify the constraint equations further, we assume that the spacetime possesses a time-symmetric hypersurface of constant time such that the black holes within this slice are momentarily at rest. Such data are characterised by the vanishing of the extrinsic curvature, $\bar{\boldsymbol{K}} \equiv 0$. In this case, the momentum constraints are identically satisfied.

In order to solve the Hamiltonian constraint, it is useful to make a conformal ansatz $\bar{\boldsymbol{g}} = \Psi^4 \tilde{\boldsymbol{g}}$ for the spatial metric. The conformal metric $\tilde{\boldsymbol{g}}$ can be chosen freely, whereas the conformal factor $\Psi$ is determined by the Hamiltonian constraint. In view of cosmology, the conformal metric is chosen to be the metric of a maximally symmetric space, of which there exist three families.

Surprisingly, the differential equation for $\Psi$ turns out to be linear. For this reason, we are able to construct solutions for an arbitrary number of black holes via the superposition principle. However, the non-linearity of Einstein's equation can still be noticed in the masses of the black holes. Each mass is determined by all black holes together. It turns out that the solutions for the three different possibilities for $\tilde{\boldsymbol{g}}$ describe the same metric, irrespective of the choice of the maximally symmetric space. For this reason, we concentrate on the spherical case. This in accordance with the fact that only a spherical dust universe possesses a time-symmetric slice.

Clearly, we do not expect that every configuration of black holes can be approximated well by a Friedmann dust universe. Our main goal is to answer the questions how to distribute the black holes on the hypersphere in order to get a Friedmann-like configuration and which dust universe is the best fit to Friedmann-like initial data. In view of the homogeneous mass distribution in cosmology, we expect that the black holes should be distributed somehow evenly on the hypersphere. Whereas regular configurations on the circle exist for an arbitrary number of points, such that the distance between two neighbouring points is the same for each pair, there is no general definition on uniform configurations on (hyper)spheres in higher dimensions. For example, there is only a finite number of non-prismatic spherical uniform polytopes in each dimension; in three dimensions, these are the 5 Platonic and 13 Archimedean solids.

Usually the notion of uniformity depends on the considered problem. There is a wide literature in mathematics and physics on this topic connected to keywords like *spherical t-design* or *Riesz s-energy*. It is also the seventh of Smale's 18 problems [Sma98], the follow-up of Hilbert's 23 problems. A well-known example in physics of this kind is the *Thomson problem*. In this case, the task is to find the best configuration of $N$ electrons on the 2-sphere such that the potential energy takes its minimum. Of course, the expectation is that the electrons distribute in such a way that they maximise their average distance. Hence, the potential energy should also be a good measure for the degree of uniformity.

For the special cases of $N = 4, 6, 8, 12, 20$, one might expect that this is achieved if the electrons are located on the vertices of inscribed Platonic solids; the tetrahedron, octahedron, cube, icosahedron, and dodecahedron, respectively. However, quite surprisingly, this is not true for the cube ($N = 8$) and dodecahedron ($N = 20$). This stresses our previous statement that the notion of uniformity depends on the considered problem.

An obvious generalisation of the Thomson problem is given by the search of configurations minimising the Riesz $s$-energy

$$E_s = \sum_A \sum_{B<A} \frac{1}{\|\boldsymbol{P}_A - \boldsymbol{P}_B\|^s}, \tag{1.4}$$

where $s = 1$ corresponds to the Thomson problem. The limit $s \to \infty$ is equivalent to the case of maximising the sum of the mutual distances, known as *Tammes problem*. In general, different choices of $s$ lead to different configurations. For further examples, see the review [AS03].

Since it is usually not possible to obtain the exact solution for the multi-black spacetime, an appropriate approximation is desirable. As discussed above, such an approximation is provided by the Lindquist-Wheeler models for regular configurations on the hypersphere and regular lattices. We will generalise this model for arbitrary initial configurations. In order to validate the approximation, we compare it with the results from the initial data solution.

After fitting a Friedmann dust universe to the initial data, the next important step would be to study the time evolution in order to investigate the deviation between the exact solution and the fitted Friedmann solution. This should give further insights if there are backreaction effects. For example, the time evolution could show an accelerated expansion although we have omitted a cosmological constant. However, this topic is mostly omitted in this thesis.

### Outline

We start in chapter 2 with the description of the 3+1 formalism of general relativity and the initial value problem using the Cartan structure equations. In order to solve the constraint equations we describe the conformal method.

The next chapter 3 provides a unified description of points and circles in maximally symmetric spaces. After a brief review of maximally symmetric spaces and their connection to each other by a stereographic projection, we present the formalism of Möbius and Lie sphere geometry. Finally, we construct most spherical uniform polytopes and Apollonian sphere packings. The latter serve as possible configurations for a wide range of multi-black hole configurations. An example is shown on the cover.

In chapter 4 we briefly review cosmological spacetimes, with focus on dust solutions. First examples of inhomogeneous models are considered in chapter 5. These are the Swiss-cheese models and our generalisation of the Lindquist-Wheeler approximation. The multi-black hole solutions are derived in chapter 6. We find three seemingly different solutions, which turn out to describe the same space. We close this chapter with the description of their most important properties.

The fitting problem is treated in chapter 7. We discuss several possibilities for the size of the fitted universe. Finally, we present a new criterion for Friedmann-like configurations in a spherical inhomogeneous universe. This criterion is based on the total mass of the black holes, providing a solution to the fitting problem. The conclusions are supported by numerical results for several example configurations in chapter 8.

Finally, we give an outlook on the time evolution in chapter 9. We discuss earlier results, our expectations and some problems which have to be taken into account if one wants to study the time evolution. We also mention an interesting observation related to Newtonian dynamics. At last, we summarise the results in chapter 10 and discuss open questions.

# 2 Initial Value Formulation of General Relativity

As described in the introduction, we are looking for a solution to Einstein's equations serving as a model for an inhomogeneous cosmology. Einstein's equations [Ein15; Ein16]

$$R[g]_{\mu\nu} - \tfrac{1}{2}\mathcal{R}[g]\, g_{\mu\nu} + \Lambda\, g_{\mu\nu} = 8\pi\, T_{\mu\nu} \tag{2.1}$$

form a system of ten coupled non-linear second-order partial differential equations for the ten components of the spacetime metric $g_{\mu\nu}$.

The gravitational interaction is represented by the curvature of the spacetime which is encoded in the *Riemann curvature tensor*

$$R[g]^{\lambda}{}_{\rho\mu\nu} = \partial_\mu \Gamma[g]^{\lambda}{}_{\rho\nu} - \partial_\nu \Gamma[g]^{\lambda}{}_{\rho\mu} + \Gamma[g]^{\lambda}{}_{\mu\sigma}\, \Gamma[g]^{\sigma}{}_{\rho\nu} - \Gamma[g]^{\lambda}{}_{\nu\sigma}\, \Gamma[g]^{\sigma}{}_{\rho\nu}, \tag{2.2}$$

where $\Gamma[g]^{\lambda}{}_{\mu\nu}$ are the Christoffel symbols of the Levi-Civita connection $\nabla[g]_\mu$ with respect to metric $g_{\mu\nu}$. The components of the Christoffel symbols are given by

$$\Gamma[g]^{\lambda}{}_{\mu\nu} = \frac{1}{2} g^{\lambda\rho} \left( \partial_\mu g_{\rho\nu} + \partial_\nu g_{\mu\rho} - \partial_\rho g_{\mu\nu} \right). \tag{2.3}$$

The *Ricci tensor* $R[g]_{\mu\nu}$ is the contraction of the curvature tensor, which is unique up to a sign. The *Ricci scalar* $\mathcal{R}[g]$ is the trace of the Ricci tensor with respect to metric. They are given by

$$R[g]_{\mu\nu} = R[g]^{\lambda}{}_{\mu\lambda\nu}, \tag{2.4a}$$

$$\mathcal{R}[g] = g^{\mu\nu} R[g]_{\mu\nu}. \tag{2.4b}$$

The energy-momentum tensor of matter $T_{\mu\nu}$ serves as the source of spacetime curvature and determines the geometry of spacetime by Einstein's equations. The energy-momentum tensor satisfies the so-called *energy-momentum conservation*

$$\nabla[g]_\lambda\, T^{\mu\lambda} = 0. \tag{2.5}$$

This is actually no real conservation law because of the covariant derivative. In general, it does not yield any conserved quantities.

The actual form of $T_{\mu\nu}$ depends on the matter model. We are mainly interested in a vacuum solution where $T_{\mu\nu} \equiv 0$. In the case of cosmology, matter is modelled as an ideal fluid whose energy-momentum tensor is

$$T^{\mu\nu}_{(\text{fluid})} = (\rho + p)\, u^\mu u^\nu + p\, g^{\mu\nu}. \tag{2.6}$$

Here $\rho$ is the fluid density, $p$ its pressure and $\boldsymbol{u}$ the corresponding velocity field. The equations of motion are given by the conservation laws $\nabla[g]_\lambda\, T^{\mu\lambda} = 0$, known as the

*relativistic Euler equations*. Actually, the dynamics of such a system can only be determined if an *equation of state* is imposed giving a relation between the density and pressure, for example, $p = w\rho$ in cosmology.

The only missing term in eq. (2.1) is the one containing the *cosmological constant* $\Lambda$. It can be interpreted either as part of the geometry or as the energy-momentum tensor of vacuum. In the former case it is written on the left-hand side as in eq. (2.1) whereas in the latter case it appears on the right side as

$$T^{(\mathrm{vac})}_{\mu\nu} = -\frac{\Lambda}{8\pi G}\, g_{\mu\nu}. \tag{2.7}$$

In this work we neglect the cosmological constant most of the time and set $\Lambda \equiv 0$.

Further details on the motivation and derivation of Einstein's equations and the mathematical background on differential geometry can be found in any introductory textbook on general relativity, for example, the standard book *Gravitation* by Misner, Thorne and Wheeler [MTW73]; we recommend the book of Straumann [Str12].

Because of the complexity of Einstein's equations, it is very difficult to find a solution for a specific model. For example, we know the full solution for a single black hole or some compact objects like the Tolman-Oppenheimer-Volkoff stars. But we do not know the exact solution for a spacetime containing multiple such objects. Due to the non-linear nature of the field equations, we cannot apply the superposition principle to combine multiple solutions. There is no general procedure known to construct such spacetimes. For this reason we restrict ourselves to the initial value problem to find a solution on a single spatial hypersurface of constant time.

We derive all necessary equations of the 3+1 decomposition of general relativity in the second section 2.2 of this chapter. In doing so, we work within the framework of the Cartan structure equations presented beforehand in the first section 2.1. Although the equations of the initial value problem are much simpler in their structure than the full Einstein system, they are still very complicated and not simple to solve in general. Fortunately, there is an approach known as the *conformal method* which simplifies our problem further. It is described in section 2.3.

## 2.1 Cartan Structure Equations

Here we present an overview of the Cartan structure equations and related topics. For this reason we state the most important facts for this work but most proofs are left out. A detailed discussion can be found in many mathematical textbooks on differential geometry and in some textbooks on general relativity. We follow the book of Straumann [Str12].

Let $\mathcal{M}$ be 4-dimensional $C^\infty$-manifold, the *spacetime*, $\Gamma\mathrm{T}\mathcal{M}$ the set of vector fields, $\Gamma\mathrm{T}^*\mathcal{M}$ the set of 1-form fields and $\Gamma\mathrm{T}^a_b\mathcal{M}$ the set of tensor fields of rank $(a, b)$ on $\mathcal{M}$. If $\boldsymbol{e}_\mu \in \Gamma\mathrm{T}\mathcal{M}$ are basis vector fields and $\boldsymbol{\theta}^\mu \in \Gamma\mathrm{T}^*\mathcal{M}$ the basis 1-form fields, we can write a tensor $\boldsymbol{S} \in \Gamma\mathrm{T}^2_1\mathcal{M}$ as $\boldsymbol{S} = S^{\lambda\mu}{}_\nu\, \boldsymbol{e}_\lambda \otimes \boldsymbol{e}_\mu \otimes \boldsymbol{\theta}^\nu$.

### Metric

On a spacetime manifold there exists a symmetric, non-degenerate bilinear form on the tangent spaces of spacetime at every point with signature $(-,+,+,+)$. This bilinear form is a covariant tensor field $\boldsymbol{g}$, called the *Lorentzian metric* of spacetime. As explained above, the metric is determined by the Einstein field equations 2.1.

The inverse metric $\boldsymbol{g}^{-1}$, denoted by $g^{\mu\nu}$ when components are used, is defined by the condition

$$g^{\mu\lambda} g_{\lambda\nu} = \delta^\mu_\nu. \tag{2.8}$$

It provides a symmetric bilinear form on the cotangent spaces at every point. The metric $\boldsymbol{g}$ and its inverse $\boldsymbol{g}^{-1}$ can be used to raise and lower indices because they give maps from the tangent space to the cotangent space and vice versa. So we have $\boldsymbol{x}^\flat = \boldsymbol{g}(\boldsymbol{x}, \cdot\,) \in \Gamma\mathrm{T}^*\mathcal{M}$ for $\boldsymbol{x} \in \Gamma\mathrm{T}\mathcal{M}$ or in components $x_\mu = g_{\mu\nu} x^\nu$. Analogously for 1-forms.

It is often useful to work with an orthonormal basis $\boldsymbol{e}_\nu$ together with the corresponding dual basis 1-form fields $\boldsymbol{\theta}^\mu$ such that $\boldsymbol{\theta}^\mu(\boldsymbol{e}_\nu) = \delta^\mu_\nu$. In this case the metric takes the simple form

$$\boldsymbol{g} = -\boldsymbol{\theta}^0 \otimes \boldsymbol{\theta}^0 + \sum_{a=1}^{3} \boldsymbol{\theta}^a \otimes \boldsymbol{\theta}^a. \tag{2.9}$$

so that the components $g_{\mu\nu} = \mathrm{diag}\,(-1, 1, 1, 1)$ are constant. Note that there is always an orthonormal basis $\boldsymbol{e}_\mu$ locally, but usually there are no coordinate vector basis fields $\boldsymbol{\partial}_\mu$ such that $\boldsymbol{e}_\mu = \boldsymbol{\partial}_\mu$. It is possible to find coordinates such that $\boldsymbol{e}_\mu = \boldsymbol{\partial}_\mu$ for a set of basis vector fields $\boldsymbol{e}_\mu$ (not necessarily orthonormal) only if all Lie brackets of the basis vector fields vanish, $[\boldsymbol{e}_\mu, \boldsymbol{e}_\nu] = 0$. However, in general we have $[\boldsymbol{e}_\mu, \boldsymbol{e}_\nu] = C^\lambda{}_{\mu\nu}\, \boldsymbol{e}_\lambda$.

### Covariant Derivative

Furthermore, we have another structure on the spacetime: The *affine connection* $\nabla$ defining a covariant derivative $\nabla_{\boldsymbol{x}} \boldsymbol{T}$ of any tensor $\boldsymbol{T} \in \Gamma\mathrm{T}^a_b\mathcal{M}$ in the direction $\boldsymbol{x} \in \Gamma\mathrm{T}\mathcal{M}$ such that $\nabla_{\boldsymbol{x}} \boldsymbol{T} \in \Gamma\mathrm{T}^a_b\mathcal{M}$ is again a tensor of the same type. The covariant derivative has the following properties:

(i) It is $C^\infty(\mathcal{M})$-linear in $\boldsymbol{x}$ so that $\nabla_{f\boldsymbol{x}} \boldsymbol{T} = f\, \nabla_{\boldsymbol{x}} \boldsymbol{T}$.

(ii) On functions we have $\nabla_{\boldsymbol{x}} f = \boldsymbol{x}(f) = \mathbf{d}f(\boldsymbol{x})$.

(iii) It satisfies the Leibniz rule $\nabla_{\boldsymbol{x}}(\boldsymbol{S} \otimes \boldsymbol{T}) = (\nabla_{\boldsymbol{x}} \boldsymbol{S}) \otimes \boldsymbol{T} + \boldsymbol{S} \otimes (\nabla_{\boldsymbol{x}} \boldsymbol{T})$.

(iv) It commutes with contractions.

Next we introduce the *connection 1-forms* $\boldsymbol{\omega}^\mu{}_\nu$ which are defined by

$$\nabla_{\boldsymbol{e}_\mu} \boldsymbol{e}_\nu = \boldsymbol{\omega}^\lambda{}_\nu(\boldsymbol{e}_\mu)\, \boldsymbol{e}_\lambda. \tag{2.10}$$

In a coordinate basis $\boldsymbol{\partial}_\mu$, the components $\omega^\lambda{}_{\mu\nu}$ of $\boldsymbol{\omega}^\lambda{}_\mu = \omega^\lambda{}_{\mu\nu}\, \boldsymbol{\theta}^\nu$ are also denoted as $\Gamma^\lambda{}_{\mu\nu}$. The connection 1-forms are no tensors because they transform inhomogeneously under a change of basis $\bar{\boldsymbol{\theta}}^\mu = A^\mu{}_\lambda\, \boldsymbol{\theta}^\lambda$ as

$$\bar{\boldsymbol{\omega}}^\mu{}_\nu = A^\mu{}_\rho \boldsymbol{\omega}^\rho{}_\sigma (A^{-1})^\sigma{}_\nu - \mathbf{d}A^\mu{}_\lambda (A^{-1})^\lambda{}_\nu. \tag{2.11}$$

As a consequence, in a coordinate basis the connection coefficients transform under the change of coordinates $x^\mu \mapsto \bar{x}^\mu(x)$ as

$$\bar{\Gamma}^\lambda{}_{\mu\nu} = \frac{\partial x^\rho}{\partial \bar{x}^\mu} \frac{\partial x^\sigma}{\partial \bar{x}^\nu} \frac{\partial \bar{x}^\lambda}{\partial x^\tau}\, \Gamma^\tau{}_{\rho\sigma} + \frac{\partial^2 x^\rho}{\partial \bar{x}^\mu \partial \bar{x}^\nu} \frac{\partial \bar{x}^\lambda}{\partial x^\rho}. \tag{2.12}$$

Note that the difference of two connections forms is a tensor because the second term in their transformation behaviour cancels.

For the covariant derivative of a vector field $\boldsymbol{y} = Y^\lambda \, \boldsymbol{e}_\lambda$ we obtain

$$\begin{aligned} \nabla_{\boldsymbol{e}_\mu} \boldsymbol{y} &= \nabla_{\boldsymbol{e}_\mu}(Y^\lambda \boldsymbol{e}_\lambda) = (\nabla_{\boldsymbol{e}_\mu} Y^\lambda)\, \boldsymbol{e}_\lambda + Y^\lambda \nabla_{\boldsymbol{e}_\mu} \boldsymbol{e}_\lambda \\ &= \left[ (\mathbf{d}Y^\lambda + Y^\nu \, \boldsymbol{\omega}^\lambda{}_\nu)(\boldsymbol{e}_\mu) \right] \boldsymbol{e}_\lambda \equiv \left( \nabla_\mu y^\lambda \right) \boldsymbol{e}_\lambda . \end{aligned} \tag{2.13}$$

Since the covariant derivation commutes with contractions we obtain for a 1-form $\boldsymbol{\alpha} = \alpha_\beta \, \boldsymbol{\theta}^\beta$

$$\nabla_{\boldsymbol{e}_\mu}(\boldsymbol{\alpha}(\boldsymbol{e}_\nu)) = \boldsymbol{\alpha}(\nabla_{\boldsymbol{e}_\mu} \boldsymbol{e}_\nu) + (\nabla_{\boldsymbol{e}_\mu} \boldsymbol{\alpha})(\boldsymbol{e}_\nu). \tag{2.14}$$

Hence, we obtain for the covariant derivative of a 1-form

$$\begin{aligned} (\nabla_{\boldsymbol{e}_\mu} \boldsymbol{\alpha})(\boldsymbol{e}_\nu) &= \boldsymbol{e}_\mu(\boldsymbol{\alpha}(\boldsymbol{e}_\nu)) - \boldsymbol{\alpha}(\nabla_{\boldsymbol{e}_\mu} \boldsymbol{e}_\nu) = \boldsymbol{e}_\mu(\alpha_\nu) - \boldsymbol{\alpha}\left( \boldsymbol{\omega}^\lambda{}_\nu(\boldsymbol{e}_\mu)\, \boldsymbol{e}_\lambda \right) \\ &= (\mathbf{d}\alpha_\nu - \alpha_\lambda \, \boldsymbol{\omega}^\lambda{}_\nu)(\boldsymbol{e}_\mu) \equiv \nabla_\mu \alpha_\nu . \end{aligned} \tag{2.15}$$

For a general tensor $\boldsymbol{S} = S^\mu{}_\nu \, \boldsymbol{e}_\mu \otimes \boldsymbol{\theta}^\nu$ we obtain

$$\nabla_{\boldsymbol{e}_\lambda} \boldsymbol{S} = \left[ \left( \mathbf{d}S^\mu{}_\nu + S^\rho{}_\nu \, \boldsymbol{\omega}^\mu{}_\rho - S^\mu{}_\rho \, \boldsymbol{\omega}^\rho{}_\nu \right) (\boldsymbol{e}_\lambda) \right] \boldsymbol{e}_\mu \otimes \boldsymbol{\theta}^\nu \equiv (\nabla_\lambda S^\mu{}_\nu)\, \boldsymbol{e}_\mu \otimes \boldsymbol{\theta}^\nu . \tag{2.16}$$

Analogously for further indices.

**Torsion and Curvature**

For an affine connection we can define the *torsion* $\boldsymbol{T} : \Gamma\mathrm{T}\mathcal{M} \times \Gamma\mathrm{T}\mathcal{M} \longrightarrow \Gamma\mathrm{T}\mathcal{M}$ by

$$\boldsymbol{T}(\boldsymbol{x}, \boldsymbol{y}) = \nabla_{\boldsymbol{x}} \boldsymbol{y} - \nabla_{\boldsymbol{y}} \boldsymbol{x} - [\boldsymbol{x}, \boldsymbol{y}] , \tag{2.17}$$

and the *curvature* $\boldsymbol{R} : \Gamma\mathrm{T}\mathcal{M} \times \Gamma\mathrm{T}\mathcal{M} \times \Gamma\mathrm{T}\mathcal{M} \longrightarrow \Gamma\mathrm{T}\mathcal{M}$ by

$$\boldsymbol{R}(\boldsymbol{x}, \boldsymbol{y})\, \boldsymbol{z} = \nabla_{\boldsymbol{x}}(\nabla_{\boldsymbol{y}} \boldsymbol{z}) - \nabla_{\boldsymbol{y}}(\nabla_{\boldsymbol{x}} \boldsymbol{z}) - \nabla_{[\boldsymbol{x}, \boldsymbol{y}]} \boldsymbol{z} . \tag{2.18}$$

It can be easily verified that the torsion and curvature are antisymmetric in the sense that $\boldsymbol{T}(\boldsymbol{x}, \boldsymbol{y}) = -\boldsymbol{T}(\boldsymbol{x}, \boldsymbol{y})$ and $\boldsymbol{R}(\boldsymbol{x}, \boldsymbol{y})\boldsymbol{z} = -\boldsymbol{R}(\boldsymbol{y}, \boldsymbol{x})\boldsymbol{z}$. Their components are obtained from $T^\lambda{}_{\mu\nu} = \boldsymbol{\theta}^\lambda(\boldsymbol{T}(\boldsymbol{e}_\mu, \boldsymbol{e}_\nu))$ and $R^\lambda{}_{\rho\mu\nu} = \boldsymbol{\theta}^\lambda(\boldsymbol{R}(\boldsymbol{e}_\mu, \boldsymbol{e}_\nu)\, \boldsymbol{e}_\rho)$, yielding

$$T^\lambda{}_{\mu\nu} = \omega^\lambda{}_{\mu\nu} - \omega^\lambda{}_{\nu\mu} - C^\lambda{}_{\mu\nu} , \tag{2.19}$$

$$R^\lambda{}_{\rho\mu\nu} = \boldsymbol{e}_\mu(\omega^\lambda{}_{\nu\rho}) - \boldsymbol{e}_\nu(\omega^\lambda{}_{\mu\rho}) + \omega^\lambda{}_{\mu\sigma} \, \omega^\sigma{}_{\nu\rho} - \omega^\lambda{}_{\nu\sigma} \, \omega^\sigma{}_{\mu\rho} - C^\sigma{}_{\mu\nu} \, \omega^\lambda{}_{\sigma\rho} . \tag{2.20}$$

In a coordinate basis, where $C^\lambda{}_{\mu\nu} = 0$ and $\omega^\lambda{}_{\mu\nu} = \Gamma^\lambda{}_{\mu\nu}$, the components of the curvature reduce to the form of eq. (2.2) shown above.

Without further conditions the affine connection is not defined uniquely on the spacetime. For this reason we demand that the connection is torsion-free $\boldsymbol{T}(\boldsymbol{x}, \boldsymbol{y}) \equiv 0$ or

$$\nabla_{\boldsymbol{x}} \boldsymbol{y} - \nabla_{\boldsymbol{y}} \boldsymbol{x} = [\boldsymbol{x}, \boldsymbol{y}] . \tag{2.21}$$

In a coordinate basis, eq. (2.19) shows that the Christoffel symbols are symmetric in the lower indices in this case, $\Gamma^\lambda{}_{\mu\nu} = \Gamma^\lambda{}_{\nu\mu}$, therefore a torsion-free connection is also called to be *symmetric*.

As a second condition, we demand that the covariant derivative of the metric vanishes

$$\nabla_{\boldsymbol{x}}\boldsymbol{g} \equiv 0, \tag{2.22}$$

which is equivalent to the Ricci identity

$$\boldsymbol{x}(\boldsymbol{g}(\boldsymbol{y},\boldsymbol{z})) = \boldsymbol{g}(\nabla_{\boldsymbol{x}}\boldsymbol{y},\boldsymbol{z}) + \boldsymbol{g}(\boldsymbol{y},\nabla_{\boldsymbol{x}}\boldsymbol{z}). \tag{2.23}$$

Such a connection is called *metric* connection.

These two conditions allow us to find a unique connection as stated in the following theorem:

**Theorem 2.1.** ***Levi-Civita connection***
*The* Levi-Civita connection $\nabla[g]$ *is defined uniquely on a spacetime with metric* $\boldsymbol{g}$ *as the only torsion-free (symmetric) and metric connection. Its connection coefficients are given by*

$$\Gamma[g]^{\lambda}{}_{\mu\nu} = \frac{1}{2}g^{\lambda\rho}\left(\partial_\mu g_{\rho\nu} + \partial_\nu g_{\mu\rho} - \partial_\rho g_{\mu\nu}\right). \tag{2.24}$$

*They are referred to as* Christoffel symbols.

#### Tensor-Valued $p$-forms

Now we change our point of view slightly: Instead of tensors we consider tensor-valued differential forms on spacetime. These are differential forms which map vector fields to tensor components rather than functions. A common tensor can be interpreted as a tensor-valued 0-form. Consider for example a tensor $\boldsymbol{S} \in \Gamma\mathrm{T}^1_3\mathcal{M}$ which is antisymmetric in its first two indices and thus can be written as

$$\boldsymbol{S} = \frac{1}{2}S_{\mu\nu\rho}{}^{\lambda}\,\boldsymbol{\theta}^\mu \wedge \boldsymbol{\theta}^\nu \otimes \boldsymbol{\theta}^\rho \otimes \boldsymbol{e}_\lambda \equiv \boldsymbol{\Phi}_\rho{}^\lambda \otimes \boldsymbol{\theta}^\rho \otimes \boldsymbol{e}_\lambda. \tag{2.25}$$

Then we call $\boldsymbol{\Phi}_\rho{}^\lambda = \frac{1}{2}S_{\mu\nu\rho}{}^{\lambda}\,\boldsymbol{\theta}^\mu \wedge \boldsymbol{\theta}^\nu$ a $(1,1)$-tensor-valued 2-form.

We have already introduced two further examples: the torsion and the curvature. We can define the torsion 1-form $\boldsymbol{\Theta}^\mu$ and the curvature 2-form $\boldsymbol{\Omega}^\mu{}_\nu$ by

$$\boldsymbol{T}(\boldsymbol{x},\boldsymbol{y}) = \boldsymbol{\Theta}^\mu(\boldsymbol{x},\boldsymbol{y})\,\boldsymbol{e}_\mu, \tag{2.26}$$

$$\boldsymbol{R}(\boldsymbol{x},\boldsymbol{y})\,\boldsymbol{e}_\nu = \boldsymbol{\Omega}^\mu{}_\nu(\boldsymbol{x},\boldsymbol{y})\,\boldsymbol{e}_\mu, \tag{2.27}$$

such that $\boldsymbol{\Theta}^\mu = \frac{1}{2}T^\mu{}_{\lambda\rho}\,\boldsymbol{\theta}^\lambda \wedge \boldsymbol{\theta}^\rho$ and $\boldsymbol{\Omega}^\mu{}_\nu = \frac{1}{2}R^\mu{}_{\nu\lambda\rho}\,\boldsymbol{\theta}^\lambda \wedge \boldsymbol{\theta}^\rho$. The main reason why we consider these objects is the following theorem:

**Theorem 2.2.** ***Cartan structure equations.***
*The torsion 1-form and the curvature 2-form satisfy the* Cartan structure equations

$$\boldsymbol{\Theta}^\mu = \mathrm{d}\boldsymbol{\theta}^\mu + \boldsymbol{\omega}^\mu{}_\lambda \wedge \boldsymbol{\theta}^\lambda, \tag{2.28a}$$

$$\boldsymbol{\Omega}^\mu{}_\nu = \mathrm{d}\boldsymbol{\omega}^\mu{}_\nu + \boldsymbol{\omega}^\mu{}_\lambda \wedge \boldsymbol{\omega}^\lambda{}_\nu, \tag{2.28b}$$

*where* $\boldsymbol{\theta}^\mu$ *are the basis 1-forms and* $\boldsymbol{\omega}^\mu{}_\nu$ *the connection 1-forms.*

The proof is just the rewriting of the definition of the torsion and curvature using the formula eq. (2.13) for the covariant derivative of a vector and the identity

$$\mathbf{d}\boldsymbol{\alpha}(\boldsymbol{x},\boldsymbol{y}) = \boldsymbol{x}(\boldsymbol{\alpha}(\boldsymbol{y})) - \boldsymbol{y}(\boldsymbol{\alpha}(\boldsymbol{x})) - \boldsymbol{\alpha}([\boldsymbol{x},\boldsymbol{y}]) \tag{2.29}$$

for 1-forms $\boldsymbol{\alpha}$. So we have for the torsion

$$\begin{aligned}
\boldsymbol{\Theta}^{\mu}(\boldsymbol{x},\boldsymbol{y})\,\boldsymbol{e}_{\mu} &= \boldsymbol{T}(\boldsymbol{x},\boldsymbol{y}) = \nabla_{\boldsymbol{x}}\boldsymbol{y} - \nabla_{\boldsymbol{y}}\boldsymbol{x} - [\boldsymbol{x},\boldsymbol{y}] \\
&= \nabla_{\boldsymbol{x}}(\boldsymbol{\theta}^{\mu}(\boldsymbol{y})\,\boldsymbol{e}_{\mu}) - \nabla_{\boldsymbol{y}}(\boldsymbol{\theta}^{\mu}(\boldsymbol{x})\,\boldsymbol{e}_{\mu}) - \boldsymbol{\theta}^{\mu}([\boldsymbol{x},\boldsymbol{y}])\,\boldsymbol{e}_{\mu} \\
&= (\boldsymbol{x}(\boldsymbol{\theta}^{\mu}(\boldsymbol{y})) - \boldsymbol{y}(\boldsymbol{\theta}^{\mu}(\boldsymbol{x})) - \boldsymbol{\theta}^{\mu}([\boldsymbol{x},\boldsymbol{y}]))\;\boldsymbol{e}_{\mu} \\
&\quad + \Big(\boldsymbol{\theta}^{\mu}(\boldsymbol{y})\,\boldsymbol{\omega}^{\lambda}{}_{\mu}(\boldsymbol{x}) - \boldsymbol{\theta}^{\mu}(\boldsymbol{x})\,\boldsymbol{\omega}^{\lambda}{}_{\mu}(\boldsymbol{y})\Big)\,\boldsymbol{e}_{\lambda} \\
&= \Big[\mathbf{d}\boldsymbol{\theta}^{\mu}(\boldsymbol{x},\boldsymbol{y}) + (\boldsymbol{\omega}^{\mu}{}_{\lambda} \wedge \boldsymbol{\theta}^{\lambda})(\boldsymbol{x},\boldsymbol{y})\Big]\,\boldsymbol{e}_{\mu},
\end{aligned} \tag{2.30}$$

and similarly for the curvature

$$\begin{aligned}
\boldsymbol{\Omega}^{\mu}{}_{\nu}(\boldsymbol{x},\boldsymbol{y})\,\boldsymbol{e}_{\mu} &= \boldsymbol{R}(\boldsymbol{x},\boldsymbol{y})\boldsymbol{e}_{\mu} = \nabla_{\boldsymbol{x}}\nabla_{\boldsymbol{y}}\boldsymbol{e}_{\nu} - \nabla_{\boldsymbol{y}}\nabla_{\boldsymbol{x}}\boldsymbol{e}_{\nu} - \nabla_{[\boldsymbol{x},\boldsymbol{y}]}\boldsymbol{e}_{\nu} \\
&= \nabla_{\boldsymbol{x}}(\boldsymbol{\omega}^{\mu}{}_{\nu}(\boldsymbol{y})\,\boldsymbol{e}_{\mu}) - \nabla_{\boldsymbol{y}}(\boldsymbol{\omega}^{\mu}{}_{\nu}(\boldsymbol{x})\,\boldsymbol{e}_{\mu}) - \boldsymbol{\omega}^{\mu}{}_{\nu}([\boldsymbol{x},\boldsymbol{y}])\boldsymbol{e}_{\mu} \\
&= (\boldsymbol{x}(\boldsymbol{\omega}^{\mu}{}_{\nu}(\boldsymbol{y})) - \boldsymbol{y}(\boldsymbol{\omega}^{\mu}{}_{\nu}(\boldsymbol{x})) - \boldsymbol{\omega}^{\mu}{}_{\nu}([\boldsymbol{x},\boldsymbol{y}]))\,\boldsymbol{e}_{\mu} \\
&\quad + \Big(\boldsymbol{\omega}^{\mu}{}_{\nu}(\boldsymbol{y})\,\boldsymbol{\omega}^{\lambda}{}_{\mu}(\boldsymbol{x}) - \boldsymbol{\omega}^{\mu}{}_{\nu}(\boldsymbol{x})\,\boldsymbol{\omega}^{\lambda}{}_{\mu}(\boldsymbol{y})\Big)\,\boldsymbol{e}_{\lambda} \\
&= \Big[\mathbf{d}\boldsymbol{\omega}^{\mu}{}_{\nu}(\boldsymbol{x},\boldsymbol{y}) + (\boldsymbol{\omega}^{\mu}{}_{\lambda} \wedge \boldsymbol{\omega}^{\lambda}{}_{\nu})(\boldsymbol{x},\boldsymbol{y})\Big]\,\boldsymbol{e}_{\mu}.
\end{aligned} \tag{2.31}$$

For tensor-valued $p$-forms $\boldsymbol{\Phi}^{\mu}{}_{\nu}$ we can introduce the *exterior covariant derivative* $\mathbf{D}\boldsymbol{\Phi}^{\mu}{}_{\nu}$ which yields a $(p+1)$-form. It is defined through

$$\mathbf{D}\boldsymbol{\Phi}^{\mu}{}_{\nu} = \mathbf{d}\boldsymbol{\Phi}^{\mu}{}_{\nu} + \boldsymbol{\omega}^{\mu}{}_{\lambda} \wedge \boldsymbol{\Phi}^{\lambda}{}_{\nu} - \boldsymbol{\omega}^{\lambda}{}_{\nu} \wedge \boldsymbol{\Phi}^{\mu}{}_{\lambda}. \tag{2.32}$$

For a general tensor-valued form with an arbitrary number of indices we have to add further terms per index in the same manner. The exterior covariant derivative is a generalisation of the exterior and the covariant derivative: For a common $p$-form $\boldsymbol{\Phi}$, the exterior covariant derivative reduces to the usual exterior derivative $\mathbf{D}\boldsymbol{\Phi} = \mathbf{d}\boldsymbol{\Phi}$. While for a tensor, that is a tensor-valued 0-form $\boldsymbol{\Phi}^{\mu}{}_{\nu} = \Phi^{\mu}{}_{\nu}$, it reduces to the usual covariant derivative, $\mathbf{D}\boldsymbol{\Phi}^{\mu}{}_{\nu}(\boldsymbol{e}_{\lambda}) = \nabla_{\lambda}\Phi^{\mu}{}_{\nu}$. Furthermore, the exterior covariant derivative satisfies, suppressing indices,

$$\mathbf{D}(\boldsymbol{\Phi} \wedge \boldsymbol{\Psi}) = \mathbf{D}\boldsymbol{\Phi} \wedge \boldsymbol{\Psi} + (-1)^{p}\,\boldsymbol{\Phi} \wedge \mathbf{D}\boldsymbol{\Psi}, \tag{2.33}$$

where $\boldsymbol{\Phi}$ is a tensor-valued $p$-form and $\boldsymbol{\Psi}$ an arbitrary tensor-valued form. Obviously, the first Cartan structure equation (2.28a) can also be written as $\boldsymbol{\Theta}^{a} = \mathbf{D}\boldsymbol{\theta}^{a}$. We just remark that the torsion 1-form and the curvature 2-form satisfy the following identities

$$\mathbf{D}\boldsymbol{\Theta}^{\mu} = \boldsymbol{\Omega}^{\mu}{}_{\lambda} \wedge \boldsymbol{\theta}^{\lambda}, \tag{2.34a}$$

$$\mathbf{D}\boldsymbol{\Omega}^{\mu}{}_{\nu} = 0, \tag{2.34b}$$

known as the *Bianchi identities*.

At last we consider the Ricci identity (2.23) yielding

$$\begin{aligned}
\mathbf{d}g_{\mu\nu}(\boldsymbol{e}_{\lambda}) &= \boldsymbol{e}_{\lambda}(\boldsymbol{g}(\boldsymbol{e}_{\mu},\boldsymbol{e}_{\nu})) = \boldsymbol{g}(\nabla_{\boldsymbol{e}_{\lambda}}\boldsymbol{e}_{\mu},\boldsymbol{e}_{\nu}) + \boldsymbol{g}(\boldsymbol{e}_{\mu},\nabla_{\boldsymbol{e}_{\lambda}}\boldsymbol{e}_{\nu}) \\
&= \boldsymbol{g}(\boldsymbol{\omega}^{\rho}{}_{\mu}(\boldsymbol{e}_{\lambda})\,\boldsymbol{e}_{\rho},\boldsymbol{e}_{\nu}) + \boldsymbol{g}(\boldsymbol{e}_{\mu},\boldsymbol{\omega}^{\rho}{}_{\nu}(\boldsymbol{e}_{\lambda})\,\boldsymbol{e}_{\rho}) \\
&= \boldsymbol{\omega}^{\rho}{}_{\mu}(\boldsymbol{e}_{\lambda})\,g_{\rho\nu} + \boldsymbol{\omega}^{\rho}{}_{\nu}(\boldsymbol{e}_{\lambda})\,g_{\mu\rho} = \boldsymbol{\omega}_{\nu\mu}(\boldsymbol{e}_{\lambda}) + \boldsymbol{\omega}_{\mu\nu}(\boldsymbol{e}_{\lambda}),
\end{aligned} \tag{2.35}$$

so that the metric condition (2.22) can also be written as

$$\mathbf{D}g_{\mu\nu} = \mathbf{d}g_{\mu\nu} - \boldsymbol{\omega}_{\mu\nu} - \boldsymbol{\omega}_{\nu\mu} = 0. \tag{2.36}$$

For an orthonormal frame with $g_{ab} = \operatorname{diag}(-1, 1, 1, 1)$, we have $\mathbf{d}g_{ab} \equiv 0$ because the metric components are constant. Therefore the connection 1-forms with lowered indices have to be antisymmetric in this case: $\boldsymbol{\omega}_{ab} = -\boldsymbol{\omega}_{ab}$.

**Application in General Relativity**

The main purpose of this formalism is that it provides an efficient way to calculate the Riemann curvature tensor which is needed to write down Einstein's equations. In general relativity, we use the Levi-Civita connection. Since it is torsion-free, that is $\boldsymbol{\Theta}^\mu = \mathbf{D}\boldsymbol{\theta}^\mu \equiv 0$, the first Cartan structure equation (2.28a) simplifies to

$$\mathbf{d}\boldsymbol{\theta}^\mu = -\boldsymbol{\omega}^\mu{}_\lambda \wedge \boldsymbol{\theta}^\lambda. \tag{2.37}$$

We can solve these equations for the connection 1-forms. Demanding additionally the metricity condition (2.36), the solution of (2.37) has to be unique due to theorem 2.1. If we work in an orthonormal frame, we simply need to demand that the connection 1-forms with lowered indices are antisymmetric. In many cases the solution can be found by good guess.

Afterwards in the second step, we can use the connection 1-forms together with the second Cartan structure equation (2.28b) in order to calculate the curvature 2-forms $\boldsymbol{\Omega}^\mu{}_\nu$. Finally, the Riemann curvature tensor and its contraction are obtained from the curvature 2-forms via

$$R^\mu{}_{\nu\rho\sigma} = \boldsymbol{\Omega}^\mu{}_\nu(\boldsymbol{e}_\rho, \boldsymbol{e}_\sigma). \tag{2.38}$$

## 2.2 Decomposition of Einstein's Equations

The aim of this section is the decomposition of spacetime and the Einstein field equations as described by York Jr [Yor79]. The idea is to consider four-dimensional tensors on the spacetime $\mathcal{M}$ as tensors on a three-dimensional manifold $\bar{\Sigma}$ which are now time-dependent. From the decomposition of Einstein's equations we obtain equations for the spatial metric and a second field, the extrinsic curvature. Similar to electrodynamics these equations can be divided into evolution and constraint equations. The latter ones restrict the allowed field configurations, compare this to $\nabla \cdot \boldsymbol{E} = 4\pi\rho$ and $\nabla \cdot \boldsymbol{B} = 0$. It can be shown that the evolution equations preserve the constraints so that we only have to take them into account when formulating the initial data.

This formulation of general relativity is based on the work of Darmois [Dar27], Lichnerowicz [Lic39], Lichnerowicz [Lic44] and Lichnerowicz [Lic52] and Choquet-Bruhat[1] [Fou52; Fou56]. A review of this topic can be found for example in [Giu14] and [Ise14]. A detailed presentation is provided by many textbooks like the one of Gourgoulhon [Gou12][2] where also many details are discussed which will be mentioned here only. The derivations presented here follow loosely Straumann [Str12] using the methods from the previous section 2.1.

[1] Her name was Fourès-Bruhat at that time.

[2] The book of Gourgoulhon is based upon his lecture notes [Gou07] which are available online.

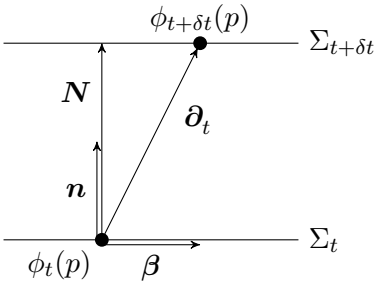


**Figure 2.1:** The vector field $\boldsymbol{\partial}_t = \boldsymbol{N} + \boldsymbol{\beta}$ is the tangent vector of the curve $\phi_t(p)$. The evolution vector $\boldsymbol{N} = \alpha\,\boldsymbol{n}$ shifts the hypersurface $\Sigma_t$ one step $\delta t$ further to $\Sigma_{t+\delta t}$ and it is proportional to the normal $\boldsymbol{n}$ of the hypersurface, where $\alpha$ is the lapse function. The tangential part of $\boldsymbol{\partial}_t$ is the shift vector field $\boldsymbol{\beta}$.

### Spacetime Structure and Adapted Basis Fields

We are interested in those spacetimes $\mathcal{M}$ on which the initial value problem of general relativity is well-posed; such spacetimes are called *globally hyperbolic*. It can be shown that the topology of these spacetimes has to be $\mathcal{M} = \bar{\Sigma} \times \mathbb{R}$. For this reason there exists a foliation of the spacetime by a family of hypersurfaces $\Sigma_t$. This means that we have a family of maps

$$\phi_t : \bar{\Sigma} \longmapsto \mathcal{M} \tag{2.39}$$

from a three-dimensional manifold $\bar{\Sigma}$ into the spacetime $\mathcal{M}$ for all $t \in \mathbb{R}$ such that $\mathcal{M} = \bigcup_{t\in\mathbb{R}} \Sigma_t$, where $\Sigma_t = \phi_t(\bar{\Sigma})$. This defines a function $\hat{t}$ on $\mathcal{M}$ by $\hat{t}(p) = t$ if $p \in \Sigma_t$. In the following we identify $\hat{t}$ and $t$ and dismiss the hat.

The vector field normal to the slices is denoted by $\boldsymbol{n}$. The corresponding normal 1-form field $\boldsymbol{n}^\flat$ must be proportional to $\mathbf{d}t$ such that

$$\boldsymbol{n}^\flat = -\alpha\,\mathbf{d}t. \tag{2.40}$$

The normalizing factor $\alpha$ is referred to as *lapse function*. We demand that the hypersurfaces $\Sigma_t$ are space-like, hence $\boldsymbol{g}^{-1}(\mathbf{d}t, \mathbf{d}t) < 0$. Tensor fields in the tensor space $\mathrm{T}^a_b\Sigma_t$ are called *tangential* or *spatial tensors*.

Furthermore we obtain the vector field $\boldsymbol{\partial}_t$ formed by the tangent vectors of the curves $\{\phi_t(p) : t \in \mathbb{R}\}$. There is no reason that $\boldsymbol{\partial}_t$ should be orthogonal to the hypersurfaces, but it may be decomposed into

$$\boldsymbol{\partial}_t = \alpha\,\boldsymbol{n} + \boldsymbol{\beta} = \boldsymbol{N} + \boldsymbol{\beta}, \tag{2.41}$$

where $\boldsymbol{\beta}$ is the tangential *shift vector field* and $\boldsymbol{N} = \alpha\,\boldsymbol{n}$ the *evolution vector field*, see also fig. 2.1. The vector field $\boldsymbol{N}$ shifts the hypersurface $\Sigma_t$ to the next one $\Sigma_{t+\delta t}$ because of

$$t(p + \delta t\,\boldsymbol{N}) = t(p) + \mathbf{d}t(\delta t\,\boldsymbol{N}) = t(p) - \delta t\,\boldsymbol{n}^\flat(\boldsymbol{n}) = t(p) + \delta t. \tag{2.42}$$

This shows that $p + \delta t\,\boldsymbol{N} \in \Sigma_{t+\delta t}$ if $p \in \Sigma_t$. In order to describe observers, the vector field $\boldsymbol{\partial}_t$ should be time-like, hence $\boldsymbol{g}(\boldsymbol{\partial}_t, \boldsymbol{\partial}_t) < 0$ or equivalently $\boldsymbol{g}(\boldsymbol{\beta}, \boldsymbol{\beta}) < \alpha^2$ because $\boldsymbol{n}$ and $\boldsymbol{\beta}$ are orthogonal.

The maps $\phi_t$ enable us to map vector fields from $\Gamma\mathrm{T}\bar{\Sigma}$ to $\Gamma\mathrm{T}\mathcal{M}$ by the push-forward $\phi_{t*}$ and 1-forms from $\Gamma\mathrm{T}^*\mathcal{M}$ to $\Gamma\mathrm{T}^*\bar{\Sigma}$ by the pull-back $\phi_t^*$. On $\Sigma_t$ the inverse $\phi_t^{-1}$ exists so that we have also $(\phi_t^{-1})_* : \Gamma\mathrm{T}\Sigma_t \mapsto \Gamma\mathrm{T}\bar{\Sigma}$ and $(\phi_t^{-1})^* : \Gamma\mathrm{T}^*\bar{\Sigma} \mapsto \Gamma\mathrm{T}^*\Sigma_t$.

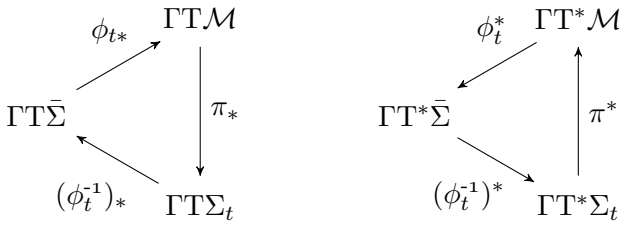


**Figure 2.2:** The foliation $\phi_t : \bar{\Sigma} \mapsto \mathcal{M}$ induces the pushforward $\phi_{t*}$ and the pullback $\phi_t^*$. On $\Sigma_t = \phi_t(\bar{\Sigma})$ there exists the inverse $\phi_t^{-1} : \Sigma_t \mapsto \bar{\Sigma}$ inducing the maps $(\phi_t^{-1})_*$ and $(\phi_t^{-1})^*$. The projection $\pi_*$ and the induced mapping $\pi^*$ close the cycle. A vector or a 1-form on $\mathcal{M}$ can be considered as tangential if they are invariant under a full cycle.

However, as shown fig. 2.2, we are missing a mapping that brings us from the tangent space of $\mathcal{M}$ to the one of the hypersurface $\Sigma_t$. This is done by the tangential projection $\pi_* : \Gamma T\mathcal{M} \mapsto \Gamma T\Sigma_t$ acting on tangential vectors $\boldsymbol{x} \in \Gamma T\Sigma_t \subset \Gamma T\mathcal{M}$ as the identity $\pi_*(\boldsymbol{x}) = \boldsymbol{x}$ and cancels the non-tangential part. Note that the specific form of $\pi_*$ depends on the given basis, see also below. The picture is completed by the induced mapping $\pi^* : \Gamma T^*\Sigma_t \mapsto \Gamma T^*\mathcal{M}$ on 1-form fields providing a continuation of tangential 1-forms to all vector fields on $\mathcal{M}$. It is defined like the pullback by $\pi^*\boldsymbol{\alpha}(\boldsymbol{x}) = \boldsymbol{\alpha}(\pi_*\boldsymbol{x})$ for $\boldsymbol{\alpha} \in \Gamma T^*\Sigma_t$ and $\boldsymbol{x} \in \Gamma T\mathcal{M}$.

Let us equip all spaces with basis fields. We start with basis vector fields $\bar{\boldsymbol{e}}_a \in \Gamma T\bar{\Sigma}$ and their dual basis 1-form fields $\bar{\boldsymbol{\theta}}^a \in \Gamma T^*\bar{\Sigma}$ on $\bar{\Sigma}$. Due to the above mappings we obtain a basis 1-form fields $\breve{\boldsymbol{\theta}}^a \in \Gamma T^*\Sigma_t$. On $\mathcal{M}$ we only get the three tangential vector fields $\boldsymbol{e}_a = \phi_{t*}\bar{\boldsymbol{e}}_a \in \Gamma T\mathcal{M}$. Of course, these vector fields are also elements of $\Gamma T\Sigma_t$ because $\pi_*$ acts on them as the identity such that $\breve{\boldsymbol{e}}_a = \pi_*\boldsymbol{e}_a = \boldsymbol{e}_a$. As one can easily check, $\breve{\boldsymbol{e}}_a$ and $\breve{\boldsymbol{\theta}}^a$ are dual. On the spacetime $\mathcal{M}$ we need a further vector field $\boldsymbol{e}_0$ which is not tangent to $\Sigma_t$ in order to obtain a complete set of basis vector fields $\boldsymbol{e}_\mu$ on $\mathcal{M}$. For these ones we can determine their dual 1-form fields $\boldsymbol{\theta}^\mu \in \Gamma T^*\mathcal{M}$. Again one easily proves that $\phi_t^*\boldsymbol{e}_a = \bar{\boldsymbol{e}}_a$ and $\phi_t^*\boldsymbol{e}_0 = 0$. If we define the projection by $\pi_*\boldsymbol{e}_a = \breve{\boldsymbol{e}}_a$ and $\pi_*\boldsymbol{e}_0 = 0$, it follows that $\pi^*\breve{\boldsymbol{\theta}}^a = \boldsymbol{\theta}^a$.

This shows that the tangential vector fields $\boldsymbol{e}_a, \bar{\boldsymbol{e}}_a, \breve{\boldsymbol{e}}_a$ and 1-form fields $\boldsymbol{\theta}^a, \bar{\boldsymbol{\theta}}^a, \breve{\boldsymbol{\theta}}^a$ are mapped to each other, respectively. In order to simplify the notation, we identify these fields. We indicate tangential tensor fields with a bar in order to distinguish them them from arbitrary tensor fields on the spacetime $\mathcal{M}$. For example, if we apply the pullback on the spacetime metric $\boldsymbol{g}$, we obtain the *spatial metric* $\bar{\boldsymbol{g}} = \phi_t^*\boldsymbol{g} = \bar{g}_{ab}\,\bar{\boldsymbol{\theta}}^a \otimes \bar{\boldsymbol{\theta}}^b$ on $\bar{\Sigma}$ or $\Sigma_t$, respectively. Using the projection operator, we can extend $\bar{\boldsymbol{g}}$ to the whole tangent space of spacetime as $\pi^*\bar{\boldsymbol{g}} = \bar{g}_{ab}\,\boldsymbol{\theta}^a \otimes \boldsymbol{\theta}^b$. As just mentioned, we use the same notation in both cases, so $\bar{\boldsymbol{g}} \equiv \pi^*\bar{\boldsymbol{g}} \neq \boldsymbol{g}$.

Next we select specific basis fields which we use in the decomposition of Einstein's equations. The tangential basis fields are chosen such that they are orthonormal. Such a basis with three tangential vectors and an arbitrary $\boldsymbol{e}_0$ is called *adapted* to the foliation. An obvious choice for $\boldsymbol{e}_0$ is the normal $\boldsymbol{n}$ so that the whole basis is orthonormal. This choice allows us to apply the methods from the previous section. In this basis the tangential projection $\pi_*$ is given by the orthogonal projection such that $\pi_*(\boldsymbol{x}) = \boldsymbol{x} + \boldsymbol{g}(\boldsymbol{x}, \boldsymbol{n})\,\boldsymbol{n}$. Since we use an orthonormal frame, the metric takes the form $\boldsymbol{g} = \eta_{\mu\nu}\,\boldsymbol{\theta}^\mu \otimes \boldsymbol{\theta}^\nu$ where $\eta_{\mu\nu} = \operatorname{diag}(-1, 1, 1, 1)$. We obtain the spatial metric by cancelling out the normal components

so that $\bar{\boldsymbol{g}} = \delta_{ab}\,\boldsymbol{\theta}^a \otimes \boldsymbol{\theta}^b = \boldsymbol{g} + \boldsymbol{n}^\flat \otimes \boldsymbol{n}^\flat$.

Finally we introduce a coordinate basis $\bar{\boldsymbol{\partial}}_a$ on $\bar{\Sigma}$ which are related to the orthonormal vector fields by $\bar{\boldsymbol{e}}_a = A^b{}_a\,\bar{\boldsymbol{\partial}}_b$. This basis is completed by $\boldsymbol{\partial}_t = \alpha\,\boldsymbol{n} + \bar{\boldsymbol{\beta}}$, which does not need to be orthogonal to the other basis vector fields $\bar{\boldsymbol{\partial}}_a$. We want to determine the dual basis 1-form fields $\{\mathbf{d}t, \mathbf{d}x^a\}$ in terms of the orthonormal basis. We still have $\boldsymbol{\theta}^0 = \alpha\,\mathbf{d}t$, whereas we obtain from the duality condition $\boldsymbol{\theta}^\mu(\boldsymbol{e}_\nu) = \delta^\mu_\nu$:

$$\delta^a_b = \boldsymbol{\theta}^a(\boldsymbol{e}_b) = A^c{}_b\,\boldsymbol{\theta}^a(\boldsymbol{\partial}_c), \tag{2.43a}$$

$$0 = \boldsymbol{\theta}^a(\boldsymbol{n}) = \boldsymbol{\theta}^a\left(\tfrac{1}{\alpha}\,\boldsymbol{\partial}_t - \tfrac{1}{\alpha}\,\boldsymbol{\beta}\right) = \tfrac{1}{\alpha}\,\boldsymbol{\theta}^a(\boldsymbol{\partial}_t) - \tfrac{1}{\alpha}\,\beta^a. \tag{2.43b}$$

Hence $\boldsymbol{\theta}^a(\boldsymbol{\partial}_t) = \beta^a$ and $\boldsymbol{\theta}^a(\boldsymbol{\partial}_b) = (A^{-1})^a{}_b$, and therefore $\boldsymbol{\theta}^a = (A^{-1})^a{}_b\,\mathbf{d}x^b + \beta^a\,\mathbf{d}t$. Note that the pullback is the same in both cases, $\phi_t^*\bar{\boldsymbol{\theta}}^a = \phi_t^*\,\mathbf{d}x^b$, because it cancels simply the $\mathbf{d}t$-terms. Altogether we have

$$\left\{\boldsymbol{e}_\mu\right\} = \{\boldsymbol{n}, \bar{\boldsymbol{e}}_a\} = \left\{\tfrac{1}{\alpha}\left(\bar{\boldsymbol{\partial}}_t - \boldsymbol{\beta}\right), A^b{}_a\,\bar{\boldsymbol{\partial}}_b\right\}, \tag{2.44a}$$

$$\{\boldsymbol{\theta}^\mu\} = \left\{-\boldsymbol{n}^\flat, \bar{\boldsymbol{\theta}}^a\right\} = \left\{\alpha\,\mathbf{d}t, (A^{-1})^a{}_b\,\mathbf{d}x^b + \beta^a\,\mathbf{d}t\right\}. \tag{2.44b}$$

In this basis, the spacetime metric is given by

$$\begin{aligned}\boldsymbol{g} &= \eta_{\mu\nu}\,\boldsymbol{\theta}^\mu \otimes \boldsymbol{\theta}^\nu \\ &= -\left(\alpha^2 - \beta_a\beta^a\right)\mathbf{d}t^2 + \beta_a\,(\mathbf{d}t \otimes \mathbf{d}x^a + \mathbf{d}x^a \otimes \mathbf{d}t) + \bar{g}_{ab}\,\mathbf{d}x^a \otimes \mathbf{d}x^b,\end{aligned} \tag{2.45}$$

where $\bar{g}_{ab} = \delta_{cd}(A^{-1})^c{}_a(A^{-1})^d{}_b$. Its spatial part, which is the time-dependent metric on $\bar{\Sigma}$, has the simple form

$$\bar{\boldsymbol{g}} = \delta_{ab}\,\bar{\boldsymbol{\theta}}^a \otimes \bar{\boldsymbol{\theta}}^b = \bar{g}_{ab}\,\mathbf{d}x^a \otimes \mathbf{d}x^b, \tag{2.46}$$

so that $g_{ab} = \bar{g}_{ab}$.

In contrast, this is not true for the inverse metric. On the one hand, we have for the inverse spacetime metric

$$\begin{aligned}\boldsymbol{g}^{-1} &= \eta^{\mu\nu}\,\boldsymbol{e}_\mu \otimes \boldsymbol{e}_\nu \\ &= -\frac{1}{\alpha^2}\,\boldsymbol{\partial}_t \otimes \boldsymbol{\partial}_t + \frac{1}{\alpha^2}\,\beta^a\,(\boldsymbol{\partial}_t \otimes \boldsymbol{\partial}_a + \boldsymbol{\partial}_a \otimes \boldsymbol{\partial}_t) + \left(\bar{g}^{ab} - \frac{1}{\alpha^2}\,\beta^a\beta^b\right)\boldsymbol{\partial}_a \otimes \boldsymbol{\partial}_b,\end{aligned} \tag{2.47}$$

and on the other hand for the inverse metric on $\bar{\Sigma}$

$$\bar{\boldsymbol{g}}^{-1} = \delta^{ab}\,\bar{\boldsymbol{e}}_a \otimes \bar{\boldsymbol{e}}_b = \bar{g}^{ab}\,\bar{\boldsymbol{\partial}}_a \otimes \bar{\boldsymbol{\partial}}_b, \tag{2.48}$$

so that in general $g^{ab} \neq \bar{g}^{ab}$ and $\pi_*\boldsymbol{g}^{-1} \neq \bar{\boldsymbol{g}}^{-1}$.

### Decomposition of the Connection 1-forms

Now we decompose the connection 1-forms $\boldsymbol{\omega}^\mu{}_\nu$ of the orthonormal basis $\{\boldsymbol{\theta}^\mu\}$ using Cartan's first structure equation (2.37). At first, let us consider their restriction to the tangential vectors. If we apply the pullback and use the fact that it commutes with the exterior derivative, that is $\phi_t^*(\mathbf{d}\boldsymbol{\theta}^\mu) = \bar{\mathbf{d}}(\phi_t^*\boldsymbol{\theta}^\mu) \equiv \bar{\mathbf{d}}\bar{\boldsymbol{\theta}}^\mu$, where $\bar{\mathbf{d}}$ is the exterior derivative on $\bar{\Sigma}$, we obtain

$$\bar{\mathbf{d}}\bar{\boldsymbol{\theta}}^a + \phi_t^*\boldsymbol{\omega}^a{}_b \wedge \bar{\boldsymbol{\theta}}^b = 0, \tag{2.49a}$$

$$\phi_t^*\boldsymbol{\omega}^0{}_b \wedge \bar{\boldsymbol{\theta}}^b = 0. \tag{2.49b}$$

Since the $\bar{\boldsymbol{\theta}}^a$ are an orthonormal basis on $\bar{\Sigma}$, they also satisfy their own structure equation

$$\bar{\mathbf{d}}\bar{\boldsymbol{\theta}}^a + \bar{\boldsymbol{\omega}}^a{}_b \wedge \bar{\boldsymbol{\theta}}^b = 0, \tag{2.50}$$

where $\bar{\boldsymbol{\omega}}^a{}_b$ are the connection 1-forms on $\bar{\Sigma}$. Due to the symmetry properties of both connection 1-forms, we conclude that $\phi_t^* \boldsymbol{\omega}^a{}_b = \bar{\boldsymbol{\omega}}^a{}_b$ because the solution to the structure equation is unique, hence

$$\left(\phi_t^* \boldsymbol{\omega}^a{}_b\right)(\boldsymbol{e}_c) = \boldsymbol{\omega}^a{}_b(\boldsymbol{e}_c) = \bar{\boldsymbol{\omega}}^a{}_b(\boldsymbol{e}_c). \tag{2.51}$$

The second equation (2.49b) shows that we have

$$\left(\phi_t^* \boldsymbol{\omega}^0{}_a\right)(\boldsymbol{e}_b) = \boldsymbol{\omega}^0{}_a(\boldsymbol{e}_b) = -\bar{K}_{ab}, \tag{2.52}$$

where $\bar{K}_{ab} = \bar{K}_{ba}$ are the components of the symmetric tensor $\bar{\boldsymbol{K}} = \bar{K}_{ab}\, \bar{\boldsymbol{\theta}}^a \otimes \bar{\boldsymbol{\theta}}^b$ on $\bar{\Sigma}$, called the *extrinsic curvature*.

For the interpretation of $\bar{\boldsymbol{K}}$, we consider the decomposition of the covariant derivative $\nabla_{\boldsymbol{e}_a} \boldsymbol{e}_b = \boldsymbol{\omega}^0{}_b(\boldsymbol{e}_a)\, \boldsymbol{n} + \boldsymbol{\omega}^c{}_b(\boldsymbol{e}_a)\, \boldsymbol{e}_c$. Its tangential part

$$\boldsymbol{\omega}^c{}_b(\boldsymbol{e}_a)\, \boldsymbol{e}_c = \bar{\boldsymbol{\omega}}^c{}_b(\boldsymbol{e}_a)\, \boldsymbol{e}_c = \bar{\nabla}_{\boldsymbol{e}_a} \boldsymbol{e}_b \tag{2.53}$$

is simply the covariant derivative defined by the connection on $\bar{\Sigma}$. For the normal part we have

$$\bar{K}_{ab} = \boldsymbol{\omega}^0{}_b(\boldsymbol{e}_a) = \boldsymbol{\theta}^0(\nabla_{\boldsymbol{e}_a} \boldsymbol{e}_b). \tag{2.54}$$

Altogether we have

$$\nabla_{\boldsymbol{x}} \boldsymbol{y} = \bar{\nabla}_{\boldsymbol{x}} \boldsymbol{y} + \bar{\boldsymbol{K}}(\boldsymbol{x}, \boldsymbol{y})\, \boldsymbol{n}, \tag{2.55}$$

where $\boldsymbol{x}, \boldsymbol{y} \in \Gamma \mathrm{T}\bar{\Sigma}$, hence

$$\bar{\boldsymbol{K}}(\boldsymbol{x}, \boldsymbol{y}) = \boldsymbol{g}(\nabla_{\boldsymbol{x}} \boldsymbol{y}, \boldsymbol{n}). \tag{2.56}$$

Using that $0 = \nabla_{\boldsymbol{x}} \boldsymbol{g}(\boldsymbol{y}, \boldsymbol{n}) = \boldsymbol{g}(\nabla_{\boldsymbol{x}} \boldsymbol{y}, \boldsymbol{n}) + \boldsymbol{g}(\boldsymbol{y}, \nabla_{\boldsymbol{x}} \boldsymbol{n})$, we can also write

$$\bar{\boldsymbol{K}}(\boldsymbol{x}, \boldsymbol{y}) = -\boldsymbol{g}(\nabla_{\boldsymbol{x}} \boldsymbol{n}, \boldsymbol{y}) = -\bar{\boldsymbol{g}}(\nabla_{\boldsymbol{x}} \boldsymbol{n}, \boldsymbol{y}) \tag{2.57}$$

showing that the extrinsic curvature is the normal part of the covariant derivative and that it is actually a spatial tensor. The symmetry of $\bar{\boldsymbol{K}}$ follows from the fact that the covariant derivative is torsion-free.

The latter eq. (2.57) provides a geometrical interpretation of the extrinsic curvature: It can be understood as the change of the direction of the normal vector when it is shifted on the hypersurface. Therefore $\bar{\boldsymbol{K}}$ describes the bending of the hypersurface in the surrounding spacetime. This explains the name extrinsic curvature. As in the case of the inverse metric on $\bar{\Sigma}$ we use the same notation for the extended tensor on $\mathcal{M}$, so $\pi^* \bar{\boldsymbol{K}} \equiv \bar{\boldsymbol{K}}$.

In the Hamiltonian formulation of general relativity, developed by Arnowitt, Deser and Misner [ADM08], it is shown that the conjugate momentum $\boldsymbol{\pi}$ of the metric is built from extrinsic curvature, $\pi^{ab} = \sqrt{\det \bar{g}} \left(\mathcal{K}\, \bar{g}^{ab} - \bar{K}^{ab}\right)$, where $\mathcal{K} = \bar{g}^{ab} \bar{K}_{ab}$ is the trace of $\bar{\boldsymbol{K}}$.

Next we compute the normal part of $\boldsymbol{\omega}^0{}_a$. On the one hand, we have from the first structure equation (2.37) $\mathbf{d}\boldsymbol{\theta}^0(\boldsymbol{e}_a, \boldsymbol{e}_0) = \boldsymbol{\omega}^0{}_a(\boldsymbol{e}_0)$. Whereas on the other hand, we obtain from $\boldsymbol{\theta}^0 = \alpha\, \mathbf{d}t$

$$\mathbf{d}\boldsymbol{\theta}^0 = \mathbf{d}(\alpha\, \mathbf{d}t) = \mathbf{d}\alpha \wedge \mathbf{d}t = \tfrac{1}{\alpha}\, \bar{\mathbf{D}}\alpha \wedge \boldsymbol{\theta}^0 = \left(\bar{\mathbf{D}} \ln \alpha\right) \wedge \boldsymbol{\theta}^0, \tag{2.58}$$

where $\bar{\mathbf{D}}$ is the covariant exterior derivative on $\bar{\Sigma}$ which can be used here because the normal part of $\mathbf{D}\alpha$ is cancelled in the wedge product with $\boldsymbol{\theta}^0$: $\mathbf{d}\alpha \wedge \boldsymbol{\theta}^0 = \mathbf{D}\alpha \wedge \boldsymbol{\theta}^0 = \bar{\mathbf{D}}\alpha \wedge \boldsymbol{\theta}^0$. Inserting the basis vector fields yields

$$\mathbf{d}\boldsymbol{\theta}^0(\boldsymbol{e}_a, \boldsymbol{e}_0) = \left(\bar{\mathbf{D}} \ln \alpha\right)(\boldsymbol{e}_a) \equiv \bar{\nabla}_a \ln \alpha. \tag{2.59}$$

Combining these results, we get

$$\boldsymbol{\omega}^0{}_a = \bar{\nabla}_a \ln \alpha\, \boldsymbol{\theta}^0 - \bar{K}_{ab}\, \boldsymbol{\theta}^b. \tag{2.60}$$

At last we have to determine $\boldsymbol{\omega}^a{}_b(\boldsymbol{e}_0)$. From the structure equation (2.37) we obtain

$$\mathbf{d}\boldsymbol{\theta}^a(\boldsymbol{e}_0, \boldsymbol{e}_b) = \boldsymbol{\omega}^a{}_0(\boldsymbol{e}_b) - \boldsymbol{\omega}^a{}_b(\boldsymbol{e}_0) = -\bar{K}^a{}_b - \boldsymbol{\omega}^a{}_b(\boldsymbol{e}_0). \tag{2.61}$$

Applying the formula $i_{\boldsymbol{N}} \circ \mathbf{d} + \mathbf{d} \circ i_{\boldsymbol{N}} = \boldsymbol{\mathcal{L}}_{\boldsymbol{N}}$ to $\mathbf{d}\boldsymbol{\theta}^a$, where $\boldsymbol{N} = \alpha\, \boldsymbol{e}_0$, yields

$$i_{\boldsymbol{e}_0}\, \mathbf{d}\boldsymbol{\theta}^a = \frac{1}{\alpha}\, (i_{\boldsymbol{N}} \circ \mathbf{d})\, \boldsymbol{\theta}^a = \frac{1}{\alpha}\, (\boldsymbol{\mathcal{L}}_{\boldsymbol{N}} + \mathbf{d} \circ i_{\boldsymbol{N}})\, \boldsymbol{\theta}^a = \frac{1}{\alpha}\, \boldsymbol{\mathcal{L}}_{\boldsymbol{N}} \boldsymbol{\theta}^a. \tag{2.62}$$

Thus we arrive at $\mathbf{d}\boldsymbol{\theta}^a(\boldsymbol{e}_0, \boldsymbol{e}_b) = \frac{1}{\alpha}\, \boldsymbol{\mathcal{L}}_{\boldsymbol{N}} \boldsymbol{\theta}^a(\boldsymbol{e}_b)$ and the decomposition of $\boldsymbol{\omega}^a{}_b$ is

$$\boldsymbol{\omega}^a{}_b = \left(\frac{1}{\alpha}\, \boldsymbol{\mathcal{L}}_{\boldsymbol{N}} \boldsymbol{\theta}^a(\boldsymbol{e}_b) - \bar{K}^a{}_b\right) \boldsymbol{\theta}^0 + \bar{\boldsymbol{\omega}}^a{}_b. \tag{2.63}$$

Before we start computing the curvature 2-forms, we take a closer look at the formula $\bar{K}_{ab} + \boldsymbol{\omega}_{ab} = -\frac{1}{\alpha}\, \delta_{ac}\, \boldsymbol{\mathcal{L}}_{\boldsymbol{N}} \boldsymbol{\theta}^c(\boldsymbol{e}_b)$ obtained from eq. (2.63) after lowering the index $a$. Since $\bar{K}_{ab}$ is symmetric and $\boldsymbol{\omega}_{ab}$ antisymmetric, we conclude

$$\bar{K}_{ab} = -\frac{1}{2\alpha} \left(\delta_{ac}\, \boldsymbol{\mathcal{L}}_{\boldsymbol{N}} \boldsymbol{\theta}^c(\boldsymbol{e}_b) + \delta_{cb}\, \boldsymbol{\mathcal{L}}_{\boldsymbol{N}} \boldsymbol{\theta}^c(\boldsymbol{e}_a)\right). \tag{2.64}$$

It can easily be verified that the term in the parentheses is the Lie derivative of the spatial metric $(\boldsymbol{\mathcal{L}}_{\boldsymbol{N}} \bar{\boldsymbol{g}})(\boldsymbol{e}_a, \boldsymbol{e}_b) = \delta_{ac}\, \boldsymbol{\mathcal{L}}_{\boldsymbol{N}} \boldsymbol{\theta}^c(\boldsymbol{e}_b) + \delta_{cb}\, \boldsymbol{\mathcal{L}}_{\boldsymbol{N}} \boldsymbol{\theta}^c(\boldsymbol{e}_a)$. Thus we can rewrite the above expression for the extrinsic curvature and get the following simple relation to the Lie derivative of the spatial metric,

$$\boldsymbol{\mathcal{L}}_{\boldsymbol{N}} \bar{\boldsymbol{g}} = -2\alpha\, \bar{\boldsymbol{K}}. \tag{2.65}$$

Because of $\boldsymbol{N} = \boldsymbol{\partial}_t - \bar{\boldsymbol{\beta}}$, this is the equation of motion for the spatial metric.

**Decomposition of the Curvarture 2-forms**

In order to determine the components of the Einstein tensor $G_{\mu\nu} = R_{\mu\nu} - \frac{1}{2}\mathcal{R}\, g_{\mu\nu}$, we need the curvature 2-forms, which can be computed from Cartan's second structure equation (2.28b). So we obtain

$$\begin{aligned}
\boldsymbol{\Omega}^0{}_a &= \mathbf{d}\boldsymbol{\omega}^0{}_a + \boldsymbol{\omega}^0{}_b \wedge \boldsymbol{\omega}^b{}_a \\
&= \mathbf{d}\left(\bar{\nabla}_a \ln \alpha\, \boldsymbol{\theta}^0\right) + \mathbf{d}\left(-\bar{K}_{ab}\, \boldsymbol{\theta}^b\right) + \left(\bar{\nabla}_b \ln \alpha\, \boldsymbol{\theta}^0 + \bar{K}_{bc}\, \boldsymbol{\theta}^c\right) \wedge \boldsymbol{\omega}^b{}_a \\
&= \mathbf{d}\left(\bar{\nabla}_a \ln \alpha\right) \wedge \boldsymbol{\theta}^0 + \bar{\nabla}_a \ln \alpha\, \bar{\nabla}_b \ln \alpha\, \boldsymbol{\theta}^b \wedge \boldsymbol{\theta}^0 - \bar{\nabla}_b \ln \alpha\, \boldsymbol{\omega}^b{}_a \wedge \boldsymbol{\theta}^0 \\
&\quad - \mathbf{d}\bar{K}_{ab} \wedge \boldsymbol{\theta}^b + \bar{K}_{ab} \boldsymbol{\omega}^b{}_c \wedge \boldsymbol{\theta}^c - \bar{K}_{ab} \bar{K}^b{}_c \boldsymbol{\theta}^c \wedge \boldsymbol{\theta}^0 + \bar{K}_{bc} \boldsymbol{\omega}^b{}_a \wedge \boldsymbol{\theta}^c \\
&= \left(-\frac{1}{\alpha}\, \bar{\nabla}_b \bar{\nabla}_a \alpha + \bar{K}_{ac} \bar{K}^c{}_b\right) \boldsymbol{\theta}^0 \wedge \boldsymbol{\theta}^b - \mathbf{D}\bar{K}_{ab} \wedge \boldsymbol{\theta}^b.
\end{aligned} \tag{2.66}$$

We need to decompose $\mathbf{D}\bar{K}_{ab}$. For the tangential part we obtain

$$\begin{aligned}\mathbf{D}\bar{K}_{ab}(\boldsymbol{e}_d) &= \left(\mathbf{d}\bar{K}_{ab} - \bar{K}_{cb}\boldsymbol{\omega}^c{}_a - \bar{K}_{ac}\boldsymbol{\omega}^c{}_b\right)(\boldsymbol{e}_d)\\ &= \left(\bar{\mathbf{d}}\bar{K}_{ab} - \bar{K}_{cb}\bar{\boldsymbol{\omega}}^c{}_a - \bar{K}_{ac}\bar{\boldsymbol{\omega}}^c{}_b\right)(\boldsymbol{e}_d)\\ &= \bar{\mathbf{D}}\bar{K}_{ab}(\boldsymbol{e}_d) = \bar{\nabla}_d\bar{K}_{ab},\end{aligned} \tag{2.67}$$

whereas the normal part is given by

$$\begin{aligned}\mathbf{D}\bar{K}_{ab}(\boldsymbol{e}_0) &= \mathbf{d}\bar{K}_{ab}(\boldsymbol{e}_0) - \bar{K}_{cb}\boldsymbol{\omega}^c{}_a(\boldsymbol{e}_0) - \bar{K}_{ac}\boldsymbol{\omega}^c{}_b(\boldsymbol{e}_0)\\ &= \frac{1}{\alpha}\boldsymbol{\mathcal{L}}_{\boldsymbol{N}}\bar{K}_{ab} + \bar{K}_{cb}\left(\frac{1}{\alpha}\boldsymbol{\mathcal{L}}_{\boldsymbol{N}}\boldsymbol{\theta}^c(\boldsymbol{e}_a) + \bar{K}^c{}_a\right) + \bar{K}_{ac}\left(\frac{1}{\alpha}\boldsymbol{\mathcal{L}}_{\boldsymbol{N}}\boldsymbol{\theta}^c(\boldsymbol{e}_b) + \bar{K}^c{}_b\right)\\ &= \frac{1}{\alpha}\left(\boldsymbol{\mathcal{L}}_{\boldsymbol{N}}\bar{K}_{ab} + \bar{K}_{cb}\boldsymbol{\mathcal{L}}_{\boldsymbol{N}}\boldsymbol{\theta}^c(\boldsymbol{e}_a) + \bar{K}_{ac}\boldsymbol{\mathcal{L}}_{\boldsymbol{N}}\boldsymbol{\theta}^c(\boldsymbol{e}_b)\right) + 2\bar{K}_{ac}\bar{K}^c{}_b\\ &= \frac{1}{\alpha}\left(\boldsymbol{\mathcal{L}}_{\boldsymbol{N}}\bar{\boldsymbol{K}}\right)_{ab} + 2\bar{K}_{ac}\bar{K}^c{}_b.\end{aligned} \tag{2.68}$$

For the calculation of the Einstein tensor, we only need the spatial part of $\boldsymbol{\Omega}^a{}_b$ given by

$$\begin{aligned}\boldsymbol{\Omega}^a{}_b(\boldsymbol{e}_c,\boldsymbol{e}_d) &= \left(\mathbf{d}\boldsymbol{\omega}^a{}_b + \boldsymbol{\omega}^a{}_c\wedge\boldsymbol{\omega}^c{}_b + \boldsymbol{\omega}^a{}_0\wedge\boldsymbol{\omega}^0{}_b\right)(\boldsymbol{e}_c,\boldsymbol{e}_d)\\ &= \left(\bar{\mathbf{d}}\bar{\boldsymbol{\omega}}^a{}_b + \bar{\boldsymbol{\omega}}^a{}_c\wedge\bar{\boldsymbol{\omega}}^c{}_b + \bar{K}^a{}_e\bar{K}_{bf}\boldsymbol{\theta}^e\wedge\boldsymbol{\theta}^f\right)(\boldsymbol{e}_c,\boldsymbol{e}_d)\\ &= \bar{\boldsymbol{\Omega}}^a{}_b(\boldsymbol{e}_c,\boldsymbol{e}_d) + \bar{K}^a{}_c\bar{K}_{bd} - \bar{K}^a{}_d\bar{K}_{bc}.\end{aligned} \tag{2.69}$$

This relation is often called *Gauss equation* and it is the generalisation of *Gauss' Theorema Egregium* to the Lorentzian case. In the Riemannian case, usually treated in differential geometry books, some signs differ. Similarly, the spatial part of $\boldsymbol{\Omega}^0{}_a$

$$\boldsymbol{\Omega}^0{}_a(\boldsymbol{e}_b,\boldsymbol{e}_c) = -\bar{\mathbf{D}}\bar{K}_{ac}(\boldsymbol{e}_b) + \bar{\mathbf{D}}\bar{K}_{ab}(\boldsymbol{e}_c) = \bar{\nabla}_c\bar{K}_{ab} - \bar{\nabla}_b\bar{K}_{ac} \tag{2.70}$$

is known as the *Codazzi-Mainardi equation.*

**Decomposition of Einstein's Equations**

Now we have everything to calculate the components of the Ricci tensor using eq. (2.38) with two contracted indices

$$R_{\mu\nu} = \boldsymbol{\Omega}^\lambda{}_\mu(\boldsymbol{e}_\lambda,\boldsymbol{e}_\nu). \tag{2.71}$$

From this we can compute the components of the Einstein tensor $G_{\mu\nu} = R_{\mu\nu} - \frac{1}{2}\eta_{\mu\nu}\mathcal{R}$. The first component is obtained from

$$G_{00} = R_{00} - \frac{1}{2}\mathcal{R}\,g_{00} = R_{00} + \frac{1}{2}\left(-R_{00} + R^a{}_a\right) = \frac{1}{2}\left(R_{00} + R^a{}_a\right), \tag{2.72}$$

where $R_{00} = \boldsymbol{\Omega}^a{}_0(\boldsymbol{e}_a,\boldsymbol{e}_0)$ and

$$R^a{}_a = \boldsymbol{\Omega}^{\mu a}(\boldsymbol{e}_\mu,\boldsymbol{e}_a) = \boldsymbol{\Omega}^{ab}(\boldsymbol{e}_a,\boldsymbol{e}_b) + \boldsymbol{\Omega}^{0a}(\boldsymbol{e}_0,\boldsymbol{e}_a) = \boldsymbol{\Omega}^{ab}(\boldsymbol{e}_a,\boldsymbol{e}_b) - \boldsymbol{\Omega}^a{}_0(\boldsymbol{e}_a,\boldsymbol{e}_0), \tag{2.73}$$

so that

$$\begin{aligned}G_{00} &= \frac{1}{2}\boldsymbol{\Omega}^{ab}(\boldsymbol{e}_a,\boldsymbol{e}_b) = \frac{1}{2}\left(\bar{\boldsymbol{\Omega}}^{ab}(\boldsymbol{e}_a,\boldsymbol{e}_b) + \bar{K}^a{}_a\bar{K}^b{}_b - \bar{K}^a{}_b\bar{K}^b{}_a\right)\\ &= \frac{1}{2}\left(\bar{\mathcal{R}} + \mathcal{K}^2 - \bar{K}^a{}_b\bar{K}^b{}_a\right).\end{aligned} \tag{2.74}$$

Here $\bar{\mathcal{R}} = \bar{R}^a{}_a = \mathcal{R}[\bar{g}]$ is the Ricci scalar with respect to the spatial metric $\bar{\boldsymbol{g}}$ on the hypersurface and $\mathcal{K} = \bar{K}^a{}_a$ is the trace of the extrinsic curvature. Next, we calculate the mixed terms

$$\begin{aligned} G_{0a} = R_{0a} &= \boldsymbol{\Omega}^b{}_0(\boldsymbol{e}_b, \boldsymbol{e}_a) = \left(-\bar{\mathbf{D}}\bar{K}^b{}_c \wedge \boldsymbol{\theta}^c\right)(\boldsymbol{e}_b, \boldsymbol{e}_a) \\ &= -\bar{\nabla}_b \bar{K}^b{}_a + \bar{\nabla}_a \mathcal{K}. \end{aligned} \tag{2.75}$$

At last, we have

$$\begin{aligned} R_{ab} &= \boldsymbol{\Omega}^0{}_a(\boldsymbol{e}_0, \boldsymbol{e}_b) + \boldsymbol{\Omega}^c{}_a(\boldsymbol{e}_c, \boldsymbol{e}_b) \\ &= -\frac{1}{\alpha}\bar{\nabla}_b\bar{\nabla}_a\alpha - \frac{1}{\alpha}\left(\boldsymbol{\mathcal{L}}_{\boldsymbol{N}}\bar{\boldsymbol{K}}\right)_{ab} - \bar{K}_{ac}\bar{K}^c{}_b + \bar{\boldsymbol{\Omega}}^c{}_a(\boldsymbol{e}_c, \boldsymbol{e}_b) + \mathcal{K}\bar{K}_{ab} - \bar{K}^c{}_b\bar{K}_{ac} \\ &= -\frac{1}{\alpha}\bar{\nabla}_b\bar{\nabla}_a\alpha - \frac{1}{\alpha}\left(\boldsymbol{\mathcal{L}}_{\boldsymbol{N}}\bar{\boldsymbol{K}}\right)_{ab} - 2\bar{K}_{ac}\bar{K}^c{}_b + \bar{R}_{ab} + \mathcal{K}\bar{K}_{ab}. \end{aligned} \tag{2.76}$$

Now we are almost ready to display Einstein's equations $G_{\mu\nu} = 8\pi\, T_{\mu\nu}$ in their 3+1 decomposition. But for this we need the decomposition of the energy-momentum tensor given by

$$\boldsymbol{T} = T_{\mu\nu}\,\boldsymbol{\theta}^\mu \otimes \boldsymbol{\theta}^\nu = E\,\boldsymbol{\theta}^0 \otimes \boldsymbol{\theta}^0 - j_a\left(\boldsymbol{\theta}^a \otimes \boldsymbol{\theta}^0 + \boldsymbol{\theta}^0 \otimes \boldsymbol{\theta}^a\right) + S_{ab}\,\boldsymbol{\theta}^a \otimes \boldsymbol{\theta}^b, \tag{2.77}$$

where $E = \phi_t^*\boldsymbol{T}(\boldsymbol{e}_0, \boldsymbol{e}_0)$ is the energy, $\bar{\boldsymbol{j}} = \phi_t^*\boldsymbol{T}(\boldsymbol{e}_0, \cdot\,)$ the momentum vector field, and $\bar{\boldsymbol{S}} = \phi_t^*\boldsymbol{T}$ the stress tensor field of matter.

Altogether Einstein's equations can be decomposed into

$$\frac{1}{2}\left(\bar{\mathcal{R}} + \mathcal{K}^2 - \bar{K}^a{}_b\bar{K}^b{}_a\right) = 8\pi E, \tag{2.78a}$$

$$-\bar{\nabla}_b\bar{K}^b{}_a + \bar{\nabla}_a\mathcal{K} = -8\pi j_a, \tag{2.78b}$$

$$-\frac{1}{\alpha}\bar{\nabla}_b\bar{\nabla}_a\alpha - \frac{1}{\alpha}\left(\boldsymbol{\mathcal{L}}_{\boldsymbol{N}}\bar{\boldsymbol{K}}\right)_{ab} + \bar{R}_{ab} - 2\bar{K}_{ac}\bar{K}^c{}_b + \mathcal{K}\bar{K}_{ab} = 8\pi S_{ab} - 4\pi(\mathcal{S} - E)\,\delta_{ab}, \tag{2.78c}$$

where $\mathcal{S} = S^a{}_a$. In the last equation we have used that

$$\mathcal{R} = -8\pi\, T^\mu{}_\mu = -8\pi(-E + S^a{}_a) = -8\pi(\mathcal{S} - E). \tag{2.79}$$

Finally, we consider the energy-conservation laws $\nabla_\mu T^{\mu\nu} = 0$. They decompose into two equations: a conservation law for the energy $E$ and one for the momentum $\bar{\boldsymbol{j}}$. Recall that these are no real conservation laws because they are not associated to any conserved quantity. We start with the energy conservation law $\mathbf{D}T^{0\mu}(\boldsymbol{e}_\mu) = \nabla_\mu T^{0\mu} = 0$ yielding

$$\begin{aligned} \mathbf{D}T^{0\mu}(\boldsymbol{e}_\mu) &= \mathbf{d}T^{00}(\boldsymbol{e}_0) + \mathbf{d}T^{0a}(\boldsymbol{e}_a) + \boldsymbol{\omega}^0{}_a(\boldsymbol{e}_0)\,T^{0a} + \boldsymbol{\omega}^0{}_a(\boldsymbol{e}_a)\,T^{00} \\ &\quad + \boldsymbol{\omega}^a{}_b(\boldsymbol{e}_a)\,T^{0b} + \boldsymbol{\omega}^0{}_a(\boldsymbol{e}_0)\,T^{0a} + \boldsymbol{\omega}^0{}_a(\boldsymbol{e}_b)\,T^{ab} \\ &= \frac{1}{\alpha}\boldsymbol{N}(E) + \left(\mathbf{d}j^a + \bar{\boldsymbol{\omega}}^a{}_b\,j^b\right)(\boldsymbol{e}_a) - \mathcal{K}E - \bar{K}_{ab}S^{ab} + 2\left(\frac{1}{\alpha}\bar{\nabla}_a\alpha\right)j^a \\ &= \frac{1}{\alpha}\boldsymbol{\mathcal{L}}_{\boldsymbol{N}}E + \bar{\nabla}_a j^a - \mathcal{K}E - \bar{K}_{ab}S^{ab} + \frac{2}{\alpha}\,j^a\,\bar{\nabla}_a\alpha. \end{aligned} \tag{2.80}$$

Similar the momentum conservation law $\mathbf{D}T_a{}^\mu(\boldsymbol{e}_\mu) = \nabla_\mu T_a{}^\mu = 0$ leads to

$$\begin{aligned}\mathbf{D}T_a{}^\mu(\boldsymbol{e}_\mu) &= \mathbf{d}T_a{}^0(\boldsymbol{e}_0) + \mathbf{d}T_a{}^b(\boldsymbol{e}_b) + \boldsymbol{\omega}^0{}_b(\boldsymbol{e}_0)\, T_a{}^b + \boldsymbol{\omega}^b{}_0(\boldsymbol{e}_b)\, T_a{}^0 + \boldsymbol{\omega}^b{}_c(\boldsymbol{e}_b)\, T_a{}^c \\ &\quad - \boldsymbol{\omega}^0{}_a(\boldsymbol{e}_0)\, T_0{}^0 - \boldsymbol{\omega}^b{}_a(\boldsymbol{e}_0)\, T_b{}^0 - \boldsymbol{\omega}^0{}_a(\boldsymbol{e}_b)\, T_0{}^b - \boldsymbol{\omega}^c{}_a(\boldsymbol{e}_b)\, T_c{}^b \\ &= \frac{1}{\alpha}\boldsymbol{N}(j_a) + \frac{1}{\alpha}\boldsymbol{\mathcal{L}}_{\boldsymbol{N}}\boldsymbol{\theta}^b(\boldsymbol{e}_a)\, j_b + \bar{K}^b{}_a j_b + \left(\mathbf{d}S_a{}^b - \bar{\boldsymbol{\omega}}^c{}_a\, S_c{}^b + \bar{\boldsymbol{\omega}}^b{}_c\, S_a{}^c\right)(\boldsymbol{e}_b) \\ &\quad + \left(\frac{1}{\alpha}\,\bar{\nabla}_b\alpha\right) S_a{}^b - \mathcal{K} j_a + \left(\frac{1}{\alpha}\,\bar{\nabla}_a\alpha\right) E - \bar{K}_{ab} j^b \\ &= \frac{1}{\alpha}\boldsymbol{\mathcal{L}}_{\boldsymbol{N}}\bar{\boldsymbol{\jmath}}(\boldsymbol{e}_a) + \bar{\nabla}_b S_a{}^b + \frac{1}{\alpha}\, S_a{}^b\, \bar{\nabla}_b\alpha - \mathcal{K} j_a + \frac{1}{\alpha}\, E\, \bar{\nabla}_a\alpha. \end{aligned} \tag{2.81}$$

For an ideal fluid with energy-momentum tensor of eq. (2.6), we would obtain the relativistic generalisations of the Euler equations.

### Change in Viewpoint

Up to here all tensors are still objects on the spacetime. But now we change our point of view: We reduce $t$ from a coordinate on the spacetime $\mathcal{M}$ to a parameter on $\bar{\Sigma}$. For this reason, tensors tangential to the sheets of the foliation may be considered as tensors on $\bar{\Sigma}$ depending on a parameter $t$.

The Lie-derivative can be decomposed into

$$\boldsymbol{\mathcal{L}}_{\boldsymbol{N}} = \boldsymbol{\mathcal{L}}_{\boldsymbol{\partial}_t} - \boldsymbol{\mathcal{L}}_{\boldsymbol{\beta}}. \tag{2.82}$$

Since the Lie-derivative of a tangential tensor $\bar{\boldsymbol{T}}$ with respect to the tangential vector field $\boldsymbol{\beta}$ is also tangential, $\boldsymbol{\mathcal{L}}_{\boldsymbol{\beta}}\bar{\boldsymbol{T}}$ can be viewed as a time-dependent tensor on $\bar{\Sigma}$. The Lie derivative with respect to $\boldsymbol{\partial}_t$ reduces in components to the partial derivative

$$\left(\boldsymbol{\mathcal{L}}_{\boldsymbol{\partial}_t}\bar{\boldsymbol{T}}\right)_{ab} = \partial_t T_{ab}\,. \tag{2.83}$$

For this reason, $\boldsymbol{\mathcal{L}}_{\boldsymbol{\partial}_t}$ becomes the derivative with respect to the parameter $t$ of any tangential tensor. From now on, we simply write $\partial_t \boldsymbol{T}$ or $\dot{\boldsymbol{T}}$ instead of $\boldsymbol{\mathcal{L}}_{\boldsymbol{\partial}_t}\boldsymbol{T}$. We forget about the vector field $\boldsymbol{\partial}_t$ as well as the embedding and consider the decomposed Einstein field equations as the equations of motions for time-evolving fields on a single three-dimensional manifold.

### Summary

So altogether, on the one hand we have the two constraint equations

$$\bar{\mathcal{R}} + \mathcal{K}^2 - \bar{K}^a{}_b \bar{K}^b{}_a = 16\pi E, \tag{2.84a}$$

$$\bar{\nabla}_b \bar{K}^b{}_a - \bar{\nabla}_a \mathcal{K} = 8\pi j_a, \tag{2.84b}$$

where eq. (2.84a) is the *Hamiltonian constraint* and eq. (2.84b) the *momentum constraint*. The constraints do not involve time derivatives, therefore they are no evolution equations but they restrict the allowed fields. Note that the constraint equations do not depend on the lapse function and the shift vector field.

On the other hand, there are the two evolution equations for the metric eq. (2.65) and the extrinsic curvature eq. (2.78c)

$$\boldsymbol{\partial}_t \bar{\boldsymbol{g}} = \left(\boldsymbol{\mathcal{L}}_{\boldsymbol{\beta}}\bar{\boldsymbol{g}}\right)_{ab} - 2\alpha\, \bar{K}_{ab}, \tag{2.85a}$$

$$\boldsymbol{\partial}_t \bar{\boldsymbol{K}} = \left(\boldsymbol{\mathcal{L}}_{\boldsymbol{\beta}}\bar{\boldsymbol{K}}\right)_{ab} - \bar{\nabla}_b\bar{\nabla}_a\alpha + \alpha\left(\bar{R}_{ab} + \mathcal{K}\bar{K}_{ab} - 2\bar{K}_{ac}\bar{K}^c{}_b + 4\pi(\mathcal{S} - E)\bar{g}_{ab} - 8\pi\, S_{ab}\right). \tag{2.85b}$$

It can be shown that the evolution equations respect the constraints. Hence they have to be taken into account only when formulating the initial data.

Fourès-Bruhat [Fou52] proved that there exist locally a unique solution to the initial value problem for smooth initial data satisfying the constraint equations. Later, Choquet-Bruhat and Geroch [CG69] could prove the global existence and uniqueness:

**Theorem 2.3.** ***Global Existence and Uniqueness of Solutions to the Initial Value Problem*** *[CG69]*
*Given a set* $(\bar{\Sigma}, \bar{\boldsymbol{g}}, \bar{\boldsymbol{K}}, E, \bar{\boldsymbol{j}})$*, where* $\bar{\Sigma}$ *is a three-dimensional manifold with a Riemannian metric* $\bar{\boldsymbol{g}}$ *and a symmetric bilinear form field* $\bar{\boldsymbol{K}}$*,* $E$ *a scalar field and* $\bar{\boldsymbol{j}}$ *a vector field on* $\bar{\Sigma}$*, such that the constraint equations* (2.84) *are satisfied, then there exists a unique maximal spacetime* $(\mathcal{M}, \boldsymbol{g}, \boldsymbol{T})$ *such that*

*(i)* $(\boldsymbol{g}, \boldsymbol{T})$ *is a solution to Einstein's equations,*

*(ii)* $(\bar{\Sigma}, \bar{\boldsymbol{g}}, \bar{\boldsymbol{K}})$ *is an embedded Cauchy hypersurface with induced metric* $\bar{\boldsymbol{g}}$ *and extrinsic curvature* $\bar{\boldsymbol{K}}$*,*

*(iii) any solution to initial value problem is isometric to a sub-part of* $(\mathcal{M}, \boldsymbol{g})$*.*

Furthermore, for the matter sources we have the energy and momentum conservation laws

$$\boldsymbol{\partial}_t E - \boldsymbol{\mathcal{L}}_\beta E + \alpha \left( \bar{\nabla}_a j^a - \mathcal{K}\, E - \bar{K}_{ab} S^{ab} \right) + 2 j^a \bar{\nabla}_a \alpha, = 0, \tag{2.86a}$$

$$\boldsymbol{\partial}_t \bar{\boldsymbol{j}} - \left( \boldsymbol{\mathcal{L}}_\beta \bar{\boldsymbol{j}} \right)_a + \alpha \bar{\nabla}_b S_a{}^b + S_a{}^b \bar{\nabla}_b \alpha - \alpha \mathcal{K} j_a + E \bar{\nabla}_a \alpha = 0. \tag{2.86b}$$

We are going to solve this system for the cosmological case in chapter 4. Later in chapter 6 we derive a vacuum solution to the constraint equations describing the initial data for multiple black holes.

## 2.3 The Conformal Method

Although the constraint equations are already much simpler than the full Einstein system, there exists no general strategy to find solutions. Here we present the conformal method as one possible approach to find solutions. Another established approach is the conformal thin sandwich method [Yor99].

The conformal method is based on a conformal decomposition of the spatial metric $\bar{\boldsymbol{g}} = \mathrm{e}^{2\psi} \tilde{\boldsymbol{g}}$ and the extrinsic curvature. It was first introduced by Lichnerowicz [Lic44], further important contributions were made by York [Yor71; Yor72; Yor73]. The idea is that one can freely choose the conformal metric $\tilde{\boldsymbol{g}}$ and some parts of the extrinsic curvature including its trace whereas the remaining components are determined by the constraint equations. Later this decomposition has also been extended to the evolution equations. The BSSN scheme, mostly used in numerical calculations, is a modification of the conformal method; it is named after Shibata and Nakamura [SN95] and Baumgarte and Shapiro [BS98],

We make the following conformal ansatz for the basis fields[3]

$$\tilde{\boldsymbol{\theta}}^i = M_a^i\, \bar{\boldsymbol{\theta}}^a = \mathrm{e}^{-\psi}\, \delta_a^i\, \bar{\boldsymbol{\theta}}^a, \tag{2.87a}$$

$$\tilde{\boldsymbol{e}}_i = M_i^a\, \bar{\boldsymbol{e}}_a = \mathrm{e}^{\psi}\, \delta_i^a\, \bar{\boldsymbol{e}}_a, \tag{2.87b}$$

where the conformal factor $\psi$ is a function on $\bar{\Sigma}$. Furthermore, we have the spatial metric $\bar{\boldsymbol{g}}$ and the conformal metric $\tilde{\boldsymbol{g}}$

$$\tilde{\boldsymbol{g}} = \delta_{ij}\, \tilde{\boldsymbol{\theta}}^i \otimes \tilde{\boldsymbol{\theta}}^j, \tag{2.88a}$$

$$\bar{\boldsymbol{g}} = \delta_{ab}\, \bar{\boldsymbol{\theta}}^a \otimes \bar{\boldsymbol{\theta}}^b, \tag{2.88b}$$

which are both orthonormal. Due to eq. (2.87) they are related by

$$\bar{\boldsymbol{g}} = \mathrm{e}^{2\psi}\, \tilde{\boldsymbol{g}}. \tag{2.89}$$

As in the previous section, we will calculate the connection 1-forms, then the curvature 2-forms and at last the components of the Ricci tensor. Finally, we substitute our ansatz into the constraint equations.

**Conformal Connection 1-forms and Curvature 2-forms**

Again, we are using the first structure equation (2.37) in order to decompose the connection 1-forms $\bar{\boldsymbol{\omega}}^a{}_b$ with respect to the conformal basis $\tilde{\boldsymbol{\theta}}^i$. On the one hand, the structure equation for $\tilde{\boldsymbol{\theta}}^i$ yields

$$\mathbf{d}\tilde{\boldsymbol{\theta}}^i = -\tilde{\boldsymbol{\omega}}^i{}_j \wedge \tilde{\boldsymbol{\theta}}^j. \tag{2.90}$$

On the other hand, we can also calculate directly the exterior derivative of $\tilde{\boldsymbol{\theta}}^i$. Using that $\mathbf{d}M_a^i = \mathbf{d}\left(\mathrm{e}^{-\psi}\, \delta_a^i\right) = -\,\mathrm{e}^{-\psi}\, \delta_a^i\, \mathbf{d}\psi = -M_a^i\, \mathbf{d}\psi$, we obtain

$$\begin{aligned}
\mathbf{d}\tilde{\boldsymbol{\theta}}^i &= \mathbf{d}\left(M_a^i\, \bar{\boldsymbol{\theta}}^a\right) \\
&= \mathbf{d}M_a^i \wedge \bar{\boldsymbol{\theta}}^a - M_a^i\, \mathbf{d}\bar{\boldsymbol{\theta}}^a \\
&= -\,\mathbf{d}\psi \wedge M_a^i\, \bar{\boldsymbol{\theta}}^a - M_a^i\, \bar{\boldsymbol{\omega}}^a{}_b \wedge \bar{\boldsymbol{\theta}}^b \\
&= -\,\mathbf{d}\psi(\tilde{\boldsymbol{e}}_j)\, \tilde{\boldsymbol{\theta}}^j \wedge \tilde{\boldsymbol{\theta}}^i - M_a^i\, \bar{\boldsymbol{\omega}}^a{}_b\, M_j^b \wedge \tilde{\boldsymbol{\theta}}^j \\
&= -\left(\bar{\boldsymbol{\omega}}^i{}_j + \psi_j\, \tilde{\boldsymbol{\theta}}^i\right) \wedge \tilde{\boldsymbol{\theta}}^j,
\end{aligned} \tag{2.91}$$

where we introduced the short-hand notation $\psi_i \equiv \mathbf{d}\psi(\tilde{\boldsymbol{e}}_i) = \tilde{\nabla}_i\, \psi$. Note that $\bar{\boldsymbol{\omega}}^i{}_j \equiv M_a^i\, \bar{\boldsymbol{\omega}}^a{}_b\, M_j^b$ are not the transformed connection 1-forms $\bar{\boldsymbol{\omega}}^a{}_b$ in the new basis $\tilde{\boldsymbol{\theta}}^i$ because the connection 1-forms do not transform like tensors. Instead, if we compare both equations (2.90) and (2.91), we conclude

$$\bar{\boldsymbol{\omega}}^i{}_j = \tilde{\boldsymbol{\omega}}^i{}_j + \psi_j\, \tilde{\boldsymbol{\theta}}^i - \psi^i\, \tilde{\boldsymbol{\theta}}_j. \tag{2.92}$$

The last term vanishes in the first structure equation. However, it is necessary to make $\bar{\boldsymbol{\omega}}_{ij}$ antisymmetric so that the connection 1-forms satisfy the metricity condition (2.36).

[3] We use Latin indices from the beginning of the alphabet $a, b, \ldots$ for the spatial frame $\bar{\boldsymbol{\theta}}^a$, which are lowered and raised with the metric $\bar{\boldsymbol{g}}$. Small Latin indices from the middle of the alphabet $i, j, \ldots$ indicate components with respect to the conformal frame $\tilde{\boldsymbol{\theta}}^i$, for which we use the conformal metric $\tilde{\boldsymbol{g}}$ to raise and lower indices.

Next we determine the curvature 2-forms $\bar{\boldsymbol{\Omega}}^i{}_j$ in the new basis. Unlike the connection 1-forms, the curvature 2-forms transform tensorially. They are obtained from the second structure equation (2.28b)

$$\bar{\boldsymbol{\Omega}}^i{}_j = \mathbf{d}\bar{\boldsymbol{\omega}}^i{}_j + \bar{\boldsymbol{\omega}}^i{}_k \wedge \bar{\boldsymbol{\omega}}^k{}_j. \tag{2.93}$$

For the first term, we obtain

$$\begin{aligned}\mathbf{d}\bar{\boldsymbol{\omega}}^i{}_j &= \mathbf{d}\tilde{\boldsymbol{\omega}}^i{}_j + \mathbf{d}\psi_j \wedge \tilde{\boldsymbol{\theta}}^i + \psi_j\, \mathbf{d}\tilde{\boldsymbol{\theta}}^i - \mathbf{d}\psi^i \wedge \tilde{\boldsymbol{\theta}}_j - \psi^i\, \mathbf{d}\tilde{\boldsymbol{\theta}}_j \\ &= \mathbf{d}\tilde{\boldsymbol{\omega}}^i{}_j + \mathbf{d}\psi_j \wedge \tilde{\boldsymbol{\theta}}^i - \psi_j\, \tilde{\boldsymbol{\omega}}^i{}_k \wedge \tilde{\boldsymbol{\theta}}^k - \mathbf{d}\psi^i \wedge \tilde{\boldsymbol{\theta}}_j - \psi^i\, \tilde{\boldsymbol{\omega}}_{jk} \wedge \tilde{\boldsymbol{\theta}}^k,\end{aligned} \tag{2.94}$$

and the second term is given by

$$\begin{aligned}\bar{\boldsymbol{\omega}}^i{}_k \wedge \bar{\boldsymbol{\omega}}^k{}_j &= \left(\tilde{\boldsymbol{\omega}}^i{}_k + \psi_k\, \tilde{\boldsymbol{\theta}}^i - \psi^i\, \tilde{\boldsymbol{\theta}}_k\right) \wedge \left(\tilde{\boldsymbol{\omega}}^k{}_j + \psi_j\, \tilde{\boldsymbol{\theta}}^k - \psi^k\, \tilde{\boldsymbol{\theta}}_j\right) \\ &= \tilde{\boldsymbol{\omega}}^i{}_k \wedge \tilde{\boldsymbol{\omega}}^k{}_j + \psi_j\, \tilde{\boldsymbol{\omega}}^i{}_k \wedge \tilde{\boldsymbol{\theta}}^k - \psi^k\, \tilde{\boldsymbol{\omega}}^i{}_k \wedge \tilde{\boldsymbol{\theta}}_j - \psi_k\, \tilde{\boldsymbol{\omega}}^k{}_j \wedge \tilde{\boldsymbol{\theta}}^i \\ &\quad + \psi_j\psi_k\, \tilde{\boldsymbol{\omega}}^i \wedge \tilde{\boldsymbol{\theta}}^k - \psi_k\psi^k\, \tilde{\boldsymbol{\omega}}^i \wedge \tilde{\boldsymbol{\theta}}_j + \psi^i\, \tilde{\boldsymbol{\omega}}^k{}_j \wedge \tilde{\boldsymbol{\theta}}_k + \psi^i\psi^k\, \tilde{\boldsymbol{\theta}}_k \wedge \tilde{\boldsymbol{\theta}}_j.\end{aligned} \tag{2.95}$$

Hence, the curvature 2-form is

$$\begin{aligned}\bar{\boldsymbol{\Omega}}^i{}_j &= \mathbf{d}\tilde{\boldsymbol{\omega}}^i{}_j + \tilde{\boldsymbol{\omega}}^i{}_k \wedge \tilde{\boldsymbol{\omega}}^k{}_j + \left(\mathbf{d}\psi_j - \psi_k\, \tilde{\boldsymbol{\omega}}^k{}_j - \psi_j\psi_k\, \tilde{\boldsymbol{\theta}}^k\right) \wedge \tilde{\boldsymbol{\theta}}^i \\ &\quad - \left(\mathbf{d}\psi^i + \psi^k\, \tilde{\boldsymbol{\omega}}^i{}_k - \psi^i\psi_k\, \tilde{\boldsymbol{\theta}}^k\right) \wedge \tilde{\boldsymbol{\theta}}_j - \psi_k\psi^k\, \tilde{\boldsymbol{\theta}}^i \wedge \tilde{\boldsymbol{\theta}}_j \\ &= \tilde{\boldsymbol{\Omega}}^i{}_j + \left(\tilde{\mathbf{D}}\psi_j - \psi_j\, \mathbf{d}\psi\right) \wedge \tilde{\boldsymbol{\theta}}^i - \left(\tilde{\mathbf{D}}\psi^i - \psi^i\, \mathbf{d}\psi\right) \wedge \tilde{\boldsymbol{\theta}}_j - \psi_k\psi^k\, \tilde{\boldsymbol{\theta}}^i \wedge \tilde{\boldsymbol{\theta}}_j.\end{aligned} \tag{2.96}$$

Now we can determine the transformed Ricci tensor $\bar{R}_{jk} \equiv R[\bar{g}]_{jk}$ with respect to metric $\bar{\boldsymbol{g}}$ in the new basis $\tilde{\boldsymbol{\theta}}^i$. We get

$$\begin{aligned}\bar{R}_{jk} &= \bar{\boldsymbol{\Omega}}^i{}_j(\tilde{\boldsymbol{e}}_i, \tilde{\boldsymbol{e}}_k) \\ &= \tilde{\boldsymbol{\Omega}}^i{}_j(\tilde{\boldsymbol{e}}_i, \tilde{\boldsymbol{e}}_k) + \left(\left(\tilde{\mathbf{D}}\psi_j - \psi_j\, \mathbf{d}\psi\right) \wedge \tilde{\boldsymbol{\theta}}^i \right. \\ &\quad \left. - \left(\tilde{\mathbf{D}}\psi^i - \psi^i\, \mathbf{d}\psi\right) \wedge \tilde{\boldsymbol{\theta}}_j - \psi_l\psi^l\, \tilde{\boldsymbol{\theta}}^i \wedge \tilde{\boldsymbol{\theta}}_j\right)(\tilde{\boldsymbol{e}}_i, \tilde{\boldsymbol{e}}_k) \\ &= \tilde{R}_{jk} - 2\left(\tilde{\mathbf{D}}\psi_j(\tilde{\boldsymbol{e}}_k) - \psi_j\psi_k\right) - \left(\tilde{\mathbf{D}}\psi^i(\tilde{\boldsymbol{e}}_i) - \psi^i\psi_i\right)\tilde{g}_{jk} \\ &\quad + \left(\tilde{\mathbf{D}}\psi_j(\tilde{\boldsymbol{e}}_k) - \psi_j\psi_k\right) - 2\psi^i\psi_i\, \tilde{g}_{jk} \\ &= \tilde{R}_{jk} - \tilde{\mathbf{D}}\psi_j(\tilde{\boldsymbol{e}}_k) + \psi_j\psi_k - \tilde{\mathbf{D}}\psi^i(\tilde{\boldsymbol{e}}_i)\, \tilde{g}_{jk} - \psi^i\psi_i\, \tilde{g}_{jk},\end{aligned} \tag{2.97}$$

where $\tilde{R}_{ij} \equiv R[\tilde{g}]_{ij}$ is the Ricci tensor with respect to the metric $\tilde{\boldsymbol{g}}$. We can bring this into the well-known form usually presented in the literature, using

$$\psi_j = \mathbf{d}\psi(\tilde{\boldsymbol{e}}_j) = \tilde{\mathbf{D}}\psi(\tilde{\boldsymbol{e}}_j) = \tilde{\nabla}_j\psi, \tag{2.98a}$$

$$\tilde{\mathbf{D}}\psi_j(\tilde{\boldsymbol{e}}_k) = \tilde{\nabla}_k\psi_j = \tilde{\nabla}_k\tilde{\nabla}_j\psi = \tilde{\nabla}_j\tilde{\nabla}_k\psi. \tag{2.98b}$$

Then eq. (2.97) can be written as

$$\bar{R}_{jk} = \tilde{R}_{jk} - \tilde{\nabla}_j\tilde{\nabla}_k\psi + \tilde{\nabla}_j\psi\, \tilde{\nabla}_k\psi - \left(\tilde{\nabla}^i\tilde{\nabla}_i\psi + \tilde{\nabla}^i\psi\, \tilde{\nabla}_i\psi\right)\tilde{g}_{jk}. \tag{2.99}$$

Finally we calculate the Ricci scalar $\bar{\mathcal{R}} \equiv \mathcal{R}[\bar{g}] = \bar{g}^{ij}\bar{R}_{ij}$ in terms of the conformal objects by contracting eq. (2.99) with the inverse metric $\tilde{g}^{jk}$. The left side gives us

$$\tilde{g}^{jk}\bar{R}_{jk} = \mathrm{e}^{2\psi}\, \bar{g}^{jk}\bar{R}_{jk} = \mathrm{e}^{2\psi}\, \bar{\mathcal{R}}, \tag{2.100}$$

and on the right side we get

$$\begin{aligned}\tilde{g}^{jk}\bar{R}_{jk} &= \tilde{g}^{jk}\left(\tilde{R}_{jk} - \tilde{\nabla}_j\tilde{\nabla}_k\psi + \tilde{\nabla}_j\psi\,\tilde{\nabla}_k\psi - \left(\tilde{\nabla}^i\tilde{\nabla}_i\psi - \tilde{\nabla}^i\psi\,\tilde{\nabla}_i\psi\right)\tilde{g}_{jk}\right)\\ &= \tilde{\mathcal{R}} - \tilde{\nabla}^i\tilde{\nabla}_i\psi + \tilde{\nabla}^i\psi\,\tilde{\nabla}_i\psi - 3\left(\tilde{\nabla}^i\tilde{\nabla}_i\psi - \tilde{\nabla}^i\psi\,\tilde{\nabla}_i\psi\right)\\ &= \tilde{\mathcal{R}} - 4\,\tilde{\nabla}^i\tilde{\nabla}_i\psi - 2\,\tilde{\nabla}^i\psi\,\tilde{\nabla}_i\psi,\end{aligned} \tag{2.101}$$

where $\tilde{\mathcal{R}} \equiv \mathcal{R}[\tilde{g}] = \tilde{g}^{ij}\tilde{R}_{ij}$. Therefore we obtain

$$\mathcal{R}[\bar{g}] = \mathrm{e}^{-2\psi}\left(\tilde{\mathcal{R}}[\tilde{g}] - 4\,\tilde{\nabla}^i\tilde{\nabla}_i\psi - 2\,\tilde{\nabla}^i\psi\,\tilde{\nabla}_i\psi\right). \tag{2.102}$$

This can be simplified further if we use that

$$8\,\mathrm{e}^{-\psi/2}\,\tilde{\Delta}\,\mathrm{e}^{\psi/2} = 4\,\mathrm{e}^{-\psi/2}\,\tilde{\nabla}^i\left(\mathrm{e}^{\psi/2}\,\tilde{\nabla}_i\psi\right) = 2\,\tilde{\nabla}^i\psi\,\tilde{\nabla}_i\psi + 4\,\tilde{\Delta}\psi, \tag{2.103}$$

where $\tilde{\Delta} = \tilde{g}^{ij}\,\tilde{\nabla}_i\tilde{\nabla}_j = \tilde{\nabla}^i\tilde{\nabla}_i$ is the Laplacian with respect to the metric $\tilde{\boldsymbol{g}}$. Hence, the Ricci scalar turns out to be

$$\bar{\mathcal{R}} = \mathrm{e}^{-2\psi}\left(\tilde{\mathcal{R}} - 8\,\mathrm{e}^{-\psi/2}\,\tilde{\Delta}\,\mathrm{e}^{\psi/2}\right). \tag{2.104}$$

This motivates us to introduce the function

$$\Psi = \mathrm{e}^{\psi/2}, \tag{2.105}$$

so that the metric becomes

$$\bar{\boldsymbol{g}} = \Psi^4\,\tilde{\boldsymbol{g}}. \tag{2.106}$$

Finally, the Ricci scalar eq. (2.104) can be written as

$$\mathcal{R} = \Psi^{-4}\,\tilde{\mathcal{R}} - 8\,\Psi^{-5}\,\tilde{\Delta}\Psi. \tag{2.107}$$

**Conformal Decomposition of Einstein's Equations**

Besides the conformal decomposition (2.106) of the metric, we also decompose the extrinsic curvature into

$$\bar{\boldsymbol{K}} = \Psi^4\left(\tilde{\boldsymbol{A}} + \frac{1}{3}\,\mathcal{K}\,\tilde{\boldsymbol{g}}\right) = \mathrm{e}^{2\psi}\,\tilde{\boldsymbol{A}} + \frac{1}{3}\,\mathcal{K}\,\tilde{g}, \tag{2.108}$$

where $\tilde{\boldsymbol{A}}$ is the conformal trace-free part of the extrinsic curvature such that $\tilde{g}^{ij}\tilde{A}_{ij} \equiv 0$. It follows that

$$\bar{K}^{ik}\bar{K}_{jk} = \tilde{A}^{ik}\tilde{A}_{jk} + \frac{2}{3}\,\mathcal{K}\,\tilde{A}^i{}_j + \frac{1}{9}\,\mathcal{K}^2\,\delta^i_j, \tag{2.109a}$$

$$\bar{K}_{ij}\bar{K}^{ij} = \tilde{A}_{ij}\tilde{A}^{ij} + \frac{1}{3}\,\mathcal{K}^2. \tag{2.109b}$$

If we insert this and eq. (2.107) into the Hamiltonian constraint (2.84a), we obtain

$$\begin{aligned}16\pi E &= \mathcal{R} + \mathcal{K}^2 - \bar{K}_{ab}\bar{K}^{ab}\\ &= \Psi^{-4}\,\tilde{\mathcal{R}} - 8\,\Psi^{-5}\,\tilde{\Delta}\Psi + \frac{2}{3}\,\mathcal{K}^2 - \tilde{A}_{ij}\tilde{A}^{ij},\end{aligned} \tag{2.110}$$

or equivalently

$$\tilde{\Delta}\Psi - \frac{1}{8}\,\tilde{\mathcal{R}}\,\Psi + \left(\frac{1}{8}\,\tilde{A}_{ij}\tilde{A}^{ij} - \frac{1}{12}\,\mathcal{K}^2 + 2\pi E\right)\Psi^5 = 0. \tag{2.111}$$

This is known as the *Lichnerowicz equation*, although Lichnerowicz [Lic44] has only considered the case of a maximal hypersurface, that is, a hypersurface with vanishing mean curvature $\mathcal{K} \equiv 0$.

Next we rewrite the momentum constraint (2.84b) $\bar{\mathbf{D}}\bar{K}^b{}_a(\bar{\boldsymbol{e}}_b) - \bar{\mathbf{D}}\mathcal{K}(\bar{\boldsymbol{e}}_a) = 8\pi\, j_a$. If we insert the ansatz (2.108)

$$\bar{K}^b{}_a = \mathrm{e}^{2\psi}\, g^{ac}\tilde{A}_{bc} + \frac{1}{3}\,\mathcal{K}\,\delta^a_b = \tilde{g}^{ac}\tilde{A}_{bc} + \frac{1}{3}\,\mathcal{K}\,\delta^a_b \tag{2.112}$$

for the extrinsic curvature into the momentum constraint, we get for the first term

$$\bar{\mathbf{D}}\bar{K}^b{}_a = \bar{\mathbf{D}}\Big(\tilde{g}^{ac}\tilde{A}_{bc}\Big) + \frac{1}{3}\,\delta^b_a\,\bar{\mathbf{D}}\mathcal{K}. \tag{2.113}$$

Now we change to the conformal frame $\{\tilde{\boldsymbol{\theta}}^i\}$. The first term can then be written as $\bar{\mathbf{D}}\Big(\tilde{g}^{jk}\tilde{A}_{ik}\Big) \equiv \bar{\mathbf{D}}\tilde{A}^j{}_i$ so that the momentum constraint is

$$\bar{\mathbf{D}}\bar{K}^j{}_i(\tilde{\boldsymbol{e}}_j) - \frac{2}{3}\,\bar{\mathbf{D}}\mathcal{K}(\tilde{\boldsymbol{e}}_i) = 8\pi\, j_i. \tag{2.114}$$

However we would like to use the conformal derivative. While the trace term is simply $\mathbf{D}\mathcal{K} = \tilde{\mathbf{D}}\mathcal{K}$, the term $\mathbf{D}\tilde{A}^j{}_i$ needs to be treated more carefully:

$$\begin{aligned}
\mathbf{D}\tilde{A}^j{}_i &= \mathbf{d}\tilde{A}^j{}_i + \bar{\boldsymbol{\omega}}^j{}_k\,\tilde{A}^k{}_i - \bar{\boldsymbol{\omega}}^k{}_i\,\tilde{A}^j{}_k \\
&= \mathbf{d}\tilde{A}^j{}_i + \Big(\tilde{\boldsymbol{\omega}}^j{}_k + \psi_k\,\tilde{\boldsymbol{\theta}}^j - \psi^j\,\tilde{\boldsymbol{\theta}}_k\Big)\,\tilde{A}^k{}_i - \Big(\tilde{\boldsymbol{\omega}}^k{}_i + \psi_i\,\tilde{\boldsymbol{\theta}}^k - \psi^k\,\tilde{\boldsymbol{\theta}}_i\Big)\,\tilde{A}^j{}_k \\
&= \tilde{\mathbf{D}}\tilde{A}^j{}_i + \tilde{A}^k{}_i\psi_k\,\tilde{\boldsymbol{\theta}}^j - \tilde{A}^k{}_i\psi^j\,\tilde{\boldsymbol{\theta}}_k - \tilde{A}^j{}_k\psi_j\,\tilde{\boldsymbol{\theta}}^k + \tilde{A}^j{}_k\psi^k\,\tilde{\boldsymbol{\theta}}_i,
\end{aligned} \tag{2.115}$$

so that

$$\bar{\mathbf{D}}\bar{K}^j{}_i(\tilde{\boldsymbol{e}}_j) = \tilde{\mathbf{D}}\bar{K}^j{}_i(\tilde{\boldsymbol{e}}_j) + 3\tilde{A}^j{}_i\,\tilde{\mathbf{D}}\psi(\tilde{\boldsymbol{e}}_j) = \tilde{\nabla}_j\tilde{A}^j{}_i + 3\tilde{A}^j{}_i\,\tilde{\nabla}_j\psi. \tag{2.116}$$

If we put this into the momentum constraint (2.114), we get

$$\tilde{\nabla}_j\tilde{A}^j{}_i + 3\tilde{A}^j{}_i\tilde{\nabla}_j\psi - \frac{2}{3}\tilde{\nabla}_i\mathcal{K} = 8\pi j_i. \tag{2.117}$$

In the treatment of the initial value problem, one often uses a slightly different ansatz for the extrinsic curvature, namely $\bar{K}^{ij} = \Psi^{-2}\hat{A}^{ij} + \frac{1}{3}\,\mathcal{K}\,\Psi^4\,\tilde{g}^{ij}$ where $\hat{A}^{ij} = \Psi^6\tilde{A}^{ij}$. This eliminates the second term with the derivative of $\Psi$ in the momentum constraint, but the evolution equations would be more complicated. However, this ansatz allows us to decompose $\hat{A}^{ij} = \hat{A}^{ij}_{\mathrm{TT}} + (\tilde{\mathrm{L}}X)^{ij}$ into a transverse-traceless part $\hat{A}^{ij}_{\mathrm{TT}}$ with $\tilde{\nabla}_i\hat{A}^{ij}_{\mathrm{TT}} = 0$ and a longitudinal part

$$(\tilde{\mathrm{L}}\boldsymbol{x})^{ij} = \tilde{\nabla}^i x^j + \tilde{\nabla}^j x^i - \frac{2}{3}\tilde{\nabla}_k\,\tilde{g}^{ij}\,x^k. \tag{2.118}$$

It can be shown that $\tilde{\nabla}_j \hat{A}^{ij} = \tilde{\nabla}_j (\tilde{\mathrm{L}}\boldsymbol{x})^{ij} \equiv \Delta_{\mathrm{L}} x^i$ so that the momentum reduces to

$$\Delta_{\mathrm{L}} x^i - \frac{2}{3}\,\Psi^6\,\tilde{\nabla}^i \mathcal{K} = 8\pi\,\tilde{\jmath}^i. \tag{2.119}$$

where $\tilde{\boldsymbol{\jmath}} = \Psi^6\,\bar{\boldsymbol{\jmath}}$. The advantage of the conformal method over other approaches like the conformal thin-sandwich method is that there are existence and uniqueness theorems [ÓY73; ÓY74a; ÓY74b] for the solutions to the Lichnerowicz equation (2.111) and equation (2.119) in many cases, in particular if $\mathcal{K} = \text{const}$. See also [Ise14] for a recent review.

The usual treatment is that the conformal metric $\tilde{\boldsymbol{g}}$, the trace $\mathcal{K}$ and the transverse-traceless part $\hat{A}^{ij}_{\mathrm{TT}}$ of the extrinsic curvature as well as the matter fields $E$ and $\tilde{\boldsymbol{\jmath}}$ can be chosen freely. The conformal factor $\Psi$ and the longitudinal part via $x^i$ are determined by the constraint equations. The best studied solutions are the so-called *CMC-data* of constant mean curvature where $\mathcal{K} = \text{const}$. In this case the momentum constraint decouples from the Hamiltonian constraint and can be used to determine $x^i$. In the following step the conformal factor can be calculated from the Hamiltonian constraint. Note that the auxiliary momentum $\tilde{\boldsymbol{\jmath}}$ is imposed in the beginning. The physical matter momentum $\boldsymbol{\jmath}$ can only be determined in the end when the conformal factor $\Psi$ is known.

For completeness we want to state that it is also possible to rewrite the evolution equation in terms of $\Psi = \mathrm{e}^{\psi/2}, \tilde{\boldsymbol{g}}, \mathcal{K}$ and $\tilde{\boldsymbol{A}}$. For a derivation see the textbook of Gourgoulhon [Gou07] for example. The result is that the evolution equations split up into the following system:

$$\dot{\psi} = \boldsymbol{\mathcal{L}}_{\boldsymbol{\beta}}\psi + \frac{1}{3}\left(\tilde{\nabla}_i \beta^i - \alpha\mathcal{K}\right), \tag{2.120a}$$

$$\dot{\tilde{\boldsymbol{g}}}_{ij} = \left(\boldsymbol{\mathcal{L}}_{\boldsymbol{\beta}}\tilde{\boldsymbol{g}}\right)_{ij} - 2\alpha\,\tilde{A}_{ij} - \frac{2}{3}\,\tilde{g}_{ij}\tilde{\nabla}_k\beta^k, \tag{2.120b}$$

$$\dot{\mathcal{K}}_{ij} = \boldsymbol{\mathcal{L}}_{\boldsymbol{\beta}}\mathcal{K} - \mathrm{e}^{-2\psi}\left(\tilde{\Delta}\alpha + \tilde{\nabla}_i\psi\,\tilde{\nabla}^i\alpha\right) + \alpha\left(4\pi\,(\mathcal{S}+E) + \tilde{A}_{ij}\tilde{A}^{ij} + \frac{1}{3}\,\mathcal{K}^2\right), \tag{2.120c}$$

$$\begin{aligned}\dot{\tilde{\boldsymbol{A}}}_{ij} = {} & \left(\boldsymbol{\mathcal{L}}_{\boldsymbol{\beta}}\tilde{\boldsymbol{A}}\right)_{ij} - \frac{2}{3}\,\tilde{A}_{ij}\tilde{\nabla}_k\beta^k + \alpha\left[\mathcal{K}\,\tilde{A}_{ij} - 2\,\tilde{A}_{ik}\tilde{A}^k{}_j - 8\pi\left(\Psi^{-4}S_{ij} - \frac{1}{3}\,\mathcal{S}\,\tilde{g}_{ij}\right)\right] \\ & + \mathrm{e}^{-2\psi}\left[-\tilde{\nabla}_i\tilde{\nabla}_j\alpha + \tilde{\nabla}_i\psi\,\tilde{\nabla}_j\alpha + \tilde{\nabla}_j\psi\,\tilde{\nabla}_i\alpha + \frac{1}{3}\left(\tilde{\Delta}\alpha - 2\,\tilde{\nabla}_k\psi\,\tilde{\nabla}^k\alpha\right)\tilde{g}_{ij}\right] \\ & + \alpha\,\mathrm{e}^{-2\psi}\left[\tilde{R}_{ij} - \frac{1}{3}\,\tilde{\mathcal{R}}\,\tilde{g}_{ij} - \tilde{\nabla}_i\tilde{\nabla}_j\psi + \tilde{\nabla}_i\psi\,\tilde{\nabla}_j\psi + \frac{1}{3}\left(\tilde{\Delta}\psi - \tilde{\nabla}_k\psi\,\tilde{\nabla}^k\psi\right)\tilde{g}_{ij}\right].\end{aligned} \tag{2.120d}$$

# 3 Geometry on Maximally Symmetric Spaces

Maximally symmetric spaces play an important role in cosmology due to the cosmological principle (see chapter 4). For this reason, they will also be used as the conformal metric for the multi-black-hole solutions in chapter 6. They are introduced in the first section 3.1 of this chapter. As we show in the second section 3.2, they are related by a stereographic projection. A unified description of points and circles on maximally symmetric spaces is given by Lie sphere geometry, presented in section 3.3. In the following sections we consider special configurations of points and circles which we will use to construct inhomogeneous cosmological models. In section 3.4 we consider evenly distributed points on the hypersphere such that the distance to the next neighbours is the same for each point. These points are the vertices of the uniform polytopes in four dimensions. Finally in section 3.5, we present the Apollonian sphere packing which fills a big ball with smaller ones. These packings will be used to construct various Swiss-cheese models in chapter 5.

## 3.1 Maximally Symmetric Spaces

For a detailed discussion of maximally symmetric spaces and constant curvature spaces see the books of Weinberg [Wei72] and Urbantke [Urb08]. Here we summarise the most important statements.

#### Killing vector fields

A symmetry of a metric manifold $\mathcal{M}$, either Riemannian, Lorentzian or with an arbitrary signature ($n$ times '+' and $m$ times '−') of the metric, is a diffeomorphism $f : \mathcal{M} \to \mathcal{M}$, $x^\alpha \mapsto y^\alpha = f(x^\alpha)$ preserving the metric, that is $\boldsymbol{g} = f^*\boldsymbol{g}$. For the components of the metric this implies

$$g_{\alpha\beta}(x) = \frac{\partial y^\gamma}{\partial x^\alpha}\frac{\partial y^\delta}{\partial x^\beta}\, g_{\gamma\delta}(y). \tag{3.1}$$

It is said that the metric is *form-invariant* under $f$ and $f$ is also called an *isometry*. All isometries form a group with the composition as group operation, the *isometry group* of $\mathcal{M}$.

Moreover, as shown by Myers and Steenrod [MS39], the isometry group is a Lie group. For this reason we may consider infinitesimal transformations $y^\alpha = x^\alpha + \epsilon k^\alpha$. Then eq. (3.1) yields the *Killing equation* $\nabla_\alpha k_\beta + \nabla_\beta k_\alpha = 0$ or

$$\boldsymbol{\mathcal{L}}_{\boldsymbol{k}}\boldsymbol{g} = 0. \tag{3.2}$$

This means that the metric is invariant under the flow of the *Killing vector field* $\boldsymbol{k}$ generating the isometry $f$ infinitesimally. The Killing vector fields form the Lie algebra of the isometry group.

There are at most $\frac{1}{2}d(d+1)$ Killing vector fields on a $d$-dimensional manifold; in general there are less, or none. This can be made plausible by the following observation: A Killing vector field is completely determined by the $d$ values of $k_\alpha(p)$ and its $\frac{1}{2}d(d-1)$ non-zero first derivatives $(\nabla_\beta k_\alpha)(p)$, $\alpha \neq \beta$, at some point $p$. Higher derivatives are determined by the *Killing identity*

$$\nabla_\gamma \nabla_\beta k_\alpha = R^\delta{}_{\gamma\beta\alpha} k_\delta, \tag{3.3}$$

which can be derived from the general formula for second derivatives, the Killing equation and the first Bianchi identity.

**Maximally symmetric and Constant Curvature Spaces**

A manifold possessing the maximal number of Killing vector fields is called *maximally symmetric*. In this case, the isometry group contains the $d$-dimensional 'translational' sub-group $\mathcal{G}_{\text{hom}}$ of the isometry group acting transitively on the manifold. That is, for any two points $p, q \in \mathcal{M}$ there is an isometry $g \in \mathcal{G}_{\text{hom}}$ such that $q = g(p)$. In an appropriate frame they are determined by $k_\alpha = \delta^A_\alpha$ and $\nabla_\beta k_\alpha = 0$ where $A = 1, \ldots, n$. Any space with a transitively group acting on it is called *homogeneous*.

Furthermore we have the $\frac{1}{2}n(n-1)$-dimensional 'rotational' sub-group $\mathcal{G}_{\text{iso}}$ isomorphic to $SO(n,m)$ such that, for any point $p \in \mathcal{M}$ and unit tangent vectors $\boldsymbol{v}, \boldsymbol{w} \in \mathrm{T}_p\mathcal{M}$, there is an isometry $g \in \mathcal{G}_{\text{iso}}$ with $g(p) = p$ and $g_* \boldsymbol{v} = \boldsymbol{w}$. In an appropriate coordinate system, they are determined by $\nabla_\beta k_\alpha = -\nabla_\alpha k_\beta$ and $k_\alpha = 0$. Such a manifold is called *(globally) isotropic* and possesses no preferred directions.

It can be shown that isotropic manifolds are also homogeneous, whereas the opposite is not true; a homogeneous space may have a preferred direction. Furthermore, it is possible to consider $\mathcal{G}_{\text{iso}}$ point-wise, that is, only for certain points $p \in \mathcal{M}$ there is an isometry $g$ such that $g(p) = p$ and $g_* \boldsymbol{v} = \boldsymbol{w}$ for any $\boldsymbol{v}, \boldsymbol{w} \in \mathrm{T}_p\mathcal{M}$. In this case we say $\mathcal{M}$ is *isotropic about* $p$. A well-known example is the Schwarzschild spacetime.

By considering higher derivatives and using eq. (3.3) we can derive further integrability conditions. These can be used to show that the curvature tensor with lowered indices of a maximally symmetric space must be of the form

$$R_{\alpha\beta\gamma\delta} = \frac{\mathcal{R}}{d(d-1)} \left( g_{\alpha\gamma} g_{\beta\delta} - g_{\alpha\delta} g_{\beta\gamma} \right). \tag{3.4}$$

From the isotropy the Bianchi identities it follows that the Ricci scalar $\mathcal{R}$ must be constant. Hence, it is a constant curvature space. If we define the *curvature constant* $k = \frac{\mathcal{R}}{d(d-1)}$, we obtain

$$R_{\alpha\beta\gamma\delta} = k \left( g_{\alpha\gamma} g_{\beta\delta} - g_{\alpha\delta} g_{\beta\gamma} \right), \tag{3.5a}$$

$$R_{\alpha\beta} = (d-1) k g_{\alpha\beta}, \tag{3.5b}$$

$$\mathcal{R} = d(d-1)k. \tag{3.5c}$$

Metric spaces exhibiting such a curvature tensor are called *constant curvature spaces*. Maximally symmetric spaces are always constant curvature spaces and vice versa.

**Construction**

At last we construct these spaces. It can be shown that two maximally symmetric spaces with the same dimension, metric signature and value of the curvature constant are (locally)

isometric. This is a consequence of the fact that constant curvature spaces are necessarily conformally flat. For this reason it is sufficient to find one example for each value of $k$.

The spaces $\mathbb{R}^{n,m}$ are maximally symmetric with vanishing curvature constant $k = 0$ and symmetry group $\mathbb{R}^{n+m} \times SO(n,m)$, where the first factor contains $n+m$ translations and the second one the rotations. Maximally symmetric spaces of positive and negative curvature are easily obtained as hypersurfaces of constant distance to the origin in $\mathbb{R}^{n,m}$. If we consider the hypersurfaces $\{\boldsymbol{X} \in \mathbb{R}^{n,m} : \|\boldsymbol{X}\| = R\}$, we lose the translational symmetry but $SO(n,m)$ remains as the symmetry group of the hypersurface. Since $SO(n,m)$ is of dimension $\frac{1}{2}d(d-1)$, where $d = m+n$, these hypersurfaces are maximally symmetric spaces of dimension $d-1$. By this method we can construct constant curvature spaces for all values of $k$ and all signatures of the metric.

We are mainly interested in the case of 3-dimensional Riemannian maximally symmetric spaces, but the generalisation to arbitrary dimensions is straightforward. The flat space with $k = 0$ is the three-dimensional Euclidean space $\mathbb{R}^3$ with the metric

$$\boldsymbol{h}_0 \equiv \boldsymbol{\delta} = \left(\mathbf{d}x^1\right)^2 + \left(\mathbf{d}x^2\right)^2 + \left(\mathbf{d}x^3\right)^2 = \mathbf{d}r^2 + r^2\,\mathbf{d}\Omega^2 \tag{3.6}$$

in Cartesian and spherical coordinates, respectively. This space is parametrised by $\boldsymbol{x} = r\,\boldsymbol{E}_3(\vartheta,\varphi)$, where $\boldsymbol{E}_3$ is the 3-dimensional unit vector

$$\boldsymbol{E}_3(\vartheta,\varphi) = \begin{pmatrix} \sin\vartheta\sin\varphi \\ \sin\vartheta\cos\varphi \\ \cos\vartheta \end{pmatrix}. \tag{3.7}$$

Later we also use an embedding into the plane $x^4 = 0$ of $\mathbb{R}^4$ via $\boldsymbol{X} = (\boldsymbol{x}, 0) = (r\,\boldsymbol{E}_3, 0)$.

For positively curved spaces, we apply the method described above: We consider the hypersurface $\{\boldsymbol{X} \in \mathbb{R}^4 : \|\boldsymbol{X}\| = R\}$, parametrised by $\boldsymbol{X} = R\,(\sin\chi\,\boldsymbol{E}_3, \cos\chi) \equiv \boldsymbol{E}_4(\chi,\vartheta,\varphi)$. The induced metric of this hypersurface is

$$\boldsymbol{h}_+ = R^2\,(\mathbf{d}\chi^2 + \sin^2\chi\,\mathbf{d}\Omega^2). \tag{3.8}$$

A straightforward calculation shows that $k = \frac{1}{R^2}$, hence we cover all positive values for the curvature constant.

The spaces of negative curvature are obtained if we consider the space-like hypersurfaces $\{\boldsymbol{X} \in \mathbb{R}^{3,1} : \|\boldsymbol{X}\|_{\mathrm{M}} = -R\}$, where $\|\cdot\|_{\mathrm{M}}$ is the Minkowski norm. They are given by $\boldsymbol{X} = R\,(\sinh u\,\boldsymbol{E}_3, \pm\cosh u) \equiv \boldsymbol{E}_{\mathrm{M}}(u,\vartheta,\varphi)$. This is the two-sheeted hyperboloid with metric

$$\boldsymbol{h}_- = R^2\,(\mathbf{d}u^2 + \sinh^2 u\,\mathbf{d}\Omega^2). \tag{3.9}$$

The curvature constant of these spaces is given by $k = -\frac{1}{R^2}$, therefore we found an example for all negative values.

Note that we can restrict ourselves to the cases $k \in \{-1, 0, 1\}$ because it is always possible to rescale the radial coordinate such that $R = 1$. For convenience, we write

$$\boldsymbol{h}_k = \mathbf{d}\chi^2 + \Sigma_k^2(\chi)\,\mathbf{d}\Omega^2, \tag{3.10}$$

where

$$\Sigma_k(\chi) = \begin{cases} \sin\chi & k = +1 \quad \text{spherical,} \\ \chi & k = \phantom{+}0 \quad \text{flat,} \\ \sinh\chi & k = -1 \quad \text{hyperbolic.} \end{cases} \tag{3.11}$$

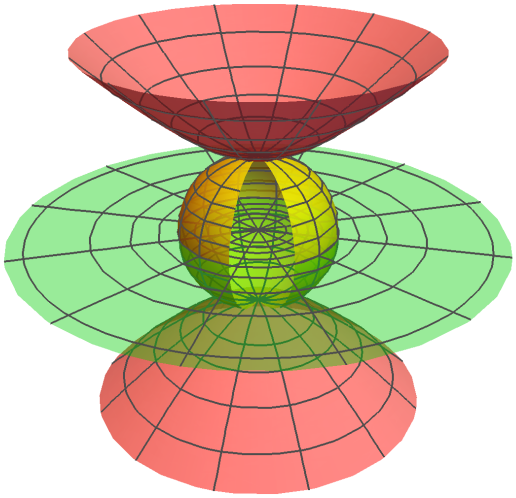

**Figure 3.1:** Embedding of the flat (green), spherical (yellow) and hyperbolic (red) space into $\mathbb{R}^3$ or $\mathbb{R}^{2,1}$, respectively. The indicated coordinate lines belong to the same values: The angular coordinates are identified and the radial coordinates are related by a stereographic projection, see section 3.2.

The embeddings of all three maximally symmetric spaces are shown in fig. 3.1.

Of particular interest in general relativity are also the maximally symmetric spaces with Lorentzian signature: These are the flat Minkowski space with vanishing curvature, the de Sitter space with positive $k$ and the negatively curved anti-de Sitter space. The (anti-)de Sitter spaces can be constructed in the same way as their Riemannian analogues. They are the vacuum solutions to Einstein's equations including the cosmological constant $\Lambda$ which determines the curvature constant $k = \frac{2\Lambda}{(d-1)(d-2)}$.

## 3.2 Stereographic Projection

The three different kinds of maximally symmetric spaces belong to the same conformal class. This means, the spherical and hyperbolic space are both conformally flat. The coordinate transformation which shows this explicitly has a nice geometrical meaning: It is a *stereographic projection*.

In order to prove this, we embed the flat, spherical and hyperbolic space again into the $\mathbb{R}^4$ or $\mathbb{R}^{3,1}$, respectively, as in the previous section 3.1 via

$$\boldsymbol{X} = \begin{cases} (r\,\boldsymbol{E}_3(\vartheta,\varphi), 0) \in \mathbb{R}^4 & \text{for } k = 0, \\ (\sin\chi\,\boldsymbol{E}_3(\vartheta,\varphi), \cos\chi) \in \mathbb{R}^4 & \text{for } k = 1, \\ (\pm\cosh u, \sinh u\,\boldsymbol{E}_3(\vartheta,\varphi)) \in \mathbb{R}^{1,3} & \text{for } k = -1, \end{cases} \tag{3.12}$$

and analogously for other dimensions. Because of the rotational symmetry around the $x^4$-axis, we can simply identify the angular coordinates

$$\{\vartheta_0, \varphi_0\} \equiv \{\vartheta_+, \varphi_+\} \equiv \{\vartheta_-, \varphi_-\}\,. \tag{3.13}$$

Hence, we can restrict ourselves to the two-dimensional case, shown in fig. 3.2.

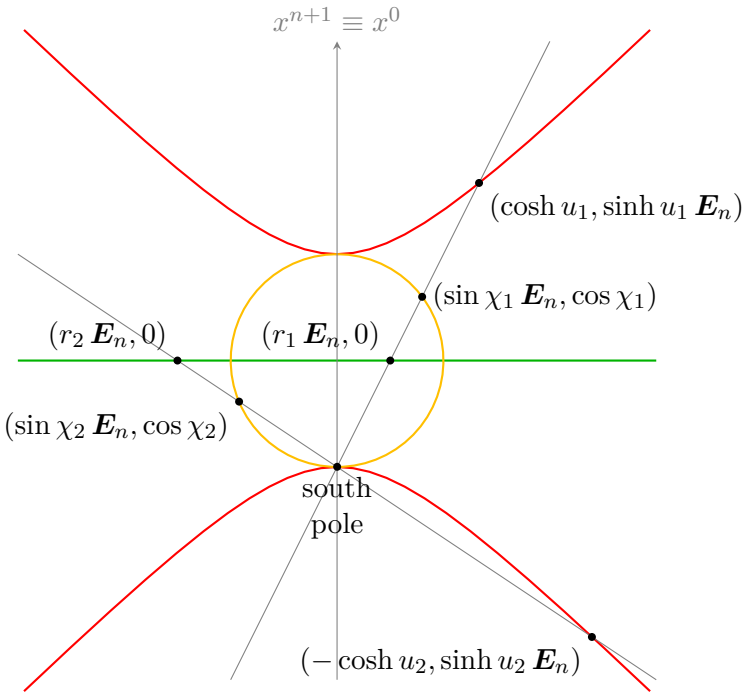


**Figure 3.2:** Stereographic projection in $\mathbb{R}^{n+1}$ and $\mathbb{R}^{n,1}$: Due to rotational symmetry around the $x^{n+1} \equiv x^0$-axis, we can restrict the considerations to any plane containing the symmetry axis. The interactions points of a line through the south pole and the maximally symmetric spaces, see fig. 3.1, are mapped to each other by a stereographic projection.

### Coordinate Transformations

Now we draw a straight line through the point $\boldsymbol{S} = (0, 0, 0, -1)$, the *south pole*, which intersects each space exactly once in another point than $\boldsymbol{S}$ if the slope is not 0 or 1. For the moment, we will ignore these special cases. The stereographic projection can be defined as the mapping between the maximally symmetric spaces which maps the intersection points on such a line to each other.

We get a relation between the radial coordinates if we apply the ray theorem, yielding

$$r = \frac{\sin \chi}{1 + \cos \chi} = \pm \frac{\sinh u}{1 + \cosh u}, \tag{3.14}$$

where the last sign depends on the intersected sheet of the hyperboloid. Using the trigonometric identities $\sin \chi = 2 \sin \frac{\chi}{2} \cos \frac{\chi}{2}$ and $1 + \cos \chi = 2 \cos^2 \frac{\chi}{2}$, and the corresponding relations in the hyperbolic case, we get

$$r = \tan \frac{\chi}{2} = \pm \tanh \frac{u}{2}. \tag{3.15}$$

These are coordinate transformations between the radial coordinates $r$, $\chi$ and $u$.

Now we show that the spherical and hyperbolic space are actually conformally flat: First, we consider the spherical case where $r(\chi) = \tan \frac{\chi}{2}$. In this case we obtain

$$\frac{\mathrm{d}r}{\mathrm{d}\chi} = \tan' \frac{\chi}{2} = \frac{1}{2} \left(1 + \tan^2 \frac{\chi}{2}\right) = \begin{cases} \frac{1}{2} \left(1 + r^2\right), \\ \frac{1}{2 \cos^2 \frac{\chi}{2}}, \end{cases} \tag{3.16}$$

hence

$$\mathbf{d}\chi = \frac{2}{1+r^2}\,\mathbf{d}r, \tag{3.17a}$$

$$\mathbf{d}r = \frac{1}{2\cos^2\frac{\chi}{2}}\,\mathbf{d}\chi. \tag{3.17b}$$

Furthermore we have the identity

$$\sin\chi = 2\sin\frac{\chi}{2}\cos\frac{\chi}{2} = 2\tan\frac{\chi}{2}\cos^2\frac{\chi}{2} = \frac{2r}{1+r^2}. \tag{3.18}$$

Therefore the round metric can also be written as

$$\boldsymbol{h}_+ = \mathbf{d}\chi^2 + \sin^2\chi\,\mathbf{d}\Omega^2 = \left(\frac{2}{1+r^2}\right)^2\left(\mathbf{d}r^2 + r^2\,\mathbf{d}\Omega^2\right) = \left(\frac{2}{1+r^2}\right)^2\boldsymbol{\delta}, \tag{3.19a}$$

or the other way round as

$$\boldsymbol{\delta} = \left(\frac{1}{2\cos^2\frac{\chi}{2}}\right)^2\boldsymbol{h}_+. \tag{3.19b}$$

Since we have for $\boldsymbol{S} = (0,0,0,-1)$

$$\|\boldsymbol{E}_4 - \boldsymbol{S}\|_4^2 = 2 - 2\,\boldsymbol{E}_4\cdot\boldsymbol{S} = 2\,(1+\cos\chi) = 4\cos^2\frac{\chi}{2} \tag{3.20}$$

where $\|\cdot\|_4$ is the standard norm in $\mathbb{R}^4$, we can also write

$$\boldsymbol{\delta} = \left(\frac{2}{4\cos^2\frac{\chi}{2}}\right)^2\boldsymbol{h}_+ = \frac{4}{\|\boldsymbol{E}_4 - \boldsymbol{S}\|_4^4}\,\boldsymbol{h}_+. \tag{3.21}$$

For the hyperbolic space the calculation is very similar to the spherical case, except for some sign changes due to the minus in the basic relation $\cosh^2 x - \sinh^2 x = 1$. This time we have $r = \tanh\frac{u}{2}$ so that

$$\mathbf{d}u = \frac{2}{1-r^2}\;\mathbf{d}r, \tag{3.22a}$$

$$\mathbf{d}r = \frac{1}{2\cosh^2\frac{u}{2}}\,\mathbf{d}u, \tag{3.22b}$$

$$\sinh x = \frac{2r}{1-r^2}. \tag{3.22c}$$

Therefore the metric becomes

$$\boldsymbol{h}_- = \left(\frac{2}{1-r^2}\right)^2\boldsymbol{\delta}, \tag{3.23a}$$

$$\boldsymbol{\delta} = \left(\frac{1}{2\cosh^2\frac{\chi}{2}}\right)^2\boldsymbol{h}_-. \tag{3.23b}$$

For $\boldsymbol{S} = (0,0,0,-1)$ we have

$$\|\boldsymbol{E}_{\mathrm{M}} - \boldsymbol{S}\|_{\mathrm{M}}^2 = 2 - 2\,\boldsymbol{E}_{\mathrm{M}}\cdot\boldsymbol{S} = 2\,(1\pm\cosh\chi) = \pm 4\cosh^2\frac{\chi}{2} \tag{3.24}$$

where $\|\cdot\|_4$ is the Minkowski norm in $\mathbb{R}^{3,1}$. Hence, we get in the hyperbolic case a result similar to the spherical case, namely

$$\boldsymbol{\delta} = \frac{4}{\|\boldsymbol{E}_{\mathrm{M}} - \boldsymbol{S}\|_{\mathrm{M}}^4}\,\boldsymbol{h}_-. \tag{3.25}$$

**Coordinate-free Representation and Relations between the Norms**

Finally, we derive a coordinate-independent formulation for the stereographic projection. We start again with the spherical case. Let us consider the line $\boldsymbol{\ell_Y}$ through the south pole $\boldsymbol{S}$ and some point $\boldsymbol{Y}$ on the hypersphere with $\boldsymbol{Y}^2 = 1$. The parametric representation of this line is given by

$$\boldsymbol{\ell_Y}(\lambda) = \boldsymbol{S} + \lambda(\boldsymbol{Y} - \boldsymbol{S}) = \lambda\,\boldsymbol{Y} + (1-\lambda)\,\boldsymbol{S}. \tag{3.26}$$

We are looking for the intersection point $\boldsymbol{X}$ in the equatorial plane. Obviously, $\boldsymbol{S}$ is normal to the equatorial plane, hence $\boldsymbol{X} \cdot \boldsymbol{S} = 0$. Since $\boldsymbol{X}$ is also on the line, it satisfies

$$\boldsymbol{X} = \lambda_{\boldsymbol{X}}\boldsymbol{Y} + (1-\lambda_{\boldsymbol{X}})\,\boldsymbol{S}. \tag{3.27}$$

After multiplying with $\boldsymbol{S}$, we obtain

$$0 = \lambda_{\boldsymbol{X}}\,\boldsymbol{Y}\cdot\boldsymbol{S} + 1 - \lambda_{\boldsymbol{X}} = 1 - \lambda_{\boldsymbol{X}}\,(1 - \boldsymbol{Y}\cdot\boldsymbol{S})\,, \tag{3.28}$$

hence

$$\lambda_{\boldsymbol{X}} = \frac{1}{1-\boldsymbol{Y}\cdot\boldsymbol{S}}. \tag{3.29}$$

Therefore the stereographic projection $\pi$ from the hypersphere to the equatorial plane is given by

$$\boldsymbol{X} = \pi(\boldsymbol{Y}) = \boldsymbol{\ell_Y}(\lambda_{\boldsymbol{X}}) = \frac{\boldsymbol{Y} - (\boldsymbol{Y}\cdot\boldsymbol{S})\,\boldsymbol{S}}{1-\boldsymbol{Y}\cdot\boldsymbol{S}}. \tag{3.30}$$

Next, we determine the inverse map $\pi^{-1}$ from the equatorial plane to the hypersphere. This time we consider the line

$$\boldsymbol{\ell_X}(\lambda) = \boldsymbol{S} + \lambda\,(\boldsymbol{X} - \boldsymbol{S}) = \lambda\,\boldsymbol{X} + (1-\lambda)\,\boldsymbol{S} \tag{3.31}$$

through the south pole $\boldsymbol{S}$ and the point $\boldsymbol{X}$ in the equatorial plane. We are looking for the intersection point $\boldsymbol{Y}$ on the hypersphere, given by $\boldsymbol{\ell}^2_{\boldsymbol{X}}(\lambda_{\boldsymbol{Y}}) = 1$ and $\lambda_{\boldsymbol{Y}} \neq 0$; $\lambda = 0$ would be the south pole $\boldsymbol{S}$. Because of $\boldsymbol{X}\cdot\boldsymbol{S} = 0$ and $\boldsymbol{S}^2 = 1$, we obtain

$$1 = \boldsymbol{\ell}^2_{\boldsymbol{X}}(\lambda_{\boldsymbol{Y}}) = \lambda^2_{\boldsymbol{Y}}\,\boldsymbol{X}^2 + (1-\lambda_{\boldsymbol{Y}})^2 = 1 - 2\lambda_{\boldsymbol{Y}} + \lambda^2_{\boldsymbol{Y}}(1+\boldsymbol{X}^2), \tag{3.32}$$

from which we get

$$\lambda_{\boldsymbol{Y}} = \frac{2}{1+\boldsymbol{X}^2}. \tag{3.33}$$

Therefore the inverse map is

$$\boldsymbol{Y} = \pi^{-1}(\boldsymbol{X}) = \boldsymbol{\ell_X}(\lambda_{\boldsymbol{Y}}) = \frac{2}{1+\boldsymbol{X}^2}\,\boldsymbol{X} - \frac{1-\boldsymbol{X}^2}{1+\boldsymbol{X}^2}\,\boldsymbol{S}. \tag{3.34}$$

Note that a vector in the equatorial plane $\boldsymbol{X} = (\boldsymbol{x}, 0)$ can be identified with a 3-dimensional vector $\boldsymbol{x} \in \mathbb{R}^3$ omitting the last component and vice versa. For this reason we write $\|\boldsymbol{X}\|_4 \equiv \|\boldsymbol{X}\|_3$ and $\|\boldsymbol{x}\|_3 \equiv \|\boldsymbol{x}\|_4$, where $\|\cdot\|_3$ is the standard norm in $\mathbb{R}^3$.

At last, we derive a relation between $\|\boldsymbol{a}-\boldsymbol{b}\|_3 \equiv \|\boldsymbol{a}-\boldsymbol{b}\|_4$ for two points $\boldsymbol{a}$ and $\boldsymbol{b}$ in the equatorial plane and $\|\boldsymbol{A}-\boldsymbol{B}\|_4$ for their projections $\boldsymbol{A} = \pi^{-1}(\boldsymbol{a})$ and $\boldsymbol{B} = \pi^{-1}(\boldsymbol{b})$ on the hypersphere. From the inverse stereographic projection (3.34) we get

$$\boldsymbol{A} = \frac{2}{1+\boldsymbol{a}^2}\,\boldsymbol{a} - \frac{1-\boldsymbol{a}^2}{1+\boldsymbol{a}^2}\,\boldsymbol{S}, \tag{3.35}$$

and analogously for $\boldsymbol{B}$. Using that $\boldsymbol{a}\cdot\boldsymbol{S} = 0 = \boldsymbol{b}\cdot\boldsymbol{S}$ by construction of the projection, we have

$$\begin{aligned}
\frac{1}{2}\,\|\boldsymbol{A}-\boldsymbol{B}\|_4^2 &= 1 - \boldsymbol{A}\cdot\boldsymbol{B} = 1 - \left(\frac{2}{1+\boldsymbol{a}^2}\,\boldsymbol{a} - \frac{1-\boldsymbol{a}^2}{1+\boldsymbol{a}^2}\,\boldsymbol{S}\right)\cdot\left(\frac{2}{1+\boldsymbol{b}^2}\,\boldsymbol{b} - \frac{1-\boldsymbol{b}^2}{1+\boldsymbol{b}^2}\,\boldsymbol{S}\right) \\
&= \frac{1+\boldsymbol{a}^2+\boldsymbol{b}^2+\boldsymbol{a}^2\,\boldsymbol{b}^2}{(1+\boldsymbol{a}^2)(1+\boldsymbol{b}^2)} - \frac{4\,\boldsymbol{a}\cdot\boldsymbol{b}}{(1+\boldsymbol{a}^2)(1+\boldsymbol{b}^2)} - \frac{1-\boldsymbol{a}^2-\boldsymbol{b}^2+\boldsymbol{a}^2\,\boldsymbol{b}^2}{(1+\boldsymbol{a}^2)(1+\boldsymbol{b}^2)} \\
&= \frac{2\,\boldsymbol{a}^2 - 4\,\boldsymbol{a}\cdot\boldsymbol{b} + 2\,\boldsymbol{b}^2}{(1+\boldsymbol{a}^2)(1+\boldsymbol{b}^2)} \\
&= \frac{2\,(\boldsymbol{a}-\boldsymbol{b})^2}{(1+\boldsymbol{a}^2)(1+\boldsymbol{b}^2)}.
\end{aligned} \tag{3.36}$$

Now we can use that

$$\|\boldsymbol{A}-\boldsymbol{S}\|_4^2 = 2\,(1-\boldsymbol{A}\cdot\boldsymbol{S}) = 2\left(1+\frac{1-\boldsymbol{a}^2}{1+\boldsymbol{a}^2}\right) = \frac{4}{1+\boldsymbol{a}^2}, \tag{3.37}$$

so that we can write eq. (3.36) as

$$\begin{aligned}
4\,\|\boldsymbol{A}-\boldsymbol{B}\|_4^2 &= \frac{16\,(\boldsymbol{a}-\boldsymbol{b})^2}{(1+\boldsymbol{a}^2)(1+\boldsymbol{b}^2)} = \left(\frac{4}{1+\boldsymbol{a}^2}\right)\left(\frac{4}{1+\boldsymbol{b}^2}\right)(\boldsymbol{a}-\boldsymbol{b})^2 \\
&= \|\boldsymbol{A}-\boldsymbol{S}\|_4^2\,\|\boldsymbol{B}-\boldsymbol{S}\|_4^2\,\|\boldsymbol{a}-\boldsymbol{b}\|_4^2\,.
\end{aligned} \tag{3.38}$$

Hence, the norms are related by

$$\|\boldsymbol{a}-\boldsymbol{b}\|_3 = \frac{2\,\|\boldsymbol{A}-\boldsymbol{B}\|_4}{\|\boldsymbol{A}-\boldsymbol{S}\|_4\,\|\boldsymbol{B}-\boldsymbol{S}\|_4}, \tag{3.39a}$$

or the other way round

$$\|\boldsymbol{A}-\boldsymbol{B}\|_4 = \frac{2\,\|\boldsymbol{a}-\boldsymbol{b}\|_3}{\sqrt{1+\boldsymbol{a}^2}\,\sqrt{1+\boldsymbol{b}^2}}. \tag{3.39b}$$

As before, the hyperbolic case is almost the same except for some signs, this time due to the scalar product. We would have to do the same calculation for $\boldsymbol{X}$ in the equatorial plane and $\boldsymbol{Z}$ on the hyperboloid using that $\boldsymbol{Z}^2 = -1 = \boldsymbol{S}^2$ and $\boldsymbol{Z}\cdot\boldsymbol{X} = 0$; note that $\boldsymbol{X}^2 = \|\boldsymbol{X}\|_{\mathrm{M}}^2 = \|\boldsymbol{X}\|_3^2$ for $\boldsymbol{X} = (\boldsymbol{x}, 0)$. Therefore the projection $\sigma$ from the hyperboloid to the equatorial plane is given by

$$\boldsymbol{X} = \sigma(\boldsymbol{Z}) = \frac{\boldsymbol{Z} + (\boldsymbol{Z}\cdot\boldsymbol{S})\,\boldsymbol{S}}{1+\boldsymbol{Z}\cdot\boldsymbol{S}}, \tag{3.40}$$

and the inverse map is

$$\boldsymbol{Z} = \sigma^{-1}(\boldsymbol{X}) = \frac{2}{1-\boldsymbol{X}^2}\,\boldsymbol{X} - \frac{1+\boldsymbol{X}^2}{1-\boldsymbol{X}^2}\,\boldsymbol{S}. \tag{3.41}$$

For the norms we get the relations

$$\|\boldsymbol{a}-\boldsymbol{b}\|_3^2 = \frac{2\,\|\boldsymbol{A}-\boldsymbol{B}\|_{\mathrm{M}}^2}{\|\boldsymbol{A}-\boldsymbol{S}\|_{\mathrm{M}}^2\,\|\boldsymbol{B}-\boldsymbol{S}\|_{\mathrm{M}}^2}, \tag{3.42a}$$

$$\|\boldsymbol{A}-\boldsymbol{B}\|_{\mathrm{M}}^2 = \frac{2\,\|\boldsymbol{a}-\boldsymbol{b}\|_3^2}{(1-\boldsymbol{a}^2)\,(1-\boldsymbol{b}^2)}, \tag{3.42b}$$

for $\boldsymbol{a}=\sigma(\boldsymbol{A})$ and $\boldsymbol{b}=\sigma(\boldsymbol{B})$. These relations are the same as in the spherical case, but this time we have to use the Minkowski norm.

Note that the distance $\|\boldsymbol{A}-\boldsymbol{B}\|_{\mathrm{M}}^2$ is positive only if both points are on the same sheet. Correspondingly, for $\boldsymbol{a}^2<1$ and $\boldsymbol{b}^2<1$, both images of $\boldsymbol{a}$ and $\boldsymbol{b}$ are on the upper sheet and $\|\boldsymbol{A}-\boldsymbol{B}\|^2>0$. For $\boldsymbol{a}^2>1$ and $\boldsymbol{b}^2>1$, the images are on the lower sheet and the norm is also positive.

## 3.3 Lie Sphere Geometry

A unified description for elementary geometry on Riemannian maximally symmetric spaces is given by the so-called *Lie sphere geometry* developed by Lie in his dissertation [Lie72]. We will introduce Lie spheres in two steps: At first we consider unoriented spheres in the so called *Möbius geometry*. In the second step, we will generalise this to oriented spheres. Here, we present an introduction to this topic, for a detailed discussion we recommend Cecil's book [Cec92] on Lie sphere geometry. This will allow us to give simple methods to construct various black hole configurations in the next sections.

### Möbius Geometry

We start with the $n$-dimensional Euclidean space $\mathbb{R}^n$. As we have seen in the previous section 3.2, this space can be mapped uniquely onto the hypersphere $S^n$, embedded in the $(n+1)$-dimensional Euclidean space, via a stereographic projection eq. (3.34) from the south pole $\boldsymbol{S}=(0,\dots,0,-1)$ to the equatorial plane

$$\begin{aligned}\pi : \mathbb{R}^n &\longrightarrow S^n \setminus \{\boldsymbol{S}\} \subset \mathbb{R}^{n+1}\\ \boldsymbol{x} &\longmapsto \pi(\boldsymbol{x}) = \left(\frac{2\boldsymbol{x}}{1+\boldsymbol{x}^2}, \frac{1-\boldsymbol{x}^2}{1+\boldsymbol{x}^2}\right) \equiv \boldsymbol{X}.\end{aligned} \tag{3.43}$$

where $\pi(\boldsymbol{x})^2=\boldsymbol{X}^2=1$. The south pole $\boldsymbol{S}$ itself can be interpreted as the image of infinity, $\boldsymbol{S}=\pi(\infty)$.

We can embed the whole $\mathbb{R}^{n+1}$ into the projective space $\mathbb{P}(\mathbb{R}^{1,n})$ via

$$\begin{aligned}\phi : \mathbb{R}^{n+1} &\longrightarrow \mathbb{M}^{n+1},\\ \boldsymbol{X} &\longmapsto [(1,\boldsymbol{X})]\,.\end{aligned} \tag{3.44}$$

Usually, one considers the projective space $\mathbb{P}(\mathbb{R}^{n+2})$ which is represented as the set of all lines through the origin in the $\mathbb{R}^{n+2}$. For our purposes, it turns out to be more useful to consider the lines through the origin in Minkowski space[1] $\mathbb{R}^{1,n+1}$ with its distinction of vectors in space-, time- and light-like vectors. If we define the equivalence relation

$$\boldsymbol{\zeta} \sim \boldsymbol{\xi} \quad \Leftrightarrow \quad \boldsymbol{\zeta} = a\,\boldsymbol{\xi}, \tag{3.45}$$

[1]The Minkowski metric is $\boldsymbol{\eta}=\mathrm{diag}\,(-1,1,\dots,1)$ and the scalar product is denoted by $\langle\,\cdot\,,\cdot\,\rangle$.

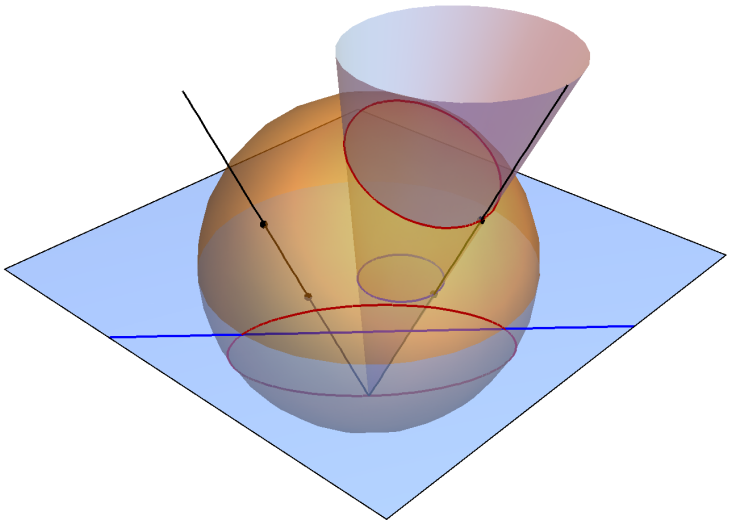

**Figure 3.3:** Points, circles and planes in flat space are mapped by a stereographic projection to points and circles on the hypersphere. The hypersphere is embedded into the projective Minkowski space where it becomes the Möbius sphere. See also the next fig. 3.4.

where $a \in \mathbb{R} \setminus \{0\}$ and $\boldsymbol{\zeta}, \boldsymbol{\xi} \in \mathbb{R}^1, n \setminus \{\mathbf{0}\}$, then the projective Minkowski space $\mathbb{M}^n$ is defined as

$$\mathbb{P}(\mathbb{R}^{1,n+1}) \cong \left(\mathbb{R}^{1,n+1} \setminus \{\mathbf{0}\}\right) / \sim . \tag{3.46}$$

Each element $[\boldsymbol{\zeta}] \in \mathbb{P}(\mathbb{R}^{1,n+1})$ is represented by all non-zero multiples of a vector $\boldsymbol{\zeta} \in \mathbb{R}^{1,n+1}$. Hence, we write $[\boldsymbol{\zeta}] \equiv [a\boldsymbol{\zeta}]$.

The combination of the two previous maps $\pi$ and $\phi$ leads to

$$\begin{aligned} \phi \circ \pi : \mathbb{R}^n &\longrightarrow \mathbb{P}(\mathbb{R}^{1,n+1}), \\ \boldsymbol{x} &\longmapsto \phi(\pi(\boldsymbol{x})) = \left[\left(1, \frac{2\boldsymbol{x}}{1+\boldsymbol{x}^2}, \frac{1-\boldsymbol{x}^2}{1+\boldsymbol{x}^2}\right)\right] \equiv [\boldsymbol{\xi}] \end{aligned} \tag{3.47}$$

where $\boldsymbol{\xi} \in \mathbb{R}^{1,n+1}$. Because of $\langle \boldsymbol{\xi}, \boldsymbol{\xi} \rangle = 0$, $\boldsymbol{\xi}$ is a light-like vector. Thus, the original Euclidean space $\mathbb{R}^n$ is mapped to the light cone in the Minkowski space $\mathbb{R}^{1,n+1}$. We can fix the representation by demanding that $\xi_0 = 1$ such that $\boldsymbol{\xi} = (1, \boldsymbol{X})$, where $\boldsymbol{X} \in S^n$. The $n$-sphere of all these vectors is called *Möbius sphere* $\Sigma$. However, we often use the more convenient representation

$$\boldsymbol{\xi} = \left(\frac{1+\boldsymbol{x}^2}{2}, \boldsymbol{x}, \frac{1-\boldsymbol{x}^2}{2}\right). \tag{3.48}$$

Next we consider circles[2] in $\mathbb{R}^n$. A circle with centre $\boldsymbol{z}$ and radius $r$ is usually described

[2] To avoid confusion we almost always use the notions of one-dimensional objects for subsets of the considered space. So $(n-1)$-spheres as subsets of $\mathbb{R}^n$ are simply called *circles*. Similar for *ellipses*, *parabolas* and *hyperbolas* instead of ellipsoids, paraboloids and hyperboloids. The only exceptions are *planes* rather than lines. The term *line* still refers to straight curves. If we use *hypersphere* and *hyperboloid*, we always mean the spaces $S^n$ and $H_2^n$ which may be embedded into $\mathbb{R}^{n+1}$. *Hyperplanes* are subsets of this embedding space. Finally, the term *sphere* refers to a general Lie sphere.

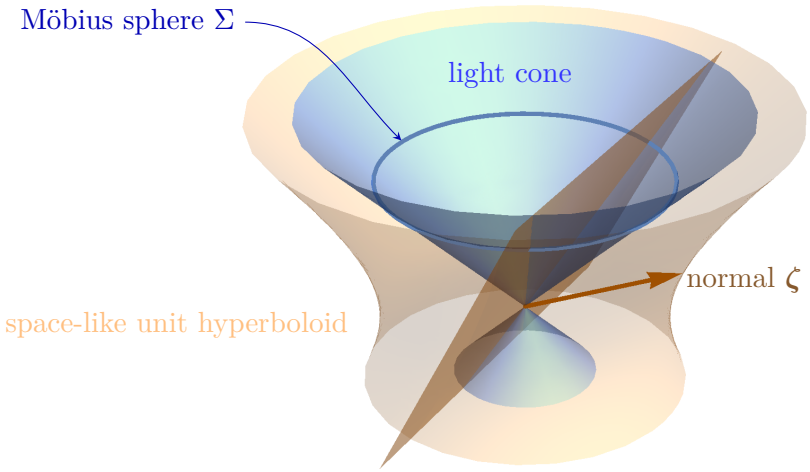


**Figure 3.4:** The flat space $\mathbb{R}^n$ is mapped to the rays of the light cone in $\mathbb{R}^{1,n+1}$. The representative $[\boldsymbol{\xi}]$ is fixed by demanding that the last component is $\xi_0 = 1$. This set forms the Möbius sphere $\Sigma$ and corresponds to the hypersphere in fig. 3.3. A hyperplane with normal $\boldsymbol{\zeta}$ intersects the Möbius in a circle which itself is the image of a circle in $\mathbb{R}^n$. The normal $\boldsymbol{\zeta}$ is then used as a representative of the circle.

by the equation

$$(\boldsymbol{x} - \boldsymbol{z})^2 = r^2. \tag{3.49}$$

However, this can also be written as

$$\langle \boldsymbol{\xi}, \boldsymbol{\zeta} \rangle = 0, \tag{3.50}$$

where $[\boldsymbol{\xi}] = \phi(\pi(\boldsymbol{x}))$ and

$$\boldsymbol{\zeta} = \left( \frac{1 + \boldsymbol{z}^2 - r^2}{2}, \boldsymbol{z}, \frac{1 - \boldsymbol{z}^2 + r^2}{2} \right) \tag{3.51}$$

is a space-like vector in $\mathbb{R}^{1,n+1}$ because of $\langle \boldsymbol{\zeta}, \boldsymbol{\zeta} \rangle = r^2 > 0$.

As eq. (3.50) shows, $\boldsymbol{\zeta}$ is the (not normalized) normal vector of the hyperplane through the origin intersecting the Möbius sphere $\Sigma$ in the image of the circle within $\mathbb{R}^{1,n+1}$. This is illustrated in fig. 3.3. Note that every multiple of $\boldsymbol{\zeta}$ satisfies eq. (3.50) so that the whole line generated by $\boldsymbol{\zeta}$ represents the mapped circle. Hence, $[\boldsymbol{\zeta}]$ is an element of the projective space $\mathbb{P}(\mathbb{R}^{1,n+1})$ representing the circle.

Of course, we also recover the single point representation if we consider a point $\boldsymbol{p}$ as a circle with radius $r = 0$. Then we have

$$\boldsymbol{\rho} = \left( \frac{1 + \boldsymbol{p}^2}{2}, \boldsymbol{p}, \frac{1 - \boldsymbol{p}^2}{2} \right), \tag{3.52}$$

but beware of the fact that these are light-like vectors rather than space-like ones in the case of circles.

This interpretation is fine for hyperplanes which do not intersect the image of the south pole $\phi(\boldsymbol{S}) = (1, \mathbf{0}, -1)$ on the Möbius sphere corresponding to infinity, $\boldsymbol{S} = \pi(\infty)$. In this case, the normal $\boldsymbol{\zeta}$ satisfies $\zeta_0 + \zeta_{n+1} = 0$. But there is no space-like[3] $\boldsymbol{\zeta}$ of the above form (3.51) such that $\phi(\boldsymbol{S})$ solves $\langle \phi(\boldsymbol{S}), \boldsymbol{\zeta} \rangle = 0$.

For this reason, let us consider the solutions to $\langle \boldsymbol{\xi}, \boldsymbol{\zeta} \rangle = 0$ containing the image of the south pole. These must be of the form

$$\boldsymbol{\pi} = (d, \boldsymbol{n}, -d)\,. \tag{3.53}$$

If we insert this into the equation $\langle \boldsymbol{\xi}, \boldsymbol{\pi} \rangle = 0$and use the representation (3.48) for $\boldsymbol{\xi}$, we obtain

$$\boldsymbol{n} \cdot \boldsymbol{x} = d. \tag{3.54}$$

This is the equation for a plane in $\mathbb{R}^n$. Hence, space-like vectors which are normals to hyperplanes intersecting the Möbius sphere in the image of the south pole describe planes in $\mathbb{R}^n$. For this reason, planes can be viewed as circles going through infinity.

In summary, light-like vectors in $\mathbb{P}(\mathbb{R}^{1,n+1})$ correspond to the points of $\mathbb{R}^n$ and form the Möbius sphere. Space-like vectors describe circles and planes in $\mathbb{R}^n$. These vectors are the normals of hyperplanes intersecting the Möbius sphere in the images of the circles and planes which they represent. Time-like objects do not represent any object in $\mathbb{R}^n$ since space-like hyperplanes through the origin do not intersect the light cone.

**Spherical and Hyperbolic Circles**

It is also possible to start with the hypersphere $S^n \subset \mathbb{R}^{n+1}$ directly by omitting the stereographic projection $\pi$ and just considering the map $\phi$. For a point $\boldsymbol{X} \in \mathbb{R}^{n+1}$ on the $n$-sphere with $\boldsymbol{X}^2 = 1$ we have simply

$$[\boldsymbol{\rho}] = \phi(\boldsymbol{X}) = [(1, \boldsymbol{X})]\,, \tag{3.55}$$

so that $\boldsymbol{\rho}$ is again light-like.

Circles on the hypersphere, which we call *(spherical) caps*, are described by their centre $\boldsymbol{Y}$ and an opening angle $\alpha \in [0, \pi]$, playing the role of the radius. This is illustrated in fig. 3.5. Caps are given by the equation

$$\boldsymbol{X} \cdot \boldsymbol{Y} = \cos\alpha, \tag{3.56}$$

or equivalently

$$\langle \phi(\boldsymbol{X}), \boldsymbol{\kappa} \rangle = 0, \tag{3.57}$$

where

$$\boldsymbol{\kappa} = (\cos\alpha, \boldsymbol{Y}) \tag{3.58}$$

is a space-like vector because of $\langle \boldsymbol{\kappa}, \boldsymbol{\kappa} \rangle = \sin^2\alpha > 0$.

Of course, this can also be done for the hyperboloid $H_2^n = H_+^n \cup H_-^n \subset \mathbb{R}^{1,n}$ with two sheets where

$$H_+^n = \left\{ \boldsymbol{X} = \left(X_0, \vec{X}\right) \in \mathbb{R}^{1,n} : \langle \boldsymbol{X}, \boldsymbol{X} \rangle = -1,\, X_0 \geq 1 \right\}, \tag{3.59}$$

$$H_-^n = \left\{ \boldsymbol{X} = \left(X_0, \vec{X}\right) \in \mathbb{R}^{1,n} : \langle \boldsymbol{X}, \boldsymbol{X} \rangle = -1,\, X_0 \leq -1 \right\}, \tag{3.60}$$

[3] Of course, there is the light-like point circle $\boldsymbol{\zeta} = \phi(\boldsymbol{S})$.

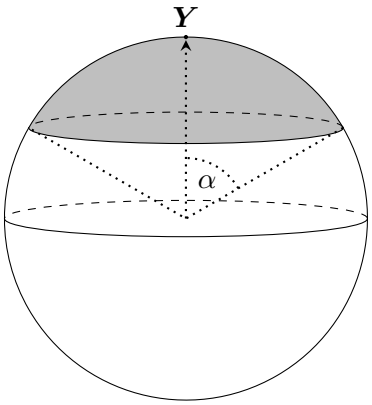


**Figure 3.5:** Spherical caps with centre $\boldsymbol{Y}$ and opening angle $\alpha$.

are the upper and the lower sheet, respectively.

The stereographic projection from the hyperboloid to the hypersphere is given by

$$\begin{aligned} &\varpi : H_2^n \subset \mathbb{R}^{1,n} \longrightarrow S^n \subset \mathbb{R}^{n+1}, \\ &\boldsymbol{X} = \left(X_0, \vec{X}\right) \longmapsto \varpi(\boldsymbol{X}) = \left(\frac{\vec{X}}{X_0}, \frac{1}{X_0}\right). \end{aligned} \tag{3.61}$$

This mapping is the combination of the stereographic projection from the hyperboloid to the equatorial plane eq. (3.40) and the one from the plane to hypersphere eq. (3.34). On the hyperboloid we have $\langle \boldsymbol{X}, \boldsymbol{X} \rangle = -1$, hence $\varpi(\boldsymbol{X})^2 = 1$. Note that the upper sheet $H_+^n$ is mapped to the northern hemisphere and the lower sheet $H_-^n$ to the southern hemisphere, whereas the equator has no preimage. After applying the map $\phi$ we obtain

$$\phi(\varpi(\boldsymbol{X})) = \left[\left(1, \frac{\vec{X}}{X_0}, \frac{1}{X_0}\right)\right] = \left[\left(X_0, \vec{X}, 1\right)\right] \equiv [(\boldsymbol{X}, 1)]\,. \tag{3.62}$$

This is again a light-like vector as in the previous cases.

Hyperbolic circles with centre $\boldsymbol{Z}$ and 'radius' $u$ are described by the equation

$$\langle \boldsymbol{X}, \boldsymbol{Z} \rangle = -\cosh u, \tag{3.63}$$

where $\langle \boldsymbol{Z}, \boldsymbol{Z} \rangle = -1$, or as before

$$\langle \boldsymbol{\xi}, \boldsymbol{\upsilon} \rangle = 0, \tag{3.64}$$

where $\boldsymbol{\xi} = \phi(\varpi(\boldsymbol{X})) = (\boldsymbol{X}, 1)$ and

$$\boldsymbol{\upsilon} = (\boldsymbol{Z}, \cosh u) \tag{3.65}$$

is space-like because of $\langle \boldsymbol{\upsilon}, \boldsymbol{\upsilon} \rangle = \sinh^2 u$. In the embedding space of the hyperboloid, eq. (3.63) describes a space-like hyperplane intersecting the hyperboloid in ellipses and, if their centre is at one of the poles $\boldsymbol{Z} = (\pm 1, \boldsymbol{0})$, in circles.

However, there are also time-like and light-like hyperplanes intersecting the hyperboloid. This corresponds to the fact that the vectors $\boldsymbol{\upsilon}$ cover only a part of the hyperboloid

**Table 3.1:** Hyperbolic circles

| 'circle' equation | kind of centre | kind of object |
|---|---|---|
| $\langle \boldsymbol{X}, \boldsymbol{Z} \rangle \leq -1$ | $\langle \boldsymbol{Z}, \boldsymbol{Z} \rangle = -1$ | ellipses on the same sheet as $\boldsymbol{Z}$ |
| $\langle \boldsymbol{X}, \boldsymbol{Z} \rangle \geq 1$ | $\langle \boldsymbol{Z}, \boldsymbol{Z} \rangle = -1$ | ellipses on the other sheet as $\boldsymbol{Z}$ |
| $\langle \boldsymbol{X}, \boldsymbol{Z} \rangle < 0$ | $\langle \boldsymbol{Z}, \boldsymbol{Z} \rangle = 0,\ Z_0 > 0$ | parabolas on the upper sheet |
| $\langle \boldsymbol{X}, \boldsymbol{Z} \rangle > 0$ | $\langle \boldsymbol{Z}, \boldsymbol{Z} \rangle = 0,\ Z_0 > 0$ | parabolas on the lower sheet |
| $\langle \boldsymbol{X}, \boldsymbol{Z} \rangle \in \mathbb{R}$ | $\langle \boldsymbol{Z}, \boldsymbol{Z} \rangle = 1$ | hyperbolas on both sheets |

$H_1^{n+1} = \{\boldsymbol{v} \in \mathbb{R}^{1,n+1} : \langle \boldsymbol{v}, \boldsymbol{v} \rangle = 1\}$, the set of all space-like unit vectors, namely those with $|v_1| = |\coth u| > 1$.

Every time-like hypersurface in the embedding space, given by

$$\langle \boldsymbol{X}, \boldsymbol{Z} \rangle = -\sinh u \tag{3.66}$$

with a space-like normal $\boldsymbol{Z}$, $\langle \boldsymbol{Z}, \boldsymbol{Z} \rangle = 1$, intersects the hyperboloid in hyperbolas. These are represented by

$$\boldsymbol{v} = (\boldsymbol{Z}, \sinh u)\,. \tag{3.67}$$

They are again space-like, $\langle \boldsymbol{v}, \boldsymbol{v} \rangle = \sinh^2 u \geq 0$, and thus cover the part of $H_1^{n+1}$ where $|v_1| = |\tanh u| < 1$. These objects are also known as *hypercycles*.

Light-like hypersurfaces intersect the hyperboloid in parabolas if they do not contain the origin. These are described by

$$\langle \boldsymbol{X}, \boldsymbol{Z} \rangle = \mp \mathrm{e}^u, \tag{3.68}$$

where $\boldsymbol{Z}$ is light-like, $\langle \boldsymbol{Z}, \boldsymbol{Z} \rangle = 0$, and $Z_0 > 0$. For $-\mathrm{e}^u$ the parabola lies on the upper sheet $H_+^n$ and for $+\mathrm{e}^u$ on the lower one $H_-^n$. These objects are also known as *horocycles*. The corresponding space-like Möbius vector is

$$\boldsymbol{v} = (\boldsymbol{Z}, \pm \mathrm{e}^u) \tag{3.69}$$

with $\langle \boldsymbol{v}, \boldsymbol{v} \rangle = \mathrm{e}^{2u}$. Hence, these are the vectors on $H_1^{n+1}$ with $|v_1| = 1$. Note that, if $v_0$ and $v_{n+2}$ have the same sign, the parabolas are on $H_+^n$, else on $H_-^n$.

Altogether we found all possible hyperbolic circles that are ellipses, parabolas and hyperbolas and can be obtained from intersections of hyperplanes with the hyperboloid in the embedding space as shown in fig. 3.6. For a summary see also table 3.1.

### Relations between the Norms

The relations between the norms, discussed in the previous section, can be easily obtained from the scalar product using the different representations for points. For example, for two points

$$\boldsymbol{\rho}_A = \left(1, \frac{2\boldsymbol{p}_A}{1+\boldsymbol{p}_A^2}, \frac{1-\boldsymbol{p}_A^2}{1+\boldsymbol{p}_A^2}\right) = (1, \boldsymbol{P}_A)\,, \tag{3.70}$$

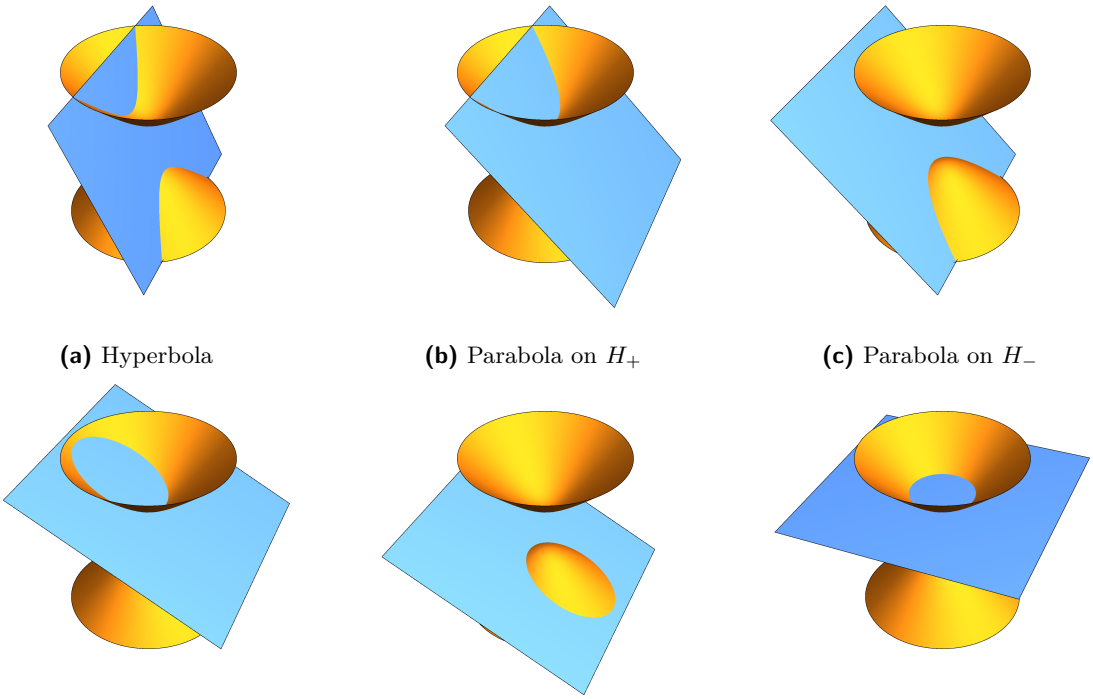

**(a)** Hyperbola **(b)** Parabola on $H_+$ **(c)** Parabola on $H_-$

**(d)** Ellipse on $H_+$ **(e)** Ellipse on $H_-$ **(f)** Circle on $H_+$

**Figure 3.6:** Circles on the hyperboloid are intersections of hyperplanes with the hyperboloid. Time-like hyperplanes intersect both sheets in hyperbolas. Light-like ones intersect only one sheet in a parabola. Space-like ones intersect just one sheet in ellipses or as a special case in a circle as shown in the last figure.

where $\pi^{-1}(\boldsymbol{p}) = \boldsymbol{P}$, we obtain on the one hand

$$\begin{aligned}\langle \boldsymbol{\rho}_1, \boldsymbol{\rho}_2 \rangle &= \frac{1}{(1+\boldsymbol{p}_1^2)(1+\boldsymbol{p}_2^2)} \left( -(1+\boldsymbol{p}_1^2)(1+\boldsymbol{p}_2^2) + 4\,\boldsymbol{p}_1 \cdot \boldsymbol{p}_2 + (1-\boldsymbol{p}_1^2)(1-\boldsymbol{p}_2^2) \right) \\ &= \frac{2}{(1+\boldsymbol{p}_1^2)(1+\boldsymbol{p}_2^2)} \left( -\boldsymbol{p}_A^2 + 2\boldsymbol{p}_A \cdot \boldsymbol{p}_B - \boldsymbol{p}_B^2 \right) = -\frac{2\,\|\boldsymbol{p}_A - \boldsymbol{p}_B\|_3^2}{(1+\boldsymbol{p}_1^2)(1+\boldsymbol{p}_2^2)}. \end{aligned} \tag{3.71}$$

while we have on the other hand

$$\langle \boldsymbol{\rho}_1, \boldsymbol{\rho}_2 \rangle = -1 + \boldsymbol{P}_1 \cdot \boldsymbol{P}_2 = -\frac{1}{2} \|\boldsymbol{P}_1 - \boldsymbol{P}_2\|_4^2 . \tag{3.72}$$

Hence, we regain the relation (3.39b)

$$-2\,\langle \boldsymbol{\rho}_1, \boldsymbol{\rho}_2 \rangle = \frac{4\,\|\boldsymbol{p}_A - \boldsymbol{p}_B\|_3^2}{(1+\boldsymbol{p}_1^2)(1+\boldsymbol{p}_2^2)} = \|\boldsymbol{P}_1 - \boldsymbol{P}_2\|_4^2 . \tag{3.73}$$

Because of $\frac{4}{1-\boldsymbol{p}_A^2} = -2\,\langle \boldsymbol{\rho}_A, \boldsymbol{\sigma} \rangle = \|\boldsymbol{P}_A - \boldsymbol{S}\|_4^2$, where $\boldsymbol{\sigma} = (1, \boldsymbol{S})$, we also obtain eq. (3.39a). Analogously, we find the relations (3.42a) and (3.42b) if we use the representations

$$\boldsymbol{\rho}_A = \left( \frac{1+\boldsymbol{p}_A^2}{1-\boldsymbol{p}_A^2}, \frac{2\boldsymbol{p}_A}{1-\boldsymbol{p}_A^2}, 1 \right) = (\boldsymbol{P}_A, 1)\,, \tag{3.74}$$

where $\boldsymbol{P}_A = \sigma^{-1}(\boldsymbol{p}_A)$.

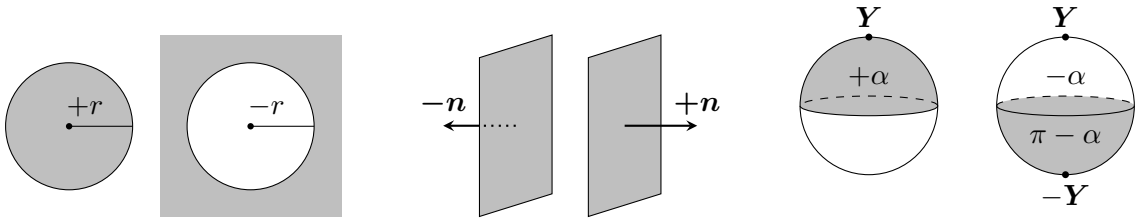


**(a)** Oriented circles **(b)** Oriented planes **(c)** Oriented spherical caps

**Figure 3.7:** Orientation of Lie spheres: A positive radius $r > 0$ corresponds to a common circle whereas a circle with negative radius $r < 0$ is the outer part. The orientation of a plane is given by the direction of the normal $\boldsymbol{n}$. A spherical cap with negative opening angle can also be interpreted as spherical cap with centre $-\boldsymbol{Y}$ and opening angle $\pi - \alpha$.

### Lie Spheres

Every element $\boldsymbol{\tau}$ on the space-like hyperboloid $H_1^{n+1} = \{\boldsymbol{\xi} \in \mathbb{R}^{1,n+1} : \langle \boldsymbol{\xi}, \boldsymbol{\xi} \rangle = 1\}$ represents a circle either in flat space or on the hypersphere or hyperboloid. But since these are actually representatives for elements of the projective space $\mathbb{P}(\mathbb{R}^{1,n+1})$, there are two representatives $\pm\boldsymbol{\zeta} \in H_1^{n+1}$ to each element $[\boldsymbol{\xi}] \in \mathbb{P}(\mathbb{R}^{1,n+1})$ such that $[\boldsymbol{\xi}] = [\pm\boldsymbol{\zeta}]$. For this reason, both vectors $\pm\boldsymbol{\zeta}$ describe the same object.

Now we may simply forget that we are coming from a projective space and distinguish between these two vectors to give all objects an orientation. More illustrative: circles get an inside or they become 'balls' and we choose a direction for the normal of planes. See also the explanation below and fig. 3.7 for an illustration. Then every point on $H_1^{n+1}$ represents an oriented circle in $\mathbb{R}^n$, $S^n$ or $H_2^n$. In contrast, a single point in these spaces is represented by an element of the Möbius sphere $\Sigma^n$.

We can repeat the previous procedure to get a unified description for points and circles. Therefore we embed the $\mathbb{R}^{1,n+1}$ into the projective space $\mathbb{P}(\mathbb{R}^{1,n+1,1}) \cong (\mathbb{R}^{1,n+1,1} \setminus \{0\}) / \sim$ via

$$\begin{aligned} \Phi : \mathbb{R}^{n+1,1} &\longrightarrow \mathbb{P}(\mathbb{R}^{1,n+1,1}), \\ \boldsymbol{\xi} &\longmapsto [(\boldsymbol{\xi}, 1)]\,. \end{aligned} \tag{3.75}$$

Here, the metric of $\mathbb{R}^{1,n+1,1}$ has signature $(-,+,\ldots,+,-)$. The elements of $\mathbb{R}(\mathbb{R}^{1,n+1,1})$ are represented again by lines through the origin in $\mathbb{R}^{1,n+1,1}$ such that $\Phi(\boldsymbol{\xi}) = [\boldsymbol{\Xi}]$ for some $\boldsymbol{\Xi} = (\Xi_0, \ldots, \Xi_{n+2}) \in \mathbb{R}^{1,n+1,1}$.

Then, for $\boldsymbol{\xi} \in H_1^{n+1}$ we have

$$\langle\!\langle \Phi(\boldsymbol{\xi}), \Phi(\boldsymbol{\xi}) \rangle\!\rangle = 0, \tag{3.76}$$

where $\langle\!\langle \cdot, \cdot \rangle\!\rangle$ is the inner product of $\mathbb{R}^{1,n+1,1}$. The sub-manifold $\Phi(H_1^{n+1})$ is the so-called *Lie quadric* $Q^{n+1}$. Each point $[\boldsymbol{\Xi}] \in Q^{n+1}$ with $\Xi_{n+2} \neq 0$ describes an oriented sphere either in $\mathbb{R}^n$, on $S^n$ or on $H_2^n$.

The remaining points $[(\boldsymbol{\rho}, 0)]$ on the Lie quadric do not have a preimage under the map $\Phi$. However, they satisfy $\langle \boldsymbol{\rho}, \boldsymbol{\rho} \rangle = 0$, so $\boldsymbol{\rho}$ must be an element of the light sphere in $\mathbb{R}^{1,n+1}$ represented by the Möbius sphere. Therefore they can be considered as representatives of the points in $\mathbb{R}^n$, $S^n$ and $H_2^n$.

Next, we derive explicit expressions for the different objects. In order to obtain an element of the Lie quadric we have to use the normalized representatives of a sphere $\boldsymbol{\tau} = \frac{1}{\|\boldsymbol{\xi}\|}\boldsymbol{\xi} \in H_1^{n+1}$, where $\|\boldsymbol{\xi}\| = \sqrt{\langle \boldsymbol{\xi}, \boldsymbol{\xi} \rangle}$. Recall that a sphere has two representatives $\pm\boldsymbol{\tau}$

**Table 3.2:** Objects in Lie sphere geometry

| object | representation | |
|---|---|---|
| point in $\mathbb{R}^n$ | $\left(\frac{1+\boldsymbol{x}^2}{2}, \boldsymbol{x}, \frac{1-\boldsymbol{x}^2}{2}, 0\right)$ | $\boldsymbol{x} \in \mathbb{R}^n$ |
| infinity | $(1, \mathbf{0}, -1, 0)$ | $\mathbf{0} = (0, \dots, 0) \in \mathbb{R}^n$ |
| circle in $\mathbb{R}^n$ | $\left(\frac{1+\boldsymbol{x}^2-r^2}{2}, \boldsymbol{x}, \frac{1-\boldsymbol{x}^2+r^2}{2}, r\right)$ | $r \in \mathbb{R}$ |
| plane in $\mathbb{R}^n$ | $(\delta, \boldsymbol{n}, -\delta, \pm \lVert\boldsymbol{n}\rVert)$ | $\delta \in \mathbb{R}$, $\lVert\boldsymbol{n}\rVert \in \mathbb{R}_+$ |
| point on the $S^n$ | $(1, \boldsymbol{Y}, 0)$ | $\boldsymbol{Y} \in \mathbb{R}^{n+1}$, $\boldsymbol{Y}^2 = 1$ |
| spherical cap on $S^n$ | $(\cos\alpha, \boldsymbol{Y}, \sin\alpha)$ | $\boldsymbol{Y}^2 = 1$, $-\pi \leq \alpha \leq \pi$ |
| point on $H_2^n$ | $(\boldsymbol{Z}, 1, 0)$ | $\boldsymbol{Z} \in \mathbb{R}^{1,n}$, $\langle \boldsymbol{Z}, \boldsymbol{Z}\rangle = -1$ |
| ellipses on $H_2^n$ | $(\boldsymbol{Z}, \cosh u, \sinh u)$ | $\langle \boldsymbol{Z}, \boldsymbol{Z}\rangle = -1$, $u \in \mathbb{R}$ |
| parabolas on $H_+^n$ | $(\boldsymbol{Z}, \mathrm{e}^u, \pm \mathrm{e}^u)$ | $\langle \boldsymbol{Z}, \boldsymbol{Z}\rangle = 0$, $Z_0 > 0$, $u \in \mathbb{R}$ |
| parabolas on $H_-^n$ | $(\boldsymbol{Z}, -\mathrm{e}^u, \pm \mathrm{e}^u)$ | $\langle \boldsymbol{Z}, \boldsymbol{Z}\rangle = 0$, $Z_0 > 0$, $u \in \mathbb{R}$ |
| hyperbolas on $H_2^n$ | $(\boldsymbol{Z}, \sinh u, \pm \cosh u)$ | $\langle \boldsymbol{Z}, \boldsymbol{Z}\rangle = 1$, $u \in \mathbb{R}$ |

and the sign designates the orientation. The two corresponding Lie sphere vectors are given by

$$[\boldsymbol{\Xi}] = \left[\left(\pm\frac{1}{\lVert\boldsymbol{\xi}\rVert}\,\boldsymbol{\xi}, 1\right)\right] = [(\boldsymbol{\xi}, \pm\lVert\boldsymbol{\xi}\rVert)]\,. \tag{3.77}$$

Hence, the last component $\Xi_{n+2}$ represents the orientation.

Let us consider circles in $\mathbb{R}^n$. We have already seen that $\lVert\boldsymbol{\zeta}\rVert = r$, therefore we have to use $\boldsymbol{\tau} = \pm\frac{1}{r}\,\boldsymbol{\zeta}$ such that

$$[(\boldsymbol{\tau}, 1)] = \left[\left(\pm\frac{1}{r}\,\boldsymbol{\zeta}, 1\right)\right] = [(\boldsymbol{\zeta}, \pm r)]\,. \tag{3.78}$$

We allow the radius to take values all over $\mathbb{R}$ so that the signed radius serves as the indicator of the orientation of the circle. We will use the convention that a negative radius corresponds to a normal pointing towards the centre and a positive one points into the opposite direction. Another interpretation is that a positive radius corresponds to the ball of radius $r$, while a negative radius describes the closure of the complement of this set.

For planes, the situation is similar: We have $\lVert\boldsymbol{\pi}\rVert = \lVert\boldsymbol{n}\rVert$ so that we get

$$[(\delta, \boldsymbol{n}, -\delta, \pm\lVert\boldsymbol{n}\rVert)]\,, \tag{3.79}$$

where $\delta = \frac{d}{\lVert\boldsymbol{n}\rVert}$. In this case, the orientation is given by the direction of the normal $\boldsymbol{n}$.

For spherical caps, we have $\lVert\boldsymbol{\kappa}\rVert = \sin\alpha$, hence

$$[(\cos\alpha, \boldsymbol{Y}, \pm\sin\alpha)] \tag{3.80}$$

Again, we can simply expand the domain of $\alpha$ to $-\pi \leq \alpha \leq \pi$ and we use the same conventions as in the flat case. This corresponds to the orientation of the intersecting hyperplane in the embedding space. Note that every oriented spherical cap can be described in two different ways: The positive oriented cap with opening angle $\alpha > 0$ around $\boldsymbol{Y}$ is the same as the negative oriented cap centred at $-\boldsymbol{Y}$ with the opening angle $\alpha - \pi < 0$ due to

$$(\cos\alpha, \boldsymbol{Y}, \sin\alpha) = -\left(\cos(\alpha-\pi), -\boldsymbol{Y}, \sin(\alpha-\pi)\right). \tag{3.81}$$

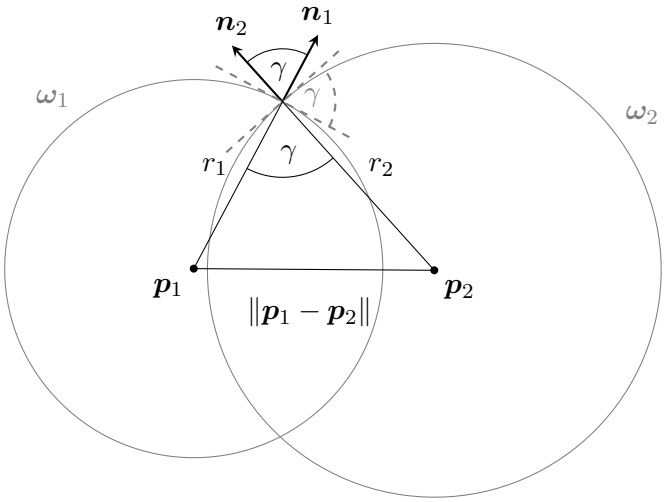


**Figure 3.8:** Two circles $\boldsymbol{\omega}_1$ and $\boldsymbol{\omega}_2$ intersect in an angle $\gamma$, given by the law of cosine $\|\boldsymbol{p}_1 - \boldsymbol{p}_2\|^2 = r_1^2 + r_2^2 - 2r_1 r_2 \cos\gamma$. In this case, this equals the product $\langle \boldsymbol{\omega}_1, \boldsymbol{\omega}_2 \rangle = \cos\gamma$ of the two circles.

For hyperbolic circles, we follow the same procedure: For ellipses and hyperbolas we can again use the orientation of the generating hyperplane. In the case of parabolas where we have a light-like hypersurface the determination of the orientation is more complicated because the light-like normal lies within the hypersurface. Here we have to demand $Z_0 \equiv Z_{n+1}$ so that the sign of the first component of $(\boldsymbol{Z}, \pm \mathrm{e}^u, \pm \mathrm{e}^u)$ indicates the sheet on which the parabola lies and the sign of the last component gives the orientation.

As mentioned before, we have $[(\boldsymbol{\rho}, 0)]$ for points which can be considered as circles with vanishing radius in all cases. For a summary of the different expressions see table 3.1. We often use $\boldsymbol{\xi} \in H_1^{n+1}$ to represent a Lie sphere $[\boldsymbol{\Xi}] = [(\boldsymbol{\xi}, 1)]$, which we call *standard form*.

### Intersection Angle and Oriented Contact

The Lie quadric $Q^{n+1}$ contains one-dimensional linear subspaces, but there are no higher dimensional linear subspaces. In general, it can be shown that the null subspace in $\mathbb{R}^{n,m}$, that is, the set of all light-like vectors, has the dimension $\max(n, m)$, see [Cec92].

Suppose, we have two Lie sphere vectors $[\boldsymbol{\Xi}]$ and $[\boldsymbol{\Theta}]$. The line $[\boldsymbol{\Xi}, \boldsymbol{\Theta}]$ through these points is given by

$$\boldsymbol{\Gamma}(s) = s\,\boldsymbol{\Xi} + (1 - s)\,\boldsymbol{\Theta}. \tag{3.82}$$

In order to be a line within the Lie quadric, $\boldsymbol{\Gamma}(s)$ must satisfy $\langle\!\langle \boldsymbol{\Gamma}(s), \boldsymbol{\Gamma}(s) \rangle\!\rangle = 0$ for all $s$. Since $\boldsymbol{\Xi}$ and $\boldsymbol{\Theta}$ are both light-like, we get

$$\langle\!\langle \boldsymbol{\Gamma}(s), \boldsymbol{\Gamma}(s) \rangle\!\rangle = 2s(1 - s) \langle\!\langle \boldsymbol{\Xi}, \boldsymbol{\Theta} \rangle\!\rangle. \tag{3.83}$$

Hence, the line lies within the Lie quadric only if the Lie sphere vectors $\boldsymbol{\Xi}$ and $\boldsymbol{\Theta}$ satisfy $\langle\!\langle \boldsymbol{\Xi}, \boldsymbol{\Theta} \rangle\!\rangle = 0$.

For the interpretation of this condition, consider two Lie spheres in standard form such that $[\boldsymbol{\Xi}_A] = [(\boldsymbol{\omega}_A, 1)]$, where $A \in \{1, 2\}$ and $\langle \boldsymbol{\omega}_A, \boldsymbol{\omega}_A \rangle = 1$. Then, we can interpret the scalar product in the following way:

**Table 3.3:** Relation between two circles $\boldsymbol{\omega}_1$ and $\boldsymbol{\omega}_2$

| $\langle \boldsymbol{\omega}_1, \boldsymbol{\omega}_2 \rangle$ | circles | |
|---|---|---|
| $< -1$ | nested |  |
| $\cos\gamma$ | intersecting |  |
| $> 1$ | non-intersecting | 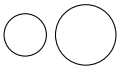 |
| $-1$ | internally tangent |  |
| $0$ | orthogonal |  |
| $1$ | externally tangent | 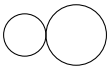 |

For two spheres $\boldsymbol{\omega}_A = \frac{1}{2r_A}\left(1 + \boldsymbol{p}_A^2 - r_A^2, 2\boldsymbol{p}_A, 1 - \boldsymbol{p}_A^2 + r_A^2\right)$ we obtain

$$\begin{aligned}\langle \boldsymbol{\omega}_A, \boldsymbol{\omega}_B \rangle &= \frac{1}{4r_A r_B}\Big(-(1 + \boldsymbol{p}_A^2 - r_A^2)(1 + \boldsymbol{p}_B^2 - r_B^2)\boldsymbol{p}_A \cdot \boldsymbol{p}_B \\ &\qquad +(1 - \boldsymbol{p}_A^2 + r_A^2)(1 - \boldsymbol{p}_B^2 + r_B^2)\Big) \\ &= \frac{1}{2r_A r_B}\left(2\boldsymbol{p}_A \cdot \boldsymbol{p}_B - \boldsymbol{p}_A^2 - \boldsymbol{p}_B^2 + r_A^2 + r_B^2\right) \\ &= \frac{1}{2r_A r_B}\left(r_A^2 + r_B^2 - \|\boldsymbol{p}_A - \boldsymbol{p}_B\|^2\right). \end{aligned} \tag{3.84}$$

If now $\|\boldsymbol{p}_A - \boldsymbol{p}_B\| \leq |r_A - r_B|$, implying that the two circles intersect, we can apply the law of cosine

$$\|\boldsymbol{p}_A - \boldsymbol{p}_B\|^2 = r_A^2 + r_B^2 - 2r_A r_B \cos\gamma_{AB}, \tag{3.85}$$

see also fig. 3.8. Hence the scalar product simplifies to

$$\langle \boldsymbol{\omega}_A, \boldsymbol{\omega}_B \rangle = \cos\gamma_{AB}. \tag{3.86}$$

So in the case that $|\langle \boldsymbol{\omega}_A, \boldsymbol{\omega}_B \rangle| < 1$, the two circles intersect and the scalar product gives the angle $\gamma_{AB}$ between their normals. If $\langle \omega_A, \omega_B \rangle = 0$, we say that these circles are *orthogonal*. The special case of $\langle \boldsymbol{\omega}_A, \boldsymbol{\omega}_B \rangle = \pm 1$ describes spheres touching each other externally or internally so that their normals are parallel or anti-parallel, respectively. If $|\langle \omega_A, \omega_B \rangle| > 1$, the circles do not intersect. For a summary see table 3.3.

The orthogonal relation $\langle\langle \boldsymbol{\Xi}, \boldsymbol{\Theta} \rangle\rangle = 0$ is equivalent to $\langle \boldsymbol{\xi}, \boldsymbol{\theta} \rangle = 1$, where $\boldsymbol{\Xi} = (\boldsymbol{\xi}, 1)$ and $\boldsymbol{\Theta} = (\boldsymbol{\theta}, 1)$. In this case the two spheres touch each other and their normal point into the same direction, we say the spheres are in *oriented contact*.

Hence, all spheres of the line $[\boldsymbol{\Xi}, \boldsymbol{\Theta}]$ touch each other with their normals pointing in the same direction. It can be shown that every line intersects the Möbius sphere $\Sigma^n$ in exactly one point and that it contains one plane in which this point lies. For this reason, the line

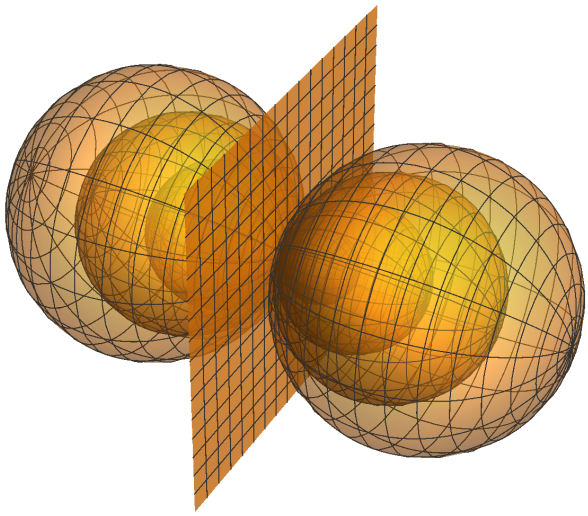

**Figure 3.9:** Line of Lie spheres: All spheres touch the plane in the same point and have the same orientation so that the spheres on one side are positively oriented and negatively on the other side.

$[\boldsymbol{\Xi}, \boldsymbol{\Theta}]$ describes all spheres touching a plane in the same point, as shown in fig. 3.9. In the case that the point is the image of infinity, the line consists of parallel planes.

### Möbius and Lie Sphere Transformations

Finally, we consider linear transformations of $\mathbb{P}(\mathbb{R}^{1,n+1,1})$, called *Lie sphere transformations*, mapping light-like vectors into each other. Similarly, linear transformations leaving the Möbius sphere or the light cone, respectively, invariant, are called *Möbius transformations*. Since the Möbius sphere is embedded in the Lie quadric as the space of $\left[\boldsymbol{e}_{n+2}^{\perp}\right]$ orthogonal to $\boldsymbol{e}_{n+2}$, a Möbius transformation $\boldsymbol{A}$ can be extended to a Lie sphere transformation $\boldsymbol{B}$ by demanding that $\boldsymbol{B}(\boldsymbol{e}_{n+2}) = \boldsymbol{e}_{n+2}$. Hence, $\boldsymbol{B}$ is of the form

$$\boldsymbol{B} = \begin{bmatrix} \boldsymbol{A} & 0 \\ 0 & 1 \end{bmatrix}. \tag{3.87}$$

Note that $-\boldsymbol{A}$ gives the same Möbius transformation on $\Sigma^n$, $[-\boldsymbol{A}] \equiv [\boldsymbol{A}]$, whereas the associated Lie sphere transformation

$$\boldsymbol{C} = \begin{bmatrix} -\boldsymbol{A} & 0 \\ 0 & 1 \end{bmatrix} \equiv \begin{bmatrix} \boldsymbol{A} & 0 \\ 0 & -1 \end{bmatrix} \tag{3.88}$$

differs from $\boldsymbol{B}$ by a change of orientation. So every Möbius transformation induces two Lie sphere transformations.

Now we have, see [Cec92],

**Theorem 3.1.** *Let $\boldsymbol{A} \in GL(n, m)$ with $n, m \geq 1$ mapping light-like vectors onto each other, then there is $\lambda \neq 0$ such that*

$$\langle \boldsymbol{A}(\boldsymbol{\xi}), \boldsymbol{A}(\boldsymbol{\zeta}) \rangle = \lambda \langle \boldsymbol{\xi}, \boldsymbol{\zeta} \rangle \tag{3.89}$$

*for all $\boldsymbol{\xi}, \boldsymbol{\zeta} \in \mathbb{R}^{n,m}$. If $n \neq m$, then $\lambda > 0$.*

Using this theorem, it can be shown that the group of Lie sphere transformations is isomorphic to $O(1, n+1, 1)/\{\pm \boldsymbol{I}\}$ and the group of Möbius transformations to $O(1, n+1)/\{\pm \boldsymbol{I}\}$. It follows that Lie sphere transformations preserve the oriented contact and Möbius transformations the intersection angle.

At last, we consider a special kind of Lie sphere transformations. First, let us define the following linear mapping: A *Möbius inversion* $\boldsymbol{\mathcal{I}}_\zeta$ in $\mathbb{R}^{1,n+1}$, where $\boldsymbol{\zeta}$ is non-null, is given by

$$\boldsymbol{\mathcal{I}}_\zeta(\boldsymbol{\xi}) = \boldsymbol{\xi} - \frac{2\langle \boldsymbol{\xi}, \boldsymbol{\zeta}\rangle}{\langle \boldsymbol{\zeta}, \boldsymbol{\zeta}\rangle}\,\boldsymbol{\zeta}. \tag{3.90}$$

This is a reflection of the vector $\boldsymbol{\xi}$ at the hyperplane with normal $\boldsymbol{\zeta}$. For two vectors $\boldsymbol{\xi}_1, \boldsymbol{\xi}_2$, we can calculate the scalar product

$$\langle \boldsymbol{\mathcal{I}}_\zeta(\boldsymbol{\xi}_1), \boldsymbol{\mathcal{I}}_\zeta(\boldsymbol{\xi}_2)\rangle = \left\langle \boldsymbol{\xi}_1 - \frac{2\langle \boldsymbol{\xi}_1, \boldsymbol{\zeta}\rangle}{\langle \boldsymbol{\zeta}, \boldsymbol{\zeta}\rangle}\,\boldsymbol{\zeta}, \boldsymbol{\xi}_2 - \frac{2\langle \boldsymbol{\xi}_2, \boldsymbol{\zeta}\rangle}{\langle \boldsymbol{\zeta}, \boldsymbol{\zeta}\rangle}\,\boldsymbol{\zeta} \right\rangle = \langle \boldsymbol{\xi}_1, \boldsymbol{\xi}_2\rangle \tag{3.91}$$

showing that an inversion is an orthogonal transformation and hence it is indeed a Möbius transformation. Furthermore, the properties of a reflection can easily be verified, that is

$$\boldsymbol{\mathcal{I}}_\zeta(\boldsymbol{\zeta}) = -\boldsymbol{\zeta}, \tag{3.92a}$$

$$\boldsymbol{\mathcal{I}}_\zeta(\boldsymbol{\zeta}^\perp) = \boldsymbol{\zeta}^\perp, \tag{3.92b}$$

and

$$\boldsymbol{\mathcal{I}}_\zeta^2(\boldsymbol{\xi}) = \boldsymbol{\mathcal{I}}_\zeta(\boldsymbol{\xi}) - \frac{2\langle \boldsymbol{\mathcal{I}}_\zeta(\boldsymbol{\xi}), \boldsymbol{\zeta}\rangle}{\langle \boldsymbol{\zeta}, \boldsymbol{\zeta}\rangle}\,\boldsymbol{\zeta} = \boldsymbol{\xi} - \frac{2\langle \boldsymbol{\xi}, \boldsymbol{\zeta}\rangle}{\langle \boldsymbol{\zeta}, \boldsymbol{\zeta}\rangle}\,\boldsymbol{\zeta} - \frac{2\langle \boldsymbol{\xi} - \frac{2\langle \boldsymbol{\xi}, \boldsymbol{\zeta}\rangle}{\langle \boldsymbol{\zeta}, \boldsymbol{\zeta}\rangle}\,\boldsymbol{\zeta}, \boldsymbol{\zeta}\rangle}{\langle \boldsymbol{\zeta}, \boldsymbol{\zeta}\rangle}\,\boldsymbol{\zeta} = \boldsymbol{\xi}. \tag{3.93}$$

We are mainly interested in the case that $\boldsymbol{\zeta}$ describes a circle with radius $R$ centred at $\boldsymbol{p}$. In this case we have

$$\boldsymbol{\zeta} = \left(\frac{1 + \boldsymbol{p}^2 - R^2}{2R}, \frac{\boldsymbol{p}}{R}, \frac{1 - \boldsymbol{p}^2 + R^2}{2R}\right) \tag{3.94}$$

with $\langle \boldsymbol{\zeta}, \boldsymbol{\zeta}\rangle = 1$. This circle is mapped to itself because of eq. (3.92); but if we consider $\boldsymbol{\zeta}$ as an oriented circle or Lie vector, respectively, it changes its orientation under $\boldsymbol{\mathcal{I}}_\zeta$. Furthermore, orthogonal circles to $\boldsymbol{\zeta}$ are mapped to themselves but they keep their orientation.

Now let us investigate in more detail what kind of transformations in $\mathbb{R}^n$ a Möbius inversion $\boldsymbol{\mathcal{I}}_\zeta$ describes. For this reason we consider some point

$$\boldsymbol{\rho} = \left(\frac{1 + \boldsymbol{x}^2}{2}, \boldsymbol{x}, \frac{1 - \boldsymbol{x}^2}{2}\right). \tag{3.95}$$

Then we have

$$\begin{aligned}
\langle \boldsymbol{\rho}, \boldsymbol{\zeta}\rangle &= \frac{1}{4R}\left(-(1 + \boldsymbol{p}^2 - R^2)(1 + \boldsymbol{x}^2) + 4\boldsymbol{p}\cdot x + (1 - \boldsymbol{p}^2 + R^2)(1 - \boldsymbol{x}^2)\right) \\
&= \frac{1}{4R}\left(4\boldsymbol{p}\cdot\boldsymbol{x} - 2\boldsymbol{p}^2 - 2\boldsymbol{x}^2 + 2R^2\right) \\
&= \frac{R^2 - \|\boldsymbol{x} - \boldsymbol{p}\|^2}{2R} \equiv -\frac{P}{2R},
\end{aligned} \tag{3.96}$$

where $P = \|\boldsymbol{x} - \boldsymbol{p}\|^2 - R^2$ is the so-called *circle power* of $\boldsymbol{\rho}$ with respect to $\boldsymbol{\zeta}$. The Möbius transformation yields

$$\begin{aligned}\boldsymbol{\mathcal{I}}_{\boldsymbol{\zeta}}\boldsymbol{\rho} &= \boldsymbol{\rho} - 2\langle\boldsymbol{\rho},\boldsymbol{\zeta}\rangle\,\boldsymbol{\zeta} = \boldsymbol{\rho} + \frac{P}{R}\,\boldsymbol{\zeta} \\ &= \left(\frac{1+\boldsymbol{x}^2}{2} + P\frac{1+\boldsymbol{p}^2-R^2}{2R^2}, \boldsymbol{x} + \frac{P}{R^2}\,\boldsymbol{p}, \frac{1-\boldsymbol{x}^2}{2} + P\frac{1-\boldsymbol{p}^2+R^2}{2R^2}\right) \\ &\equiv a\left(\frac{1+\boldsymbol{y}^2}{2}, \boldsymbol{y}, \frac{1-\boldsymbol{y}^2}{2}\right),\end{aligned} \tag{3.97}$$

where we used in the last line that the image of a point under a Möbius transformation must also be a point and hence of that form. The factor $a$ is given by

$$a = (\boldsymbol{\mathcal{I}}_{\boldsymbol{\zeta}}(\boldsymbol{\rho}))_0 + (\boldsymbol{\mathcal{I}}_{\boldsymbol{\zeta}}(\boldsymbol{\rho}))_{n+1} = \frac{R^2+P}{R^2} = \frac{\|\boldsymbol{x}-\boldsymbol{p}\|^2}{R^2}. \tag{3.98}$$

Therefore the coordinates of the image point are given by

$$\begin{aligned}\boldsymbol{y} &= \frac{1}{a}\boldsymbol{\mathcal{I}}_{\boldsymbol{\zeta}}(\boldsymbol{\rho}) = \frac{R^2}{\|\boldsymbol{x}-\boldsymbol{p}\|^2}\left(\boldsymbol{x} + \frac{P}{R^2}\,\boldsymbol{p}\right) = \frac{R^2}{\|\boldsymbol{x}-\boldsymbol{p}\|^2}\,\boldsymbol{x} + \frac{P}{\|\boldsymbol{x}-\boldsymbol{p}\|^2}\,\boldsymbol{p} \\ &= \boldsymbol{p} + \frac{R^2}{\|\boldsymbol{x}-\boldsymbol{p}\|^2}(\boldsymbol{x}-\boldsymbol{p}) = \boldsymbol{p} + \frac{R^2}{P-R^2}(\boldsymbol{x}-\boldsymbol{p}).\end{aligned} \tag{3.99}$$

This shows that $\boldsymbol{y}$ lies on the ray from the centre $\boldsymbol{p}$ of the circle $\boldsymbol{\zeta}$ through the point $\boldsymbol{x}$ and satisfies

$$\|\boldsymbol{x}-\boldsymbol{p}\|\,\|\boldsymbol{y}-\boldsymbol{p}\| = R^2. \tag{3.100}$$

This is simply the inversion of point at a circle in $\mathbb{R}^n$.

Next let us derive the formulas for the inversion of another circle

$$\boldsymbol{\xi} = \left(\frac{1+\boldsymbol{x}^2-r^2}{2r}, \frac{\boldsymbol{x}}{r}, \frac{1-\boldsymbol{x}^2+r^2}{2r}\right) \tag{3.101}$$

at $\boldsymbol{\zeta}$. This transformation can be considered as a Lie sphere transformation if we extend it as described above. Hence, the image of the circle $\boldsymbol{\xi}$ is again a circle. This time we have

$$\langle\boldsymbol{\xi},\boldsymbol{\zeta}\rangle = -\frac{P}{2Rr} \tag{3.102}$$

with the power $P = \|\boldsymbol{x}-\boldsymbol{p}\|^2 - r^2 - R^2$ between two circles. For the inverted circle we obtain

$$\boldsymbol{\mathcal{I}}_{\boldsymbol{\zeta}}(\boldsymbol{\xi}) = \frac{1}{2r}\begin{pmatrix}(1+\boldsymbol{x}^2-r^2) + \frac{P}{R^2}\,(1+\boldsymbol{p}^2-R^2) \\ 2\left(\boldsymbol{x} + \frac{P}{R^2}\,\boldsymbol{p}\right) \\ (1-\boldsymbol{x}^2+r^2) + \frac{P}{R^2}\,(1-\boldsymbol{p}^2+R^2)\end{pmatrix} \equiv \frac{1}{2\bar{r}}\begin{pmatrix}1+\bar{\boldsymbol{x}}^2-\bar{r}^2 \\ 2\bar{\boldsymbol{x}} \\ 1-\bar{\boldsymbol{x}}^2+\bar{r}^2\end{pmatrix}, \tag{3.103}$$

where

$$\bar{r} = \frac{R^2}{P+R^2}\,r, \tag{3.104a}$$

$$\bar{\boldsymbol{x}} = \boldsymbol{p} + \frac{R^2}{P+R^2}\,(\boldsymbol{x}-\boldsymbol{p})\,. \tag{3.104b}$$

So the non-linear equations eq. (3.104) for a circle inversion in $\mathbb{R}^n$ become linear if we use Lie sphere vectors and Möbius inversions. Note that the centre $\bar{\boldsymbol{x}}$ of the inverted circle is not the inverted centre $\boldsymbol{x}$ of the original circle: If $\boldsymbol{\rho} = \left(\frac{1+\boldsymbol{x}^2}{2}, \boldsymbol{x}, \frac{1-\boldsymbol{x}^2}{2}\right)$ is the Lie sphere vector of the centre $\boldsymbol{x}$ and analogously $\bar{\boldsymbol{\rho}}$ that one of $\bar{\boldsymbol{x}}$, we have $\bar{\boldsymbol{\rho}} \neq \boldsymbol{\mathcal{I}}_{\boldsymbol{\zeta}}(\boldsymbol{\rho})$. Although the formulas for points and circles look equal, they differ because of the additional $r^2$ in the circle power $P$.

We can repeat this procedure for planes but it is easily verified that the Möbius inversion reduces to the common reflection at a plane

$$\bar{\boldsymbol{x}} = \boldsymbol{x} - \frac{2\,\boldsymbol{x}\cdot\boldsymbol{n}}{\boldsymbol{n}^2}\,\boldsymbol{n}. \tag{3.105}$$

Similarly, Möbius inversions describe inversions on caps and hyperbolic circles in the spherical and hyperbolic case, respectively.

## 3.4 Uniform Polytopes

A special kind of point distributions on the hypersphere, which can be generated by Möbius inversions, are the *spherical uniform polytopes*. A uniform polytope is defined as a *vertex-transitive* polytope with uniform facets. The two-dimensional uniform polytopes are the regular polygons. Three-dimensional polytopes are called *polyhedrons* and the four-dimensional polytopes are referred to as *polychorons*.

Loosely speaking, vertex-transitivity means that all vertices are equal. Every vertex can be mapped by inversions to any other such that the polytope still looks the same. For example, a cuboid is vertex-transitive but not uniform if the faces are no squares.

All edges of uniform polytopes have the same length. Hence, two neighbouring vertices always have the same distance. However, higher-dimensional sub-elements like faces, cells, and so on, may differ. If this is not the case so that they are all equal, the polytope is called *regular*. If the vertices of a polytope lie on a hypersphere, we speak of a spherical polytope.

Here we give a brief introduction to spherical uniform polytopes with focus on the 4-dimensional case. For a detailed discussion and further reading we refer to the following books: The standard work on this topic is the book *Regular polytopes* of Coxeter [Cox73]. Furthermore, we recommend the book of Humphreys [Hum92] and the one of Grove and Benson [GB96].

### Coxeter Groups

It is possible to find configurations of points on the circle or 1-sphere, respectively, such that the distance between any two neighbouring points is the same. These configurations are simply all kinds of regular polygons with $n$ vertices, called $n$-gon and denoted as $\{n\}$, like the equilateral triangle, the square and so on. They are constructed by putting $n$ points on the circle at the position $\boldsymbol{x}_k = (\cos(k\,\alpha_n), \sin(k\,\alpha_n))$, where $\alpha_n = \frac{2\pi}{n}$ is the angle between any two neighbouring points viewed from the centre and $k = 0, \ldots, n-1$; see also fig. 3.10. Obviously, this construction is possible for any positive integer $n \geq 3$.

The symmetry group $\mathrm{Dih}_n$ of the $n$-gon, called *dihedral group*, consists of the $n$ discrete rotations by an angle of $k\,\alpha_n$ and $n$ reflections; hence it is of order $2n$. Every orthogonal transformation can be composed into two reflections in the two-dimensional case. Actually

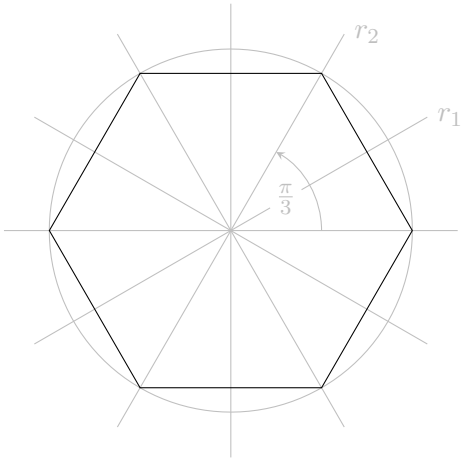


**Figure 3.10:** Regular hexagon ($n = 6$) with all its symmetry axes. The hexagon is invariant under the $2n = 12$ reflections $r_i$ at these lines. These reflections form the symmetry group $\mathrm{Dih}_6$. Furthermore, it is invariant under rotations of multiples of $\frac{2\pi}{n} = \frac{\pi}{3}$ but these can also be represented as certain combinations of reflections. For example, the indicated rotation is $r_2 \circ r_1$.

it can be shown that the dihedral group is generated by two reflections, say $r_1$ and $r_2$ such that

$$\mathrm{Dih}_n = \langle r_1, r_2 : r_1^2 = r_2^2 = (r_1 r_2)^n = 1 \rangle. \tag{3.106}$$

The first two relations are a consequence of the fact that $r_1$ and $r_2$ are reflections. The combination $r_1 r_2$ describes a rotation, as one can easily convince oneself, and the relation $(r_1 r_2)^n = 1$ then describes a full rotation by a multiple of $2\pi$. Every reflection can be visualised by a hyperplane, in our case two lines. The angle between the normals of the hyperplane is $\frac{\pi}{n}$. The polygon is then created by putting one point at only one hyperplane and perform all possible reflections in order to get all vertices.

The dihedral group is an example of a *Coxeter group* which are of the form

$$\mathrm{Cox} = \langle r_1, \ldots, r_n : (r_A r_B)^{m_{AB}} = 1 \rangle, \tag{3.107}$$

where $m_{AA} = 1$ and $m_{AB} \geq 2$, $A \neq B$. If there is no such relation for certain pairs $A, B$, we write $m_{AB} = \infty$. Sometimes, the *Coxeter matrix* $m_{AB}$ is used to represent a Coxeter group. It follows that the Coxeter matrix is symmetric, $m_{AB} = m_{BA}$. If $m_{AB} = 2$, the reflections $r_A$ and $r_B$ commute, this means $r_A r_B = r_B r_A$. Every finite Coxeter group can be represented as a reflection group. The Coxeter matrix determines the angle between the normals $\boldsymbol{n}_A$ and $\boldsymbol{n}_B$ of two reflection hyperplanes by $\boldsymbol{n}_A \cdot \boldsymbol{n}_B = \cos \frac{\pi}{m_{AB}}$.

Another way of representing a Coxeter group are the *Coxeter diagrams*. Every reflection is denoted by a point. These points are connected with lines labelled with the number $m_{AB}$. If $m_{AB} = 3$, the number is usually omitted. In the case of $m_{AB} = 2$, no connecting line is drawn in order to stress the fact that theses reflections commute. Therefore the dihedral group $\mathrm{Dih}_n$ is represented as $\bullet\overset{n}{—}\bullet$ for $n \geq 4$, while $\mathrm{Dih}_3$ is simply $\bullet—\bullet$. For two orthogonal hyperplanes, $n = 2$, we have $\bullet \quad \bullet$, separated into two unconnected parts stating that $\mathrm{Dih}_2 = \langle r_1 \rangle \times \langle r_2 \rangle$ is reducible. The diagram $\bullet\overset{\infty}{—}\bullet$ corresponds to the case of two parallel hyperplanes. But in this case, the corresponding group is not finite.

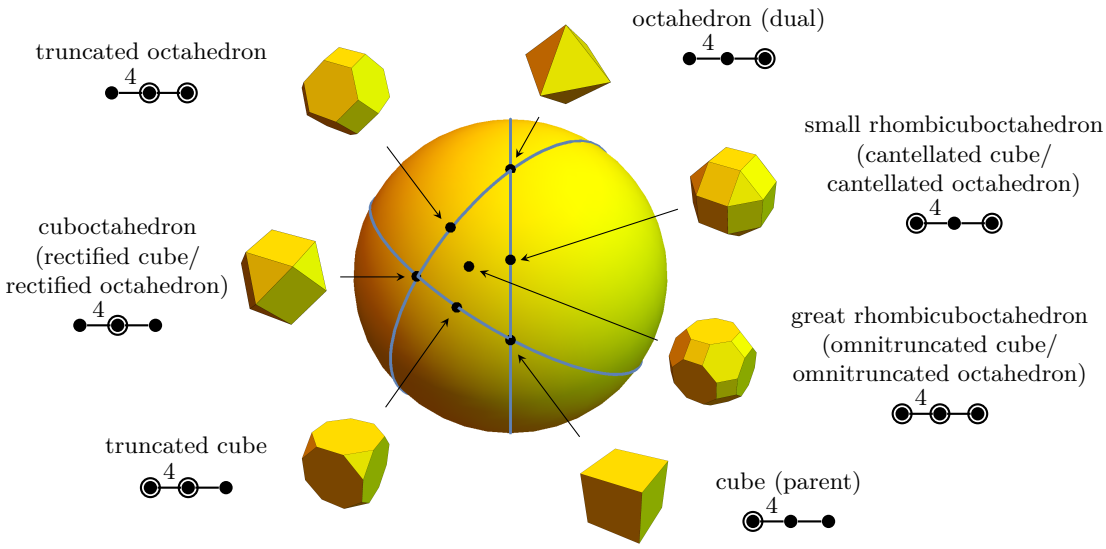


**Figure 3.11:** Uniform polyhedrons generated by $B_3$: The blue great circles, determined by the symmetry group, indicate the reflection planes or mirrors. These define the triangular fundamental region where the generators (the black points) lie. If such a point is reflected as often as possible at the mirrors, it generates the vertices of a polyhedron. The different outcomes for all generators are shown together with the general naming scheme.

### Construction of Spherical Uniform Polytopes

In view of the construction described above, a polygon can be represented by its symmetry group diagram in which each reflection plane is marked with a circle if the generating vertex is *not* contained. These planes are called *active mirrors* because they create new points from the generator. For example, the equilateral triangle is ◉—●, for the square we have ◉—4—●, and so on.

The reflection planes define an $n$-simplex on the hypersphere, called *fundamental region*. The generator is put at certain locations of this simplex depending on the number of marked notes in the Coxeter diagram. A single marked node corresponds to a generator on a vertex. If two nodes are marked, the generator lies on the edge with equal distance to the adjacent vertices. Three marks denote a generator on a face with equal distance to all adjacent edges. This goes on until all nodes are marked and the generator lies in the region enclosed by the mirrors with equal distance to all mirrors. This is shown in fig. 3.11 for the 3-dimensional case for the symmetry group of a cube.

Every polytope has a *dual* whose vertices are the centres of all facets of the original. If the dual polytope is the same as the original, it is called *self-dual*. An example is the self-dual tetrahedron. In general, the dual of a uniform polytope is not uniform. However, a polytope and its dual share the same symmetry group.

The most symmetric polytopes are the regular ones. Most uniform polytopes can be derived from these. Hence, they are of special interest.

**Theorem 3.2.** ***Regular polytopes***
*The Coxeter diagram of a regular polytope has the form*

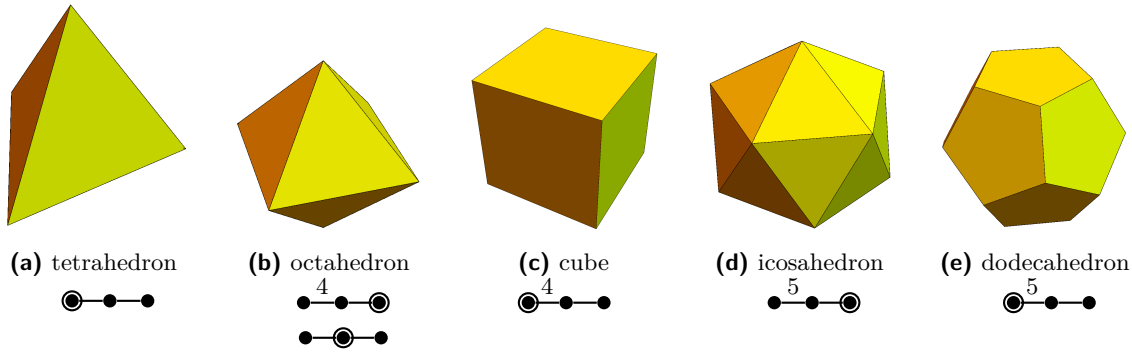


**Figure 3.12:** Platonic solids: In three dimensions there are only five configurations of vertices on the sphere such that the polyhedron is regular.

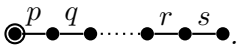


*They are also denoted by the* Schläfli symbol $\{p, q, \ldots, r, s\}$. *Regular polytopes are formed by regular facets of one kind (by definition). For this reason, regular polytopes are vertex-transitive, edge-transitive, face-transitive and so on. This means, all sub-elements (vertices, edges, faces, ...) are invariant under actions of the symmetry group.*

*Their duals are also regular and given by the reversed Schläfli symbol* $\{s, r, \ldots, q, p\}$. *Hence, their Coxeter diagram is*

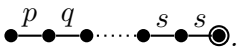


It is a well-known fact that there are only five regular spherical polyhedrons in three dimensions. These are the five Platonic solids shown in fig. 3.12: the self-dual tetrahedron $\{3, 3\}$, the cube $\{4, 3\}$ and its dual the octahedron $\{3, 4\}$, the dodecahedron $\{5, 3\}$ and its dual the icosahedron $\{3, 5\}$. The other Schläfli symbols $\{p, q\}$ correspond to tessellations of the Euclidean or hyperbolic space. The uniform polyhedrons, which can be derived from the regular ones, are the *13 Archimedean solids* shown in fig. 3.13. Most one of these are constructed as described above and shown in fig. 3.11 for the cube. The snub cube and snub dodecahedron are special constructions.

In order to get a regular convex polytope the corresponding Coxeter group must be finite, else we would generate infinitely many images of a vertex point. The classification of the Coxeter groups is very similar to that of Lie algebras and groups. The normals of the reflection hypersurfaces form the so-called *root system*. Here the notion of a root system is less restrictive than for Lie algebras since the so-called *crystallographic condition* is not imposed. This condition restricts the angle between two roots to $\frac{\pi}{k}$, where $k = 2, 3, 4, 6$, whereas we allow all integers $k \geq 2$. Furthermore, the length of the roots is not important. It can also be shown that every Coxeter group is the direct product of connected Coxeter groups. For this reason we can restrict ourselves to those diagrams that are connected.

From a root system, a set of simple roots $\{\boldsymbol{f}_\alpha\}$ is chosen generating all other roots by reflections at the corresponding mirrors; these correspond to the generators of the Coxeter groups. If the group is finite, the root system also forms a basis of the Euclidean space so that every vector $\boldsymbol{x} \in \mathbb{R}^n$ can be decomposed into $\boldsymbol{x} = x^i \boldsymbol{f}_i$. Hence, the scalar product of

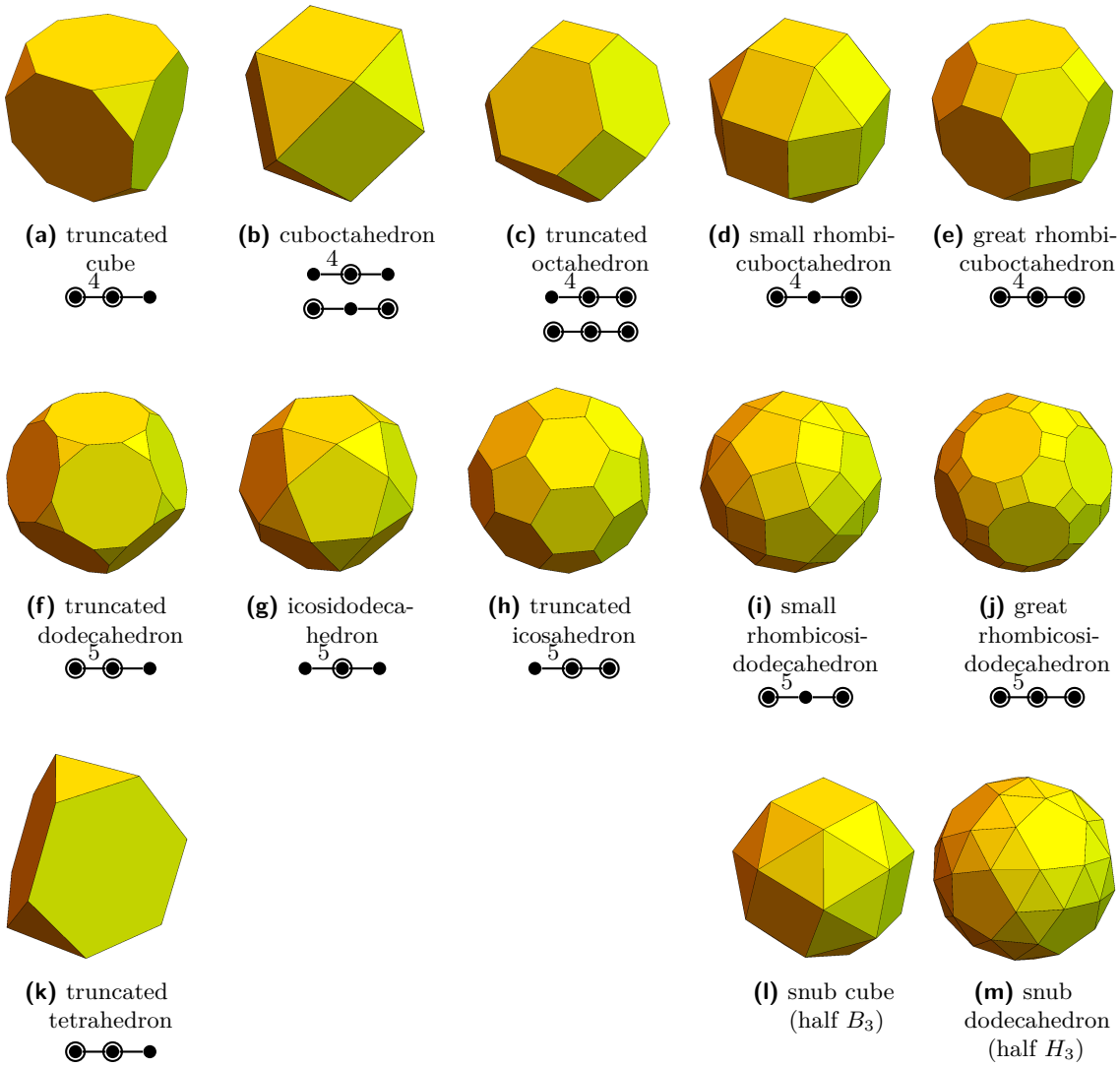


**Figure 3.13:** 13 Archimedean solids. Sometimes one speaks of 15 Archimedean solids because there are two versions of the snub cube and the snub dodecahedron differing in their chirality.

two vectors $\boldsymbol{x}, \boldsymbol{y}$ is

$$(x^\alpha \, \boldsymbol{f}_\alpha) \cdot (y^\beta \, \boldsymbol{f}_\beta) = A_{\alpha\beta} \, x^\alpha y^\beta \tag{3.108}$$

where $A_{\alpha\beta} = \boldsymbol{f}_\alpha \cdot \boldsymbol{f}_\beta \equiv \cos \frac{\pi}{m_{\alpha\beta}}$. Therefore the matrix $\boldsymbol{A}$ must be equivalent to the unit matrix, especially its eigenvalues must be positive. This strongly restricts the number of finite Coxeter groups.

**Theorem 3.3.** ***Finite Coxeter groups***
*The finite Coxeter groups consist of the regular families*

| | | |
|---|---|---|
| $A_n$ | $n \geq 1$ |  |
| $B_n$ | $n \geq 3$ | 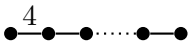 |
| $D_n$ | $n \geq 4$ | 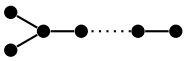 |
| $I_2(n)$ | $n \geq 3$ |  |

*and the exceptional groups*

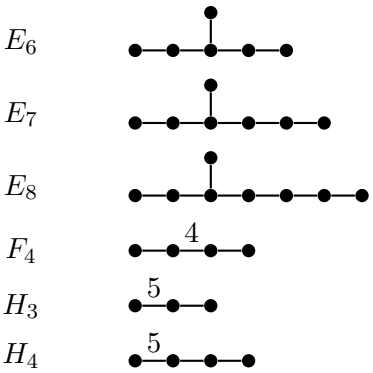


Note that the groups $H_3, H_4$ and $I_2(n) \equiv \mathrm{Dih}_2(n)$ are the non-crystallographic groups except for $I_2(n)$ with $n = 2, 3, 4, 6$. $I_2(6)$ is usually denoted as $G_2$ in the context of Lie algebras. Furthermore, $I_2(3) \equiv A_2$ and $I_2(4) \equiv B_2$, whereas $I_2(2) \equiv A_1 \times A_1$ is unconnected.

In three dimensions we have just $A_3 =$  , $B_3 =$  and $H_3 =$  as symmetry groups for regular convex polytopes. $A_3$ is the symmetry group of the tetrahedron {3,3}, $B_3$ of the cube {4,3} and the octahedron {3,4}, and $H_3$ being the one of the dodecahedron {5,3} and the icosahedron {3,5}. Note that there are crystal lattices in nature with $A_3$ and $B_3$ symmetry, whereas the $H_3$ symmetry is realized almost nowhere; this is the origin of the term 'crystallographic'.

In four dimensions the possible symmetry groups for regular polytopes are $A_4 =$  , $B_4 =$  and $H_4 =$  and additionally $F_4 =$  . These correspond to the pentatope with five vertices ($A_4$), the tesseract with 16 vertices and orthoplex with 8 vertices ($B_4$), the dodecaplex with 600 vertices and tetraplex with 120 vertices ($H_4$), and the self-dual octaplex with 24 vertices ($F_4$). Projections of these objects are shown in fig. 3.14. Further properties are listed in table 3.4.

If we go to higher dimensions $n \geq 5$, the only remaining symmetry groups are $A_n$ and $B_n$. The former one belongs to $n$-simplex that is the generalisation of the tetrahedron: a

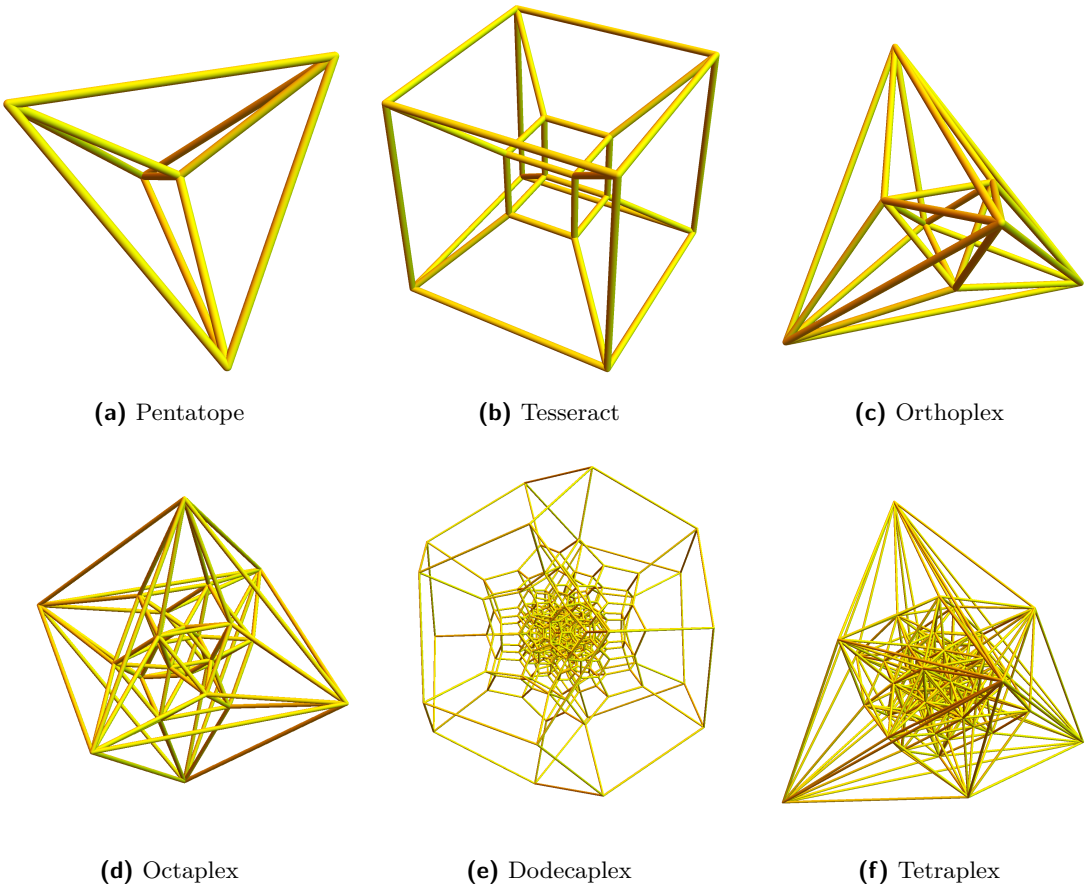

**(a)** Pentatope **(b)** Tesseract **(c)** Orthoplex

**(d)** Octaplex **(e)** Dodecaplex **(f)** Tetraplex

**Figure 3.14:** Stereographic projections of the six 4-dimensional Platonic bodies such that the south pole is in the centre of a cell.

configuration of $n+1$ points with equal distance to each other. The $n$-cube and $n$-orthoplex, being the generalization of the cube and octahedron, are symmetric with respect to $B_n$. The $n$-orthoplex is easily constructed by marking all axes at the same distance from the origin: $\{(\pm 1, 0, 0, \dots), (0, \pm 1, 0, \dots), \dots, (0, \dots, 0, \pm 1)\}$. Similarly, the $n$-cube consists of all permutations of $(\pm 1, \pm 1, \dots, \pm 1)$.

As discussed previously, many more uniform polytopes can be generated if the generating point is set on different reflection hyperplanes or even on none. Uniform polytopes have uniform facets which do not have to be all of the same kind as it is in the case of regular polytopes. These are often rectified, truncated, or cantellated versions of the regular ones, as we have seen in fig. 3.11 using the example of a cube.

It is also possible to include rational values at the edges of Coxeter diagrams to generate star polytopes. Furthermore, there are special operations leading to uniform polytopes in some cases like the snub cube and snub dodecahedron. For a detailed discussion of the different kinds of polytopes see Coxeter [Cox73].

### Uniform Spherical Polychorons

Finally, we give an overview of the uniform spherical polychorons on the 3-sphere in four dimensions. These can be divided into four groups:

**Table 3.4:** Properties of the 4-dimensional Platonic bodies

| body | symmetry | Coxeter | vertices | edges | faces | cells |
|---|---|---|---|---|---|---|
| pentatope | $A_4$ | 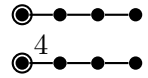 | 5 | 10 | 10 | 5 |
| tesesract | $B_4$ |  | 16 | 32 | 24 | 8 |
| orthoplex | $B_4$ | 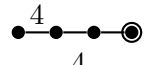 | 8 | 24 | 32 | 16 |
| octaplex | $F_4$ | 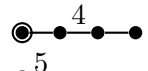 | 24 | 96 | 96 | 24 |
| dodecaplex | $H_4$ | 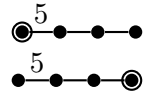 | 600 | 1200 | 720 | 120 |
| tetraplex | $H_4$ | 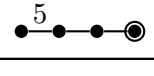 | 120 | 720 | 1200 | 600 |

- 47 non-prismatic polychorons derived from the regular ones,
- 17 prismatic polychorons which are prisms constructed from the uniform polyhedrons,
- two infinite series of duoprisms and antiprismatic prisms.

As explained above, the finite reflection groups are built from direct products of the simple finite ones $A_n, B_n, D_n, E_{6,7,8}, F_4, H_{3,4}, I_2(p)$. First, we determine the connected non-prismatic symmetry groups: there are five finite reflection groups in four dimensions, namely $A_4$ , $B_4$  , $D_4$  , $F_4$ 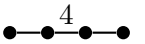 and $H_4$ 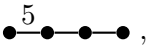 , generating almost all convex uniform non-prismatic polychorons. They are constructed as described above by putting generators on special points of the fundamental region, which is a 3-simplex in this case. The different possibilities are shown in fig. 3.15.

The polychorons are named after the operations applied to the regular ones:

***Truncation***: The vertices are cut away in such a way that new cells appear until all edges have the same length.

***Rectification***: A truncation of vertices until the edges are points, higher order rectifications truncate until the faces (=birectified) and cells (=trirectified) are reduced to points. Also called complete-truncation.

***Cantellation***: This is a truncation of vertices and edges simultaneously. It is a progression between a regular polychoron and its birectified form.

***Runcination***: A truncation applied to vertices, edges and faces simultaneously. It intermediates between a polychoron and its dual.

Besides the 45 polychorons generated in this way, there are the two special cases of the *snub 24-cell* with half of the $F_4$-symmetry and the *grand antiprism* with diminished $H_4$-symmetry.

All these 47 polychorons are listed in table B.1, sorted by their symmetry group. Note that $D_4$ generates only polychorons which are also contained in other symmetry families. Hence, $D_4$ provides just another possible construction for these polychorons. Furthermore, the polychorons #22, #23, #24 are members of the $B_4$- and $F_4$-family.

The second set of uniform polychorons are the prismatic ones whose symmetry groups are the direct product of $A_1$ and one of three-dimensional groups $A_3, B_3, H_3$. Hence, their

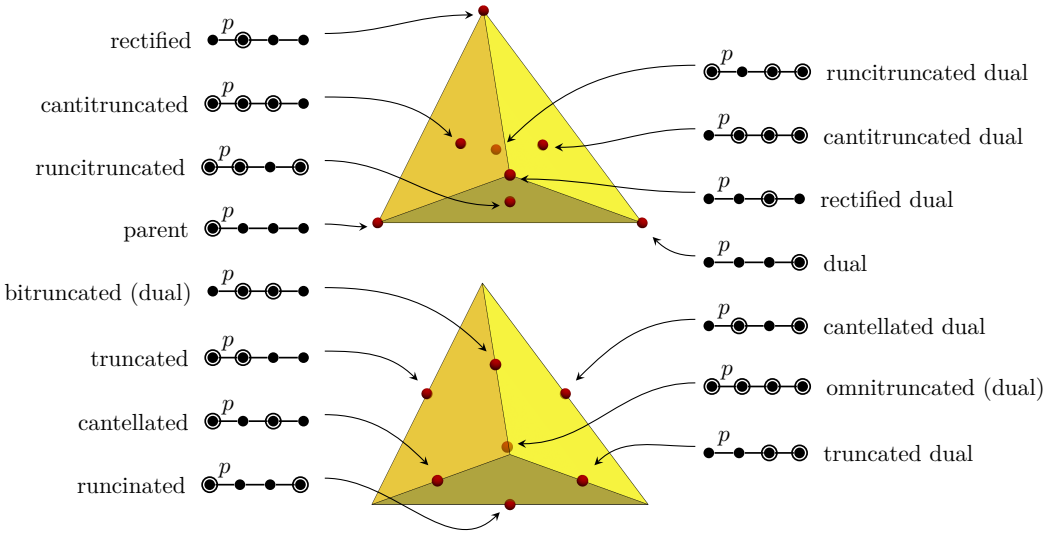


**Figure 3.15:** Naming scheme for most of the uniform polychorons: The reflection hyperplanes define a non-uniform (curved) tetrahedron on the hypersphere on which we can mark 15 generators altogether: 4 on the vertices and 4 on the faces, shown in the upper part; 6 on the edges and 1 inside, shown in the lower part. The polychorons are named after a regular polychoron or its dual, respectively, with the corresponding adjective describing the applied operation.

symmetry groups are $\bullet\!\!-\!\!\overset{p}{\bullet}\!\!-\!\!\bullet\ \bullet$ with $p = 3, 4, 5$. These polychorons are the prismatic versions of the 5 Platonic and 13 Archimedean solids: two copies of such an object connected by edges of the same length. The cube prism one is the same as the tesseract so that there are 17 new polychorons, listed in table B.2.

Besides these 64 polychorons, we just want to mention the two infinite series of uniform polychorons: On the one hand, we have the duoprisms $\overset{p}{\bullet}\!\!-\!\!\bullet\ \ \overset{q}{\bullet}\!\!-\!\!\bullet$ with symmetry groups $I_2(p) \times I_2(q)$, which are direct products of polygons. On the other hand, there are duoantiprisms or antiprismatic prisms, which are prisms of two uniform antiprisms.

## 3.5 Apollonian Sphere Packings

Later, we need a procedure to cover a hypersphere with spherical caps in a systematic way in order to construct Swiss-cheese models in which most of the dust is removed. By a stereographic projection, this is equivalent to filling up a sphere with smaller spheres. Such a space-filling sphere packing is given by the *Apollonian sphere packing*[4]. Using the methods of Lie sphere geometry, this provides a simple algorithm, based upon the *Descartes theorem*, starting with five mutually tangent spheres in 3-dimensional space ($n+2$ spheres in $n$ dimensions) and filling the space iteratively with smaller spheres tangent to the previous ones.

[4]We also call an Apollonian sphere packing on the hypersphere with spherical caps an *Apollonian covering*

### Descartes Theorem

The Apollonian sphere packing is named after Apollonius of Perga (ca. 262 – 190 BC), who posed the problem to find all circles tangent to three given ones in the Euclidean plane. He also solved this problem but his work was destroyed in the fire of Alexandria and only a report about his results survived.

It took many centuries until the solution was rediscovered by Descartes in 1643 [DS42][5] for the special case of mutually tangent circles. His result is known as *Descartes Circle Theorem* nowadays. About 300 years later, this theorem was rediscovered again and extended to three dimensions by Soddy and published as the poem 'The Kiss Precise' [Sod36] in 1936. One year later, Gosset generalised the theorem to arbitrary dimensions and added another stanza to Soddy's poem [Gos37]:

**The Kiss Precise** by F. Soddy

*For pairs of lips to kiss maybe*
*Involves no trigonometry.*
*This not so when four circles kiss*
*Each one the other three.*
*To bring this off the four must be*
*As three in one or one in three.*
*If one in three, beyond a doubt*
*Each gets three kisses from without.*
*If three in one, then is that one*
*Thrice kissed internally.*

*Four circles to the kissing come.*
*The smaller are the benter.*
*The bend is just the inverse of*
*The distance form the center.*
*Though their intrigue left Euclid dumb*
*There's now no need for rule of thumb.*
*Since zero bend's a dead straight line*
*And concave bends have minus sign,*
*The sum of the squares of all four bends*
*Is half the square of their sum.*

*To spy out spherical affairs*
*An oscular surveyor*
*Might find the task laborious,*
*The sphere is much the gayer,*
*And now besides the pair of pairs*
*A fifth sphere in the kissing shares.*
*Yet, signs and zero as before,*
*For each to kiss the other four*
*The square of the sum of all five bends*
*Is thrice the sum of their squares.*

**The Kiss Precise** by T. Gosset

*And let us not confine our cares*
*To simple circles, planes and spheres,*
*But rise to hyper flats and bends*
*Where kissing multiple appears,*
*In n-ic space the kissing pairs*
*Are hyperspheres, and Truth declares,*
*As* $n+2$ *such osculate*
*Each with an* $n+1$ *fold mate*
*The square of the sum of all the bends*
*Is n times the sum of their squares.*

Mathematically, this can be stated as:

**Theorem 3.4.** ***Descartes Circle Theorem/Soddy-Gosset Theorem.***
*In the n-dimensional Euclidean space* $n+2$ *mutually tangent circles, that are* $(n-1)$*-spheres, with radius* $r_A$ *satisfy*

$$\sum_{A=1}^{n+2} \left(\frac{1}{r_A}\right)^2 = \frac{1}{n} \left(\sum_{A=1}^{n+2} \frac{1}{r_A}\right)^2 . \tag{3.109}$$

In two dimensions, the centres of the circles satisfy a similar relation if we work in the complex plane rather than $\mathbb{R}^2$:

**Theorem 3.5.** ***Complex Descartes Theorem.***
*The centres* $x_A + \mathrm{i}\, y_A \in \mathbb{C}$ *of 4 mutually tangent circles with radius* $r_A \in \mathbb{R}$ *in the complex*

[5] See [Des+91] for an English translation.

*plane* $\mathbb{C}$ *satisfy*

$$\sum_{A=1}^{4}\left(\frac{x_A+\mathrm{i}\,y_A}{r_A}\right)^2=\frac{1}{2}\left(\sum_{A=1}^{4}\frac{x_A+\mathrm{i}\,y_A}{r_A}\right)^2. \tag{3.110}$$

There is a generalisation of the Descartes theorem into a matrix form by Lagarias, Mallows and Wilks [LMW02] which can be applied in any dimension and also includes the centres of the circles. Of course, in two dimensions the Complex Descartes theorem is retrieved. It is also possible to include planes. The Descartes Circle Theorem is still valid if we consider planes as circles with infinite radius or vanishing curvature, respectively, such that $\frac{1}{r}=0$.

Mauldon [Mau62] extended the Descartes theorem to spherical caps and hyperbolic circles on the hypersphere and hyperboloid, respectively. Lagarias, Mallows and Wilks [LMW02] included the centres in a matrix formulation using special coordinates which they called *augmented curvature-centre coordinates*.

However, the origin of these coordinates does not become clear. Although a connection to algebra for the flat case, first noticed by Pedoe [Ped67], and to the stereographic projection are mentioned, there is still a lack of geometrical interpretation. We present a unified description of all these cases explaining the geometrical origin using the methods of Lie sphere geometry, developed in the previous section 3.3.

For this reason, let us consider the case of $n+2$ pairwise externally tangent circles $\left\{\boldsymbol{\omega}_A\in H_1^{n+1}:A=1,\dots,n+2\right\}$ in $n$ dimensions. On the one hand, we have $\langle\boldsymbol{\omega}_A,\boldsymbol{\omega}_A\rangle=1$ because they describe circles; on the other hand, they must satisfy $\langle\boldsymbol{\omega}_A,\boldsymbol{\omega}_B\rangle=-1$ for $A\neq B$ in order to be externally tangent. These conditions can be summarised as

$$\langle\boldsymbol{\omega}_A,\boldsymbol{\omega}_B\rangle=2\delta_{AB}-1\equiv\mathcal{G}_{AB}. \tag{3.111}$$

Such a set $\{\boldsymbol{\omega}_A\}$ is referred to as *Descartes set*.

If we introduce the *Descartes matrix* $\boldsymbol{\mathcal{W}}^\top=\left(\boldsymbol{\omega}_1^\top,\dots,\boldsymbol{\omega}_{n+2}^\top\right)$, where $\boldsymbol{\omega}_A^\top$ is a column vector, we can write eq. (3.111) as

$$\boldsymbol{\mathcal{W}}\,\boldsymbol{\eta}\,\boldsymbol{\mathcal{W}}^\top\equiv\langle\boldsymbol{\mathcal{W}},\boldsymbol{\mathcal{W}}\rangle=\boldsymbol{\mathcal{G}}, \tag{3.112}$$

where $\eta_{AB}=\operatorname{diag}(-1,1,\dots,1)$ is the Minkowski metric. By inverting this equation we obtain

**Theorem 3.6.** ***Generalised Descartes Theorem.***
*A set of* $n+2$ *mutually tangent Lie spheres* $\{\boldsymbol{\Omega}_A:A=1,\dots,n+2\}$ *described by the Lie vectors* $\boldsymbol{\Omega}_A=(\boldsymbol{\omega}_A,1)$ *satisfy the matrix equation*

$$\boldsymbol{\mathcal{W}}^\top\boldsymbol{\mathcal{G}}^{-1}\boldsymbol{\mathcal{W}}=\boldsymbol{\eta}, \tag{3.113}$$

*where* $\boldsymbol{\mathcal{W}}=\left(\boldsymbol{\omega}_1^\top,\dots,\boldsymbol{\omega}_{n+2}^\top\right)$. *Conversely, any solution to eq.* (3.113) *corresponds to a Descartes set.*

This is basically the result of Lagarias, Mallows and Wilks. Instead of $\boldsymbol{\eta}$, they used the matrix

$$\boldsymbol{\eta}'=\begin{pmatrix}0&-2&0\\-2&0&0\\0&0&\boldsymbol{I}_n\end{pmatrix}, \tag{3.114}$$

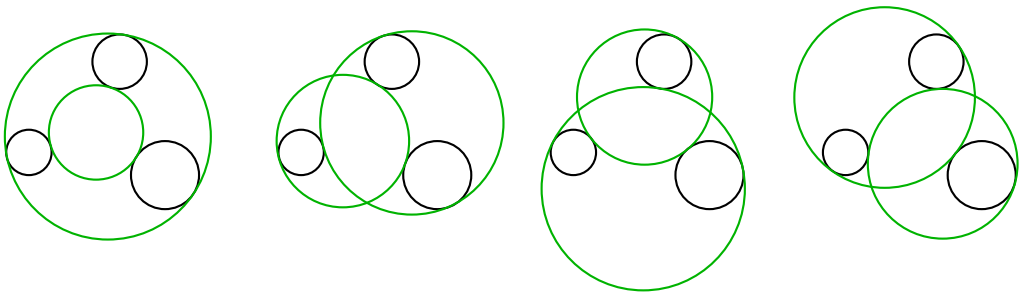

**Figure 3.16:** Solutions to the Apollonius problem: There are eight different green circles which are tangent to the given three black ones. If the orientation is included, we have 16 solutions because each circle can have two different orientations.

where $\boldsymbol{I}_n$ is the $n \times n$-identity matrix. $\boldsymbol{\eta}'$ is congruent to $\boldsymbol{\eta}$, that is $\boldsymbol{\eta} = \boldsymbol{A}\boldsymbol{\eta}'\boldsymbol{A}^\top$. If we apply $\boldsymbol{A}$ to a Lie sphere vector $\boldsymbol{\omega}$ describing a circle, we obtain their augmented curvature-centre coordinates.

Our result can be applied to the flat, spherical and hyperbolic case simultaneously, whereas Lagarias, Mallows and Wilks consider them separately. By substituting the different expressions for Lie spheres from table 3.2 for the Lie vectors $\boldsymbol{\omega}$ we cannot only derive formulas for all three cases. For example, the 00-component of this equation provides a relation between the opening angles similar to eq. (3.109)

$$2 + \sum_{A=1}^{n+2} (\cot \alpha_A)^2 = \frac{1}{n} \left( \sum_{A=1}^{n+2} \cot \alpha_A \right)^2, \tag{3.115}$$

which could be called *spherical Descartes theorem*. Similarly, we obtain the *hyperbolic Descartes theorem* for ellipses

$$\sum_{A=1}^{n+2} (\coth u_A)^2 = \frac{1}{n} \left( \sum_{A=1}^{n+2} \coth u_A \right)^2 + 2. \tag{3.116}$$

These results were also obtained by Lagarias, Mallows and Wilks. However, they do not consider hyperbolas and parabolas in the hyperbolic case which are included in our formulation. The Descartes Circle Theorem can be regained by adding the last two diagonal components of the matrix eq. (3.113). The other diagonal components would give us the equations for the centres of the circles.

The solution to the general Apollonius problem to find all circles tangent to three arbitrary circles, which need not to be mutually tangent, can be treated similarly. Given the Lie vectors $\boldsymbol{\omega}_A$ of the three circles in $n = 2$ dimensions, we need to find a fourth circle $\boldsymbol{\omega}_4$ which satisfies $\langle \boldsymbol{\omega}_4, \boldsymbol{\omega}_A \rangle = \pm 1$. The sign depends on the choice if the new circle should be internally or externally tangent to the given ones; this corresponds to a choice of an orientation for each circle. These conditions determine the matrix $\mathcal{G}_{AB} = \langle \boldsymbol{\omega}_A, \boldsymbol{\omega}_B \rangle$ so that we can solve the equation $\langle \boldsymbol{\mathcal{W}}, \boldsymbol{\mathcal{W}} \rangle = \boldsymbol{\mathcal{G}}$ for $\boldsymbol{\omega}_4$. Depending on the choice of sign in the tangency condition there are $2^{n+2} = 16$ oriented solutions as shown in fig. 3.16. The generalisation to higher dimensions is obvious.

Furthermore, it is even possible to impose other conditions than tangency. For example, we could demand that the new circle should be orthogonal to some of the given ones such

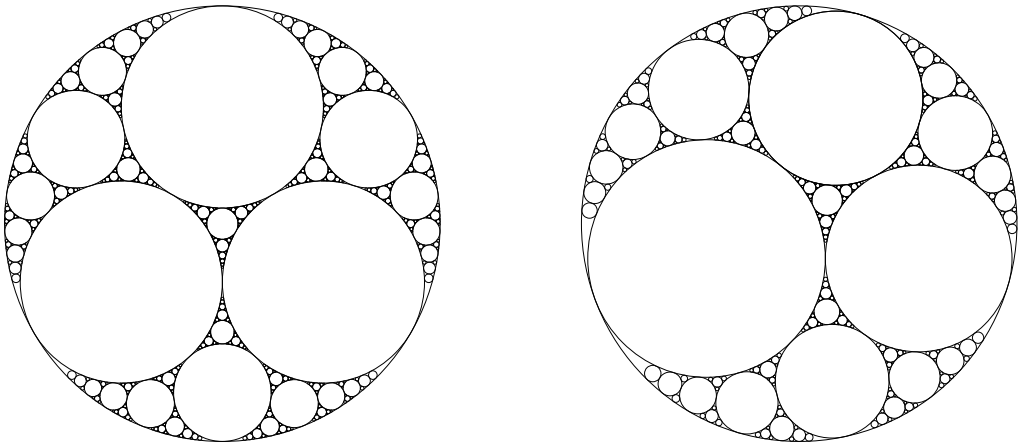

**(a)** Packing based upon regular triangle **(b)** Arbitrary packing

**Figure 3.17:** Two examples for a two-dimensional Apollonian circle packing

that $\langle \boldsymbol{\omega}_4, \boldsymbol{\omega}_A \rangle = 0$ for some $A$. However, in general there need not to be solution to these cases, compare to [Koc07].

### Apollonian Packing Algorithms

An Apollonian circle packing is a configuration of circles within a big circle in two dimensions which consists of Descartes sets, shown in fig. 3.17. Analogously, an Apollonian sphere packing fills a ball with smaller ones. Alternatively, this corresponds to the covering of a hypersphere with spherical caps if we apply a stereographic projection.

We present an algorithm generating such an Apollonian sphere packing which is a modification of the one given by Borkovec, De Paris and Peikert [BDP94]. The algorithm starts with a Descartes set and iteratively adds further balls which are part of new Descartes sets. This is shown in fig. 3.18 for the 3-dimensional case.

We start with a Descartes set $\{\boldsymbol{\omega}_A : A = 1, \ldots, n+2\}$ in $n$ dimensions satisfying $\langle \boldsymbol{\omega}_A, \boldsymbol{\omega}_B \rangle = \mathcal{G}_{AB}$ as shown above. Next, we define a set of *dual* spheres $\{\boldsymbol{\varpi}_A\}$ to a set of mutually tangent circles $\{\boldsymbol{\omega}_A\}$ by

$$\boldsymbol{\varpi}_A = \kappa \sum_{B=1}^{n+2} \mathcal{G}^{-1}_{AB} \boldsymbol{\omega}_B, \tag{3.117}$$

where $\kappa^2 = \frac{2n}{n-1}$ and $\mathcal{G}^{-1}_{AB} = \frac{1}{2}\left(\delta_{AB} - \frac{1}{n}\right)$, compare to [Söd92]. The dual spheres satisfy

$$\langle \boldsymbol{\varpi}_A, \boldsymbol{\varpi}_B \rangle = \kappa^2 \, \mathcal{G}^{-1}_{AB} = \frac{1}{n-1}\left(n\,\delta_{AB} - 1\right) \leq 1, \tag{3.118a}$$

$$\langle \boldsymbol{\varpi}_A, \boldsymbol{\omega}_B \rangle = \kappa \, \delta_{AB}. \tag{3.118b}$$

In order to be a Lie sphere vector in standard form $(\boldsymbol{\varpi}, 1)$, the normalization constant $\kappa$ is needed so that $\langle \boldsymbol{\varpi}_A, \boldsymbol{\varpi}_A \rangle = 1$. Note that the dual spheres are only externally tangent, this means $\langle \boldsymbol{\varpi}_A, \boldsymbol{\varpi}_B \rangle = -1$ for $A \neq B$, in two dimensions; in higher dimensions they always overlap as eq. (3.118a) shows. A dual sphere $\boldsymbol{\varpi}_A$ is orthogonal to all spheres $\boldsymbol{\omega}_B$ with $B \neq A$ as the second property (3.118b) shows.

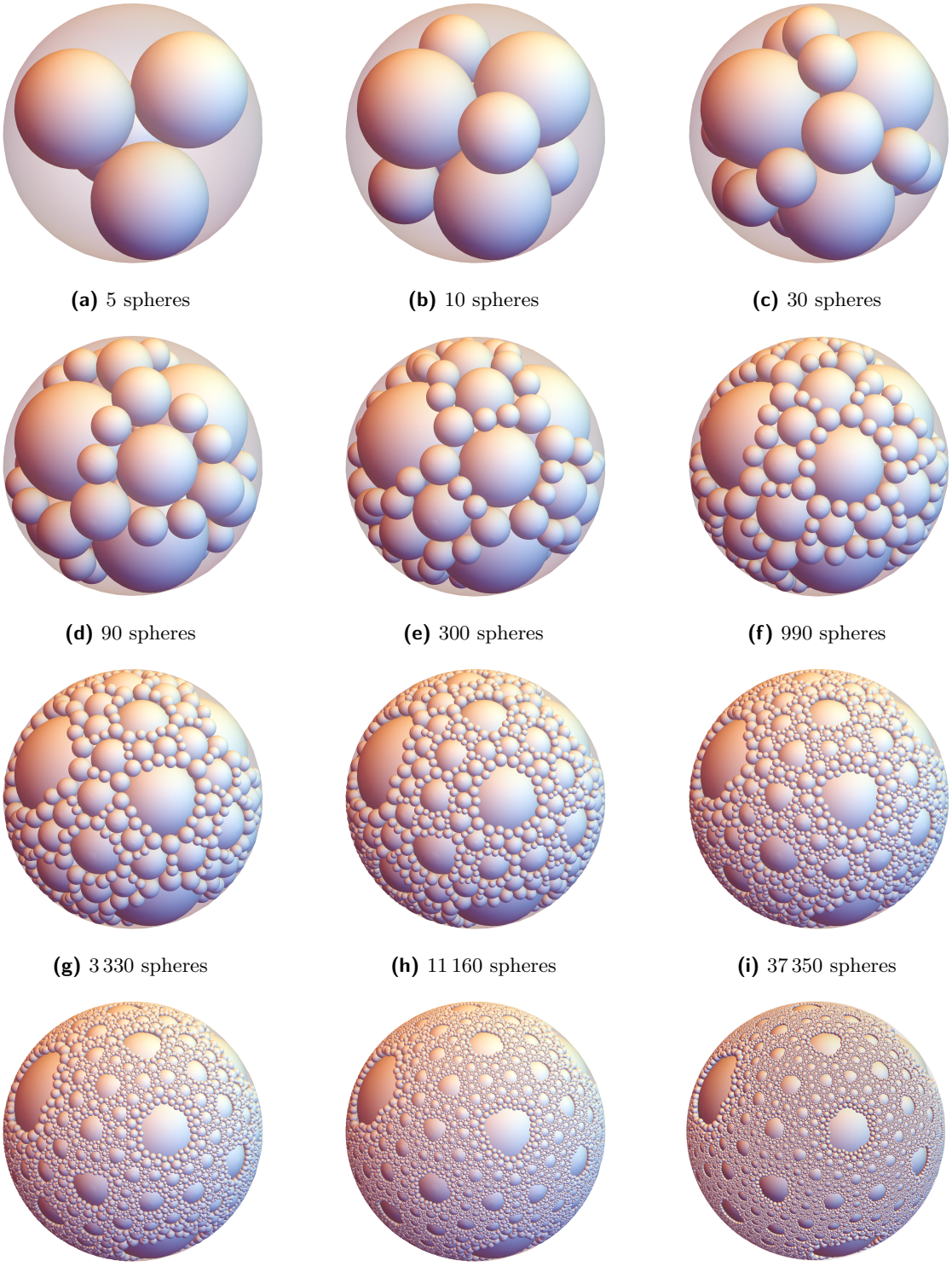

**(a)** 5 spheres **(b)** 10 spheres **(c)** 30 spheres

**(d)** 90 spheres **(e)** 300 spheres **(f)** 990 spheres

**(g)** 3 330 spheres **(h)** 11 160 spheres **(i)** 37 350 spheres

**(j)** 126 090 spheres **(k)** 423 900 spheres **(l)** 1 424 790 spheres

**Figure 3.18:** First steps of an Apollonian sphere packing. The last figure is the one shown on the cover. An enlarged version of the last figure can be found in appendix A. There we also explain the construction of this packing.

Now we can formulate the algorithm to generate an Apollonian packing. We describe the flat case, the spherical and hyperbolic case can be treated analogously. The procedure is based on the Apollonian problem for $n+1$ given mutually tangent spheres. We can generate new spheres by directly applying the Soddy-Gosset theorem 3.4 assuming that the spheres are always externally tangent. If we solve eq. (3.109) for one radius, say $r_{n+2}$, we obtain the two solutions

$$\frac{1}{r_{n+2}^{(\pm)}} = \frac{1}{n-1}\sum_{A=1}^{n+1}\frac{1}{r_A} \pm \sqrt{\frac{n}{(n-1)^2}\left(\sum_{A=1}^{n+1}\frac{1}{r_A}\right)^2 - \frac{n}{n-1}\sum_{A=1}^{n+1}\left(\frac{1}{r_A}\right)^2}. \tag{3.119}$$

Similarly, we can find the centres of the new spheres. This way, we can add new spheres iteratively if we take always four mutually tangent spheres .

However, this is not the best solution for numerical calculations because of the square root. We obtain a better one if we start with a full set of $n+2$ mutually tangent spheres. If we add the two previous solutions of eq. (3.119), where we now set $r_{n+2} = r_{n+2}^{(+)}$ and $r_{\text{new}} = r_{n+2}^{(-)}$, we get the linear equation

$$\frac{1}{r_{\text{new}}} = -\frac{1}{r_{n+2}} + \frac{2}{n-1}\sum_{A=1}^{n+1}\frac{1}{r_A}. \tag{3.120}$$

This is much better to handle in numerical calculations. The new sphere is tangent to the first $n+1$ spheres. There are similar formulas for the centres of the spheres and for the spherical case. Note that in two and three dimensions all curvatures $\frac{1}{r}$ are integers if we start with integer curvatures.

Using this formula, we are able to iteratively determine new spheres. This algorithm works pretty well in two dimensions but there are also some problems. For this procedure we have to save the position and size of each sphere during the whole computation because there are always new spheres tangent to the first ones. This is not a mathematical problem but a computational one strongly limiting the number of spheres which can be calculated in reasonable time.

But there is an even worse problem if we go to three dimensions. In two dimension we have the advantage that the new circles will always be getting smaller and each circle is only calculated once. Both statements are wrong in three dimensions. However, the fact that size of the new spheres does not always decrease is no problem. In contrast, the fact that most spheres are calculated multiple times is problematic due to computational limitations. Since the number of calculated spheres grows exponentially, it would be worse if we do not remove the duplicates because our storage is limited. But removing these duplicates needs also a lot of computational effort if we do it by comparing the new spheres with the already obtained ones because the comparing time grows quadratically with the number of spheres. Therefore we need a more efficient procedure.

A better way to find new spheres avoiding these problems is obtained by the methods of Lie sphere geometry from the previous section 3.3. For a given set of $n+2$ mutually tangent spheres $\{\boldsymbol{\omega}_A\}$ we can compute new spheres using

$$\boldsymbol{\omega}'_A = -\boldsymbol{\omega}_A + \frac{2}{n-1}\sum_{B\neq A}\boldsymbol{\omega}_B, \tag{3.121}$$

which is a generalisation of eq. (3.120). We have to check if $\boldsymbol{\omega}'_A$ is actually a Lie sphere vector, this means, if $\langle \boldsymbol{\omega}'_A, \boldsymbol{\omega}'_A \rangle = 1$. For this reason we consider at first

$$\begin{aligned}
\langle \boldsymbol{\omega}'_A, \boldsymbol{\omega}_B \rangle &= -\langle \boldsymbol{\omega}_A, \boldsymbol{\omega}_B \rangle + \frac{2}{n-1} \sum_{C \neq A} \langle \boldsymbol{\omega}_C, \boldsymbol{\omega}_B \rangle \\
&= \begin{cases} -1 - \frac{2}{n-1}(n+1) & \text{if } A = B \\ 1 - \frac{2}{n-1}(n-1) & \text{if } A \neq B \end{cases} \\
&= -1 - 2\,\frac{n+1}{n-1}\,\delta_{AB},
\end{aligned} \tag{3.122}$$

where we used that $\langle \boldsymbol{\omega}_A, \boldsymbol{\omega}_B \rangle = \mathcal{G}_{AB} = 2\,\delta_{AB} - 1$. It follows that

$$\langle \boldsymbol{\omega}'_A, \boldsymbol{\omega}'_A \rangle = -\langle \boldsymbol{\omega}'_A, \boldsymbol{\omega}_A \rangle + \frac{2}{n-1} \sum_{B \neq A} \langle \boldsymbol{\omega}'_A, \boldsymbol{\omega}_B \rangle = 1. \tag{3.123}$$

Hence, $\boldsymbol{\omega}'_A$ describes a Lie sphere. Since we have $\langle \boldsymbol{\omega}'_A, \boldsymbol{\omega}_B \rangle = -1$ for $B \neq A$, this sphere is externally tangent to the spheres $\boldsymbol{\omega}_B,\ B \neq A$. Hence, the set $\{\boldsymbol{\omega}'_A, \boldsymbol{\omega}_B : B \neq A\}$ is again a Descartes set.

If we rewrite the mapping eq. (3.121) as

$$\begin{aligned}
\boldsymbol{\omega}'_A &= \boldsymbol{\omega}_A - 2\boldsymbol{\omega}_A + \frac{2}{n-1} \sum_{B \neq A} \boldsymbol{\omega}_B \\
&= \boldsymbol{\omega}_A - 2\frac{1}{n-1} \sum_{B=1}^{n+2} (n\,\delta_{AB} - 1)\,\boldsymbol{\omega}_B \\
&= \boldsymbol{\omega}_A - 2\kappa^2 \sum_{B=1}^{n+2} \mathcal{G}^{-1}_{AB}\,\boldsymbol{\omega}_B \\
&= \boldsymbol{\omega}_A - 2\langle \boldsymbol{\omega}_A, \boldsymbol{\varpi}_A \rangle\, \boldsymbol{\varpi}_A = \boldsymbol{\mathcal{I}}_{\boldsymbol{\varpi}_A} \boldsymbol{\omega}_A,
\end{aligned} \tag{3.124}$$

we find that this is the inversion of $\boldsymbol{\omega}_A$ at its dual sphere $\boldsymbol{\varpi}_A$ leaving the other spheres invariant, $\boldsymbol{\mathcal{I}}_{\boldsymbol{\varpi}_A} \boldsymbol{\omega}_B = \boldsymbol{\omega}_B$.

### Decision Criterion for New Spheres

As mentioned before, in the 3-dimensional case we have the problem that some spheres are calculated multiple times. The reason for this is probably that the dual spheres overlap. In contrast, the dual circles form also a Descartes set in the 2-dimensional case. One way to deal with this problem was given by Borkovec, De Paris and Peikert [BDP94] by defining *target regions*. An inverted sphere will only be accepted if its centre is mapped into the target region. Borkovec, De Paris and Peikert could not prove rigorously that their procedure does not discard too many spheres, but a cross-check with another algorithm indicates that this is not the case. Hence, we adapt their decision criterion.

The area on the hypersphere uncovered by the initial Descartes set is covered by the dual spheres. In the two-dimensional case, each point of this area is contained in only one dual sphere. In contrast, the dual spheres overlap in higher dimensions, as shown above. The idea is that we divide the interior of the dual spheres into target regions such that each interior point is associated to only one dual sphere. In our case, the overlapping region will be separated into two parts by the intersection hyperplane $\boldsymbol{\pi}_{AB}$ of two dual spheres.

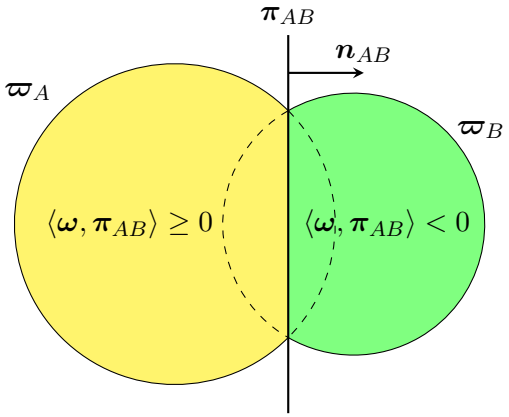


**Figure 3.19:** The separation plane $\boldsymbol{\pi}_{AB}$ divides the overlapping region of the two dual sphere $\boldsymbol{\varpi}_A$ and $\boldsymbol{\varpi}_B$ into two regions which are associated to the dual spheres. The target region of $\boldsymbol{\varpi}_A$ is coloured in yellow. Similarly, the green part is the target region of $\boldsymbol{\varpi}_B$. A new sphere $\boldsymbol{\omega}$ is only accepted if its centre is mapped into the target region which can be decided with the scalar product $\langle \boldsymbol{\omega}, \boldsymbol{\pi}_{AB} \rangle$.

The hyperplane itself is associated to one of the target regions. Using the scalar product $\langle \boldsymbol{\omega}', \boldsymbol{\pi}_{AB} \rangle$, it can easily be tested if an inverted sphere $\boldsymbol{\omega}'$ is mapped into the target region as shown in fig. 3.19.

**Apollonian Lie Sphere Packing Algorithm**

Now we are able to give an algorithm which iteratively generates an Apollonian sphere packing up to the desired accuracy:

(i) Choose an initial Descartes set (zeroth iteration step) and calculate their Lie sphere vectors $\boldsymbol{\omega}_A$.

(ii) Determine the dual spheres $\boldsymbol{\varpi}_A$ in order to obtain the inversion matrices $\boldsymbol{\mathcal{I}}_{\boldsymbol{\varpi}_A}$.

(iii) Compute the separation hyperplanes $\boldsymbol{\pi}_{AB}$ in order to determine the target regions.

(iv) Apply the inversion matrices on the spheres of the last iteration but accept only spheres within the target regions.

(v) Repeat the last step as often as desired.

(vi) Obtain the packing by regaining the original coordinates from the Lie sphere vectors.

This algorithm possesses many advantages against the previously discussed ones: We do not need to save all calculated spheres but only the ones resulting from the last iteration because we need only the Descartes sets from the last step. Previously calculated spheres can be saved somewhere else. Although the number of new spheres grows approximately exponentially, this procedure allows us to get many more spheres than with the method described first using the Descartes theorem. This is also much faster because we do not have to calculate any square roots. In some cases it is even possible to use integers so that we can calculate the exact Lie coordinates of the spheres without any loss in accuracy due to numerical errors. Especially, we have a criterion to decide quickly if a new sphere has already been calculated without comparing it to all previously found spheres.

The construction of the tetrahedron based Apollonian sphere packing, shown in fig. 3.18 and on the cover, is described in appendix A.

**Apollonian Group**

Finally, we want to spend a few words on the mathematical background of Apollonian packings:

If we consider again a Descartes matrix $\boldsymbol{\mathcal{W}}^\top = \{\boldsymbol{\omega}_1^\top, \ldots, \boldsymbol{\omega}_{n+2}^\top\}$ and its image $\boldsymbol{\mathcal{W}'}^\top = \{\boldsymbol{\omega'}_1^\top, \ldots, \boldsymbol{\omega'}_{n+2}^\top\}$, where $\boldsymbol{\omega}'_B$ is given by eq. (3.121) and $\boldsymbol{\omega}'_A = \boldsymbol{\omega}_A$ for $A \neq B$ so that just one Lie sphere is transformed, then these Descartes sets are related by $\boldsymbol{\mathcal{W}}' = \boldsymbol{A}_B \boldsymbol{\mathcal{W}}$ and

$$\boldsymbol{A}_B = \boldsymbol{I}_{n+2} - \frac{2}{n-1} \sum_{C=1}^{n+2} (n\,\delta_{BC} - 1)\, \boldsymbol{e}_B \otimes \boldsymbol{e}_C^\top, \tag{3.125}$$

where $\boldsymbol{I}_{n+2}$ is the $(n+2) \times (n+2)$-identity matrix and $\boldsymbol{e}_A$ are the Cartesian unit vectors. These matrices satisfy $\boldsymbol{A}_B^2 = \boldsymbol{E}$. The group generated by these matrices,

$$\mathcal{A} = \langle \boldsymbol{A}_1, \ldots, \boldsymbol{A}_{n+2} \rangle = \{ \boldsymbol{A}_{B_1} \boldsymbol{A}_{B_2} \cdots \boldsymbol{A}_{B_n} : n \geq 0 \}, \tag{3.126}$$

is the so-called *Apollonian group*, which is a subgroup of the Lorentz group $O(1, n+1)$. In two and three dimensions, the generators $\{\boldsymbol{A}_B\}$ are integer matrices; so in two dimensions we have

$$\begin{aligned} \boldsymbol{A}_1 &= \begin{pmatrix} -1 & 2 & 2 & 2 \\ 0 & 1 & 0 & 0 \\ 0 & 0 & 1 & 0 \\ 0 & 0 & 0 & 1 \end{pmatrix}, \quad \boldsymbol{A}_2 = \begin{pmatrix} 1 & 0 & 0 & 0 \\ 2 & -1 & 2 & 2 \\ 0 & 0 & 1 & 0 \\ 0 & 0 & 0 & 1 \end{pmatrix}, \\ \boldsymbol{A}_3 &= \begin{pmatrix} 1 & 0 & 0 & 0 \\ 0 & 1 & 0 & 0 \\ 2 & 2 & -1 & 2 \\ 0 & 0 & 0 & 1 \end{pmatrix}, \quad \boldsymbol{A}_4 = \begin{pmatrix} 1 & 0 & 0 & 0 \\ 0 & 1 & 0 & 0 \\ 0 & 0 & 1 & 0 \\ 0 & 2 & 2 & -1 \end{pmatrix}, \end{aligned} \tag{3.127}$$

and in three dimensions

$$\begin{aligned} \boldsymbol{A}_1 &= \begin{pmatrix} -1 & 1 & 1 & 1 & 1 \\ 0 & 1 & 0 & 0 & 0 \\ 0 & 0 & 1 & 0 & 0 \\ 0 & 0 & 0 & 1 & 0 \\ 0 & 0 & 0 & 0 & 1 \end{pmatrix}, \quad \boldsymbol{A}_2 = \begin{pmatrix} 1 & 0 & 0 & 0 & 0 \\ 1 & -1 & 1 & 1 & 1 \\ 0 & 0 & 1 & 0 & 0 \\ 0 & 0 & 0 & 1 & 0 \\ 0 & 0 & 0 & 0 & 1 \end{pmatrix}, \quad \boldsymbol{A}_3 = \begin{pmatrix} 1 & 0 & 0 & 0 & 0 \\ 0 & 1 & 0 & 0 & 0 \\ 1 & 1 & -1 & 1 & 1 \\ 0 & 0 & 0 & 1 & 0 \\ 0 & 0 & 0 & 0 & 1 \end{pmatrix}, \\ \boldsymbol{A}_4 &= \begin{pmatrix} 1 & 0 & 0 & 0 & 0 \\ 0 & 1 & 0 & 0 & 0 \\ 0 & 0 & 1 & 0 & 0 \\ 1 & 1 & 1 & -1 & 1 \\ 0 & 0 & 0 & 0 & 1 \end{pmatrix}, \quad \boldsymbol{A}_5 = \begin{pmatrix} 1 & 0 & 0 & 0 & 0 \\ 0 & 1 & 0 & 0 & 0 \\ 0 & 0 & 1 & 0 & 0 \\ 0 & 0 & 0 & 1 & 0 \\ -1 & 1 & 1 & 1 & 1 \end{pmatrix}. \end{aligned} \tag{3.128}$$

Therefore, they form a discrete subgroup of the Lorentz group of infinite order. In higher dimensions the matrix components are rational and the Apollonian group is not discrete.

The Apollonian group acts on sets of Descartes configurations $\boldsymbol{\mathcal{W}}$ from the left. Alternatively, we can use the inversion maps acting from the right on the Descartes matrix $\boldsymbol{\mathcal{W}}$ or equivalently from the left on $\boldsymbol{\mathcal{W}}^\top$. Unlike the Apollonian group elements, the inversions can be viewed as Möbius transformations acting on a single Lie sphere vector whereas the

Apollonian group acts only on Descartes sets. However, the disadvantage of considering inversions is the fact that their representation depends on the Descartes set which we take as the initial set for an Apollonian packing. In contrast, the Apollonian group is defined independently of any Descartes set; that is why they are useful for mathematical considerations. For numerical calculations, we use the inversions rather than the Apollonian matrices $\boldsymbol{A}_B$ in our algorithm because it is more efficient to work with single spheres than with full Descartes sets.

Every orbit of the Apollonian group is a so-called *Apollonian cluster ensemble* consisting of an infinite number of Descartes sets. Since the Apollonian group is discrete only in two and three dimensions, Apollonian cluster ensembles correspond to Apollonian circle and sphere packings only in these dimensions, whereas in higher dimensions the spheres overlap and thus do not correspond to any packing. The residual sets in two and three dimensions, which are the sets of points not contained in the interior of any sphere, have zero measure but they form fractals of Hausdorff dimensions of about 1.3057 in the two-dimensional case [Gra+05] and 2.4739 in the three-dimensional one [BDP94]. The Hausdorff dimension is independent of the starting set. The reason for this is that, given two Descartes sets $\boldsymbol{\mathcal{W}}_1$ and $\boldsymbol{\mathcal{W}}_2$, it is always possible to find a Lorentz transformation $\boldsymbol{L}$ mapping one set to the other because the Lorentz group acts transitively on the space of all Descartes sets. For this reason, one may say that there is only one Apollonian circle/sphere packing up to a Lorentz transformation.

This also shows that there are infinitely many Descartes sets in each dimension if there exists one. One can easily construct a Descartes set in each dimension if we take $n+1$ pairwise tangent $n$-spheres with equal radius and centres on the vertices of a regular $n$-simplex. Using the Generalised Descartes theorem 3.6, this set can be completed to a Descartes set. All other sets can be obtained by a Lorentz transformation.

For detailed discussion of all these statements, further details and extensions, see the articles of Graham et al. [Gra+05] and [Gra+06a] for the two-dimensional case. In a subsequent article [Gra+06b], they discuss the generalisation to higher dimensions. Because of the connection to Lie sphere geometry, all these results generalise directly to the spherical and hyperbolic case, one simply has to use the corresponding Lie sphere representations in table 3.2.

# 4 Cosmological Spacetimes

In this chapter we briefly review the basics of cosmology. In section 4.1 we derive the FLRW metric and the Friedmann equations describing the dynamics of a cosmological spacetime. In the second section 4.2 we solve the Friedmann equations for the three different shapes of dust universes. For more details and further reading, we recommend the book of Weinberg [Wei08].

## 4.1 Friedmann-Lemaître-Robertson-Walker Spacetimes

In the standard model of cosmology, the FLRW metric, named after Friedman [Fri22; Fri24], Lemaître [Lem27], Robertson [Rob35; Rob36a; Rob36b] and Walker [Wal37], is used to describe the large-scale behaviour of the Universe[1]. The FLRW metric is the solution to Einstein's field equations implementing the cosmological principle on which the standard model of cosmology is based.

### Cosmological Principle and FLRW Metric

As discussed in the introduction 1, observations show that our Universe appears to be homogeneous and isotropic at the largest scales. High evidence for isotropy is given by the cosmic microwave background radiation showing a uniform radiation in the microwave band from all directions. Homogeneity is based on the assumption that we are at no special point in the Universe so that one observes the isotropic CMB everywhere. This assumption is supported by number counting of galaxies. However, the Universe is homogeneous and isotropic only in space because the distance between galaxies grows in time on sufficiently large scales; see fig. 4.1.

These properties are referred to as the *cosmological principle*: The Universe is homogeneous and isotropic at the largest scales for cosmic observers. Physically, this means that there exists a preferred normalized, time-like vector field $\boldsymbol{u}$, associated to the *cosmic observers* moving along the flow of $\boldsymbol{u}$, and the space of each observer is isotropic.

Mathematically, this can be stated as follows [Str74]: The group of local isometries $\mathrm{Iso}_p(\mathcal{M})$ of the spacetime $\mathcal{M}$ fixing the point $p \in \mathcal{M}$ and the vector $\boldsymbol{u}_p \in \mathrm{T}_p\mathcal{M}$ contains as a subgroup the group of orthogonal transformations $SO(3)(\boldsymbol{u}_p)$ in $\mathrm{T}_p\mathcal{M}$ on the orthogonal complement of $\boldsymbol{u}_p$ leaving $\boldsymbol{u}_p$ invariant. Hence, the following condition is satisfied

$$\{\mathrm{T}_p\phi : \phi \in \mathrm{Iso}_p(\mathcal{M}), \phi_*\boldsymbol{u} = \boldsymbol{u}\} \supseteq SO(3)(\boldsymbol{u}_p) \tag{4.1}$$

at every point $p$. This condition implies:

(i) The vector field $\boldsymbol{u}$ is hypersurface-orthogonal, that is, the spacetime can be foliated such that $\boldsymbol{n} = \boldsymbol{u} \propto \boldsymbol{\partial}_t$.

[1] Recall that the term 'Universe' always refers to our Universe, whereas 'universe' refers to a general solution of the Friedmann equations.

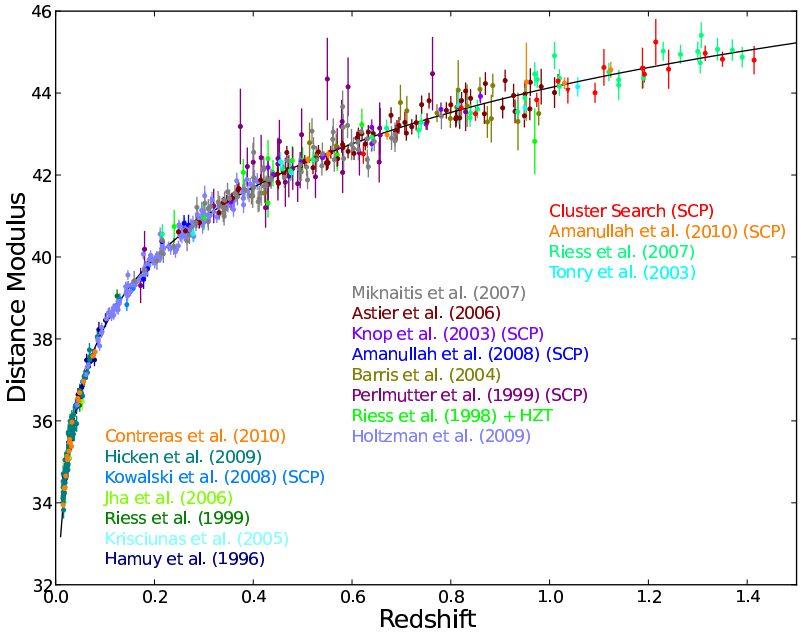


Credit [7]: ©AAS. Reproduced with permission.

**Figure 4.1:** 'Hubble diagram for the Union2.1 compilation. The solid line represents the best-fit cosmology for a flat ΛCDM universe for supernovae alone.' [Suz+12]

(ii) The integral curves of $\boldsymbol{u}$ are geodesics and $t$ is the proper time of the cosmic observers, hence $\boldsymbol{u} = \boldsymbol{\partial}_t$.

(iii) The slices of constant time $t$ are maximally symmetric spaces.

(iv) In comoving coordinates, the spatial metrics of the slices are equal up to a scaling factor depending on $t$.

Note that isotropy for each observers implies homogeneity of the spatial slices.

As we know from section 3.1, there are three families of maximally symmetric spaces, characterised by their curvature constant $k$: First, there is the flat space with vanishing curvature $k \equiv 0$. Second, we have the family of spherical spaces with positive curvature constant $k > 0$. Third, there is the family of hyperbolic spaces with negative curvature $k < 0$. By an appropriate choice of coordinates, the curvature constant can always be rescaled such that we can restrict ourselves to the cases $k \in \{0, \pm 1\}$.

The metric of maximally symmetric spaces has the form (3.10)

$$\boldsymbol{h}_k = \mathbf{d}\chi^2 + \Sigma_k^2(\chi)\, \mathbf{d}\Omega^2, \tag{4.2}$$

where

$$\Sigma_k(\chi) = \begin{cases} \sin\chi & k = +1 \quad \text{spherical}, \\ \chi & k = \phantom{+}0 \quad \text{flat}, \\ \sinh\chi & k = -1 \quad \text{hyperbolic}. \end{cases} \tag{4.3}$$

From eq. (3.5), we obtain that the Ricci tensor of a such a space in $d = 3$ dimensions is given by

$$\boldsymbol{R}[h_k] = 2k\, \boldsymbol{h}_k, \tag{4.4a}$$

and the Ricci scalar by

$$\mathcal{R}[h_k] = 6k. \tag{4.4b}$$

Then, the conditions (iii) and (iv) imply, that the spatial metric must be

$$\bar{\boldsymbol{g}} = a^2(t)\, \boldsymbol{h}_k(x), \tag{4.5}$$

where the function $a(t)$ is called *scale factor* of the universe. The scale factor depends only on time because of the cosmological principle, whereas $\boldsymbol{h}_k$ is the time-independent metric (4.2) of a maximally symmetric space.

Due to the first two conditions (i) and (ii), it follows that $\alpha = 1$ and $\boldsymbol{\beta} = 0$. Hence, the spacetime metric of a FLRW universe takes the form

$$\boldsymbol{g} = -\,\mathbf{d}t^2 + a^2(t)\left(\mathbf{d}\chi^2 + \Sigma_k^2(\chi)\,\mathbf{d}\Omega^2\right). \tag{4.6}$$

Note that the spacetime metric is determined almost completely by the cosmological principle up to the scale factor $a(t)$. This latter is determined by Einstein's equation, which we will discuss below.

### Cosmic fluid

So far, we did not say anything about the origin of the preferred vector field $\boldsymbol{u}$. It is assumed that matter[2] moves in average along the flow of this vector field. Hence, a cosmic observer is comoving with the cosmic matter.

Since the matter distributions in the Universe appears to be uniform at the largest scales, they are modelled as ideal fluids in analogy to continuum mechanics. The energy-momentum tensor of an ideal fluid is given by eq. (2.6). The cosmological principle implies that the density $\rho$ and the pressure $p$ of the cosmic fluid can only depend on the time of the cosmic observers. Hence, the energy-momentum tensor is

$$T_{\mu\nu} = (\rho(t) + p(t))\, u_\mu u_\nu + p(t)\, g_{\mu\nu}. \tag{4.7}$$

We describe the different kinds of matter by their equations of state which are also needed to solve the equations of motion. In cosmology, the equations of state take the simple form

$$p(t) = w\,\rho(t) = (\gamma - 1)\,\rho(t). \tag{4.8}$$

Common matter and dark matter are described as a non-interacting fluid, that is, as matter without pressure, hence $w = 0$ or $\gamma = 1$. Special-relativistic considerations show that a photon gas satisfies $p = \frac{1}{3}\rho$, hence $w = \frac{1}{3}$ or $\gamma = \frac{4}{3}$.

If we regard the cosmological constant term $\Lambda g_{\mu\nu}$, usually written at the left-hand side of Einstein's equations, as an energy-momentum tensor written on the right-hand side, the comparison with the ideal fluid eq. (4.7) shows that $p = -\rho = -\frac{\Lambda}{8\pi}$, hence $w = -1$ or $\gamma = 0$, respectively. This kind of matter is also referred to as *dark energy*, whose origin is unknown. See table 4.1 for a summary of the different kinds of matter.

[2] The term 'matter' refers to everything described by the energy-momentum tensor. This includes common matter, but also dark matter, radiation and the cosmological constant, also referred to as *dark energy*. Common and dark matter are usually referred to as dust.

**Table 4.1:** Parameters for different kinds of matter

| kind of matter | $w$ | $\gamma$ |
|---|---|---|
| dust | 0 | 1 |
| radiation | $^1/_3$ | $^4/_3$ |
| classical ideal gas | $^2/_3$ | $^5/_3$ |
| stiff matter | 1 | 2 |
| cosmological constant | $-1$ | 0 |

### Friedmann Equations

Next, we determine the equations of motion using the methods of the 3+1 formalism described in chapter 2. As discussed above, in coordinates adapted to the symmetry, the spatial metric must be

$$\bar{\boldsymbol{g}} = a^2(t)\, \boldsymbol{h}_k(x). \tag{4.9}$$

For the extrinsic curvature, we make the ansatz that it has only a time-dependent trace component, such that

$$\bar{\boldsymbol{K}} = \frac{1}{3}\, \mathcal{K}(t)\, \bar{\boldsymbol{g}} \equiv -H(t)\, \bar{\boldsymbol{g}}, \tag{4.10}$$

where $H(t) \equiv -\frac{1}{3}\mathcal{K}(t)$ is the so-called *Hubble parameter*, following the standard notation in cosmology. Furthermore, we have $\alpha = 1$ and $\boldsymbol{\beta} = 0$.

Before we start exploring the constraint and evolution equations, we do some preliminary calculations: Since the scale factor $a(t)$ depends only on time, the conformal decomposition of the Ricci tensor $\boldsymbol{R}[\bar{g}]$ eq. (2.97) reduces to $\boldsymbol{R}[\bar{g}] = \boldsymbol{R}[h_k]$, yielding

$$\boldsymbol{R}[\bar{g}] = \boldsymbol{R}[h_k] = 2k\, \boldsymbol{h} = \frac{2k}{a^2(t)}\, \bar{\boldsymbol{g}}, \tag{4.11a}$$

$$\mathcal{R}[\bar{g}] = \frac{6k}{a^2(t)}, \tag{4.11b}$$

where we used eq. (4.4). Furthermore, we obtain for the extrinsic curvature

$$\mathcal{K} = -3H(t), \tag{4.12a}$$

$$\bar{K}_{ac}\bar{K}^c{}_b = H^2(t)\, \bar{g}_{ab}, \tag{4.12b}$$

$$\bar{K}_{ab}\bar{K}^{ab} = 3H^2(t). \tag{4.12c}$$

Last, the decomposition of the energy-momentum tensor yields

$$E = \rho(t), \tag{4.13a}$$

$$S_{ab} = p(t)\, \bar{g}_{ab}, \tag{4.13b}$$

$$\mathcal{S} = 3p(t). \tag{4.13c}$$

Now we can insert these results into the constraints (2.84) and evolution equations (2.85). From the Hamiltonian constraint we get

$$16\pi\rho = \mathcal{R} + \mathcal{K}^2 - \bar{K}_{ab}\bar{K}^{ab} = 6\, \frac{k}{a^2} + 6\, H^2, \tag{4.14}$$

or after some rearrangements

$$H^2(t) = \frac{8\pi}{3}\,\rho(t) - \frac{k}{a^2(t)}. \tag{4.15}$$

This is the *first Friedmann equation*. Since the scale factor only depends on time and the metric $\bar{\boldsymbol{g}}$ is covariantly constant, the momentum constraint vanishes identically.

Note that we easily obtain the first Friedmann equation (4.15) if we use the Lichnerowicz equation (2.111), where the conformal factor is given by $\Psi^2 = a(t)$, taking into account that the trace-free part of the extrinsic curvature vanishes, $\boldsymbol{A} \equiv 0$.

The evolution equation for the metric is given by

$$\partial_t \bar{\boldsymbol{g}} = -2\,\bar{\boldsymbol{K}} = -2H(t)\,\bar{\boldsymbol{g}}. \tag{4.16}$$

We can also compute the time derivative of the metric directly from eq. (4.9), yielding

$$\partial_t \bar{\boldsymbol{g}} = -2\dot{a}(t)a(t)\,\boldsymbol{h}_k(x) = -2\,\frac{\dot{a}(t)}{a(t)}\,\bar{\boldsymbol{g}}. \tag{4.17}$$

If we compare both equations, we get the relation

$$H(t) = \frac{\dot{a}(t)}{a(t)}. \tag{4.18}$$

This is usually the definition of the Hubble parameter in cosmology.

Finally, we derive an evolution equation for the Hubble parameter which we obtain from the equation of motion of the extrinsic curvature

$$\begin{aligned}
\partial_t \bar{K}_{ab} &= R_{ab} + \mathcal{K}\,\bar{K}_{ab} - 2\bar{K}_{ac}\bar{K}^{c}{}_{b} + 4\pi(p-\rho)\,g_{ab} \\
&= \left(\frac{2k}{a^2} + H^2 + 4\pi(p-\rho)\right) g_{ab} \\
&= \left(-H^2 + \frac{4\pi}{3}(\rho + 3p)\right) g_{ab}.
\end{aligned} \tag{4.19}$$

In the last line we used the first Friedmann equation (4.15) in order to eliminate the curvature term $\frac{2k}{a^2}$. The direct computation of the time derivative of the extrinsic curvature yields

$$\partial_t \bar{\boldsymbol{K}} = -\dot{H}\,\bar{\boldsymbol{g}} - H\,\partial_t \bar{\boldsymbol{g}} = \left(-\dot{H} - 2\,H^2\right)\bar{\boldsymbol{g}}. \tag{4.20}$$

If we combine these results, we obtain the *second Friedmann equation*

$$\dot{H}(t) + H^2(t) = -\frac{4\pi}{3}\left(\rho(t) + 3p(t)\right). \tag{4.21}$$

We can bring the Friedmann equations into their well-known form if we use the evolution equation for $\dot{a}$ (4.18) in order to substitute the Hubble parameter $H$. Using $\dot{H} + H^2 = \frac{\ddot{a}}{a}$, we get

$$\left(\frac{\dot{a}(t)}{a(t)}\right)^2 = \frac{8\pi}{3}\,\rho(t) - \frac{k}{a^2(t)}, \tag{4.22a}$$

$$\frac{\ddot{a}(t)}{a(t)} = -\frac{4\pi}{3}\left(\rho(t) + 3p(t)\right). \tag{4.22b}$$

**Conservation Law**

At last we consider the conservation laws (2.86). While it can easily be verified that the momentum conservation is identically satisfied, the energy conservation yields

$$0 = \dot{E} - \mathcal{K}\, E - \bar{K}_{ab} S^{ab} = \dot{\rho} + 3H(\rho + p). \tag{4.23}$$

Since the energy-momentum conservation laws are a consequence of Einstein's equations due to the Bianchi identities, eq. (4.23) is not an independent equation but it can also be derived from the Friedmann equations. However, it can be used to replace one of the Friedmann equations so that the equations of motion may be simpler to solve.

We can use the equation of state (4.8) in order to eliminate the pressure $p$ in the conservation law and substitute eq. (4.18). We obtain

$$\frac{\dot{\rho}}{\rho} = -3\gamma\, \frac{\dot{a}}{a}, \tag{4.24}$$

which can be integrated to

$$\rho(t) = \frac{C}{a^{3\gamma}(t)}, \tag{4.25}$$

where $C$ is some integration constant. This also shows that the combination $\rho(t)a^{3\gamma}(t)$ does not depend on time.

## 4.2 Dust Universes

In particular, we are interested in Friedmann universes containing only common matter and no radiation, dark matter or dark energy. Common matter is modelled as an only gravitationally interacting fluid, that is, as an fluid without pressure, $p \equiv 0$, such that $\gamma = 1$. In this case the density function (4.25) yields

$$\rho(t) = \frac{C}{a^3(t)}. \tag{4.26}$$

Inserting this into the first Friedmann equation (4.22a), we obtain the differential equation

$$\frac{\dot{a}^2}{a^2} = \frac{8\pi C}{3a^3} - \frac{k}{a^2} \tag{4.27}$$

for the scale factor $a(t)$.

It is convenient to use a new time coordinate $\eta$, the so-called *conformal time*, defined by

$$\frac{\mathrm{d}\eta}{\mathrm{d}t} = \frac{1}{a(t)}, \tag{4.28}$$

or the other way round[3] $t'(\eta) = a(\eta)$ and we set $t = 0$ if $\eta = 0$. In this case, the metric is given by

$$\boldsymbol{g} = a^2(\eta)\left(-\mathbf{d}\eta^2 + \boldsymbol{h}_k\right). \tag{4.29}$$

[3] A dot denotes the derivation with respect to the cosmological time $t$: $\dot{a} = \frac{\mathrm{d}a}{\mathrm{d}t}$; whereas a prime means the derivative with respect to the conformal time $\eta$: $a' = \frac{\mathrm{d}a}{\mathrm{d}\eta}$. Furthermore, we use the same symbol for $a(t)$ and $a(\eta) \equiv a(t(\eta))$, but this should not lead to confusion.

Hence, the lapse function equals the scale factor, $\alpha = a(\eta)$.

Using that $\dot{a} = \frac{a'}{a}$, we can rewrite the differential equation (4.27) to

$$a'^2 + ka^2 = \mathcal{C}a, \tag{4.30}$$

where $\mathcal{C} = \frac{8\pi C}{3}$. We choose $a(\eta = 0) = 0$ as the initial condition for the scale factor so that the universe starts as a point with a *big bang*.

**Flat case**

In the flat case where $k = 0$, we make the power-law ansatz $a(\eta) = \kappa\,\eta^\lambda$. Inserting this into eq. (4.30), we obtain

$$\kappa^2\lambda^2\eta^{2\lambda-2} = \mathcal{C}\kappa\eta^\lambda. \tag{4.31}$$

Both sides match if $\lambda = 2$ and $\kappa = \frac{\mathcal{C}}{4}$. The cosmological time is obtained from $t' = a$. Hence, the solution of Friedmann equations is given by

$$a(\eta) = \frac{\mathcal{C}}{4}\eta^2, \tag{4.32a}$$

$$t(\eta) = \frac{\mathcal{C}}{12}\eta^3. \tag{4.32b}$$

The second equation can be solved for $\eta$ such that $\eta = \sqrt[3]{\frac{12}{\mathcal{C}}t}$, hence

$$a(t) = \frac{\mathcal{C}}{4}\left(\frac{12}{\mathcal{C}}\right)^{\frac{2}{3}} t^{\frac{2}{3}} = \left(\frac{3}{2}\sqrt{\mathcal{C}}t\right)^{\frac{2}{3}}. \tag{4.33}$$

The scale factor is plotted in fig. 4.2.

**Spherical case**

We have $k = 1$ in the spherical case. Using the ansatz $a(\eta) = \kappa\,(1 - \cos\eta)$, we obtain from eq. (4.30)

$$\kappa^2\sin^2\eta + \kappa^2\,(1-\cos\eta)^2 = 2\kappa^2\,(1-\cos\eta) = \mathcal{C}\kappa\,(1-\cos\eta)\,, \tag{4.34}$$

yielding $\kappa = \frac{\mathcal{C}}{2}$. Hence, the solution is given by

$$a(\eta) = \frac{\mathcal{C}}{2}\,(1-\cos\eta)\,, \tag{4.35a}$$

$$t(\eta) = \frac{\mathcal{C}}{2}\,(\eta - \sin\eta)\,, \tag{4.35b}$$

where $\eta \in [0, 2\pi]$. The time evolution of the scale factor is described by a cycloid as shown in fig. 4.2.

The finite time range is due to the fact that the universe has recollapsed to a point at $\eta = 2\pi$; we say that the universe ends with a *big crunch*. The maximum of the expansion is reached at $\eta = \pi$. Because of $a(\pi) = \mathcal{C}$, the constant $\mathcal{C}$ is the maximal 'radius' $a_0$ of the spherical universe, $\mathcal{C} = a_0$.

In order to describe a spherical universe, we often use the total mass $M = \rho V = 2\pi^2\rho(t)a^3(t)$. The total mass is finite because the volume $V = 2\pi^2 a(t)^3$ of each slice is finite. Because of eq. (4.25), $M$ is also constant in time. Substituting the constant $\mathcal{C}$, we get

$$M = 2\pi^2\,C = 2\pi^2\,\frac{3\mathcal{C}}{8\pi} = \frac{3}{4\pi}\,a_0. \tag{4.36}$$

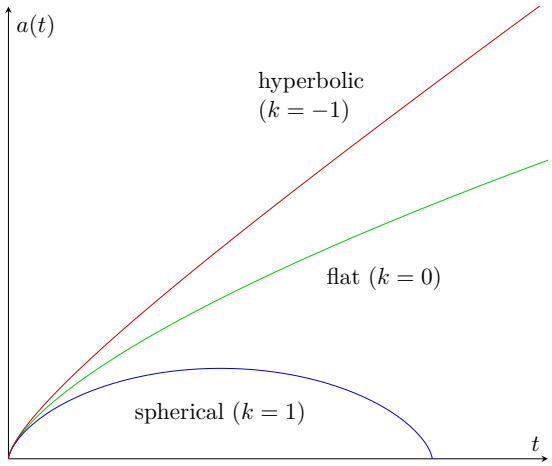


**Figure 4.2:** Time evolution of the scale factor of dust universes: The flat and hyperbolic universe are always expanding after the big bang. In contrast, the spherical Friedmann universe reaches a maximum, then recollapses and finally ends in a big crunch.

### Hyperbolic case

Finally, we consider the hyperbolic case with $k = -1$. We use an ansatz similar to the spherical case, namely $a(\eta) = \kappa\,(\cosh\eta - 1)$. Then eq. (4.30) yields

$$\kappa^2 \sinh^2\eta - \kappa^2\,(\cosh\eta - 1)^2 = 2\kappa^2\,(\cosh\eta - 1) = \mathcal{C}\kappa\,(\cosh\eta - 1)\,. \tag{4.37}$$

This shows that $\kappa = \frac{\mathcal{C}}{2}$ and we obtain

$$a(\eta) = \frac{\mathcal{C}}{2}\,(\cosh\eta - 1)\,, \tag{4.38a}$$

$$t(\eta) = \frac{\mathcal{C}}{2}\,(\sinh\eta - \eta)\,. \tag{4.38b}$$

The time evolution is also shown in fig. 4.2.

# 5 Lindquist-Wheeler Models

In this chapter we present a generalisation of the Lindquist-Wheeler approach to inhomogeneous cosmological models. The basic idea of Lindquist and Wheeler was to construct an approximation for a spherical universe by using overlapping Schwarzschild spacetimes with regularly distributed black holes. This construction is very similar to the Swiss-cheese models by Einstein and Straus, presented in the first section 5.1, bu we need not assume the existence of a Friedmann universe. The construction of the Lindquist-Wheeler model is described in section 5.2 where we also provide a generalisation of the construction to arbitrary black hole configurations.

## 5.1 Swiss-cheese Models

One simple example for an inhomogeneous cosmological model is the so-called *Swiss-cheese model*, described by Einstein and Straus [ES45] and worked out further by Schücking [Sch54]. The basic idea is very simple: We take a Friedmann dust universe, cut out a ball of dust and embed a Schwarzschild spacetime into this hole. At the boundary between the dust universe and the Schwarzschild spacetime, we have to satisfy the *Israel junction conditions* [Isr66][1] if the boundary is not light-like. Then the resulting joined spacetime is a solution to Einstein's equations. However, the metric is not smooth at the boundary but only continuously differentiable.

### Junction Conditions

Consider two spacetimes $\mathcal{M}_\pm$ with metrics $\boldsymbol{g}_\pm$ and non-null boundary hypersurfaces $\Sigma_\pm$. We need a diffeomorphism $\phi : \Sigma_+ \mapsto \Sigma_-$ identifying points on the boundaries. Furthermore, we choose basis vector fields $\{\boldsymbol{n}^\pm, \boldsymbol{e}^\pm{}_\alpha\}$ and their duals $\{\boldsymbol{n}^\flat_\pm, \boldsymbol{\theta}_\pm{}^\alpha\}$ adapted to the boundary, such that $\boldsymbol{e}^\pm{}_\alpha|_{\Sigma_\pm} \in \Gamma T\Sigma_\pm$, $\boldsymbol{n}^+$ is the outward-pointing normal to $\Sigma_+$, and $\boldsymbol{n}^-$ is the inward-pointing normal to $\Sigma_-$. It follows that the induced metrics $\bar{\boldsymbol{g}}_\pm$ of $\Sigma_k\pm$ are given by

$$\bar{\boldsymbol{g}} = g_{\alpha\beta}\, \boldsymbol{\theta}^\alpha \otimes \boldsymbol{\theta}^\beta, \tag{5.1}$$

omitting the $\pm$-label. Similar to the 3+1 decomposition, we can define the extrinsic curvature of the boundary surface by

$$\bar{\boldsymbol{K}}(\boldsymbol{x}, \boldsymbol{y}) = -\epsilon\, \boldsymbol{g}(\nabla_{\boldsymbol{x}} \boldsymbol{n}, \boldsymbol{y}) = \epsilon\, \boldsymbol{g}(\boldsymbol{n}, \nabla_{\boldsymbol{x}} \boldsymbol{y}), \tag{5.2}$$

where the sign depends on whether the hypersurface is time-like or space-like, indicated by the normal $\epsilon = \boldsymbol{g}(\boldsymbol{n}, \boldsymbol{n})$. In the case of a space-like hypersurface as in the 3+1 formalulation such that $\epsilon = 1$, the extrinsic curvature is defined just as in eq. (2.57).

Not every gluing of boundary surfaces is a solution to Einstein's equations. This is the case only if the Israel Junction Conditions are satisfied:

[1] For a modern version see the textbook of Poisson [Poi04] which also describes the light-like case.

**Theorem 5.1.** ***Israel Junction Conditions***
*The joined spacetime is a regular solution to Einstein's equation, that is, the Riemann curvature tensor is continuous across the boundary, if the induced metrics and the extrinsic curvatures of the boundaries are equal, that is*

$$\bar{\boldsymbol{g}}_1 = \phi^* \bar{\boldsymbol{g}}_2, \tag{5.3a}$$
$$\bar{\boldsymbol{K}}_1 = \phi^* \bar{\boldsymbol{K}}_2. \tag{5.3b}$$

The first junction condition (5.3a) guarantees that the geometry is well-defined across the boundary. The second condition ensures the regularity of the curvature tensor. However, the equality of the extrinsic curvature is not always demanded. In this case, a non-vanishing energy-momentum tensor on the boundary surface, involving the delta-distribution, is needed; one speaks of a *singular shell*.

Light-like hypersurfaces have to be treated separately because the normal is tangent to the hypersurface in this case. For this reason, the extrinsic curvature always vanishes and gives no information about the metric derivatives. In this case, one defines the so-called *transverse curvature*, involving another light-like vector, in order to formulate the junction conditions [BI91].

In general, we need the map $\phi$ between the two boundary surfaces in order to compare two tensors in different spacetimes with their own coordinate systems. However, in the case of spherically symmetric spacetimes, there are geometrically preferred orthonormal basis vector fields $\{\boldsymbol{e}_\mu\}$ and their duals $\{\boldsymbol{\theta}^\mu\}$ adapted to the boundary surface simplifying the problem.

Suppose that the boundary surface is time-like, that is $\epsilon = -1$, and given by the function $f(t, r) = R(t) - r = 0$. We can construct an orthonormal basis as follows: First, we have the space-like vector field $\boldsymbol{e}_1 = \boldsymbol{n}$ normal to the hypersurface. Its dual 1-form field is given by $\boldsymbol{\theta}^1 = \boldsymbol{n}^\flat \propto \mathbf{d}f$. Second, there are two space-like orthonormal vectors $\boldsymbol{e}_2$ and $\boldsymbol{e}_3$ tangent to the $SO(3)$-orbits of spherical symmetry within a constant-time slice. Because of the symmetry, it does not matter which ones we take. Third, the basis is completed with the time-like vector $\boldsymbol{e}_0 = \boldsymbol{u}$ within the hypersurface orthogonal to the orbits. Then the metric can be written as

$$\boldsymbol{g} = \eta_{\mu\nu}\, \boldsymbol{\theta}^\mu \otimes \boldsymbol{\theta}^\nu = -\boldsymbol{u}^\flat \otimes \boldsymbol{u}^\flat + \boldsymbol{n}^\flat \otimes \boldsymbol{n}^\flat + R^2\, \mathbf{d}\Omega^2, \tag{5.4}$$

where $\mathbf{d}\Omega^2 = \boldsymbol{\theta}^2 \otimes \boldsymbol{\theta}^2 + \boldsymbol{\theta}^3 \otimes \boldsymbol{\theta}^3 = \mathbf{d}\vartheta^2 + \sin^2\vartheta\, \mathbf{d}\varphi^2$ in standard spherical coordinates $\vartheta, \varphi$. This is illustrated in fig. 5.1a using the example of a Swiss-cheese model.

The flow of the vector field $\boldsymbol{u}$ generates the boundary hypersurface. Observers moving along these curves $\gamma$, such that $\dot{\boldsymbol{\gamma}} = \boldsymbol{u}$, are called *matching observers*. Adapted to the symmetry, there is the following reformulation of the Israel junction conditions:

**Theorem 5.2.** ***Spherically Symmetric Junction Conditions*** *[CG10]*
*The equality of the induced metrics and extrinsic curvatures imply the equality of*

*(i) the arc length of $\gamma$, that is the proper time $\tau$ of the matching observer,*

*(ii) the extrinsic curvature $\boldsymbol{g}(\boldsymbol{n}, \nabla_{\boldsymbol{u}}\boldsymbol{u})$ of $\gamma$,*

*(iii) the areal radius $R|_\gamma$ of the boundary spheres,*

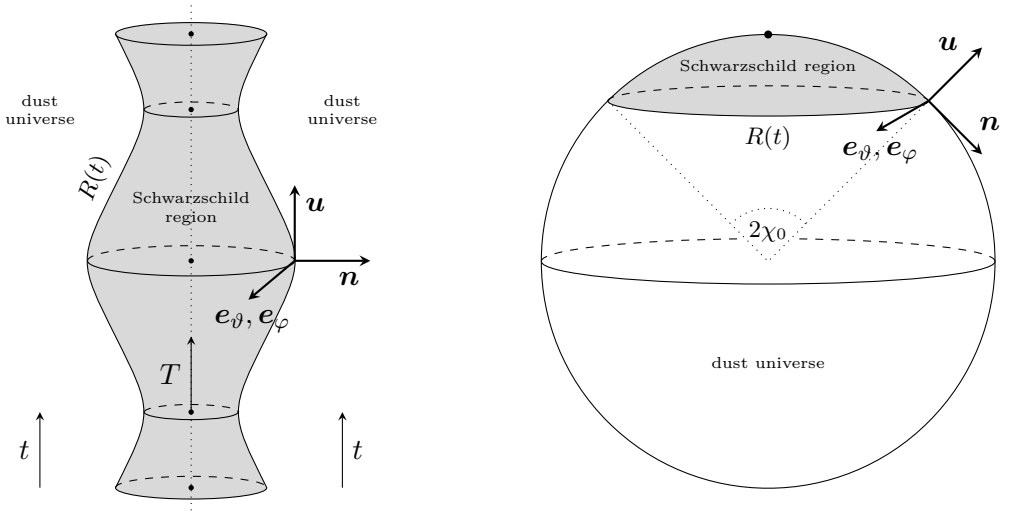


**(a)** Boundary moving in time **(b)** Constant time slice

**Figure 5.1:** Gluing a Schwarzschild spacetime to a dust universe: The left figure shows a boundary sphere moving in time. The inner tube is the Schwarzschild spacetime with a black hole in its centre. This region is surrounded by a dust universe. The matching observers, whose velocity vector is $\boldsymbol{u}$, move along this hypersurface. The right figure shows a spatial slice at some moment of time for a spherical dust universe. On the top, some region is replaced by a Schwarzschild spacetime. Note that a more appropriate representation of the Schwarzschild spacetime would be the isometric embedding fig. 6.1 rather than a spherical cap.

*(iv) Misner-Sharp energy* $M|_\gamma = \frac{R}{2}\left(1 - \boldsymbol{g}^{-1}(\mathbf{d}R, \mathbf{d}R)\right)\Big|_\gamma$.

The proof goes as follows: In the adapted basis the induced metrics take the form

$$\bar{\boldsymbol{g}}_\pm = -\boldsymbol{u}_\pm^\flat \otimes \boldsymbol{u}_\pm^\flat + R_\pm^2\, \mathbf{d}\Omega^2. \tag{5.5}$$

Comparing the coefficients, condition (i) states that $\bar{\boldsymbol{g}}_+(\boldsymbol{u}_+, \boldsymbol{u}_+) = \bar{\boldsymbol{g}}_-(\boldsymbol{u}_-, \boldsymbol{u}_-)$ and condition (iii) is simply $R_+ = R_-$.

Similarly, we have for the extrinsic curvature

$$\bar{\boldsymbol{K}}_\pm = K^\pm{}_{00}\, \boldsymbol{u}_\pm^\flat \otimes \boldsymbol{u}_\pm^\flat + R_\pm\, \mathbf{d}R_\pm(\boldsymbol{n})\, \mathbf{d}\Omega^2. \tag{5.6}$$

Condition (ii) follows from $K_{00} = \boldsymbol{K}(\boldsymbol{u}, \boldsymbol{u}) = -\boldsymbol{g}(\boldsymbol{n}, \nabla_{\boldsymbol{u}}\boldsymbol{u})$, whereas condition (iv) implies the continuity of the normal derivative of the radial coordinate $\mathbf{d}R_+(\boldsymbol{n}) = \mathbf{d}R_-(\boldsymbol{n})$. Since $R$ is continuous along $\gamma$, this is also true for the tangent derivative $\mathbf{d}R(\boldsymbol{u})$. Hence, it follows the equality of the Misner-Sharp energy

$$M = \frac{R}{2}\left(1 - \boldsymbol{g}^{-1}(\mathbf{d}R, \mathbf{d}R)\right) = \frac{R}{2}\left(1 - (\mathbf{d}R(\boldsymbol{u}))^2 + (\mathbf{d}R(\boldsymbol{n}))^2\right). \tag{5.7}$$

**Gluing of Schwarzschild Space-times and a Friedmann Dust Universe**

Let us now consider the case of a Schwarzschild spacetime glued to a Friedmann dust universe. This is illustrated in fig. 5.1. The Schwarzschild spacetime with a central black hole of mass $m$ is described by the metric

$$\boldsymbol{g}_\mathrm{S} = -V(r)\, \mathbf{d}T^2 + V^{-1}(r)\, \mathbf{d}r^2 + r^2\, \mathbf{d}\Omega^2, \tag{5.8}$$

where $V(r) = 1 - \frac{2m}{r}$. The Schwarzschild spacetime will be discussed in more detail in section 6.1. The metric of a Friedmann dust universe is given by (4.6)

$$\boldsymbol{g}_{\mathrm{D}} = -\,\mathbf{d}t^2 + a^2(t)\,\mathbf{d}\chi^2 + a^2(t)\Sigma_k^2(\chi)\,\mathbf{d}\Omega^2. \tag{5.9}$$

We consider matching observers at rest on the boundary surface in both spacetimes, that is, their angular coordinates do not change. Hence, we will identify their angular coordinates. Note that, in general, it need not be possible to match observers at rest on both boundary hypersurfaces. Irrespective thereof, the matching observers still move in space if the boundary hypersurface does.

The curves of the matching observers in both spacetimes are given by

$$\gamma_{\mathrm{D}} = (t(\tau), \chi(\tau), \vartheta_0, \varphi_0)\,, \tag{5.10a}$$
$$\gamma_{\mathrm{S}} = (T(\tau), r(\tau), \vartheta_0, \varphi_0)\,, \tag{5.10b}$$

where $\tau$ is the proper time of the observers which is the same for both curves because of condition (i). The tangent vectors are given by

$$\boldsymbol{u}_{\mathrm{D}} = \boldsymbol{\partial}_\tau = \dot{t}\,\boldsymbol{\partial}_t + \dot{\chi}\,\boldsymbol{\partial}_\chi, \tag{5.11a}$$
$$\boldsymbol{u}_{\mathrm{S}} = \boldsymbol{\partial}_\tau = \dot{T}\,\boldsymbol{\partial}_T + \dot{r}\,\boldsymbol{\partial}_r, \tag{5.11b}$$

where the dot indicates a derivation with respect to proper time[2], for example $\dot{r} = \frac{\mathrm{d}r}{\mathrm{d}\tau}$. Note that $\|\boldsymbol{u}_{\mathrm{D}}\| = 1 = \|\boldsymbol{u}_{\mathrm{D}}\|$ .

The areal radius in the dust universe is $R_{\mathrm{D}} = a(t)\sin\chi$ and the one of the Schwarzschild spacetime is simply $R_{\mathrm{S}} = r$. For this reason the condition (iii) yields

$$r(\tau) = a(t(\tau))\,\Sigma_k(\chi(\tau)). \tag{5.12}$$

Next we determine the Misner-Sharp energies in both spacetimes. For the dust universe we have

$$\mathbf{d}R_{\mathrm{D}} = \dot{a}\Sigma_k\,\mathbf{d}t + a\Sigma_k'\,\mathbf{d}\chi. \tag{5.13}$$

Hence, the Misner-Sharp energy at an arbitrary point in the spacetime is

$$M_{\mathrm{D}} = \frac{a\Sigma_k}{2}\left(1 + \dot{a}^2\Sigma_k^2 - (\Sigma_k')^2\right) = \frac{a}{2}\left(\dot{a}^2 + k\right)\Sigma_k^3 = \frac{4\pi}{3}\rho a^3\,\Sigma_k^3, \tag{5.14}$$

where we used the identity

$$1 - (\Sigma_k')^2(\chi) = \left\{\begin{array}{l} 1 - \cos^2\chi \\ 1 - 1 \\ 1 - \cosh^2\chi \end{array}\right\} = \left\{\begin{array}{l} \sin^2\chi \\ 0 \\ \sinh^2\chi \end{array}\right\} = k\,\Sigma_k^2(\chi), \tag{5.15}$$

in the second step and the first Friedmann equation (4.22a) in the last step.

In the Schwarzschild spacetime, we simply have $\mathbf{d}R_{\mathrm{S}} = \mathbf{d}r$, hence

$$M_{\mathrm{S}} = \frac{r}{2}\left(1 - \left(1 - \frac{2m}{r}\right)\right) = m. \tag{5.16}$$

[2]We also use $\dot{a} \equiv \dot{a}(t) = \frac{\mathrm{d}a}{\mathrm{d}t}$ because $t$ equals the proper time for observers at rest in Friedmann universes.

Equality of the Misner-Sharp energies by condition (iv) yields

$$m = \frac{4\pi}{3}\rho a^3\,\Sigma_k^3(\chi(\tau)) = \frac{4\pi}{3}\rho(t)\,r^3(t). \tag{5.17}$$

Since the expression $\rho a^3$ is constant due to the conservation law (4.23) and the mass $m$ is also constant, it follows that $\Sigma_k(\chi(\tau))$ must be constant, hence $\chi(\tau) = \chi_0 = \text{const}$. We were expecting this because a non-constant $\chi(\tau)$ implies that dust is created and destroyed at the boundary during the evolution, which is not physical. In contrast, a moving boundary in the Schwarzschild spacetime is no problem because it is a vacuum solution.

It follows $\dot{\chi} = 0$, hence $\dot{t} = 1$ because of $\|\boldsymbol{u}_\mathrm{D}\| = 1$. Thus, we have $\boldsymbol{u}_\mathrm{D} = \boldsymbol{\partial}_t$ and the proper time $\tau$ of the matching observers is equal to the cosmological time $t$, that is, $\mathbf{d}\tau = \mathbf{d}t$. Matching observers are comoving observers on geodesics in the dust universe.

The areal radius (5.12) simplifies to

$$r(t) = a(t)\,\Sigma_k(\chi_0). \tag{5.18}$$

Hence, the time-dependence of the boundary surface is completely determined by the scale factor and the Friedmann equations. The global behaviour of the total spacetime is still that of a Friedmann dust universe.

Taking the norm of the tangent vectors $\|\boldsymbol{u}_\mathrm{S}\| = \|\boldsymbol{u}_\mathrm{D}\|$ yields

$$-V\,\dot{T}^2 + \frac{\dot{r}^2}{V} = -1, \tag{5.19}$$

If we substitute eq. (5.18) for $r$ and use the first Friedmann equation (4.22a), we obtain

$$\begin{aligned} V^2\dot{T}^2 &= \dot{r}^2 + 1 - \frac{2m}{r} = \dot{a}^2\Sigma_k^2(\chi_0) + 1 - \frac{8\pi}{3}\rho a^2\,\Sigma_k^2(\chi_0) \\ &= 1 - k\,\Sigma_k^2(\chi_0) = (\Sigma_k')^2(\chi_0), \end{aligned} \tag{5.20}$$

where we used again the identity (5.15). Hence, the Schwarzschild time $T(t)$ satisfies the differential equation

$$\dot{T} \equiv \frac{\mathrm{d}T}{\mathrm{d}t} = \frac{\Sigma_k'(\chi_0)}{V(a(t)\,\Sigma_k(\chi_0))}. \tag{5.21}$$

In order to obtain an equation of motion for the radial coordinate, this can be substituted into eq. (5.19), yielding

$$\dot{r}^2 + V(r) = E^2, \tag{5.22}$$

where $E = V\,\dot{T} = \Sigma_k'(\chi_0)$. This is the equation of motion for an particle in the Schwarzschild spacetime moving on a radial geodesic. The constant of motion $E$ is the energy of the particle. Hence, matching observers move on geodesics in both spacetimes. For this reason, their accelerations $\nabla_{\boldsymbol{u}}\boldsymbol{u}$ vanish so that $K_{00} = 0$ in both cases and condition (ii) is already satisfied.

We can repeat the gluing for several Schwarzschild spacetimes to the same dust universe as long as the vacuoles do not overlap. Imagining the dust as cheese, the picture of a Swiss cheese should be obvious. A scheme for a spherical dust universe is shown in fig. 5.2. It is also possible to do this the other way round and substitute the black hole by a spherical

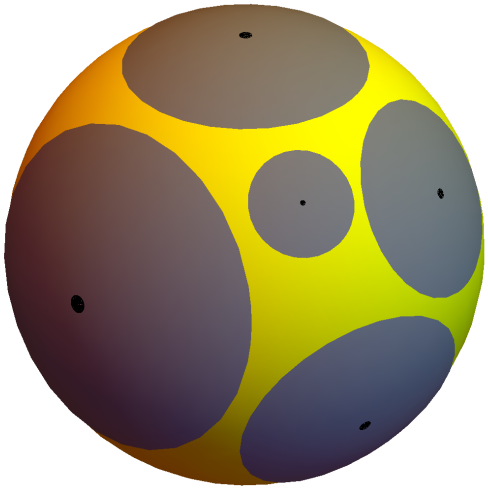

**Figure 5.2:** Swiss-cheese model for a spherical dust universe with several Schwarzschild spacetimes: The dust universe (yellow) corresponds to the cheese, whereas the Schwarzschild spacetimes (grey) are the holes in the cheese. As long as they do not overlap, we can add further Schwarzschild spacetimes.

dust universe. Usually, this case is referred to as a constant density star, which is an example of a *TOV-star*[3] rather than speaking of a dust universe.

Furthermore, it is possible to nest Schwarzschild spacetimes and spherical dust universes: We start with a dust universe and insert some Schwarzschild spacetimes. The black holes are substituted by a constant density star. Since the star is the same as a dust universe, we can repeat this procedure in order to construct a nested structure. Such a model was considered by Korzyński [Kor15] in order to discuss backreaction effects on the mass of the dust due to the structure.

## 5.2 Lindquist-Wheeler Approach

We take a step back from the Swiss-cheese models and consider a similar, but more approximative approach to an inhomogeneous cosmological model suggested by Lindquist and Wheeler [LW57]. Motivated by the Wigner-Seitz approach in solid state physic, they approximated the spacetime around every mass, assuming that it is almost spherically symmetric, by a Schwarzschild solution. These regions are connected in a similar way as in the Swiss-cheese approach: Every Schwarzschild cell is put onto a hypersphere, called *comparison sphere*, such that the boundary is tangent to the comparison sphere. The radius $a$ of the comparison sphere corresponds to the scale factor of the fitted dust universe. Regions uncovered by any Schwarzschild cell are called *no-man's land*, other regions may be covered by two or even more cells. This is shown in fig. 5.3.

The comparison sphere is no part of the solution but an auxiliary object in the sense that it is not a solution to Einstein's equations. It only serves to determine the tangency conditions for each Schwarzschild cell independently. In contrast to the Swiss-cheese models,

[3] TOV is the abbreviation of Tolman [Tol34; Tol39], Oppenheimer and Volkoff [OV39], who studied fluid models for stars. For more details on this topic see, for example, the textbook of Straumann [Str12].

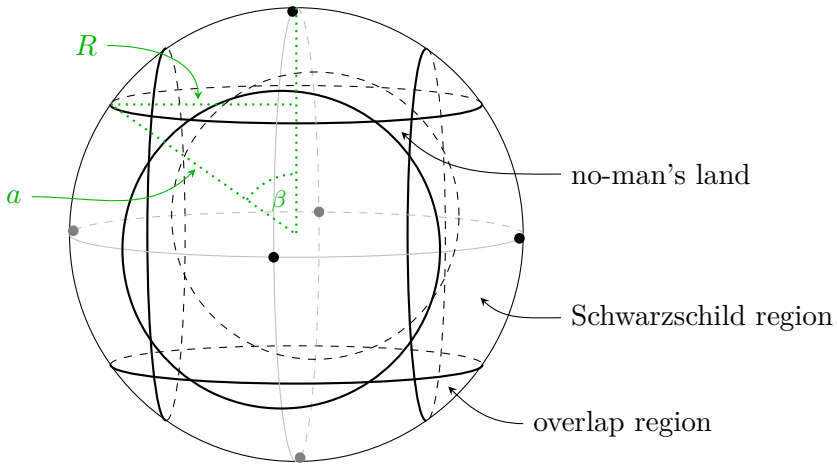


**Figure 5.3:** 2D-scheme of the Lindquist-Wheeler model: Six Schwarzschild spacetimes are put onto the comparison sphere with radius $a_0$. Each boundary sphere with radius $R$ is tangent to the comparison sphere. The opening angle $\beta$ satisfies $R = a_0 \cos\beta$. There are regions on the comparison sphere where two or more Schwarzschild spacetimes overlap and other regions, called no-man's land, which are uncovered. Unlike the scheme suggests, the Schwarzschild regions are only tangent to each other where their boundary spheres cross. This is false in the overlap regions because the actual geometry of the Schwarzschild spacetime is the one shown in fig. 6.1 rather than a spherical cap.

the junction conditions are relaxed in the sense that the Schwarzschild cells are allowed to overlap so that the junction conditions cannot be satisfied everywhere at the boundary. For this reason, two different Schwarzschild spacetimes are only tangent where their boundary spheres cross.

We need a condition telling us how much the cells are allowed to overlap. There are three obvious conditions:

(i) The cells do not overlap, as in the Swiss-cheese models, but they touch.

(ii) The cells are so big that there is no no-man's land.

(iii) The cells partly overlap but there is also no-man's land.

In the first two cases, there are only deviations from tangency between cells of one kind: no overlapping regions and a large no-man's land in case (i) and the other way round in case (ii). Lindquist and Wheeler argued for the intermediate condition (iii) as the most reasonable so that the different deviations counterbalance each other somehow and the result may be a good approximation to the exact solution.

Since they considered $N$ black holes of equal mass regularly distributed on th e comparison sphere, they demanded that each cell should cover the same part $\Omega$ of the comparison sphere such that the total volume of all cells equals the volume of the comparison sphere. Thus, the solid angle $\Omega$ covered by each cell is the $N$-th part of the solid angle of the whole hypersphere, which is $2\pi^2$, hence

$$\Omega_{\text{com}} = \frac{2\pi^2}{N}. \tag{5.23}$$

It follows that the opening angle must be constant in time in order to satisfy the condition during the whole time evolution.

The solid angle of a spherical cap with an opening angle $\beta$ is given by

$$\Omega = \int_0^\beta \mathrm{d}\chi \int_0^\pi \mathrm{d}\vartheta \int_0^{2\pi} \mathrm{d}\varphi \, \sin^2\chi \sin\vartheta = 2\pi \left(\beta - \sin\beta\cos\beta\right). \tag{5.24}$$

Hence, $\beta$ is given implicitly by the condition

$$\pi = N\left(\beta - \sin\beta\cos\beta\right). \tag{5.25}$$

The spacetime in every cell is described by a Schwarzschild metric (5.8) with mass $m$ of the central black hole. Since all masses are equal, the total mass is $M = Nm$. The Schwarzschild region is cut off at some radius $R$ such that $r \leq R(T)$. The opening angle $\beta$, the size $a$ of the comparison sphere and the radius $R$ of the boundary sphere of a Schwarzschild cell are related by

$$R = a\sin\beta, \tag{5.26}$$

see again fig. 5.3. This ensures continuity at the boundary. In contrast to the Wigner-Seitz approach, the boundary spheres need not be constant in time: On the one hand, a particle on the boundary should fall towards the black hole. On the other, due to the mirror symmetry, the particle on two boundaries should remain at its position. This apparent contradiction can be resolved if the boundary spheres themselves move, implying that the comparison sphere is not a fixed object but it also changes its size in time. Because of the mirror symmetry, the evolution has to be orthogonal to the comparison sphere in the embedding space. Instead of using the Schwarzschild time $T$, we parametrise the evolution of the boundary sphere by the curves $\gamma = (T(\tau), R(\tau), \vartheta_0, \varphi_0)$ where $\tau$ is the proper time. Then, boundary evolves along the vector field

$$\boldsymbol{\partial}_\tau = \dot{T}\,\boldsymbol{\partial}_T + \dot{R}\,\boldsymbol{\partial}_r \tag{5.27}$$

such that $\|\boldsymbol{\partial}_\tau\| = 1$. Hence, the normal to the boundary is given by

$$\boldsymbol{n} = -V^{-1}\dot{R}\,\boldsymbol{\partial}_T + V\dot{T}\,\boldsymbol{\partial}_r. \tag{5.28}$$

In order to be tangent to the comparison sphere, the areal radius $r$ has to satisfy

$$(\mathbf{d}r)(\boldsymbol{n})|_\gamma = \cos\beta. \tag{5.29}$$

Since each Schwarzschild cell should always satisfy eq. (5.25), $\beta$ must be constant. Using the expression for the normal, we obtain

$$V\dot{T} = \cos\beta. \tag{5.30a}$$

If take the norm of $\boldsymbol{\partial}_\tau$ and use eq. (5.30a), we get the equation of motion for the radius

$$-1 = -V\dot{T}^2 + V^{-1}\dot{R}^2 = V^{-1}\left(-\cos^2\beta + \dot{R}^2\right). \tag{5.31}$$

This is again the equation of motion (5.22) of a radially freely-falling particle in the Schwarzschild spacetime. Hence, points on the boundary sphere follow geodesics. At the

moment $\tau_0$ of maximal expansion, we have $\dot{R}(\tau_0) = 0$. Hence, using eq. (5.26), the equation of motion (5.31) implies

$$m = \frac{R_0}{2} \sin^2 \beta = \frac{a_0}{2} \sin^3 \beta, \tag{5.32}$$

where $R_0 = R(\tau_0)$ and $a_0 = a(\tau_0)$. If substitute eq. (5.26) for $r$ in eq. (5.31) and use eq. (5.32), we obtain after some rearrangements

$$\left(\frac{\dot{a}}{a}\right)^2 = \frac{a_0}{a^3} - \frac{1}{a^2}. \tag{5.33}$$

This is the first Friedmann equation (4.27) for a dust universe with maximal size

$$a_0 = \frac{2M}{N \sin^3 \beta}, \tag{5.34}$$

where $M = Nm$. For $N \to \infty$, using eq. (5.25), we finally obtain

$$a_0 \longrightarrow \frac{4M}{3\pi}. \tag{5.35}$$

This is the same result as eq. (4.36) for a dust universe. Hence, the Schwarzschild-cell method by Lindquist and Wheeler predicts a Friedmann-like evolution.

This result is not so surprising as it may seem on the first view. If we compare the assumptions of Lindquist and Wheeler to the Swiss-cheese models, we notice that the comparison sphere exactly corresponds to dust universe: It is the same construction except for the fact that the cells overlap in the Lindquist-Wheeler models. So, Lindquist and Wheeler demand that each Schwarzschild cell is put on a hypersphere tangent at its boundary, the opening angles of the cell do not change in time and the boundaries move orthogonal to the intersection surfaces. The latter condition implies that the boundary spheres move orthogonal to the comparison sphere. These are exactly the conditions which need to be satisfied in the Swiss-cheese model to match a Schwarzschild spacetime to a dust universe as we have shown in section 5.1. For this reason, the global behaviour of the Lindquist-Wheeler model must correspond to a dust universe. However, the size $a_0$ of the comparison sphere deviates from the Friedmann value but the difference vanishes for large numbers of black holes.

#### Non-regular Lindquist-Wheeler Models

Since there exist only six regular configurations on the 3-sphere, as discussed in chapter 3, we are not able to perform the limit $N \to \infty$ explicitly. Therefore, we generalise the Lindquist-Wheeler model to arbitrary configurations of black holes with different masses. As just discussed, Lindquist-Wheeler and Swiss-cheese models are based on the same construction. Therefore, the generalisation to arbitrary configurations is straight-forward: We simply adapt the Swiss-cheese model to the ideas of Lindquist and Wheeler. In both cases, the mass is determined by the opening angle $\beta_A$ of the cell

$$m_A = \frac{a_0}{2} \sin^3 \beta_A. \tag{5.36}$$

The size $a_0$ of the comparison sphere is not determined yet. As before, we allow the cells to overlap such that the sum of the solid angles $\Omega_A = 2\pi \left(\beta_A - \sin \beta_A \cos \beta_A\right)$ covered by

the cells is the same as the total solid angle $2\pi^2$ of the comparison sphere, which means

$$\frac{1}{2\pi^2}\sum_A \Omega_A = \sum_A \frac{1}{\pi}\left(\beta_A - \sin\beta_A\cos\beta_A\right) = 1. \tag{5.37}$$

Together with eq. (5.36), this system of $N+1$ equations for $\{a_0, \beta_A\}$ can be solved for a given set of $N$ black holes with masses $\{m_A\}$ to determine the size $a_0$ of the universe.

Other authors [CF09a; Liu15] do not seem to be aware of the connection to Swiss-cheese models and they generalised Lindquist-Wheeler models in a slightly different way to regular lattices. Liu [Liu15] discusses some conditions for arbitrary configurations but does not work out a complete model. However, we can satisfy his conditions if we take the matching conditions of Swiss-cheese models, $R_A = a\sin\beta_A$ and $m_A = \frac{a_0}{2}\sin^3$ in the spherical case and similarly for the other cases. However, we only have an overlapping condition for the spherical which can easily adapted to regular lattices in the other cases. For arbitrary configurations in the other cases, such a condition is still missing.

In order to be a Friedmann-like configuration, we expect that the distribution of the black holes on the comparison sphere should be almost uniform. Furthermore, the mass of the black holes should not be too big, that is, a single cell should not cover too big regions of the comparison sphere. If the cells are small, we have $\beta_A \ll 1$ and we can approximate the masses by

$$m_A = \frac{a_0}{2}\sin^3\beta_A = \frac{a_0}{2}\,\beta_A^3 + \mathcal{O}\left(\beta_A^5\right) \tag{5.38}$$

and the solid angles by

$$\Omega_A = 2\pi\left(\beta_A - \sin\beta_A\cos\beta_A\right) = \frac{4\pi}{3}\,\beta_A^3 + \mathcal{O}\left(\beta_A^5\right). \tag{5.39}$$

Using this in the volume condition eq. (5.37), we obtain

$$\sum_A \beta_A^3 = \frac{3\pi}{2} + \mathcal{O}\left(\beta^5\right). \tag{5.40}$$

Therefore, in this case, the total mass $M$ is given by

$$M = \sum_A m_A = \frac{a_0}{2}\sum_A \beta_A^3 = \frac{3\pi}{4}\,a_0 + \mathcal{O}\left(\beta^5\right), \tag{5.41}$$

which is the desired result.

This shows that for a Friedmann-like approximation the masses should not too big. However, in order to be similar to a Swiss-cheese model, the black holes should be distributed on the comparison sphere in such a way that the cells cover most parts of the comparison spheres. This means that the cells do not overlap much and, accordingly, the amount of no-man's land is small. In other words, the black holes are not too close to each other. Hence, we have to find a criterion characterising such Friedmann-like configurations. This will be discussed in chapter 7.

At last, some words on the time evolution. By construction, the time evolution of the comparison sphere is that of a Friedmann dust universe whose size $a_0$ is determined as discussed above. In the Lindquist-Wheeler models, it is assumed that the evolution of the boundary spheres is orthogonal to the intersection hypersurface based on the assumption that neighbouring black holes attract particle on the common boundary equally. However, the boundary spheres cross only in certain points. Hence, in the overlapping regions, the assumption is should be violated. For this reason, the time evolution may deviate from a Friedmann dust universe.

# 6 Multi Black Hole Solutions

We are looking for a vacuum solution to Einstein's field equations which is a generalisation of the Schwarzschild spacetime in the sense that this solution should describe multiple black holes. The Schwarzschild spacetime is reviewed briefly in the first section 6.1.

We want to investigate if there are black hole configurations such that the space looks somehow similar to a Friedmann dust universe with a similar time evolution. Unfortunately, we are not able to find such a solution to the general Einstein equations. However, we can solve the constraint equation such that the initial data have the desired properties. In the second section 6.2 we present three seemingly different vacuum solutions to the constraint equations. These are spaces with an arbitrary number of Schwarzschild-like black holes that are momentarily at rest. Actually, as we show in section 6.3, the three solutions describe the same space. Finally in section 6.4, we will investigate the properties of these spaces, in particular, we determine the mass of the black holes.

## 6.1 Black Holes

We want to model the matter as black holes. A black hole is a region in a spacetime with such strong gravitational effects that no particle is able to escape. The origin of the name is that this is also the case for light so that this regions is dark. Usually a black hole goes along with a curvature singularity. Since this causes some severe problems, the singularity should be hidden behind the *event horizon* which is the boundary of a black hole; no particle which crossed the horizon can escape. However, there are solutions containing a curvature singularity but possess no horizon, for example, the over extremal Kerr black holes. It is still an open question, known as the *cosmic censorship hypothesis* [Pen69], if every singularity formed in a physical process is hidden behind a horizon.

The best known black hole solution and one of the most important spacetimes in General Relativity is the *Schwarzschild black hole* [Sch16]. This is the unique spherically symmetric vacuum solution to Einstein's field equations which is asymptotically flat.

A spacetime is spherically symmetric if it admits an action of the rotation group $SO(3)$ such that the action is an isometry and the group orbits are space-like two-dimensional hypersurfaces. As shown in the textbook of Straumann [Str12], these orbits are 2-spheres, parametrised by the radial coordinate $R$ such that the surface area of a sphere is $4\pi R^2$. Hence, in standard spherical coordinates $\vartheta, \varphi$, the line element is given by

$$R^2\,\mathbf{d}\Omega^2 = R^2\left(\mathbf{d}\vartheta^2 + \sin^2\vartheta\,\mathbf{d}\varphi^2\right). \tag{6.1}$$

Furthermore, it can be shown that radial geodesics orthogonal to one sphere are orthogonal to all spheres, hence the spatial metric takes the form

$$\bar{\boldsymbol{g}} = A^2(R)\,\mathbf{d}R^2 + R^2\,\mathbf{d}\Omega^2. \tag{6.2}$$

In order to use the conformal methods from section 2.3, we define a new radial coordinate $r = r(R)$ such that the spatial metric becomes conformally flat

$$\bar{\boldsymbol{g}} = \Psi^4(r)\,\boldsymbol{\delta}, \tag{6.3}$$

where $\boldsymbol{\delta} = \mathbf{d}r^2 + r^2\,\mathbf{d}\Omega^2$ is the flat metric in spherical coordinates.

The conformal factor is determined by the equations of 3+1 decomposition. Since we are looking for a vacuum solution, we have $E \equiv 0$, $\boldsymbol{j} \equiv 0$ and $\boldsymbol{S} \equiv 0$. Furthermore, we set the shift vector to zero, $\boldsymbol{\beta} \equiv 0$.

Due to Birkhoff's theorem, a spherically symmetric vacuum spacetime must be necessarily static. Hence, the metric components do not depend on the time $t$. For this reason, the evolution equation for the metric (2.65) implies that the extrinsic curvature vanishes, $\bar{\boldsymbol{K}} \equiv 0$. Hence, the momentum constraint (2.84b) is identically satisfied. Furthermore, the spatial metric is completely determined by the Hamiltonian constraint or the Lichnerowicz equation (2.111), respectively,

$$\tilde{\Delta}\Psi = \frac{1}{8}\,\tilde{\mathcal{R}}\,\Psi = 0, \tag{6.4}$$

where we used that the Ricci scalar $\tilde{\mathcal{R}} = \mathcal{R}[\tilde{g}]$ of the flat metric $\tilde{\boldsymbol{g}} = \boldsymbol{\delta}$ vanishes.

Unlike the cosmological case in section 4.1, the second evolution equation (2.78c) implies that the choice $\alpha = 1$ is not possible but we have

$$\bar{\nabla}_a \bar{\nabla}_b \alpha = \alpha\,\bar{R}_{ab}, \tag{6.5}$$

where $\alpha = \alpha(r)$ depends only on the radial coordinate due to the symmetries.

Both differential equations are solved by

$$\Psi = 1 + \frac{m}{2r}, \tag{6.6a}$$

$$\alpha = \frac{1 - \frac{m}{2r}}{1 + \frac{m}{2r}}. \tag{6.6b}$$

Hence, the Schwarzschild metric in *isotropic coordinates* takes the form

$$\boldsymbol{g} = -\left(\frac{1 - \frac{m}{2r}}{1 + \frac{m}{2r}}\right)^2 \mathbf{d}t^2 + \left(1 + \frac{m}{2r}\right)^4 \left(\mathbf{d}r^2 + r^2\,\mathbf{d}\Omega^2\right). \tag{6.7}$$

Using the coordinate transformation $R = r\left(1 + \frac{m}{2r}\right)^2$ for $r > \frac{m}{2}$, we can bring the metric into its standard form

$$\boldsymbol{g} = -\left(1 - \frac{2m}{R}\right)\mathbf{d}t^2 + \left(1 - \frac{2m}{R}\right)^{-1}\mathbf{d}R^2 + R^2\,\mathbf{d}\Omega^2. \tag{6.8}$$

The constant $m$, appearing as an integration constant, corresponds to the mass of the black hole. An isometric embedding of the equatorial plane is shown in fig. 6.1.

At $R = 2m$, the standard Schwarzschild metric (6.8) possesses a coordinate singularity. The metric itself remains regular because the metric in isotropic coordinates (6.7) is well-defined at the corresponding radius $r = \frac{m}{2}$. However, the metric is degenerate on the null hypersurface given by $r = \frac{m}{2}$, which is called *event horizon*.

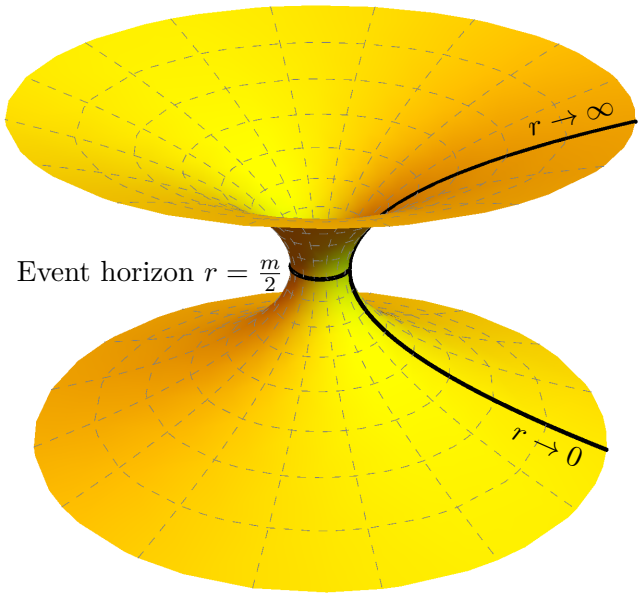


**Figure 6.1:** Isometric embedding of a constant-time slice of the Schwarzschild spacetime (6.7) in isotropic coordinates: The image shows the equatorial plane $\vartheta = \frac{\pi}{2}$ which is a rotated parabola, also known as Flamm's paraboloid. The upper half is described by the metric (6.8) in standard Schwarzschild coordinates. Both halves are causally disconnected by the event horizon in the middle at $r = \frac{m}{2}$, see also fig. 6.2.

Within the horizon $R < 2m$, which is the upper grey region in the Penrose diagram shown in fig. 6.2, the time coordinate $t$ and the radial coordinate $R$ change their roles: $R$ becomes time-like, whereas $t$ is space-like. For this reason, it is inevitable to hit the curvature singularity at $R = 0$ after crossing the horizon.

In contrast, the Schwarzschild metric in isotropic coordinates (6.7) is regular for all values of $r$. It is divided into two regions by the event horizon at $r = \frac{m}{2}$. As shown above, the part $r > \frac{m}{2}$ is isometric to the region $R > 2m$ described by the standard Schwarzschild metric (6.8). This is the white region on the right in fig. 6.2.

The part $0 < r < \frac{m}{2}$ is also isometric to the former. They are mapped to each other by a sphere inversion at the horizon given by $\hat{r} = \frac{m^2}{4r}$. This second region is the white one on the left of fig. 6.2. As the Penrose diagram of the maximally extended Schwarzschild spacetime shows, both regions are causally disconnected.

A detailed discussion of the Schwarzschild spacetime can be found in any introductory textbook on general relativity, we recommend the textbook of Straumann [Str12].

## 6.2 Vacuum Solutions to the Lichnerowicz Equation

We are looking for a solution for a spatial metric describing a discrete matter distribution. As we have discussed in the introduction 1, it should not really be important what kind of matter we consider; in the far-region – whatever this exactly means – all kinds of matter should behave similarly. This is comparable to the case of a spherically symmetric (and thus static) vacuum spacetime: Irrespective of the central object, which might be a

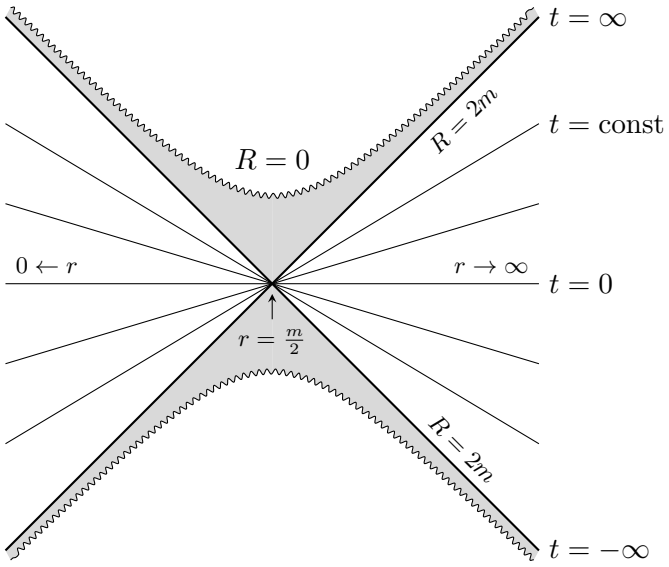


**Figure 6.2:** Penrose diagram of the maximally extended Schwarzschild spacetime: The diagram shows the $(R, t)$-plane such that every point corresponds to a 2-sphere. Light moves on straight lines of $\pm 45°$. The snake lines are the curvature singularities and the thick diagonal lines are the event horizons at $R = 2m$. The upper grey region is the black hole, whereas the lower one would be a white hole. The standard Schwarzschild coordinates describe the right region. The diagonal lines are constant-time slices of the Schwarzschild spacetime in isotropic coordinates. An isometric embedding of such a constant-time slice is shown in fig. 6.1 above.

TOV-star, a dust cloud or simply a black hole, the exterior spacetime is always given by the Schwarzschild solution.

Clearly, the situation is not that simple in a general context without these symmetries. However, it is a reasonable assumption that far away from the massive objects we are not really able to distinguish between different but similar sources of the gravitational field. Therefore we take the simplest objects to replace the matter in space: black holes. This means we are looking for vacuum solutions to Einstein's equations. Hence, we do not have to bother with probably complicated matter equations.

Since we are not able to find an exact solution to the full system of Einstein's equations, we restrict ourselves to the initial value problem. This means that we have to solve the constraint equations (2.84)

$$\bar{\mathcal{R}} + \mathcal{K}^2 - \bar{K}^a{}_b \bar{K}^b{}_a = 16\pi E, \tag{6.9a}$$

$$\bar{\nabla}_b \bar{K}^b{}_a - \bar{\nabla}_a \mathcal{K} = 8\pi j_a, \tag{6.9b}$$

in order to determine the spatial metric and the extrinsic curvature.

These are still complicated equations so that we have to make further assumptions in order to simplify our problem. Since we are looking for vacuum solutions, we have $E = 0$ and $\bar{\boldsymbol{j}} = 0$.

Furthermore, we assume that the initial hypersurface is time-symmetric, that is, the black holes are momentarily at rest. This means that, assuming that the universe started with a big bang and has been growing, the space has reached its maximal expansion at this moment and starts recollapsing now. Such a constant-time slice is characterised by a vanishing extrinsic curvature, $\bar{\boldsymbol{K}} = 0$. Note that this is a very restrictive assumption excluding a lot of cosmological models. However, we are willing to pay this price for the sake of an exact solution.

It follows that the momentum constraint is identically satisfied while the Hamiltonian constraint reduces to $\bar{\mathcal{R}} = 0$ or equivalently to the Lichnerowicz equation (2.111)

$$\tilde{\Delta}\Psi = \frac{1}{8}\tilde{\mathcal{R}}\,\Psi. \tag{6.10}$$

In view of the cosmological solutions where the spatial metric is of the form $\bar{\boldsymbol{g}} = a_0^2\,\boldsymbol{h}_k$, we make the conformal ansatz

$$\bar{\boldsymbol{g}} = \Psi^4\,\tilde{\boldsymbol{g}} = \Psi^4\,\boldsymbol{h}_k \tag{6.11}$$

for the spatial metric, where the conformal metric is chosen to be

$$\tilde{\boldsymbol{g}} = \boldsymbol{h}_k = \mathbf{d}\chi^2 + \Sigma_k^2(\chi)\,\mathbf{d}\Omega^2, \tag{6.12}$$

with $k \in \{0, \pm 1\}$. Hence, we keep the metric of the maximally symmetric spaces as the conformal metric as in cosmology but we allow the conformal factor to vary over space. In contrast, the scale factor, corresponding to the squared conformal factor $a_0 = \Psi^2$, is constant.

As we already know, the Ricci scalar $\mathcal{R}[h_k]$ of a maximally symmetric space is simply

$$\tilde{\mathcal{R}} \equiv \mathcal{R}[h_k] = 6k. \tag{6.13}$$

The Laplacian $\tilde{\Delta} \equiv \Delta_k$ with respect to the metric $\boldsymbol{h}_k$ is given by

$$\Delta_k = \frac{1}{\sqrt{\det \boldsymbol{h}_k}}\,\partial_i\left((h_k)^{ij}\,\sqrt{\det \boldsymbol{h}_k}\,\partial_j\right) = \frac{1}{\Sigma_k^2 \sin\vartheta}\,\partial_i\left(\Sigma_k^2 \sin\vartheta\,(h_k)^{ij}\,\partial_j\right). \tag{6.14}$$

Altogether, we are looking for solutions to the Lichnerowicz equation

$$\Delta_k\Psi = \frac{3}{4}k\,\Psi. \tag{6.15}$$

Note that although Einstein's equations are non-linear, the Hamiltonian constraint becomes a linear differential equation in our case.

Next we derive the solutions for each value of $k \in \{0, \pm 1\}$. Here, we only present the different solutions. Their physical interpretations are discussed in the following sections 6.3 and 6.4.

**Flat Case**

In the flat case, we have $k = 0$ and $\boldsymbol{h}_0 = \boldsymbol{\delta}$ is the flat Euclidean metric. Hence, eq. (6.15) becomes

$$\Delta_0\Psi_0 = 0, \tag{6.16}$$

with the well-known solution on $\mathbb{R}^3 \setminus \{\boldsymbol{p}_A : A = 1, \dots, N-1\}$

$$\Psi_0(\boldsymbol{x}) = 1 + \sum_{A=1}^{N-1} \frac{\mu_A}{\|\boldsymbol{x} - \boldsymbol{p}_A\|}, \tag{6.17}$$

where $\boldsymbol{x} = (x^1, x^2, x^3) = r\,\boldsymbol{E}_3$ parametrises the whole $\mathbb{R}^3$. The $\mu_A$ are parameters whose meaning is explained later, and $\|\cdot\|_3$ is the Euclidean norm in $\mathbb{R}^3$.

The metric $\bar{\boldsymbol{g}} = \Psi^4\,\boldsymbol{\delta}$ has $N-1$ *inner ends* at $\boldsymbol{p}_A \in \mathbb{R}^3$ where the conformal factor diverges, and one asymptotically flat end at infinity. This solution was first described by Misner and Wheeler [MW57].

We can easily prove that eq. (6.17) solves the Lichnerowicz equation if we use Cartesian coordinates

$$x^1 = r \sin\vartheta \cos\varphi, \tag{6.18a}$$
$$x^2 = r \sin\vartheta \sin\varphi, \tag{6.18b}$$
$$x^3 = r \cos\vartheta. \tag{6.18c}$$

In this case, the metric is simply $h_{ij} = \delta_{ij}$. Hence, the Laplace operator takes the form

$$\Delta_0 = \partial_1^2 + \partial_2^2 + \partial_3^2 = \partial^i\,\partial_i. \tag{6.19}$$

Obviously, the Lichnerowicz equation is solved by any constant term. The other terms in the conformal factor can be written as

$$\Psi_0 = \frac{1}{\|\boldsymbol{x} - \boldsymbol{p}\|_3} = \frac{1}{\sqrt{(\boldsymbol{x}^j - \boldsymbol{p}^j)(\boldsymbol{x}_j - \boldsymbol{p}_j)}}, \tag{6.20}$$

surpressing the parameter $\mu$. Then we have

$$\begin{aligned}\partial^i\partial_i\Psi_0 &= -\partial^i \frac{\boldsymbol{x}_i - \boldsymbol{p}_i}{\sqrt{(\boldsymbol{x}^j - \boldsymbol{p}^j)(\boldsymbol{x}_j - \boldsymbol{p}_j)}^3} \\ &= \frac{3(\boldsymbol{x}^i - \boldsymbol{p}^i)(\boldsymbol{x}_i - \boldsymbol{p}_i)}{\sqrt{(\boldsymbol{x}^j - \boldsymbol{p}^j)(\boldsymbol{x}_j - \boldsymbol{p}_j)}^5} - \frac{\delta^i_i}{\sqrt{(\boldsymbol{x}^j - \boldsymbol{p}^j)(\boldsymbol{x}_j - \boldsymbol{p}_j)}^3} = 0.\end{aligned} \tag{6.21}$$

Since the Lichnerowicz equation is linear, we can apply the superposition principle and add up arbitrarily many solutions with different $\boldsymbol{p}_A$ and $\mu_A$.

**Spherical Case**

Next, we consider the spherical case where $k = +1$. The conformal metric is the round metric of the 3-sphere, $\boldsymbol{h}_+ = \mathbf{d}\chi^2 + \sin^2\chi\,\mathbf{d}\Omega^2$. The solution with $N$ inner ends to the Lichnerowicz equation

$$\Delta_+\Psi_+ = \frac{3}{4}\,\Psi_+, \tag{6.22}$$

where

$$\Delta_+ = \Delta_{S^3} = \frac{1}{\sin^2\chi}\,\partial_\chi\left(\sin^2\chi\,\partial_\chi\right) + \frac{1}{\sin^2\chi}\left(\frac{1}{\sin\vartheta}\,\partial_\vartheta\left(\sin\vartheta\,\partial_\vartheta\right) + \frac{1}{\sin^2\varphi}\,\partial_\varphi^2\right), \tag{6.23}$$

is given by

$$\Psi(\chi,\vartheta,\varphi) = \sum_{A=1}^{N} \mu_A \Big[(\sin\chi\sin\vartheta\sin\varphi - a_A)^2 + (\sin\chi\sin\vartheta\cos\varphi - b_A)^2 + (\sin\chi\cos\vartheta - c_A)^2 + (\cos\chi - d_A)^2\Big]^{-1/2}, \tag{6.24}$$

where ${a_A}^2 + {b_A}^2 + {c_A}^2 + {d_A}^2 = 1$.

If we use the four-dimensional Euclidean space $\mathbb{R}^4$ to embed the spherical space as the unit sphere, there is an illustrative way to write this solution, namely

$$\Psi_+(\chi,\vartheta,\varphi) = \sum_{A=1}^{N} \frac{\mu_A}{\|\boldsymbol{E}_4(\chi,\vartheta,\varphi) - \boldsymbol{P}_A\|_4}, \tag{6.25}$$

where $\|\cdot\|_4$ is the Euclidean norm in $\mathbb{R}^4$ and

$$\boldsymbol{E}_4(\chi,\vartheta,\varphi) = (\sin\chi\,\boldsymbol{E}_3(\vartheta,\varphi), \cos\chi) = \begin{pmatrix} \sin\chi\sin\vartheta\sin\varphi \\ \sin\chi\sin\vartheta\cos\varphi \\ \sin\chi\cos\vartheta \\ \cos\chi \end{pmatrix} \tag{6.26}$$

is the radial unit vector, $\|\boldsymbol{E}_4\|_4 = 1$, parametrising the embedded 3-sphere. The inner ends are located at $\boldsymbol{P}_A = (a_A, b_A, c_A, d_A)$ with $\|\boldsymbol{P}_A\|_4 = 1$.

This solution was obtained by Clifton, Rosquist and Tavakol [CRT12]. They used a form similar to eq. (6.24). Later, Korzyński [Kor14] used a form in which the 4-dimensional norm is expressed by the geodesic distance with respect to the conformal metric; see also the next section 6.3. In these cases, no embedding space is needed. However, many considerations are more intuitive if we keep our point of view imagining an embedded sphere.

For the proof, we extend the function $\Psi_+ = \frac{1}{\|\boldsymbol{E}_4 - \boldsymbol{P}\|_4}$, surpressing $\mu$, to the whole embedding space $\mathbb{R}^4$, parametrised by $\boldsymbol{X} = \rho\,\boldsymbol{E}_4$, via the function

$$\hat{\Psi}(\rho,\chi,\vartheta,\varphi) = \frac{1}{\|\rho\,\boldsymbol{E}_4(\chi,\vartheta,\varphi) - \boldsymbol{P}\|_4} = \frac{1}{\sqrt{\rho^2 + 2\rho f + 1}}, \tag{6.27}$$

where $\|\boldsymbol{P}\|_4 = 1$ and $f \equiv f(\chi,\vartheta,\varphi) = \boldsymbol{P}\cdot\boldsymbol{E}_4$. The dot denotes the standard scalar product in $\mathbb{R}^4$. On the 3-sphere $\rho = 1$, we get

$$\hat{\Psi}|_{\rho=1} = \frac{1}{\|\boldsymbol{E}_4 - \boldsymbol{P}\|_4} = \frac{1}{\sqrt{2(1+f)}} = \Psi_+. \tag{6.28}$$

On the one hand, the four-dimensional flat Laplacian can be decomposed into

$$\begin{aligned} \Delta_4 &= \frac{1}{\sqrt{\det\delta}}\,\partial_\alpha\left(\delta^\alpha\sqrt{\det\delta}\,\partial_\beta\right) \\ &= \frac{1}{\rho^3}\,\partial_\rho\left(\rho^3\,\partial_\rho\right) + \frac{1}{\rho^2}\frac{1}{\sqrt{\det h}}\,\partial_i\left(h^{ij}\sqrt{\det h}\,\partial_j\right) \\ &= \partial_\rho^2 + \frac{3}{\rho}\,\partial_\rho + \frac{1}{\rho^2}\,\Delta_{S^3}. \end{aligned} \tag{6.29}$$

with respect to the flat metric $\boldsymbol{\delta} = \mathbf{d}\rho^2 + \rho^2\, \boldsymbol{h}_+$ in spherical coordinates. Applying this to $\hat{\Psi}$, we obtain

$$\begin{aligned}
\Delta_4 \hat{\Psi} &= \left(\partial_\rho^2 + \frac{3}{\rho}\,\partial_\rho\right) \frac{1}{\sqrt{\rho^2 + 2\rho f + 1}} + \frac{1}{\rho^2}\,\Delta_{S^3}\hat{\Psi} \\
&= -\left(\partial_\rho + \frac{3}{\rho}\right) \frac{\rho + f}{\sqrt{\rho^2 + 2\rho f + 1}^3} + \frac{1}{\rho^2}\,\Delta_{S^3}\hat{\Psi} \\
&= -\frac{1}{\sqrt{\rho^2 + 2\rho f + 1}^3} + \frac{3(\rho+f)^2}{\sqrt{\rho^2 + 2\rho f + 1}^5} - \frac{3(\rho+f)}{\rho\sqrt{\rho^2 + 2\rho f + 1}^3} + \frac{1}{\rho^2}\,\Delta_{S^3}\hat{\Psi} \\
&= -\hat{\Psi}^3 + 3(\rho+f)^2\hat{\Psi}^5 - \frac{3}{\rho}(\rho+f)\hat{\Psi}^3 + \frac{1}{\rho^2}\,\Delta_{S^3}\hat{\Psi}.
\end{aligned} \tag{6.30}$$

On the other hand, in Cartesian coordinates we have $\boldsymbol{X} = (X^\alpha) = \rho \boldsymbol{E}_4$, hence

$$\hat{\Psi}(\boldsymbol{X}) = \frac{1}{\|\boldsymbol{X} - \boldsymbol{P}\|_4} = \frac{1}{\sqrt{(X^\alpha - P^\alpha)(X_\alpha - P_\alpha)}}. \tag{6.31}$$

In this case, the metric components are simply $\delta_{\alpha\beta}$, hence the Laplacian is given by $\Delta_4 = \partial^\alpha \partial_\alpha$. In contrast to the 3-dimensional case, the Laplacian of $\hat{\Psi}$ does not vanish, $\Delta_4 \hat{\Psi} \neq 0$, but we have

$$\begin{aligned}
\Delta_4 \hat{\Psi} = \partial^\alpha \partial_\alpha \hat{\Psi} &= -\partial^\alpha \frac{X_\alpha - P_\alpha}{\sqrt{(X^\beta - P^\beta)(X_\beta - P_\beta)}^3} \\
&= \frac{3(X^\alpha - P^\alpha)(X_\alpha - P_\alpha)}{\sqrt{(X^\beta - P^\beta)(X_\beta - P_\beta)}^5} - \frac{\delta^\alpha_\alpha}{\sqrt{(X^\beta - P^\beta)(X_\beta - P_\beta)}^3} \\
&= 3\hat{\Psi}^3 - 4\hat{\Psi}^3 = -\hat{\Psi}^3.
\end{aligned} \tag{6.32}$$

Comparing this result with eq. (6.30), we obtain

$$\frac{1}{\rho^2}\Delta_{S^3}\hat{\Psi} = 3\left(\frac{1}{\rho}(\rho+f)\hat{\Psi}^2 - (\rho+f)^2\hat{\Psi}^4\right)\hat{\Psi}. \tag{6.33}$$

Because of $(\rho+f)\hat{\Psi}^2|_{\rho=1} = \frac{1}{2}$, this reduces on the hypersphere to

$$\Delta_{S^3}\Psi_+ = \frac{3}{4}\Psi_+. \tag{6.34}$$

**Hyperbolic Case**

In the hyperbolic case $k = -1$, we have $\boldsymbol{h}_- = \mathbf{d}u^2 + \sinh^2 u\, \mathbf{d}\Omega^2$, which is the hyperbolic metric. The solution with $N$ inner ends to the Lichnerowicz equation

$$\Delta_- \Psi_- = -\frac{3}{4}\,\Psi_-, \tag{6.35}$$

where

$$\Delta_- = \Delta_{H^3_2} = \frac{1}{\sinh^2 u}\,\partial_u\left(\sinh^2 u\,\partial_u\right) + \frac{1}{\sinh^2 u}\left(\frac{1}{\sin\vartheta}\,\partial_\vartheta\left(\sin\vartheta\,\partial_\vartheta\right) + \frac{1}{\sin^2\varphi}\,\partial_\varphi^2\right), \tag{6.36}$$

is given by

$$\Psi_-(u,\vartheta,\varphi) = \sum_{A=1}^{N} \mu_A \Big[ -(\pm\cosh u - a_A)^2 + (\sinh u \sin\vartheta \sin\varphi - b_A)^2 + (\sinh u \sin\vartheta \cos\varphi - c_A)^2 + (\sinh u \cos\vartheta - d_A)^2 \Big]^{-1/2}, \tag{6.37}$$

where $a_A^2 + b_A^2 + c_A^2 - d_A^2 = -1$. In addition to the inner ends, there are two further ends at infinity $u \to \pm\infty$.

Similar to the spherical case, we embed the hyperbolic space into the four-dimensional Minkowski space $\mathbb{R}^{1,3}$ with the metric $\eta_{\alpha\beta} = \operatorname{diag}(-1,1,1,1)$. Norm and scalar product are taken with respect to this metric. Then, the hyperbolic space is the three-dimensional hyperboloid of two sheets $H_2^3$. In this case, we can write the solution as

$$\Psi_-(u,\vartheta,\varphi) = \sum_{A=1}^{N} \frac{\mu_A}{\|\boldsymbol{E}_{\mathrm{M}}(u,\vartheta,\varphi) - \boldsymbol{P}_A\|_{\mathrm{M}}}, \tag{6.38}$$

where

$$\boldsymbol{E}_{\mathrm{M}}(u,\vartheta,\varphi) = (\sinh u\, \boldsymbol{E}_3(\vartheta,\varphi), \pm\cosh u) = \begin{pmatrix} \pm\cosh u \\ \sinh u \sin\vartheta \sin\varphi \\ \sinh u \sin\vartheta \cos\varphi \\ \sinh u \cos\vartheta \end{pmatrix} \tag{6.39}$$

is the unit vector, $\|\boldsymbol{E}_{\mathrm{M}}\|_{\mathrm{M}} = -1$, parametrising both sheets of the hyperboloid distinguished by the sign in the last component. The inner ends are located at $\boldsymbol{P}_A = (a_A, b_A, c_A, d_A)$ with $\|\boldsymbol{P}_A\|_{\mathrm{M}} = -1$. This solution appears to be new.

The proof is almost the same as in the spherical case except for some changes of signs due to the negative last component of the Minkowski metric. Consider the function

$$\hat\Psi(t,u,\vartheta,\varphi) = \frac{1}{\|t\,\boldsymbol{E}_{\mathrm{M}}(u,\vartheta,\varphi) - \boldsymbol{P}\|_{\mathrm{M}}} = \frac{1}{\sqrt{-t^2 + 2tf - 1}}, \tag{6.40}$$

where $\|\boldsymbol{P}\|_{\mathrm{M}} = -1$ and $f \equiv f(u,\vartheta,\varphi) = \langle \boldsymbol{P}, \boldsymbol{E}_{\mathrm{M}} \rangle$. For $t = 1$, we have

$$\hat\Psi|_{t=1} = \frac{1}{\|\boldsymbol{E}_{\mathrm{M}} - \boldsymbol{P}\|_{\mathrm{M}}} = \frac{1}{\sqrt{2(-1+f)}} = \Psi_-. \tag{6.41}$$

Note that $\boldsymbol{X} = t\,\boldsymbol{E}_{\mathrm{M}}$, $t > 0$, parametrises only the inner of the light cone in $\mathbb{R}^{1,3}$.

On the one hand, the four-dimensional Laplacian in Minkowski space $\Box \equiv \Delta_{\mathbb{R}^{1,3}}$, usually referred to as *D'Alembert operator*, can be decomposed into

$$\Box = -\left(\partial_t^2 + \frac{3}{t}\,\partial_t\right) + \frac{1}{t^2}\,\Delta_{H_2^3} \tag{6.42}$$

with respect to the Minkowski metric $\boldsymbol{\delta} = -\,\mathrm{d}t^2 + t^2\,\boldsymbol{h}_-$. Applying this to $\hat\Psi$, we obtain

$$\Delta_4\hat\Psi = -\hat\Psi^3 - 3(-t+f)^2\,\hat\Psi^5 + \frac{3}{t}(-t+f)\,\hat\Psi^3 + \frac{1}{t^2}\,\Delta_{H_2^3}\hat\Psi. \tag{6.43}$$

On the other hand, in Cartesian coordinates we have $\boldsymbol{X} = (X^\alpha) = t\,\boldsymbol{E}_{\mathrm{M}}$, hence

$$\hat\Psi(\boldsymbol{X}) = \frac{1}{\|\boldsymbol{X} - \boldsymbol{P}\|_{\mathrm{M}}} = \frac{1}{\sqrt{(X^\alpha - P^\alpha)(X_\alpha - P_\alpha)}}. \tag{6.44}$$

In this case, the Minkowski metric is simply $\eta_{\alpha\beta} = \operatorname{diag}(1,1,1,-1)$ and the D'Alembertian $\Box = \eta^{\alpha\beta}\partial_\alpha\partial_\beta$. It follows that

$$\Box\hat{\Psi} = -\hat{\Psi}^3. \tag{6.45}$$

Comparing both expressions, we obtain

$$\frac{1}{t^2}\Delta_{H_2^3}\hat{\Psi} = -3\left(\frac{1}{t}\left(-t+f\right)\hat{\Psi}^2 - \left(-t+f\right)^2\hat{\Psi}^4\right)\hat{\Psi}. \tag{6.46}$$

Because of $(-t+f)\hat{\Psi}^2|_{t=1} = \frac{1}{2}$, this reduces on the upper sheet $t=1$ to

$$\Delta_{H_2^3}\Psi_- = -\frac{3}{4}\Psi_-. \tag{6.47}$$

## 6.3 Equivalence of the Solutions

It seems that we found three initial data sets

$$\bar{\boldsymbol{g}}_0 = \Psi_0^4\,\boldsymbol{h}_0 \qquad \text{on } \bar{\Sigma}_0 = \mathbb{R}^3 \setminus \boldsymbol{p}_A : A = 1,\dots,N-1, \tag{6.48a}$$

$$\bar{\boldsymbol{g}}_+ = \Psi_+^4\,\boldsymbol{h}_+ \qquad \text{on } \bar{\Sigma}_+ = S^3 \setminus \boldsymbol{P}_A : A = 1,\dots,N, \tag{6.48b}$$

$$\bar{\boldsymbol{g}}_- = \Psi_-^4\,\boldsymbol{h}_- \qquad \text{on } \bar{\Sigma}_- = H_2^3 \setminus \boldsymbol{P}_A : A = 1,\dots,N, \tag{6.48c}$$

corresponding to the three different shapes of Friedmann universes. But actually, this is not the case because the three seemingly different solutions describe the same initial data, that is, $\bar{\Sigma}_\pm$ and $\bar{\Sigma}_0$ are isometric. This means that there exists diffeomorphisms $\phi_{t+\delta t}\pm$ from $\bar{\Sigma}_\pm$ to $\bar{\Sigma}_0$ such that $\bar{\boldsymbol{g}}_\pm = \phi_\pm^*\,\bar{\boldsymbol{g}}_0$, or simply $\bar{\boldsymbol{g}}_\pm = \bar{\boldsymbol{g}}_0$.

The reason for this correspondence of the solutions is simple: We already know from section 3.2 that all three maximally symmetric spaces, the flat, the spherical, as well as the hyperbolic space, are conformally flat and related by stereographic projections. As we will show below, the diffeomorphisms $\phi_\pm$ are given by these stereographic projections combined with an isotropic scaling of $\bar{\Sigma}_0$.

If we recall the results on Friedmann dust universes from section 4.2, the equivalence of the solutions is not so surprising. As already stated above, the assumption that the spacetime possesses a time-symmetric hypersurface is very restrictive. In the case of Friedmann universes, the extrinsic curvature is proportional to the time derivative of the scale factor, $\bar{\boldsymbol{K}} = -\frac{\dot{a}}{a}\,\bar{\boldsymbol{g}}$. This implies that a constant-time slice is time-symmetric only if the scale factor possesses a maximum such that $\dot{a} = 0$, that is, the dust universe reaches its maximal expansion and is momentarily at rest before it starts recollapsing. Hence, only the spherical dust universe possesses a time-symmetric constant-time slice. Therefore, assuming that a dust universe can be fitted to a multi-black hole solution, we might expect that all three solutions are equivalent so that they can be approximated by a spherical dust universe.

Although some people seem to be aware of this connection, for example Lindquist and Wheeler [LW57] consider the projection of the pentatope and Bentivegna and Korzyński [BK12] the projection of the tesseract and use the flat solution, the equivalence of the different metrics has not yet been shown explicitly for the general case, as far as we know.

We start with the spherical case. First, we rotate the spherical solution so that the $N$-th end is at the south pole, $\boldsymbol{P}_N = \boldsymbol{S}$. This is always possible because the hypersphere is

a homogeneous space. If we set $\boldsymbol{A} = \boldsymbol{E}_4$ and $\boldsymbol{B} = \boldsymbol{P}_A$, the relation (3.39a) between the norms $\|\cdot\|_3$ and $\|\cdot\|_4$ yields

$$\frac{\|\boldsymbol{E}_4 - \boldsymbol{P}_N\|_4}{\|\boldsymbol{E}_4 - \boldsymbol{P}_A\|_4} = \frac{2}{\|\boldsymbol{P}_A - \boldsymbol{P}_N\|_4 \, \|\pi(\boldsymbol{E}_4) - \pi(\boldsymbol{P}_A)\|_3} = \frac{2}{\|\boldsymbol{P}_A - \boldsymbol{P}_N\|_4 \, \|R\,\boldsymbol{E}_3 - \pi(\boldsymbol{P}_A)\|_3}, \tag{6.49}$$

where $\pi(\boldsymbol{E}_4)(\chi, \vartheta, \varphi) = R\,\boldsymbol{E}_3(\vartheta, \varphi)$ and $R = \tan\frac{\chi}{2}$. Recall that an arbitrary point $(\sin\chi\,\boldsymbol{E}_3, \cos\chi)$ is projected to $(R\,\boldsymbol{E}_3, 0)$, see eq. (3.12).

Now, we can rewrite the metric as follows

$$\begin{aligned}
\bar{\boldsymbol{g}} = \Psi_+^4\,\boldsymbol{h}_+ &= \left(\sum_{A=1}^{N-1} \frac{\mu_A}{\|\boldsymbol{E}_4 - \boldsymbol{P}_A\|_4} + \frac{\mu_N}{\|\boldsymbol{E}_4 - \boldsymbol{P}_N\|_4}\right)^4 \boldsymbol{h}_+ \\
&= \left(1 + \sum_{A=1}^{N-1} \frac{\mu_A}{\mu_N} \frac{\|\boldsymbol{E}_4 - \boldsymbol{P}_N\|_4}{\|\boldsymbol{E}_4 - \boldsymbol{P}_A\|_4}\right)^4 \frac{\mu_N^4}{4} \frac{4}{\|\boldsymbol{E}_4 - \boldsymbol{P}_N\|_4^4}\,\boldsymbol{h}_+ \\
&= \left(1 + \sum_{A=1}^{N-1} \frac{\mu_A\mu_N}{\|\boldsymbol{P}_A - \boldsymbol{P}_N\|_4} \frac{1}{\frac{\mu_N^2}{2}\,\|R\,\boldsymbol{E}_3 - \pi(\boldsymbol{P}_A)\|_3}\right)^4 \left(\frac{\mu_N^2}{2}\right)^2 \left(\mathrm{d}R^2 + R^2\,\mathrm{d}\Omega^2\right).
\end{aligned} \tag{6.50}$$

In the last line we used that $\boldsymbol{\delta} = \mathrm{d}R^2 + R^2\,\mathrm{d}\Omega^2 = \frac{4}{\|\boldsymbol{E}_4 - \boldsymbol{P}_N\|_4^4}\,\boldsymbol{h}_+$, see eq. (3.21).

If we set

$$\boldsymbol{p}_A = \frac{\mu_N^2}{2}\,\pi(\boldsymbol{P}_A), \tag{6.51a}$$

$$\lambda_A = \frac{\mu_A\mu_N}{\|\boldsymbol{P}_A - \boldsymbol{P}_N\|_4}, \tag{6.51b}$$

and rescale the radial coordinate by $r = \frac{\mu_N^2}{2}\,R$, we obtain

$$\bar{\boldsymbol{g}}_+ = \Psi_+^4\,\boldsymbol{h}_+ = \left(1 + \sum_{A=1}^{N-1} \frac{\lambda_A}{\|\boldsymbol{x} - \boldsymbol{p}_A\|_3}\right)^4 \left(\mathrm{d}r^2 + r^2\,\mathrm{d}\Omega^2\right) = \Psi_0^4\,\boldsymbol{h}_0 = \bar{\boldsymbol{g}}_0, \tag{6.52}$$

where $\boldsymbol{x} = r\,\boldsymbol{E}_3$. Hence, we have proven the equivalence of $\bar{\boldsymbol{g}}_+$ and $\bar{\boldsymbol{g}}_0$.

In the hyperbolic case, we have to use the stereographic projection $\sigma$ (3.40) where $\sigma(\boldsymbol{E}_{\mathrm{M}}) = R\,\boldsymbol{E}_3$ with $R = \tanh\frac{u}{2}$. Since the Minkowski norm $\|\cdot\|_{\mathrm{M}}$ satisfies the relation (3.42a) for $\|\cdot\|_3$, analogously to the spherical case, the calculation is basically the same as before, we just have to substitute $\|\cdot\|_4$ by $\|\cdot\|_{\mathrm{M}}$. Hence, it follows

$$\bar{\boldsymbol{g}}_- = \Psi_-^4\,\boldsymbol{h}_- = \Psi_0^4\,\boldsymbol{h}_0 = \bar{\boldsymbol{g}}_0. \tag{6.53}$$

Altogether, all three solutions describe the same spatial metric

$$\bar{\boldsymbol{g}}_+ = \bar{\boldsymbol{g}}_0 = \bar{\boldsymbol{g}}_-. \tag{6.54}$$

Because of this, we will concentrate on one solution in the following.

The flat and the hyperbolic solution possess some peculiarities making things more complicated than necessary. In the flat case, one end is treated differently than the others, namely the asymptotically flat end at infinity corresponding to the '1'-term. Whereas

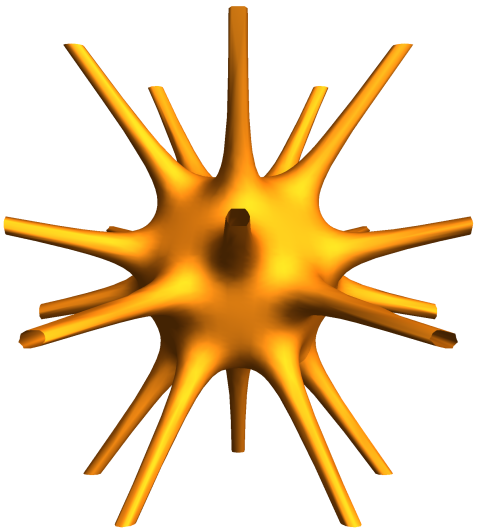

**Figure 6.3:** Plot of the conformal factor $\Psi(\chi,\vartheta,\varphi) = \sum_A \frac{\mu_A}{\|\boldsymbol{E}_4(\chi,\vartheta,\varphi)-\boldsymbol{P}_A\|}$ over the equatorial sphere $\chi = \frac{\pi}{2}$: If a point $\boldsymbol{P}_A$ is approached, the conformal factor diverges so that a spike forms.

the conformal factor diverges at the inner ends, all metric components remain finite if we approach infinity. Actually, all inner ends are asymptotically flat because any inner end of the spherical solution can be set to the south pole. However, the flat solution may be interesting for the comparison with a (post-)Newtonian approach because of the three-dimensional flat metric.

The hyperbolic case is even more peculiar because of the two separated hypersurfaces. Each one has an additional end at $u \to \pm\infty$. But as the stereographic projection shows, this is caused by a coordinate singularity. The coordinate transformation associated to the stereographic projection is not invertible on the unit-sphere in the flat space because the interior of the unit-sphere is projected to the upper sheet whereas the exterior is projected to the lower sheet.

The advantage of the spherical solution is that it does not possess any of these problems. In particular, all ends are treated in the same way. Since only the spherical dust universe possesses a time-symmetric slice, it is most natural to take the spherical initial data solution to study the fitting problem.

For these reasons, we restrict ourselves to the spherical solution from now on and drop the labels such that

$$\boldsymbol{g} = \Psi_+^4\, \boldsymbol{h}_+ \equiv \Psi^4\, \boldsymbol{h}, \tag{6.55a}$$

$$\Psi = \sum_{A=1}^{N} \frac{\mu_A}{\|\boldsymbol{E} - \boldsymbol{P}_A\|}. \tag{6.55b}$$

In fig. 6.3 the conformal factor at the equatorial sphere is plotted.

We want to mention that it is possible to express the distance $\|\boldsymbol{P}_A - \boldsymbol{P}_B\|$ in the embedding space in terms of the geodesic distance $\Lambda(\boldsymbol{P}_A, \boldsymbol{P}_B)$ on the hypersphere. Hence, it is possible to write the metric $\bar{\boldsymbol{g}}_+$ completely in terms of intrinsic properties of the hypersphere without the use of an embedding space.

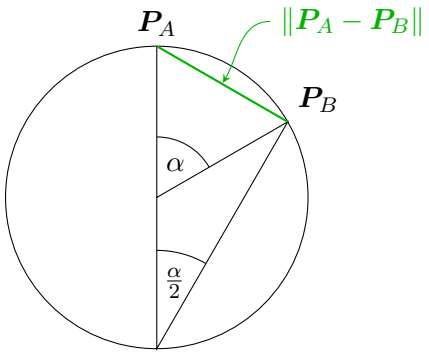


**Figure 6.4:** Relation between the geodesic distance on the sphere $\Lambda(\boldsymbol{P}_A, \boldsymbol{P}_B)$ and the distance $\|\boldsymbol{P}_A - \boldsymbol{P}_B\|$ in the embedding space for two points $\boldsymbol{P}_A$ and $\boldsymbol{P}_B$. The geodesic distance is given by the the angle $\alpha$ between the two points, $\cos\alpha = \boldsymbol{P}_A \cdot \boldsymbol{P}_B$.

The geodesic distance equals the angle $\Lambda(\boldsymbol{P}_A, \boldsymbol{P}_B) = \alpha_{AB}$ between $\boldsymbol{P}_A$ and $\boldsymbol{P}_B$ given by $\boldsymbol{P}_A \cdot \boldsymbol{P}_B = \cos\alpha_{AB}$. Hence, we obtain

$$\|\boldsymbol{P}_A - \boldsymbol{P}_B\| = \sqrt{2(1 - \boldsymbol{P}_A \cdot \boldsymbol{P}_B)} = \sqrt{2(1 - \cos\alpha_{AB})} = 2\sin\frac{\alpha_{AB}}{2} = 2\sin\frac{\Lambda(\boldsymbol{P}_A, \boldsymbol{P}_B)}{2}. \tag{6.56}$$

A geometric illustration of this relation is shown in fig. 6.4.

### Unified Description

It is also possible to drop the geometric view and take a more algebraic point of view: If we use Lie sphere vectors, see section 3.3, we obtain a unified description for the initial data solution.

Recall that a point $\boldsymbol{P}$ on the hypersphere is given by the Lie sphere vector $\boldsymbol{\omega} = (1, \boldsymbol{P})$. Therefore, we obtain for the conformal factor

$$\Psi = \sum_A \frac{\mu_A}{\|\boldsymbol{E}_4 - \boldsymbol{P}_A\|} = \sum_A \frac{\mu_A}{\sqrt{-2\,(\boldsymbol{E}_4 \cdot \boldsymbol{P}_A - 1)}} = \sum_A \frac{\mu_A}{\sqrt{-2\,\langle\boldsymbol{\xi}, \boldsymbol{\omega}_A\rangle}}, \tag{6.57}$$

where $\boldsymbol{\xi} = (1, \boldsymbol{E}_4)$ and $\boldsymbol{E}_4 = (\sin\chi\,\boldsymbol{E}_3, \cos\chi)$. The Lie sphere vector $\boldsymbol{\xi}$ parametrises the Möbius sphere on the light cone in $\mathbb{R}^{4,1}$. The induced metric of the Möbius sphere is the round metric, hence

$$\boldsymbol{h} = \eta_{\alpha\beta}\,\mathbf{d}\xi^\alpha\,\mathbf{d}\xi^\beta \equiv \mathbf{d}\boldsymbol{\xi}^2, \tag{6.58}$$

where $\eta_{\alpha\beta} = \mathrm{diag}\,(1, 1, 1, 1, -1)$. Therefore, the spatial metric is given by

$$\bar{\boldsymbol{g}} = \left(\frac{1}{\mu_N}\sum_{A=1}^{N} \frac{\mu_A}{\sqrt{-\langle\boldsymbol{\xi}, \boldsymbol{\omega}_A\rangle}}\right)^4 \mathbf{d}\boldsymbol{\xi}^2, \tag{6.59}$$

where we divided the conformal factor by $\frac{\mu_N}{\sqrt{2}}$ in order to get rid of the additional scaling which we needed to show the isometry.

The flat and hyperbolic solutions can be derived from this form of the spatial metric if we use the corresponding Lie vectors: In the flat case, we have

$$\boldsymbol{\omega} = \left(1, \frac{2\boldsymbol{p}}{1+\boldsymbol{p}^2}, \frac{1-\boldsymbol{p}^2}{1+\boldsymbol{p}^2}\right), \tag{6.60a}$$

$$\boldsymbol{\xi} = \left(1, \frac{2r}{1+r^2}\,\boldsymbol{E}_3, \frac{1-r^2}{1+r^2}\right), \tag{6.60b}$$

and in the hyperbolic case

$$\boldsymbol{\omega} = \left(\frac{\boldsymbol{P}}{P_0}, \frac{1}{P_0}\right), \tag{6.61a}$$

$$\boldsymbol{\xi} = \left(\frac{\boldsymbol{E}_\mathrm{M}}{\cosh u}, \frac{1}{\cosh u}\right) = \left(1, \tanh u\,\boldsymbol{E}_3, \pm\frac{1}{\cosh u}\right). \tag{6.61b}$$

Note that we have to use a fixed representation such that the first component is $\omega_0 = 1$ in all cases in order to obtain the correct results.

## 6.4 Inner Ends and Schwarzschild-like Behaviour

Finally, we investigate the asymptotic behaviour of the metric if we approach an inner end at $\boldsymbol{P}_A$. The considerations from the previous section already show that the space is asymptotically flat because any inner end of the spherical solution can be projected to infinity of the flat solution which is asymptotically flat.

### Mass of the Black Holes

Actually, each end $\boldsymbol{P}_A$ is asymptotically Schwarzschild-like and thus describes a black hole of mass $m_A$, determined by the parameters $\mu_A$ [Cli14]. This means that, using appropriate coordinates such that $r \to \infty$ if $\|\boldsymbol{E}_4 - \boldsymbol{P}_A\| \to 0$, the metric can be written as

$$\boldsymbol{h} = \left(1 + \frac{m_A}{2r} + \mathcal{O}\left(r^{-2}\right)\right)^4 \left(\mathrm{d}r^2 + r^2\,\mathrm{d}\Omega^2\right), \tag{6.62}$$

where the mass $m_A$ of the black hole at $\boldsymbol{P}_A$ is given by

$$m_A = \sum_{B\neq A} \frac{2\mu_A\mu_B}{\|\boldsymbol{P}_B - \boldsymbol{P}_B\|}. \tag{6.63}$$

This is the spherical analogue of the results in the flat case which have already been obtained by Brill and Lindquist [BL63]: In the flat case, the masses are given by

$$m_A = 2\lambda_A\left(1 + \sum_{B\neq A}\frac{\lambda_B}{\|\boldsymbol{p}_A - \boldsymbol{p}_B\|}\right) \qquad \text{for } A \neq N, \tag{6.64a}$$

$$m_N = \sum_{B=1}^{N-1} 2\lambda_B \qquad \text{at inifinty}, \tag{6.64b}$$

where $\lambda_A = \frac{\mu_A\mu_N}{\|\boldsymbol{P}_A - \boldsymbol{P}_N\|}$ and $\boldsymbol{p}_A = \frac{\mu_A^2}{2}\,\pi(\boldsymbol{P}_A)$.

Although the Lichnerowicz equation is linear in our case, we want to stress that the mass of a black hole is determined by all black holes. Hence, if we add another black hole, the masses of all others change. Here, the non-linear nature of Einstein's equations becomes apparent.

For the proof, we perform a Taylor expansion of the conformal factor $\Psi$ using an appropriate radial coordinate $r$ such that $r = f\left(\frac{1}{\|\boldsymbol{E}_4 - \boldsymbol{P}_A\|}\right)$. The calculation is very similar to the one in the previous section 6.3 showing the equivalence of the flat and the spherical solution.

The metric has the form

$$\boldsymbol{g} = \Psi^4\, \boldsymbol{h} = \left(\sum_{B=1}^{N} \frac{\mu_B}{\|\boldsymbol{E}_4 - \boldsymbol{P}_B\|}\right)^4 \left(\mathbf{d}\chi^2 + \sin^2\chi\, \mathbf{d}\Omega^2\right). \tag{6.65}$$

In contrast to the previous calculations, we use a coordinates such that the $A$-th black hole is located at the north pole $\boldsymbol{P}_A = (0, 0, 0, 1)$. Then, the limit $\|\boldsymbol{E}_4 - \boldsymbol{P}_A\| \to 0$ corresponds to the limit $\chi \to 0$. Now we define a new radial coordinate by

$$r = \frac{\mu_A^2}{2} \cot\frac{\chi}{2}, \tag{6.66}$$

corresponding to a stereographic projection from the black hole at $\boldsymbol{P}_A$ combined with a rescaling by the factor $\frac{\mu_A^2}{2}$. Using

$$\mathbf{d}\chi = -\frac{4\mu_A^2}{\mu_A^4 + 4r^2}\, \mathbf{d}r, \tag{6.67a}$$

$$\sin\chi = \frac{4\mu_A^2 r}{\mu_A^4 + 4r^2}, \tag{6.67b}$$

$$\cos\chi = -\frac{\mu_A^4 - 4r^2}{\mu_A^4 + 4r^2}, \tag{6.67c}$$

the round metric $\boldsymbol{h}$ can be written as

$$\boldsymbol{h} = \left(\frac{4\mu_A^2}{\mu_A^4 + 4r^2}\right)^2 \left(\mathbf{d}r^2 + r^2\, \mathbf{d}\Omega^2\right) = \left(\frac{2\mu_A}{\sqrt{\mu_A^4 + 4r^2}}\right)^4 \boldsymbol{\delta}. \tag{6.68}$$

The $A$-th term of the conformal factor is

$$\frac{\mu_A}{\|\boldsymbol{E}_4 - \boldsymbol{P}_A\|} = \frac{\mu_A}{\sqrt{2\,(1 - \cos\chi)}} = \frac{\sqrt{\mu_A^4 + 4r^2}}{2\mu_A}. \tag{6.69}$$

so that we obtain

$$\Psi = \frac{\sqrt{\mu_A^4 + 4r^2}}{2\mu_A} + \sum_{B \neq A} \frac{\mu_B}{\|\boldsymbol{E}_4 - \boldsymbol{P}_B\|}. \tag{6.70}$$

Therefore the metric becomes

$$\boldsymbol{g} = \Psi^4\, \boldsymbol{h} = \left(1 + \frac{2\mu_A}{\sqrt{4r^2 + \mu_A^4}} \sum_{B \neq A} \frac{\mu_B}{\|\boldsymbol{E}_4(r, \vartheta, \varphi) - \boldsymbol{P}_B\|}\right)^4 \boldsymbol{\delta}. \tag{6.71}$$

where $\boldsymbol{E}_4(r,\vartheta,\varphi) = \left(\frac{4\mu_A^2 r}{4r^2+\mu_A^4}\,\boldsymbol{E}_3(\vartheta,\varphi), \frac{4r^2-\mu_A^4}{4r^2+\mu_A^4}\right)$.

Now, we can perform a Taylor series for small $\chi$ corresponding to an expansion in $\frac{1}{r}$, yielding

$$\boldsymbol{g} = \left(1 + \frac{\mu_A}{r}\sum_{B\neq A}\frac{\mu_B}{\|\boldsymbol{P}_A - \boldsymbol{P}_B\|} + \mathcal{O}\left(\frac{1}{r^2}\right)\right)^4 \boldsymbol{\delta}. \tag{6.72}$$

If we compare this with the spatial part of the Schwarzschild metric in isotropic coordinates (6.7)

$$\boldsymbol{h}_{\mathrm{S}} = \left(1 + \frac{m}{2r}\right)^4 \boldsymbol{\delta}, \tag{6.73}$$

this shows that the metric is asymptotically Schwarzschild-like and the associated mass is given by

$$m_A = \sum_{B\neq A}\frac{2\mu_A\mu_B}{\|\boldsymbol{P}_A - \boldsymbol{P}_B\|}. \tag{6.74}$$

Of course this is true for any end.

The equivalence to the result of Brill and Lindquist follows easily if we take into account an additional factor $\frac{\mu_N^2}{2}$ in the norm formula (3.39a) due to the rescaling of the radial coordinate. We are assuming again that the $N$-th mass is located at infinity. So for $A = N$ we obtain directly

$$m_N = \sum_{B\neq N}\frac{2\mu_B\mu_N}{\|\boldsymbol{P}_B - \boldsymbol{P}_N\|} = \sum_{B=1}^{N-1} 2\lambda_B. \tag{6.75}$$

using eq. (6.51b). In all other cases we get

$$\begin{aligned} m_A &= \sum_{B\neq A}\frac{2\mu_A\mu_B}{\|\boldsymbol{P}_A - \boldsymbol{P}_B\|} = \frac{2\mu_A\mu_N}{\|\boldsymbol{P}_A - \boldsymbol{P}_N\|} + \sum_{B\neq A}^{N-1}\frac{2\mu_A\mu_B}{\|\boldsymbol{P}_A - \boldsymbol{P}_B\|} \\ &= \frac{2\mu_A\mu_N}{\|\boldsymbol{P}_A - \boldsymbol{P}_N\|} + \sum_{B\neq A}^{N-1}\frac{2}{\|\boldsymbol{p}_A - \boldsymbol{p}_B\|}\frac{\mu_A\mu_N}{\|\boldsymbol{P}_A - \boldsymbol{P}_N\|}\frac{\mu_B\mu_N}{\|\boldsymbol{P}_B - \boldsymbol{P}_N\|} \\ &= 2\lambda_A + \sum_{B\neq A}^{N-1}\frac{2\lambda_A\lambda_B}{\|\boldsymbol{p}_A - \boldsymbol{p}_B\|}. \end{aligned} \tag{6.76}$$

Another possibility to determine the masses is given by the ADM-mass, named after Arnowitt, Deser and Misner [ADM59]. The ADM-mass is an attempt to associate energy to the gravitational field of asymptotically flat spacetimes. It can be calculated even if we consider only a single slice; it is not necessary to know the complete spacetime metric. The ADM-energy is defined as

$$E \equiv P^0 = \frac{1}{16\pi}\lim_{R\to\infty}\int_{S_R^2}(\partial_a g_{ab} - \partial_b g_{aa})\,n^b\,\mathrm{d}S, \tag{6.77}$$

where $S_r^2$ is a 2-sphere with radius $r$, $n^a$ its normal and $\mathbf{d}S$ its surface element. Similarly, it is possible to define a momentum vector

$$P_a = \frac{1}{8\pi}\lim_{R\to\infty}\int_{S_R^2}(K_{ab} - \delta_{ab}\,\mathcal{K})\,n^b\,\mathrm{d}S. \tag{6.78}$$

Therefore, it is possible to associate a 4-momentum $P_\mu$ to a gravitational field. The ADM-mass is defined as its norm $M^2 = -\eta^{\mu\nu} P_\mu P_\nu$. It can be shown that the $P_\mu$ is a future-directed time-like or light-like vector if the dominant energy condition for the matter energy-momentum tensor holds. This is known as the *Positive Energy Theorem* [SY79; SY81; Wit81].

In general, for a metric of the form $\boldsymbol{g} = \left(1 + \frac{m}{2r} + \mathcal{O}\left(\frac{1}{r^2}\right)\right)^4 \boldsymbol{\delta}$ we obtain $P_0 = -m$ since the higher order terms $\mathcal{O}\left(\frac{1}{r^2}\right)$ do not contribute to the integral in the limit $r \to \infty$.

Obviously the momentum vanishes identically, $P_a \equiv 0$, because we are considering a time-symmetric initial surface with $\boldsymbol{K} \equiv 0$. This corresponds to the fact that the black holes are momentarily at rest.

**Apparent Horizons and Minimal Surfaces**

So we have $N$ asymptotically flat ends each associated with a mass $m_A$. The usual interpretation is based on the flat form. In this case, it is assumed that we have an asymptotically flat space containing $N-1$ black holes with mass $m_A$. The asymptotically flat end at infinity does not correspond to a black hole but the associated mass equals the total mass of all black holes including their mutual interaction energy given by $m_N - \sum_{A=1}^{N-1} m_A$.

According to the Schwarzschild case in section 6.1, we expect that the ends are causally disconnected by an event horizon. Since an event horizon is defined only globally with respect to the spacetime metric, we need a local characterisation of a black hole which we can apply in a single slice. One characterisation is given by the so-called *apparent horizons*.

An apparent horizon is the outermost trapped surface, that is, the boundary of a region from which nothing can escape. Technically, this means that the expansion $\theta$ of any outgoing congruence inside this region is non-positive. In particular, the outermost trapped surface satisfies

$$\theta = \bar{\nabla}_a s^a + \bar{K}_{ab} s^a s^b - \mathcal{K} = 0, \tag{6.79}$$

where $\boldsymbol{s}$ is the outward-pointing vector normal to the trapped surface inside $\bar{\Sigma}$.

Apparent horizons are no invariants objects because they depend on the slicing. For example, there exists slicings of the Schwarzschild spacetime which does not possess an apparent horizon [WI91]. However, the existence of an apparent horizon implies, under certain technical assumptions like the dominant energy condition, the existence of a black hole and the apparent horizon coincides with or is at least contained in the event horizon [HE73].

In the case of time-symmetric initial data such that $\bar{\boldsymbol{K}} = 0$, apparent horizons are determined by $\bar{\nabla}_a s^a = 0$. It can be shown that this condition implies that the area of the surface is minimal, hence they are called *minimal surfaces*. We associate a black hole to an end only if the end is enclosed by such a minimal surface.

In an asymptotically flat space with $N$ black holes, it is possible that another minimal surface forms around infinity when the black holes approach each other. This is illustrated in fig. 6.5. These are the solutions we are interested in. Such a solution corresponds to a spherical solution with $N+1$ inner ends, each enclosed by an apparent horizon. In the following, we are always assuming that this is the case. Note that observers at ends enclosed by a minimal surfaces observe only one black hole, the other ones are hidden behind the horizon.

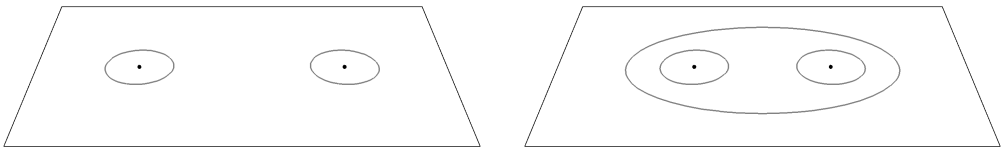

**(a)** Asymptotically flat space with two black holes

**(b)** Closed space with three black holes

**Figure 6.5:** The left figure shows an asymptotically flat spacetime with two black holes. Only these are enclosed by a minimal surface but not the flat end. In the right figure the two black holes are so close to each other that another minimal surface has formed enclosing both black holes. In the outer region, one would observe only a single black hole. In the inner region between the minimal surfaces, an observer would see a closed space with three black holes.

Before we go on, we want to mention two cases in which this assumption is false. At first consider the case of only one end. We would expect that this describes a space with a single black hole. However, this is not true. As eq. (3.19a) shows, this is just the flat space looking like a single black hole space on the 3-sphere,

$$\boldsymbol{\delta} = \left(\frac{\mu}{\|\boldsymbol{E}_4 - \boldsymbol{P}\|^4}\right)^4 \boldsymbol{h}. \tag{6.80}$$

This is also confirmed by calculating the mass of this end that turns out to be zero, $m = 0$, so that the space must be flat as a consequence of the Positive Energy Theorem.

This may raise the question which initial data describe a single black hole. For this reason we reconsider the Schwarzschild solution $\boldsymbol{g} = (1 + \frac{m}{2r})^4 \boldsymbol{\delta}$ which can be written as

$$\boldsymbol{g} = \left(\frac{\mu_+}{\|\boldsymbol{E}_4 - \boldsymbol{S}\|} + \frac{\mu_-}{\|\boldsymbol{E}_4 + \boldsymbol{S}\|}\right) \boldsymbol{h}, \tag{6.81}$$

where $\boldsymbol{S} = (0, 0, 0, -1)$. Hence, the Schwarzschild spacetime is described by two antipodal ends on the hypersphere. This follows easily from the previous considerations:

$$\begin{aligned} \boldsymbol{g} &= \left(\frac{\mu_+}{\|\boldsymbol{E}_4 - \boldsymbol{S}\|} + \frac{\mu_-}{\|\boldsymbol{E}_4 + \boldsymbol{S}\|}\right)^4 \boldsymbol{h} \\ &= \left(1 + \frac{\mu_- \|\boldsymbol{E}_4 - \boldsymbol{S}\|}{\mu_+ \|\boldsymbol{E}_4 + \boldsymbol{S}\|}\right)^4 \left(\frac{\mu_+}{\|\boldsymbol{E}_4 - \boldsymbol{S}\|}\right)^4 \boldsymbol{h} \\ &= \left(1 + \frac{\mu_+\mu_-}{\mu_+^2 \cot \frac{\chi}{2}}\right)^4 \boldsymbol{\delta} = \left(1 + \frac{m}{2r}\right)^4 \boldsymbol{\delta}, \end{aligned} \tag{6.82}$$

where $m = m_\pm = \mu_+\mu_-$. In this case, there is no inner region between the minimal surfaces because both coincide at the equator so that there is only one apparent horizon.

Note that, in the case of two ends, we always associate the same mass $m_{1,2} = \frac{2\mu_1\mu_2}{\|\boldsymbol{P}_1 - \boldsymbol{P}_2\|}$ to each end, irrespectively of their positions and mass parameters. For this reason0, the questions remain whether it is possible to find a time-symmetric space with two black holes with different masses and whether a solution with two antipodal black holes exists. Maybe this is possible by superposing multiple black holes such that they form two groups enclosed by an apparent horizon and one observes only two horizons in the interior region.

# 7 Friedmann-like Configurations

In this chapter, we study which black hole configurations $\{\boldsymbol{P}_A, \mu_A\}$, being solutions to the Hamiltonian constraint discussed in the previous chapter 6, possess an approximation by a spherical dust universe at the moment of maximal expansion. The main goal of this chapter is to explain in which sense they are similar and to give a quantifiable criterion for the degree of similarity.

The two main properties describing a spherical dust universe are the size $a_0$ of the universe and the constant density $\rho_0$ at the moment of maximal expansion. However, these are not independent of each other. As shown in chapter 4, we have

$$2\pi^2 \rho_0 a_0^3 = M_0 \equiv \frac{3\pi}{4}\, a_0, \tag{7.1}$$

hence $\rho_0 = \frac{3}{8\pi a_0^2}$. Here, $M_0 = 2\pi^2 \rho_0 a_0^3 = \int_{S^3} \rho \,\mathrm{d}V$ is the total mass of the dust which we will usually consider instead of the density.

We say that a multi-black hole solution is *Friedmann-like*, that is, similar to a spherical dust universe, if the size of the black hole space and the total mass of all black holes match those of a Friedmann solution.

The total mass of the black holes is simply

$$M = \sum_A m_A = \sum_A \sum_{B \neq A} \frac{2\mu_A \mu_B}{\|\boldsymbol{P}_A - \boldsymbol{P}_B\|}. \tag{7.2}$$

In contrast, there is no obvious choice for the radius of a sphere which approximates best the black hole solution, see also fig. 7.1. Comparing the spatial metric of a dust universe, $\bar{\boldsymbol{g}} = a_0^2 \boldsymbol{h}$, and the initial data, $\bar{\boldsymbol{g}} = \Psi^4 \boldsymbol{h}$, the squared conformal factor $\Psi^2$ may be considered as the radius. However, it is not constant on the hypersphere unlike $a(t)$ for cosmological solutions. Therefore we have to find a procedure to select a radius, for example, some average scheme for the conformal factor. In section 7.1 we will discuss several possibilities.

Of course, there will be huge deviations from the fitting sphere close to the inner ends because the conformal factor diverges here. However, we do not expect the space to be Friedmann-like close to the masses but only far away from them. In the vicinity of the black holes, the behaviour should be dominated by the black holes, analogously to our Universe where the local dynamics are not Friedmann-like in the domain of galaxies.

Recently, Korzyński [Kor14] suggested an averaging procedure for these black hole solutions. He proved two theorems characterising the deviation from a spherical dust universe depending on a certain property called *modified cap discrepancy*. But these theorems do not allow to predict if a solution is Friedmann-like as he shows in an example. We will discuss his results in section 7.2.

Finally in section 7.3, as one of the main results of this thesis, we suggest a characterisation of Friedmann-like configurations based on mean inverse distance. This provides a value for the size of the universe based on the total mass of the black holes. In contrast, the result of Korzyński is based on an ad hoc averaging procedure without good justification.

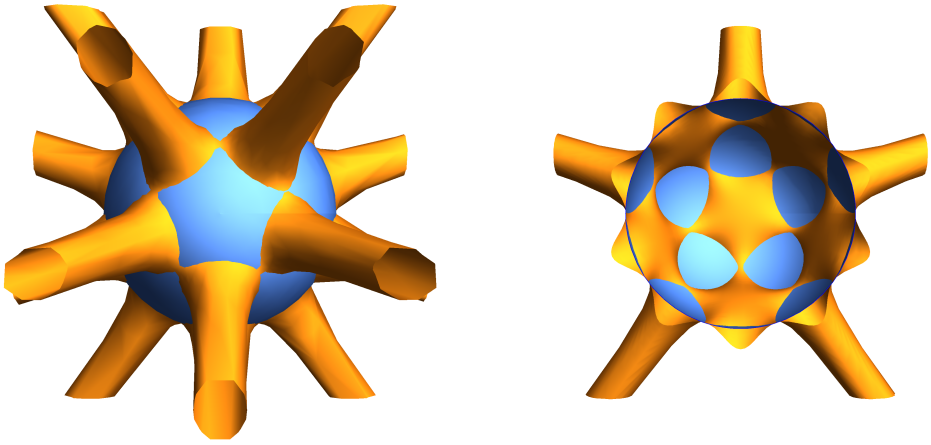

**(a)** View from the outside **(b)** View from the inside

**Figure 7.1:** There is no obvious choice for the size $a_0$ of the fitting sphere approximating the squared conformal factor $\Psi^2$. The shown sphere is chosen arbitrarily. How do we decide if it is a good fit?

We stress again that we are not yet interested in the time evolution but we characterise the initial data only. Hence, we cannot tell if Friedmann-like initial data also have a time evolution similar to a spherical dust universe. A first outlook to this topic will be part of the next chapter 9.

## 7.1 Fitting a Dust Universe

There are several candidates to select a specific dust universe approximating the initial data solution which are more or less reasonable. We will explain the motivations for each choice and discuss their disadvantages.

### Minimum Value

It seems reasonable to assume that the space is most Friedmann-like far away from the black holes because we expect that the black holes dominate the dynamics in their environment and distort the spacetime. This is similar to our Universe where the dynamics in the region of galaxies are clearly not Friedmann-like. Therefore it is reasonable to choose a certain value of the conformal factor in the far-field. Since the conformal factor is positive everywhere and diverges only close to the black holes, the regions far away are those around the local minima of the conformal factor. Thus we may suggest that a good candidate for the best fit is given by

$$a_0 = \Psi^2_{\min}. \tag{7.3}$$

### Averaging the Conformal Factor

In the above case, we have only deviation of the conformal factor from the fitting sphere in one direction. It seems more natural to take some average value of $\Psi$ so that the deviations occur in both directions similar to the Lindquist-Wheeler models discussed in section 5.2. Since the conformal factor is a scalar, it should be possible to apply the usual averaging

schemes and take the spatial average as in

$$\langle f \rangle = \frac{1}{\operatorname{vol} V} \int_V f \, \mathrm{d}V. \tag{7.4}$$

However, there are two main problems.

First, there is the ambiguity which function to average. The spatial metric is $\bar{\boldsymbol{g}} = a_0^2 \boldsymbol{h}$ in the cosmological case and $\bar{\boldsymbol{g}} = \Psi^4 \boldsymbol{h}$ for the initial data. If we compare both metrics, there are two obvious choices we can make: Since the radius corresponds to the squared conformal factor $a_0 \leftrightarrow \Psi^2$, we may set

$$a_0 = \langle \Psi \rangle^2, \tag{7.5}$$

or alternatively

$$a_0 = \langle \Psi^2 \rangle. \tag{7.6}$$

The second problem concerns the volume form. Usually, we would average with respect to the volume form obtained from the metric $\bar{\boldsymbol{g}} = \Psi^4 \boldsymbol{h}$. But as mentioned above the conformal factor diverges at the boundaries of our space. Furthermore, our manifold is $S^3 \setminus \{\boldsymbol{P}_A\}$ which is not compact and its volume is infinite.

However, if we use the picture that the conformal factor $\Psi$ is a function on the round hypersphere with the interpretation of $\Psi^2$ as height, it seems more appropriate to take averages with respect to the round metric $\boldsymbol{h}$ in order to obtain the mean height. Such a procedure was already suggested by Korzyński [Kor14]. For some function $f$ on the hypersphere, its average is given by

$$\langle f \rangle = \frac{1}{2\pi^2} \int_{S^3} f(\chi, \vartheta, \varphi) \sin^2 \chi \, \mathrm{d}\chi \sin \vartheta \, \mathrm{d}\vartheta \, \mathrm{d}\varphi, \tag{7.7}$$

where the factor $2\pi^2$ in the denominator is the volume of the hypersphere.

Next we determine the average of the conformal factor

$$\Psi = \sum_{A=1}^{N} \frac{\mu_A}{\|\boldsymbol{X} - \boldsymbol{P}_A\|}. \tag{7.8}$$

Since the averaging is linear, we can consider each term on its own and choose an adapted coordinate system such that the black hole is always located at the north pole, hence $\boldsymbol{P}_A = (0,0,0,1)$ and $\|\boldsymbol{X} - \boldsymbol{P}_A\| = \sqrt{2(1-\cos\chi)} = 2\sin\frac{\chi}{2}$. This yields

$$\begin{aligned}
\langle \Psi \rangle &= \sum_{A=1}^{N} \frac{\mu_A}{2\pi^2} \int_{S^3} \frac{1}{\|\boldsymbol{X} - \boldsymbol{P}_A\|} \sin^2 \chi \, \mathrm{d}\chi \sin \vartheta \, \mathrm{d}\vartheta \, \mathrm{d}\varphi \\
&= \sum_{A=1}^{N} \frac{\mu_A}{\pi} \int_0^{\pi} \frac{\sin^2 \chi}{\sin \frac{\chi}{2}} \, \mathrm{d}\chi = \sum_{A=1}^{N} \frac{8\mu_A}{\pi} \int_0^{\frac{\pi}{2}} \sin\chi' \cos^2 \chi' \, \mathrm{d}\chi' \\
&= -\sum_{A=1}^{N} \frac{8\mu_A}{3\pi} \left[\cos^3 \chi'\right]_0^{\frac{\pi}{2}} = \frac{8}{3\pi} \sum_A \mu_A,
\end{aligned} \tag{7.9}$$

where $\chi' = \frac{\chi}{2}$. Hence, the size of the fitted universe is given by

$$a_0 = \langle \Psi \rangle^2 = \frac{64}{9\pi^2} \sum_{A,B=1}^{N} \mu_A \mu_B. \tag{7.10}$$

Perhaps surprisingly, this is independent of the distribution of black holes because neither their positions nor mutual distances appear.

The calculation of the average of $\Psi^2$ takes some more work, therefore we only show the most important steps. Again, we can treat each term on its own and choose an adapted coordinate system such that one black hole is located at the north pole $\boldsymbol{P}_A = (0,0,0,1)$ while the second can be placed at $\boldsymbol{P}_B = (0,0,\sin\alpha_{AB},\cos\alpha_{AB})$, where $\alpha_{AB}$ is the angle between the black holes, $\cos\alpha_{AB} = \boldsymbol{P}_A \cdot \boldsymbol{P}_B$. Then the denominator of $\Psi^2$ can be written as

$$\|\boldsymbol{X}-\boldsymbol{P}_A\|\,\|\boldsymbol{X}-\boldsymbol{P}_B\| = 2\sqrt{1-\cos\chi}\sqrt{1-\sin\alpha_{AB}\sin\chi\cos\vartheta-\cos\alpha_{AB}\cos\chi}. \tag{7.11}$$

In the following we use the abbreviations $s \equiv \sin\alpha_{AB}$ and $c \equiv \cos\alpha_{AB}$. In the first steps, we perform the integration with respect to $\vartheta$ and $\varphi$, yielding

$$\begin{aligned}
\langle\Psi^2\rangle &= \sum_{A,B}\frac{\mu_A\mu_B}{2\pi^2}\int_{S^3}\frac{1}{\|\boldsymbol{X}-\boldsymbol{P}_A\|\,\|\boldsymbol{X}-\boldsymbol{P}_B\|}\sin^2\chi\,\mathrm{d}\chi\sin\vartheta\,\mathrm{d}\vartheta\,\mathrm{d}\varphi\\
&= \sum_{A,B}\frac{\mu_A\mu_B}{2\pi^2}\int_0^\pi \mathrm{d}\chi\,\frac{\sin\chi}{\sqrt{1-\cos\chi}}\int_0^\pi \mathrm{d}\vartheta\,\frac{\sin\chi\sin\vartheta}{\sqrt{1-s\sin\chi\cos\vartheta-c\cos\chi}}\\
&= \sum_{A,B}\frac{\mu_A\mu_B}{\pi\,s}\int_0^\pi \mathrm{d}\chi\,\frac{\sin\chi}{\sqrt{1-\cos\chi}}\left(\sqrt{1+s\sin\chi-c\cos\chi}-\sqrt{1-s\sin\chi-c\cos\chi}\right).
\end{aligned} \tag{7.12}$$

In order to perform the $\chi$-integration, it is useful to change to the coordinate $t = \tan\frac{\chi}{2}$. This enables us to do some further simplifications so that we obtain

$$\begin{aligned}
\langle\Psi^2\rangle &= \sum_{A,B}\frac{2\sqrt{2}\mu_A\mu_B}{\pi\,s}\int_0^\infty \mathrm{d}t\,\frac{\sqrt{(1+c)t^2+2st+(1-c)}-\sqrt{(1+c)t^2-2st+(1-c)}}{(1+t^2)^2}\\
&= \sum_{A,B}\frac{2\sqrt{2}\mu_A\mu_B}{\pi\,s\sqrt{1+c}}\int_0^\infty \mathrm{d}t\,\frac{(1+c)t+s-|(1+c)t-s|}{(1+t^2)^2}\\
&= \sum_{A,B}\frac{4\sqrt{2}\mu_A\mu_B}{\pi\,s\sqrt{1+c}}\left((1+c)\int_0^{\frac{s}{1+c}}\mathrm{d}t\,\frac{t}{(1+t^2)^2}+s\int_{\frac{s}{1+c}}^\infty \mathrm{d}t\,\frac{1}{(1+t^2)^2}\right)\\
&= \sum_{A,B}\frac{2\mu_A\mu_B}{\pi\,s\cos\frac{\alpha_{AB}}{2}}\left[\left((1+c)-\frac{1+c}{1+\frac{s^2}{(1+c)^2}}\right)+s\left(\frac{\pi}{2}-\frac{\frac{s}{1+c}}{1+\frac{s^2}{(1+c)^2}}-\arctan\frac{s}{1+c}\right)\right]\\
&= \sum_{A,B=1}^{N}\mu_A\mu_B\,\frac{\pi-\alpha_{AB}}{\pi\cos\frac{\alpha_{AB}}{2}}.
\end{aligned} \tag{7.13}$$

Note the splitting of the integral in the third line due to the appearance of the absolute value in the second line. Because of $a_0 = \langle\Psi^2\rangle$, we obtain

$$a_0 = \sum_{A,B=1}^{N}\mu_A\mu_B\,\frac{\pi-\alpha_{ij}}{\pi\cos\frac{\alpha_{ij}}{2}}. \tag{7.14}$$

In contrast to $\langle\Psi\rangle^2$, this result depends on the distribution of black holes on the hypersphere because of the appearance of the mutual angles $\alpha_{AB}$ between two points. Since the second average takes the distribution into account, it may be a better choice.

### Total Mass

The average density must also fit to the chosen Friedmann dust universe $\rho_0 = \frac{3}{8\pi a_0^2}$. The average density is simply the total mass $M = \sum_A m_A$ of all black holes divided by the volume $V = 2\pi^2 a_0^3$ of the fitting hypersphere such that

$$\langle \rho \rangle = \frac{M}{V} = \frac{\sum_A m_A}{2\pi^2 a_0^3}. \tag{7.15}$$

For this reason we have to check if $\langle \rho \rangle \approx \rho_0$ or equivalently, after multiplying with $2\pi^2 a_0^3$, if

$$M = \sum_A m_A \approx \frac{3\pi}{4} a_0 = M_0. \tag{7.16}$$

This is simply the statement that the total masses in both solutions coincide for the chosen size $a_0$ of the universes. We could ensure this by demanding that the size of the fitted dust universe should be

$$a_0 = \frac{4}{3\pi} \sum_A m_A = \frac{8}{3\pi} \sum_A \sum_{B \neq A} \frac{\mu_A \mu_B}{\|\boldsymbol{P}_A - \boldsymbol{P}_B\|}. \tag{7.17}$$

### Approximations by Swiss-cheese and Lindquist-Wheeler models

Furthermore, for a configuration $\{\boldsymbol{P}_A, m_A\}$ we also have the two possibilities discussed in chapter 5: We construct the corresponding Swiss-cheese and Lindquist-Wheeler models for black holes with the same masses $m_A$ at the same positions $\boldsymbol{P}_A$ on the hypersphere and determine the size $a_0$ of the model.

In the case of a Swiss-cheese model, the masses $m_A$ determine spherical caps with opening angle $\beta_A$ via $m_A = \frac{a_0}{2} \sin^3 \beta_A$ and $a_0$ is the minimal value such that the spherical caps do not overlap. However, this probably yields a good approximation only if almost all dust is removed, that is, the dust universe is almost completely filled by Schwarzschild regions, and if the black holes are not too massive.

In the case of a Lindquist-Wheeler model, the size $a_0$ is the solution of the system $m_A = \frac{a_0}{2} \sin^3 \beta_A$ and $\pi = \sum_A (\beta_A - \sin \beta_A \cos \beta_A)$. Similar to the Swiss-cheese models, we expect a good approximation if the black holes are not too massive and too close to each other, that is, if the comparison sphere is almost completely covered.

### Summary

Altogether, we have six different candidates for the size of the fitted Friedmann dust universe, namely

$$a_0 = \Psi_{\min}^2 = \left( \min_{\boldsymbol{X} \in S^3} \sum_A \frac{\mu_A}{\|\boldsymbol{X} - \boldsymbol{P}_A\|} \right)^2, \tag{7.18a}$$

$$a_0 = \langle \Psi \rangle^2 = \left( \frac{8}{3\pi} \sum_A \mu_A \right)^2, \tag{7.18b}$$

$$a_0 = \langle \Psi^2 \rangle = \sum_{A,B} \mu_A \mu_B \frac{\pi - \alpha_{AB}}{\pi \cos \frac{\alpha_{AB}}{2}}, \tag{7.18c}$$

$$a_0 = \frac{4}{3\pi} \sum_A m_A = \frac{8}{3\pi} \sum_A \sum_{B \neq A} \frac{\mu_A \mu_B}{\|\boldsymbol{P}_A - \boldsymbol{P}_B\|}, \tag{7.18d}$$

and the ones obtained from the Swiss-cheese and Lindquist-Wheeler models. Furthermore, we will add another candidate in section 7.3. We will compare all these possibilities in more detail for different example configurations in chapter 8.

## 7.2 Korzyński's Theorems

We need a criterion to decide if a configuration is Friedmann-like in the sense that the space is almost a round sphere with radius $a_0$ far away from the black holes and the total mass satisfies $\sum_A m_A = \frac{3\pi}{4} a_0$. First results in this direction were given by Korzyński [Kor14] in two theorems. In his first theorem, he gives upper boundaries for the deviation of the averaged scale factor $\langle\Psi\rangle$ from the conformal factor $\Psi$. In the case that $\Psi - \langle\Psi\rangle \approx 0$ in the far region, this also implies $\langle\Psi\rangle \approx \Psi_{\min}$. The deviation of the total masses is treated in his second theorem.

As we will see below, the main parameters controlling the deviation from the fitted sphere are the distance to the closest black hole $\lambda_{\min}$ and the so-called *global modified cap discrepancy* $\mathcal{E}$. The deviation between the total masses depends on the mutual distances between the black holes, the maximal mass parameter and the global modified cap discrepancy.

#### Global Modified Cap Discrepancy

The global modified cap discrepancy is a possible parameter rating the uniformity of a configuration. It is defined as follows: Let us introduce the *cap discrepancy function*

$$\operatorname{disc}_{\boldsymbol{X}}(\lambda) = \frac{1}{2\pi^2} \operatorname{vol}(B(\boldsymbol{X}, \lambda)) - \sum_{\boldsymbol{P}_A \in B(\boldsymbol{X}, \lambda)} \frac{\mu_A}{\mu}, \tag{7.19}$$

where $\mu = \sum_A \mu_A$ and $B(\boldsymbol{X}, \lambda)$ is the spherical cap around $\boldsymbol{X}$ with opening angle $\lambda$ and $\operatorname{vol}(B(\boldsymbol{X}, \lambda))$ gives its volume

$$\operatorname{vol} B(\boldsymbol{X}, \lambda) = 2\pi \left(\lambda - \sin\lambda \cos\lambda\right). \tag{7.20}$$

The cap discrepancy function gives the part of the volume of the hypersphere covered by the spherical cap $B(\boldsymbol{X}, \lambda)$ diminished by the normalized mass parameter $\frac{\mu_A}{\mu}$ of every black hole lying within the cap. It satisfies $\operatorname{disc}_{\boldsymbol{X}}(0) = 0$ if $\boldsymbol{X} \notin \{\boldsymbol{P}_A\}$, else $\operatorname{disc}_{\boldsymbol{P}_A}(0) = -\frac{\mu_A}{\mu}$, and in both cases $\operatorname{disc}_{\boldsymbol{X}}(\pi) = 0$. The more evenly the black holes are distributed on the hypersphere and the less their masses vary, the lower is the maximum of the cap discrepancy function at every point. Hence, it appears to be a reasonable measure for the uniformity of a multi-black hole configuration.

In order to get an upper bound for the cap discrepancy function, we would usually take the supremum of $\operatorname{disc}_{\boldsymbol{X}}(\lambda)$ over the whole hypersphere, called *total cap discrepancy*, given by

$$E = \sup_{\boldsymbol{X} \in S^3} \sup_{0 \le \lambda \le \pi} \operatorname{disc}_{\boldsymbol{X}}(\lambda). \tag{7.21}$$

Unfortunately, the total cap discrepancy is a too weak upper bound for the following theorems. Actually, we need something bounding the discrepancy function more strongly for small values of $\lambda$. For this reason, we introduce a new function

$$F_D(\lambda) = \begin{cases} \frac{4D}{\pi} \sin^2(\lambda + D) & \text{for } 0 \le \lambda \le \frac{\pi}{2} - D, \\ \frac{4D}{\pi} & \text{for } \frac{\pi}{2} - D \le \lambda \le \pi. \end{cases} \tag{7.22}$$

At every point $\boldsymbol{X} \in S^3$, we can define the *modified cap discrepancy at* $\boldsymbol{X}$ by

$$\mathcal{E}_{\boldsymbol{X}} = \min\left\{D : \mathrm{disc}_{\boldsymbol{X}}(\lambda) \leq F_D(\lambda)\ \forall\ 0 \leq \lambda \leq \pi\right\}. \tag{7.23}$$

Taking the supremum of the modified cap discrepancy for all points of the hypersphere, we finally obtain the *global modified cap discrepancy*

$$\mathcal{E} = \sup_{\boldsymbol{X}\in S^3} \mathcal{E}_{\boldsymbol{X}}, \tag{7.24}$$

so that for all $\boldsymbol{X} \in S^3$

$$\mathrm{disc}_{\boldsymbol{X}}(\lambda) \leq F_{\mathcal{E}}(\lambda). \tag{7.25}$$

### Korzyński's Theorems

Now we are able to state the two theorems by Korzyński. Recall that $\Lambda(\boldsymbol{X}, \boldsymbol{Y})$ is the geodesic distance between two points $\boldsymbol{X}$ and $\boldsymbol{Y}$ on the hypersphere or equivalently the angle between the vectors $\boldsymbol{X}$ and $\boldsymbol{Y}$ in the embedding space so that $\boldsymbol{X} \cdot \boldsymbol{Y} = \cos\Lambda(\boldsymbol{X}, \boldsymbol{Y})$.

The first theorem gives upper bounds for the deviation of the conformal factor $\Psi$ from its average $\langle\Psi\rangle$:

**Theorem 7.1.** ***Deviation between the average and the conformal factor*** *[Kor14] Let $\boldsymbol{X} \in S^3 \setminus \{\boldsymbol{P}_1, \ldots, \boldsymbol{P}_N\}$, let $\lambda_{\min} = \min_{A=1,\ldots,N} \Lambda(\boldsymbol{X}, \boldsymbol{P}_A)$ and let $\mathcal{E}$ be the modified discrepancy of the configuration. Let $\epsilon$ satisfy $0 < \epsilon \leq 1$. Then, assuming that $\mathcal{E} + \lambda_{\min} < \frac{\pi}{2}$, the following inequality is satisfied:*

$$\Delta\Psi(\boldsymbol{X}) = \frac{|\Psi(\boldsymbol{X}) - \langle\Psi\rangle|}{\langle\Psi\rangle} \leq C_\epsilon U_\epsilon(\mathcal{E}, \lambda_{\min}),$$

*where*

$$\begin{aligned}
U_\epsilon(\mathcal{E}, \lambda_{\min}) &= \max(U_{1,\epsilon}, U_{2,\epsilon}, U_{3,\epsilon}),\\
U_{1,\epsilon}(\mathcal{E}, \lambda_{\min}) &= \frac{2\pi^\epsilon}{3}\lambda_{\min}^{2-\epsilon},\\
U_{2,\epsilon}(\mathcal{E}, \lambda_{\min}) &= \frac{4\mathcal{E}}{\pi}\left(1 + 2\mathcal{E}\lambda_{\min}^{-\frac{1+\epsilon}{2}}\right)^2,\\
U_{3,\epsilon}(\mathcal{E}, \lambda_{\min}) &= \frac{4\mathcal{E}}{\pi\cos^{1+\epsilon}\mathcal{E}},
\end{aligned}$$

*and the $\epsilon$-dependent constant $C_\epsilon$ is*

$$C_\epsilon = \frac{3\pi}{16}\int_0^\pi \left|\left(\frac{1}{\sin\frac{\lambda}{2}}\right)'\right| V^{1+\epsilon}(\lambda)\,\mathrm{d}\lambda$$

*with*

$$V(\lambda) = \begin{cases} \sin\lambda & \text{for } 0 \leq \lambda \leq \frac{\pi}{2},\\ 1 & \text{for } \frac{\pi}{2} \leq \lambda \leq \pi. \end{cases}$$

The second theorem gives upper bounds for the difference between the total mass $\sum_A m_A$ and the corresponding dust mass $M_0 = \frac{3\pi}{4}a_0$:

**Theorem 7.2.** ***Deviation between the total masses*** *[Kor14]*
*Let*

$$\begin{aligned}\delta_{\min} &= \min_{A=1,\dots,N} \min_{\substack{B=1,\dots,N,\\ B\neq A}} \Lambda(\boldsymbol{P}_A, \boldsymbol{P}_B),\\ \delta_{\max} &= \max_{A=1,\dots,N} \min_{\substack{B=1,\dots,N,\\ B\neq A}} \Lambda(\boldsymbol{P}_A, \boldsymbol{P}_B),\\ \alpha_{\max} &= \max_{A=1,\dots,N} \alpha_A,\end{aligned}$$

*and let $\mathcal{E}$ be the modified discrepancy of the configuration. Let $\epsilon$ satisfy $0 < \epsilon \leq 1$. Then, assuming that $\mathcal{E} + \delta_{\min} < \frac{\pi}{2}$, the following inequality holds*

$$\Delta M = \frac{|\sum_A m_A - M_0|}{M_0} \leq C_\epsilon W_\epsilon(\mathcal{E}, \frac{\alpha_{\max}}{\alpha}, \delta_{\max}, \delta_{\min}) + \tfrac{\alpha_{\max}}{\alpha},$$

*where*

$$\begin{aligned}W_\epsilon(\mathcal{E}, \lambda_{\min}) &= \max(W_{1,\epsilon}, W_{2,\epsilon}, W_{3,\epsilon}),\\ W_{1,\epsilon}(\mathcal{E}, \frac{\alpha_{\max}}{\alpha}, \delta_{\max}, \delta_{\min}) &= \frac{2\pi^\epsilon}{3}\delta_{\max}^{2-\epsilon},\\ W_{2,\epsilon}(\mathcal{E}, \frac{\alpha_{\max}}{\alpha}, \delta_{\max}, \delta_{\min}) &= \frac{4\mathcal{E}}{\pi}\left(1 + \mathcal{E}\delta_{\min}^{-\frac{1+\epsilon}{2}}\right)^2 + 2\pi^{1+\epsilon}\frac{\alpha_{\max}}{\alpha}\delta_{\min}^{-1-\epsilon},\\ W_{3,\epsilon}(\mathcal{E}, \frac{\alpha_{\max}}{\alpha}, \delta_{\max}, \delta_{\min}) &= \frac{\frac{4\pi}{\mathcal{E}} + \frac{\alpha_{\max}}{\alpha}}{\cos^{1+\epsilon}\mathcal{E}},\end{aligned}$$

*and $C_\epsilon$ is defined just like in theorem 7.1.*

**Open Questions and Problems**

These theorems give upper bounds for the deviation from the fitted dust universe with $a_0 = \langle\Psi\rangle^2$. Hence, any reasonable choice for $a_0$ must be close to $\langle\Psi\rangle^2$ for a uniform configuration. However, the global modified cap discrepancy $\mathcal{E}$ is not a good parameter to decide if a given configuration is uniform. The reason for this is that, even for a small modified cap discrepancy $\mathcal{E} \ll 1$, it is not guaranteed that both deviations, $\Delta\Psi(\boldsymbol{X})$ in the far region as well as $\Delta M$, are small.

Korzyński himself presented a counterexample in the same article [Kor14]: He considered a configuration constructed by the tesseract projection, which we will also study in the next chapter 8, with pairs of black holes in every cell. In this case, we have $\Delta\Psi(\boldsymbol{X}) \approx 0$ in most regions but $\Delta M \approx 2$.

However, we were expecting problems in such a scenario because it violates our assumption to hide the local dynamics by replacing bound systems by a single black hole. If we take a pair of black holes, this is not the case because they form an interacting bound system. It would be more reasonable to substitute the black hole pair by a single black hole with an appropriate mass. This is supported by the observation that the model with single black holes is Friedmann-like, that is, it satisfies $\Delta\Psi(\boldsymbol{X}) \approx 0$ and $\Delta M \approx 0$. Hence, it can be approximated well by a dust universe.

Another disadvantage of the global modified cap discrepancy is that it is a very unhandy parameter which cannot be determined easily. For practical reasons it would be desirable to have a parameter which can be calculated easily and has a more physical interpretation.

Furthermore, we have the problem that there is no reason why $a_0 = \langle\Psi\rangle^2$ is a good approximation in many cases and in some ones not. Korzyński simply proposes an average scheme which seems to be very natural when we interpret the conformal factor as a function on the hypersphere. However, we already know that the solution of the constraint equation can also be written with respect to the flat or hyperbolic metric, respectively. There is no reason not to take the average of the conformal factors with respect to the corresponding conformal metrics in these cases.

Let us consider the flat case in more detail. If we write the metric as $\bar{\boldsymbol{g}} = \Psi^4 \boldsymbol{h} = \Psi_0^4 \boldsymbol{\delta}$, a natural choice for an averaging scheme in the flat case would be

$$\langle\Psi_0\rangle = \lim_{R\to\infty} \frac{1}{\frac{4\pi}{3} R^3} \int_{S^2_R} \Psi_0(\boldsymbol{x}) \,\mathrm{d}\boldsymbol{x}. \tag{7.26}$$

For $\Psi_0 = 1 + \sum_A \frac{\mu_A}{\|\boldsymbol{x}-\boldsymbol{p}_A\|}$ we can integrate each term on its own considering a sphere centred at $\boldsymbol{p}_A$. Obviously, the first term gives $\langle 1\rangle = 1$, whereas for the other terms we obtain

$$\left\langle \frac{\mu_A}{\|\boldsymbol{x}-\boldsymbol{p}_A\|} \right\rangle = \lim_{R\to\infty} \frac{1}{\frac{4\pi}{3} R^3} \int_0^R \mathrm{d}r\, r^2 \int_0^\pi \mathrm{d}\vartheta \sin\vartheta \int_0^{2\pi} \mathrm{d}\varphi \,\frac{\mu_A}{r} = \lim_{R\to\infty} \frac{3\mu_A}{2R} = 0, \tag{7.27}$$

using spherical coordinates centred at $\boldsymbol{p}_A$.

This shows that we have always $\langle\Psi_0\rangle = 1$ irrespective of the black hole configuration so that we gain nothing. Perhaps it would be reasonable to cut off the integral at the horizon so that the different treatment of the black hole at infinity is taken into account somehow. However, this clearly shows that there are problems if we try to average with respect to some other conformal metric. So the question remains why the average with respect to the round metric is preferred against conformally equivalent metrics.

Another resolution avoiding these problems could be to define the average with respect to the Lie sphere vector representation discussed in section 6.3. However, at the moment we do not know yet how to define a volume form properly.

We admit that, in view of the results from the last chapter 6, the round metric appears to be the most natural choice for the conformal metric. For this reason, we will also keep this point of view in the following considerations. However, the above discussion shows that Korzyński's averaging procedure is somehow arbitrary, in particular, it depends on the form of the metric. Therefore, we want provide another approach in next section.

## 7.3 Unifoamy Configurations

Studies of examples[1] indicate that there exists a good approximation by a dust universe if the black holes are distributed almost evenly on the hypersphere and if they are not too massive. For these black hole configurations, the size of the dust universe is close to $a_0 = \langle\Psi\rangle^2$ and the total mass satisfies $\sum_A m_A = \frac{3\pi}{4} a_0$. Furthermore, there are no cases where the total mass matches but the size differs. In other words: If the total mass fits to the size, $a_0$ is also a good approximation in most regions. For this reason, we want to develop a criterion ensuring that the total mass fits to $a_0$.

[1] See Korzyński's results [Kor14] and the next chapter 8.

### Mean Inverse Distance

In view of the uniform polytopes, we call a configuration $\{(\boldsymbol{P}_A, \mu_A)\}$ of black holes on the sphere *uniform* if the distribution looks the same for every black hole. This implies that the mass parameter is equal for every black hole such that $\mu_A = \mu \; \forall A$. For this reason, all black holes have the same mass $m_A = m$ in this case. As we already know from our study of uniform polytopes in section 3.4, there is only a certain number of these configurations. For this reason we are looking for a generalisation.

Let us consider a *homogeneous* distribution, that is, a continuous matter distribution with constant density $\rho$. Such a matter distribution appears in the cosmological case where $\rho = \frac{3}{8\pi a^2}$. In this case, the probability density $\mathrm{d}P$ to pick up a certain mass element should be proportional to the volume element such that

$$\mathrm{d}P = \frac{1}{2\pi^2} \sin^2\chi \sin\vartheta \, \mathrm{d}\chi \, \mathrm{d}\vartheta \, \mathrm{d}\varphi, \tag{7.28}$$

using standard spherical coordinates. The mean value of any function $f$ can be calculated from

$$\langle f \rangle = \int_{S^3} f \, \mathrm{d}P. \tag{7.29}$$

It follows that the mean inverse distance between any two mass elements is given by

$$\left\langle \frac{1}{\|\boldsymbol{P}_A - \boldsymbol{P}_B\|} \right\rangle = \frac{1}{2\pi^2} \int_0^\pi \mathrm{d}\chi \int_0^\pi \mathrm{d}\vartheta \int_0^{2\pi} \mathrm{d}\varphi \sin^2\chi \sin\vartheta \frac{1}{\sqrt{2(1-\cos\chi)}} = \frac{8}{3\pi}, \tag{7.30}$$

where we used again that $\|\boldsymbol{P}_A - \boldsymbol{P}_B\| = \sqrt{2(1 - \boldsymbol{P}_A \cdot \boldsymbol{P}_B)} = \sqrt{2(1-\cos\chi)}$, if we choose the coordinate system such that $\boldsymbol{P}_A$ is at the north pole $(0,0,0,1)$.

For a discrete, uniform configuration, we expect a similar result so that the mean inverse distance should approximately satisfy

$$\left\langle \frac{1}{\|\boldsymbol{P}_A - \boldsymbol{P}_B\|} \right\rangle_A = \frac{1}{N-1} \sum_{B \neq A}^{N} \frac{1}{\|\boldsymbol{P}_A - \boldsymbol{P}_B\|} = \frac{8}{3\pi}. \tag{7.31}$$

Since $\mu_A = \mu$ for all black holes, this can also be written in the form

$$\frac{1}{\sum_{B\neq A} \mu} \sum_{B \neq A} \frac{\mu}{\|\boldsymbol{P}_A - \boldsymbol{P}_B\|} = \frac{8}{3\pi}. \tag{7.32}$$

The generalisation to black holes with arbitrary mass parameters $\mu_A$ is obvious: We simply substitute $\mu$ by the individual parameters $\mu_B$ so that the inverse distances are weighted by the mass parameters. For this reason we define:

A configuration $\{(\boldsymbol{P}_A, \mu_A)\}$ of black holes on the hypersphere is called *unifoamy* if

$$\sum_{B\neq A} \frac{\mu_A \mu_B}{\|\boldsymbol{P}_A - \boldsymbol{P}_B\|} = \frac{8}{3\pi} \sum_{B \neq A} \mu_A \mu_B \quad \forall A, \tag{7.33}$$

which is equivalent to the weighted mean

$$\left\langle \frac{1}{\|\boldsymbol{P}_A - \boldsymbol{P}_B\|} \right\rangle_{A,\mu} = \frac{1}{\sum_{B\neq A} \mu_B} \sum_{B \neq A} \frac{\mu_B}{\|\boldsymbol{P}_A - \boldsymbol{P}_B\|} = \frac{8}{3\pi} \quad \forall A. \tag{7.34}$$

The term ‘unifoamy’ is a composition of ‘uniform’ and ‘foamy’. The origin of this notion is the observation that for unifoamy configurations the spherical caps in the corresponding Lindquist-Wheeler models are distributed quite evenly on the hypersphere and no very big caps appear. So if we imagine the spherical caps as bubbles, the picture of a uniform foam arises, see also fig. 7.2.

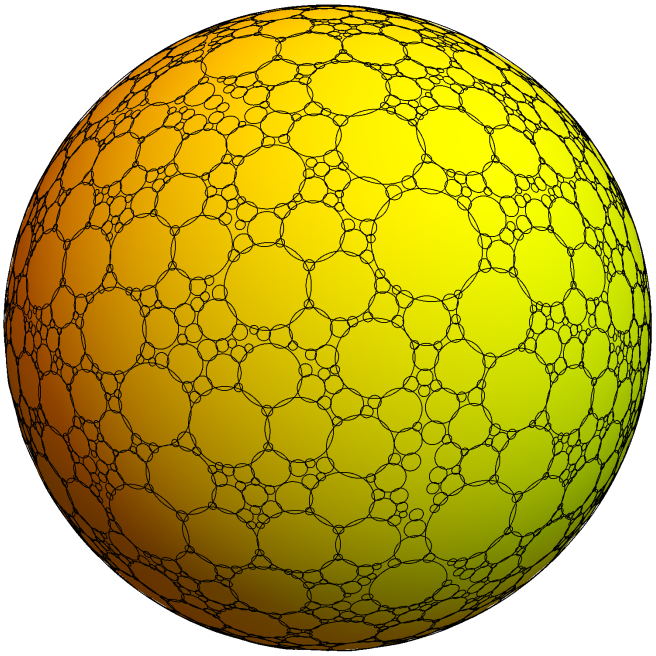

**Figure 7.2:** The figure shows a two-dimensional illustration of the Lindquist-Wheeler model of a unifoamy configuration (the central black holes are not plotted): The cells are distributed quite evenly on the sphere, they are not too big and do not overlap too much. Since this pictures gives the impression of a uniform foam on a sphere, we called such configurations unifoamy.

### Properties of Unifoamy Configurations

The unifoamy conditions (7.33) ensure that the black holes are not too close to each other: In order to satisfy the unifoamy condition, the biggest summand in the sum on the left-hand side has to be smaller than the whole sum on the right-hand side, that is, we have to demand

$$\max_{B\neq A} \frac{\mu_B}{\|\boldsymbol{P}_A - \boldsymbol{P}_B\|} \leq \frac{8}{3\pi} \sum_{B\neq A} \mu_B. \tag{7.35}$$

Let us consider the case that all mass parameters are equal, $\mu_A = \mu \ \forall A$. Then, the maximum is taken for the minimal distance $d_{\min} = \min \|\boldsymbol{P}_A - \boldsymbol{P}_B\|$. Hence, it follows that

$$d_{\min} \geq \frac{3\pi}{8\,(N-1)}. \tag{7.36}$$

A similar relation should also be true in the case of non-equal mass parameters because the term with the minimal distance should still be the dominant one if the black holes are close to each other. However, we could not derive such a relation yet.

Similarly, example configurations indicate that the unifoamy conditions seem not to allow too big mass parameters with respect to the mean value. In contrast, small mass parameters are not forbidden. However, we could not prove this yet but we will often assume this property.

For unifoamy configurations, the masses are much simpler to determine than for arbitrary ones. If we multiply the unifoamy condition by a factor 2, we recognize the expression for the mass of a black hole. Hence, we have

$$m_A = \sum_{B\neq A} \frac{2\mu_A\mu_B}{\|\boldsymbol{P}_A - \boldsymbol{P}_B\|} = \frac{16}{3\pi}\,\mu_A \sum_{B\neq A} \mu_B. \tag{7.37}$$

Therefore, the unifoamy conditions are constraints for the masses of the black holes.

If we assume that the mass parameters are of the same order or at least not too big, we are allowed to approximate the sum by $\sum_{B\neq A}\mu_A \approx \sum_B \mu_B$ such that the masses are given by

$$m_A \approx \frac{16}{3\pi}\mu_A \sum_{B=1}^{N} \mu_B. \tag{7.38}$$

This means that the mass of a black hole in a unifoamy configuration is basically determined by its mass parameter allowing us to estimate the masses without the extensive computation of the norms. Of course, the same is true for the total mass which is approximately

$$M = \sum_A m_A \approx \frac{16}{3\pi}\left(\sum_A \mu_A\right)^2. \tag{7.39}$$

There are cases where it is more appropriate to work with the masses instead of the mass parameters, for example, if we consider Swiss-cheese and Lindquist-Wheeler models. For these cases, we need an alternative version of the unifoamy condition using the masses. If we substitute $\sum_A \mu_A$ in eq. (7.38) by the total mass from eq. (7.39), we get

$$\mu_A \approx m_A\sqrt{\frac{3\pi}{16M}}, \tag{7.40}$$

or equivalently

$$\frac{\mu_A}{\sum_A \mu_A} \approx \frac{m_A}{M}. \tag{7.41}$$

Therefore, we can simply replace the mass parameters in the unifoamy condition and take the masses as weights.

Let us take a step back and reconsider the total mass. If we sum up the masses (7.37) for all black holes of a unifoamy configuration, we obtain

$$M = \sum_A m_A = \frac{16}{3\pi}\sum_A \sum_{B\neq A} \mu_A\mu_B. \tag{7.42}$$

For a homogeneous mass distribution in cosmology, we have $M = \frac{3\pi}{4}a_0$. Since we are assuming that unifoamy configurations are a generalisation of cosmological solutions to discrete configurations, they should satisfy the same relation. Hence, if we use this relation to determine the size $a_0$ of the fitted universe, we obtain

$$a_0 = \frac{4}{3\pi}M = \left(\frac{8}{3\pi}\right)^2 \sum_A \sum_{B\neq A} \mu_A\mu_B. \tag{7.43}$$

For unifoamy configurations with a large number $N$ of black holes, we expect that all masses are of the same order to get a uniform mass density. Due to eq. (7.40), this should also be true for the mass parameters so that $\mu_A \approx \langle\mu\rangle$ where $\langle\mu\rangle$ is the mean value of all mass parameters. Now we have

$$\sum_A \sum_{B\neq A} \mu_A \mu_B = \sum_{A,B} \mu_A \mu_B - \sum_A \mu_A^2. \tag{7.44}$$

The first term is approximately $\sum_{A,B} \mu_A \mu_B \approx N^2 \langle\mu\rangle^2$, whereas the second term $\sum_A \mu_A^2 \approx N\langle\mu\rangle^2$ is negligible for large $N$. Hence, we obtain

$$a_0 \approx \left(\frac{8}{3\pi} \sum_A \mu_A\right)^2 = \langle\Psi\rangle^2, \tag{7.45}$$

rediscovering Korzyński's suggestion without using an averaging procedure. Note that due to eq. (7.40) the mass parameters $\mu_A$, the masses $m_A$ and the size $a_0$ of the universe are related by

$$\mu_A \approx \frac{m_A}{2\sqrt{a_0}}. \tag{7.46}$$

Next we consider the following configurations: We divide the hypersphere in $N$ non-overlapping regions $\mathcal{V}_A$ covering the whole hypersphere such that $S^3 = \cup_{i=1}^n \mathcal{V}_A$ and $\mathcal{V}_A \cap \mathcal{V}_B = \emptyset$ if $A \neq B$. We put a black hole into each region at $\boldsymbol{P}_A \in \mathcal{V}_A$. Its mass parameter $\mu_A$ is chosen such that it is proportional to the volume $\operatorname{vol}\mathcal{V}_A$ of its cell, hence

$$\mu_A = \kappa \operatorname{vol}\mathcal{V}_A, \tag{7.47}$$

where $\kappa$ is some constant.

Korzyński has shown that the global modified cap discrepancy $\mathcal{E}$ for such configurations is bounded from above by the maximum of the diameters $\operatorname{diam}\mathcal{V}_A$ of all regions $\mathcal{V}_A$. Hence, the upper bound for $\mathcal{E}$ is given by [Kor14]

$$\mathcal{E} \leq \max_{A=1,\ldots,N} \operatorname{diam}\mathcal{V}_A, \tag{7.48}$$

where the diameter of a region $\mathcal{V}_A$ on the hypersphere is defined as

$$\operatorname{diam}\mathcal{V}_A = \sup_{\boldsymbol{X},\boldsymbol{Y}\in\mathcal{V}_A} \Lambda(\boldsymbol{X},\boldsymbol{Y}). \tag{7.49}$$

Let us assume that unifoamy configurations may be approximated well by Lindquist-Wheeler models. In these models, we associate to each black hole a volume in form of a spherical cap determined by the mass. We obtain for small masses, corresponding to small opening angles,

$$m_A = \frac{a_0}{2}\sin^3\beta_A \approx \frac{2M}{3\pi}\beta_A^3. \tag{7.50}$$

For unifoamy configurations the caps should not overlap much such that most parts of the hypersphere are covered. If we take these regions on the hypersphere, it should be possible to deform them slightly so that we get a covering of non-overlapping regions as illustrated

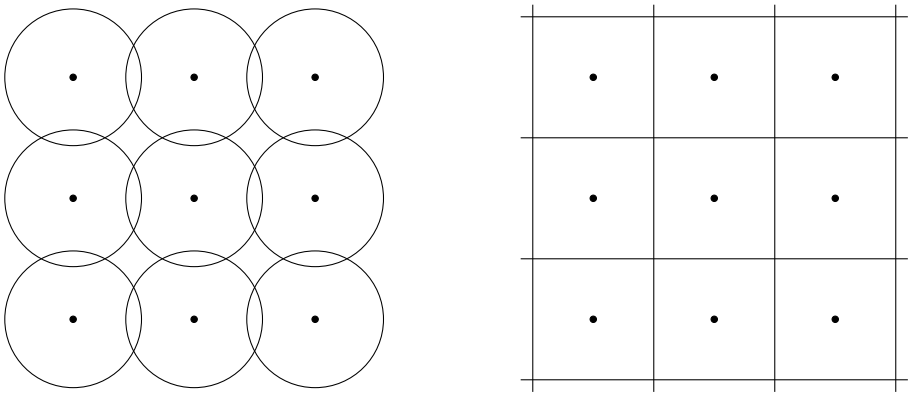

**(a)** Lindquist-Wheeler model **(b)** Deformed regions for the initial solution

**Figure 7.3:** The spherical cap regions of the Lindquist-Wheeler models are deformed in such a way that they do not overlap any more. The diameters in both cases should still be of the same order for unifoamy configurations.

in fig. 7.3. The diameter of the spherical caps and the deformed regions should still be of the same order for these configurations. For this reason, the modified cap discrepancy may be estimated by the size of the spherical caps such that $\operatorname{diam} \mathcal{V}_A \approx 2\beta_A$. Using the approximation (7.50) for the mass, the upper bound for the modified cap discrepancy $\mathcal{E}$ should be approximately

$$\mathcal{E} \lesssim 2\kappa \max_{A=1,\dots,N} \beta_A \approx \sqrt[3]{12\pi}\, \kappa \max_{A=1,\dots,N} \sqrt[3]{\frac{m_A}{M}}. \tag{7.51}$$

With this upper bound, we are able to apply Korzyński's first theorem to unifoamy configurations. Since the unifoamy size is approximately the squared mean value of the conformal factor, $a_0 \approx \langle \Psi \rangle^2$, the theorem shows that

$$\Psi^2 \approx \langle \Psi \rangle^2 \approx a_0 \tag{7.52}$$

in the far-field of the black holes. Of course, it would be better if we could derive a rigorous upper bound in order to get exact results. The optimal case would be the derivation of a new theorem for unifoamy configurations replacing Korzyński's first theorem. Unfortunately, we have not been successful yet. However, the described method should still lead to good estimates for the deviation of the conformal factor.

### Minimizing the Total Mass and Central Configurations

At last, we present a connection between unifoamy configurations and a special kind of configurations which related to Friedmann-like solutions in Newtonian point particle dynamics.

For this reason, we consider the function

$$\mathcal{M}(\boldsymbol{P}_1, \dots, \boldsymbol{P}_N) = \sum_A \sum_{B \neq A} \frac{2\mu_A \mu_B}{\|\boldsymbol{P}_A - \boldsymbol{P}_B\|}. \tag{7.53}$$

We are looking for the extrema of this function on the hypersphere. $\mathcal{M}$ is bounded from below due to $\|\boldsymbol{P}_A - \boldsymbol{P}_B\| \leq 2$, hence

$$\mathcal{M} \geq \sum_A \sum_{B \neq A} \mu_A \mu_B. \tag{7.54}$$

Therefore, there exists a global minimum. In contrast, $\mathcal{M}$ is not bounded from above because the denominator can take arbitrary small values if two mass are close together. Since we are using an embedding in four dimensions, we have to impose the constraints $\boldsymbol{P}_A^2 = 1$ to the positions of all black holes. Hence, we have to look for the extrema of the function

$$\mathcal{L}_{\mathcal{M}} = \mathcal{M}(\boldsymbol{P}_1, \ldots, \boldsymbol{P}_N) + \sum_A \lambda_A (\boldsymbol{P}_A^2 - 1) \tag{7.55}$$

where the $\lambda_A$ are Lagrange multipliers to ensure the constraints.

In order to find the extrema, we have to determine those points where the gradient $\nabla\mathcal{L} = 0$ vanishes with respect to all coordinates $\boldsymbol{P}_1, \ldots, \boldsymbol{P}_N$ and $\lambda_1, \ldots, \lambda_N$. The gradient with respect to the positions yields

$$\lambda_A \boldsymbol{P}_A = \sum_{B \neq A} 4\mu_A\mu_B \frac{\boldsymbol{P}_A - \boldsymbol{P}_B}{\|\boldsymbol{P}_A - \boldsymbol{P}_B\|^3}, \tag{7.56a}$$

while the derivatives with respect to Lagrange multipliers return the constraints

$$\boldsymbol{P}_A^2 = 1. \tag{7.56b}$$

We can determine the Lagrange multipliers if we multiply the first set of equations with $\boldsymbol{P}_A$. Using that $\|\boldsymbol{P}_A - \boldsymbol{P}_B\|^2 = 2\,(1 - \boldsymbol{P}_A \cdot \boldsymbol{P}_B)$, we get

$$\lambda_A = \sum_{B \neq A} 4\mu_A\mu_B \frac{1 - \boldsymbol{P}_A \cdot \boldsymbol{P}_B}{\|\boldsymbol{P}_A - \boldsymbol{P}_B\|^3} = \sum_{B \neq A} \frac{2\mu_A\mu_B}{\|\boldsymbol{P}_A - \boldsymbol{P}_B\|} = m_A. \tag{7.57}$$

Hence, the Lagrange multipliers return the masses.

We are not able to characterise eq. (7.56a) further without additional assumptions. Therefore, let us consider the case that the Lagrange multipliers are proportional to the mass parameters, $\lambda_A = \mathcal{C}\,\mu_A$. Then, eq. (7.56a) becomes

$$\mathcal{C}\,\mu_A \boldsymbol{P}_A = \sum_{B \neq A} 4\mu_A\mu_B \frac{\boldsymbol{P}_A - \boldsymbol{P}_B}{\|\boldsymbol{P}_A - \boldsymbol{P}_B\|^3}. \tag{7.58}$$

Configurations satisfying these kind of equations are known as *central configurations*, see for example [BGS03; EG14]. Note that central configurations are not restricted to the hypersphere in general. In interesting fact is that central configurations appear in Newtonian point particle dynamics as particle ensembles with a Friedmann-like behaviour. We will briefly discuss this topic in chapter 9. In general, $\mathcal{C}$ is an arbitrary constant. However, in the special case that all mass parameters are equal, $\mu_A = \mu\ \forall A$ and that the constant is given by $\mathcal{C} = \frac{16}{3\pi}\,(N-1)\,\mu$, central configurations are also unifoamy because the masses are

$$m_A = \lambda_A = \mathcal{C}_A\,\mu_A = \frac{16}{3\pi}\,(N-1)\,\mu^2. \tag{7.59}$$

This shows that, on the hypersphere, the set of unifoamy configurations and the set of central configurations are not disjoint; the latter one is a subset of configurations minimising the functional (7.55), that is, the total mass. In general, unifoamy configurations are not central configurations because we have $m_A = \lambda_A = \mathcal{C}_A\,\mu_A$, where $\mathcal{C}_A = \frac{16}{3\pi}\sum_{B\neq A}\mu_B$ is not

constant for all masses. However, if the mass parameters are not too big, we can use the approximation (7.46) for the masses, $\lambda_A = m_A \approx 2\sqrt{a_0}\,\mu_A$. Hence, we would expect that approximately unifoamy central configurations satisfy

$$\frac{\sqrt{a_0}}{2}\,\mu_A \boldsymbol{P}_A = \sum_{B\neq A} \mu_A \mu_B \,\frac{\boldsymbol{P}_A - \boldsymbol{P}_B}{\|\boldsymbol{P}_A - \boldsymbol{P}_B\|^3}. \tag{7.60}$$

If we substitute the mass parameters by the masses using eq. (7.40), we obtain

$$a_0\, m_A \boldsymbol{P}_A = \sum_{B\neq A} m_A m_B \,\frac{\boldsymbol{P}_A - \boldsymbol{P}_B}{\|\boldsymbol{P}_A - \boldsymbol{P}_B\|^3}. \tag{7.61}$$

In might be interesting if there is a deeper connection between unifoamy, central and minimal configurations since each configuration is related to a Friedmann universe in a certain way: We claim that unifoamy configurations possess a Friedmann-like configuration as discussed above. Central configurations are related to point-particle configurations with a Friedmann-like time evolution in Newtonian physics, as we will discuss in more detail in section 9.2. Minimal configurations would establish a connection to an extremal property of Friedmann universes. The minimal configuration should be an unstable minimum. Due to the gravitational attraction, black holes should approach towards each other causing an increasing total mass. Similarly, the homogeneous mass density in Friedmann universes is also an extremal state because perturbations of the homogeneous matter distributions grow. We started to investigate possible connections between these configurations but we have not been successful yet. For this reason, central and minimal configurations are mostly omitted in the discussion of example configurations in the next chapter.

# 8 Numerical Results

In this chapter we want to validate the previous discussions with the help of some example configurations. We start our studies in section 8.1 with the investigation of the uniform polychorons discussed in section 3.4. We compare the different possibilities of the size $a_0$ of the fitted dust universe discussed in chapter 7. The second kind of configurations, considered in section 8.2, are based on random distributions. Here we study the influence of the minimum distance between two points. Random configurations with a big minimal distance can only be generated with much computational effort. Hence, we consider configurations based on Apollonian packings in section 8.3. Apollonian sphere packings allow us to construct various configurations very efficiently. In particular, we know how much space of the hypersphere is covered. However, their disadvantage is much computational effort which is needed to compute the mass parameters. Korzyński considered configurations based on the tesseract projection which he showed to be Friedmann-like. They are considered in section 8.4. Finally, we construct configurations minimising the total mass in section 8.5 in order to give some evidence to our conjecture that such configurations are Friedmann-like.

## 8.1 Uniform Polychorons

A natural choice for a uniform distribution of black holes is to put the black holes at the vertices $\boldsymbol{P}_A$ of the non-prismatic uniform polychorons described in section 3.4. Because of the vertex-transitivity all black holes have the same mass $m_A = m\ \forall A$ if the mass parameters are equal for all black holes, $\mu_A = \mu\ \forall A$. In this case, the conformal factor is given b

$$\Psi = \sum_{A=1}^{N} \frac{\mu}{\|\boldsymbol{X} - \boldsymbol{P}_A\|}, \tag{8.1}$$

and the mass of each black holes is

$$m \equiv m_1 = \sum_{A=2}^{N} \frac{2\mu^2}{\|\boldsymbol{P}_A - \boldsymbol{P}_1\|}. \tag{8.2}$$

Here we want to compare the possible candidates

$$a_0^{(1)} = \langle\Psi\rangle^2 = \left(\frac{8}{3\pi}\sum_A \mu_A\right)^2 = \left(\frac{8}{3\pi} N\mu\right)^2, \tag{8.3a}$$

$$a_0^{(2)} = \langle\Psi^2\rangle = \sum_{A,B} \mu_A\mu_B \frac{\pi - \alpha_{AB}}{\pi\cos\frac{\alpha_{AB}}{2}} = \sum_A N\mu^2 \frac{\pi - \alpha_A}{\pi\cos\frac{\alpha_A}{2}}, \tag{8.3b}$$

$$a_0^{(3)} = \psi_{\min}^2, \tag{8.3c}$$

$$a_0^{(4)} = \frac{4}{3\pi}\sum_A m_A = \frac{8\mu^2}{3\pi}\sum_{A=2}^{N} \frac{1}{\|\boldsymbol{P}_A - \boldsymbol{P}_1\|}, \tag{8.3d}$$

for the size of the fitted dust universe, discussed in the last chapter 7. Here $N$ is the number of vertices. In eq. (8.3b), we used $\alpha_A = \arccos(\boldsymbol{P}_1 \cdot \boldsymbol{P}_A)$.

Furthermore, we check if these configurations are unifoamy and calculate the size

$$a_0^{(5)} = \frac{64}{9\pi^2} \sum_A \sum_{B \neq A} \mu_A \mu_B = \frac{N-1}{N} \left( \frac{8}{3\pi} N\mu \right)^2 = \frac{N-1}{N} \langle \Psi \rangle^2. \tag{8.4}$$

In our case, a configuration is unifoamy if $m = \frac{16}{3\pi}(N-1)\mu^2$ or equivalently if

$$a_0^{(4)} = \frac{4}{3\pi} Nm = \frac{64}{9\pi^2} N(N-1)\mu^2 = a_0^{(5)}. \tag{8.5}$$

Besides the initial data solutions, we also consider the corresponding Swiss-cheese models and Lindquist-Wheeler models. 'Corresponding' means that the black holes are located at the same positions and have the same mass as in the exact solution. The opening angle $\beta$ of the spherical caps is determined by the mass of the black holes

$$m = \frac{a_0}{2} \sin^3 \beta. \tag{8.6}$$

Of course, the opening angle is the same for each cap. The size $a_0$ of these two models is determined as discussed in section 7.1, that is, the caps in the Swiss-cheese models should not overlap but touch at most. For this reason, we set the opening to half of the angle between to neighbouring vertices, hence

$$\beta = \min_{A=2,\dots,N} \arccos(\boldsymbol{P}_1 \cdot \boldsymbol{P}_A). \tag{8.7}$$

The opening angle in the Lindquist-Wheeler models is determined by the condition

$$\frac{\pi}{N} = \beta - \sin\beta \cos\beta. \tag{8.8}$$

So in addition to the above possibilities, we also consider

$$a_0^{(6,7)} = \frac{2m}{\sin^3 \beta}, \tag{8.9}$$

where $\beta$ is obtained from either eq. (8.7) ($\rightarrow a_0^{(6)}$), or eq. (8.8) ($\rightarrow a_0^{(7)}$). Recall that $a_0^{(6)}$ should converge to $a_0^{(4)}$, the value of Friedmann dust universe, for $N \rightarrow \infty$, if the configuration is uniform and its total mass constant.

We set for all configurations $m = \frac{1}{N}$ so that the total mass $M = Nm = 1$ for all configurations is the same. Then, the mass parameters are calculated from eq. (8.2). The results for the different possibilities for the size $a_0$ are listed in table B.3. Note that $a_0^{(4)} = \frac{4}{3\pi}$ for each configuration by construction, therefore sizes are given in units of $a_0^{(4)}$. We discuss some observations in more detail.

As discussed above, configurations are unifoamy if $\Delta a_0 = a_0^{(5)} - a_0^{(4)} = 0$. This is plotted in fig. 8.2 showing that polychorons become more unifoamy with an increasing number of vertices as we were expecting.

The deviation of the candidates $a_0^{(1)}, a_0^{(2)}, a_0^{(5)}$ and $a_0^{(7)}$ from the value $a_0^{(4)}$, obtained from the total mass, is plotted in fig. 8.3. It can be seen the the first three choices $a_0^{(1)}, a_0^{(2)}$ and

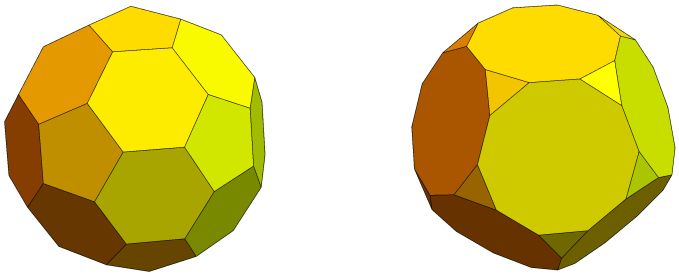

**(a)** truncated icosahedron **(b)** truncated dodecahedron

**Figure 8.1:** Although the truncated icosahedron and the truncated dodecahedron belong to the same family, the vertices of the former one are spread more evenly on the sphere than those of the latter one.

$a_0^{(5)}$ lead to similar results for most polychorons. Furthermore, the value $a_0^{(7)}$ from the Lindquist-Wheeler model, plotted in green, is often a good approximation.

However, the deviation of these values $a_0^{(1)}, a_0^{(2)}, a_0^{(5)}, a_0^{(7)}$ from squared minimum $a_0^{(3)} = \Psi_{\min}^2$ of the conformal factor varies a lot, although there is a tendency that the deviation decreases with an increasing number of vertices. This is plotted in fig. 8.4. Recall that Korzyński's first theorem 7.1 gives upper bounds for $\Delta\Psi = \frac{|\Psi - \langle\Psi\rangle|}{\langle\Psi\rangle}$.

It can also be observed that polychorons possessing the same number of vertices or belonging to the same family have a big variance in their fitted sizes. The origin of this behaviour is probably the different structure of the polychorons. For an example, consider the truncated dodecahedron and the truncated icosahedron shown in fig. 8.1 in one dimension less. Although both polyhedron belong to the same family, we expect that the former one may be approximated better by a sphere than the latter one because the vertices are spread more evenly on the sphere. The modified cap discrepancy $\mathcal{E}$ is at least constrained by the biggest spherical cap which does not contain a vertex. Therefore, $\mathcal{E}$ is probably bigger in configurations like the truncated dodecahedron than the truncated icosahedron. This yields to weaker for the deviation $\Delta\Psi$. Similar effects should explain the irregularities, mentioned above, in the case of polychorons.

This is also confirmed if we consider the fraction of space covered by the spherical caps in the corresponding Swiss-cheese models. In most of the cases, the hypersphere is mostly uncovered. For this reason the values for $a_0^{(6)}$ from the Swiss-cheese models strongly differ from the other ones. However, if we plot $a_0^{(6)}$ of the Swiss-cheese model against the covering as shown in fig. 8.5, we observe that the fitted size becomes a good approximation if the hypersphere is mostly covered as we were expecting, see the discussion in section 5.1. This is another evidence that the covering condition of the Lindquist-Wheeler models is reasonable. Furthermore, it shows that the covered fraction of the hypersphere is a good measure for the reliability of the fit. Interestingly, the values follow roughly the curve $\frac{1}{x}$ where $x$ is the covered part.

The covering of the hypersphere can be improved if we insert further spherical caps into the centres of the cells such that they touch the previous caps. The centres of the cells form the vertices of the dual polychorons which are not uniform in general. Unfortunately, we are not able to compute the centres and sizes of these additional caps efficiently. However,

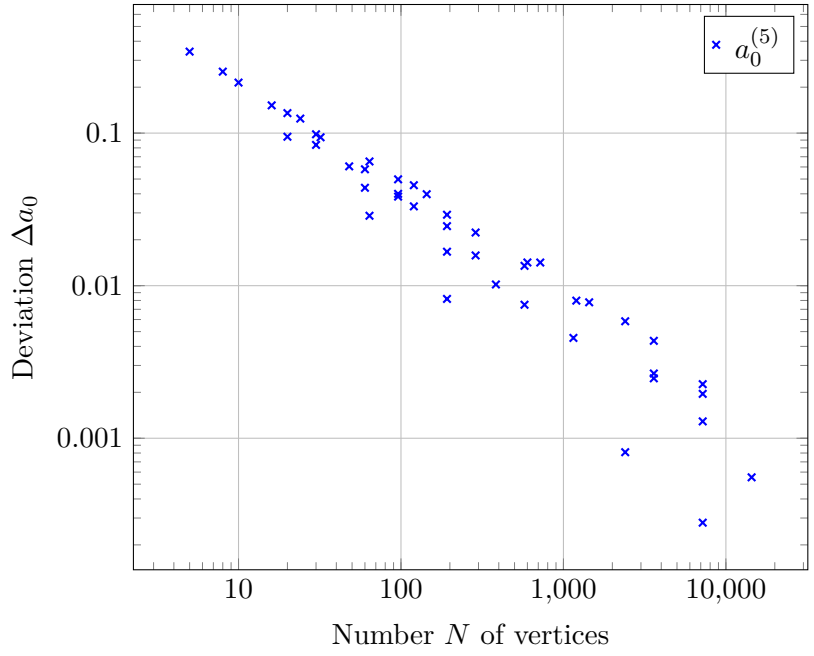


**Figure 8.2:** Unifoamity in dependence of the number of vertices: A configuration is unifoamy if the deviation $\Delta a_0 = a_0 - a_0^{(4)} = 0$.

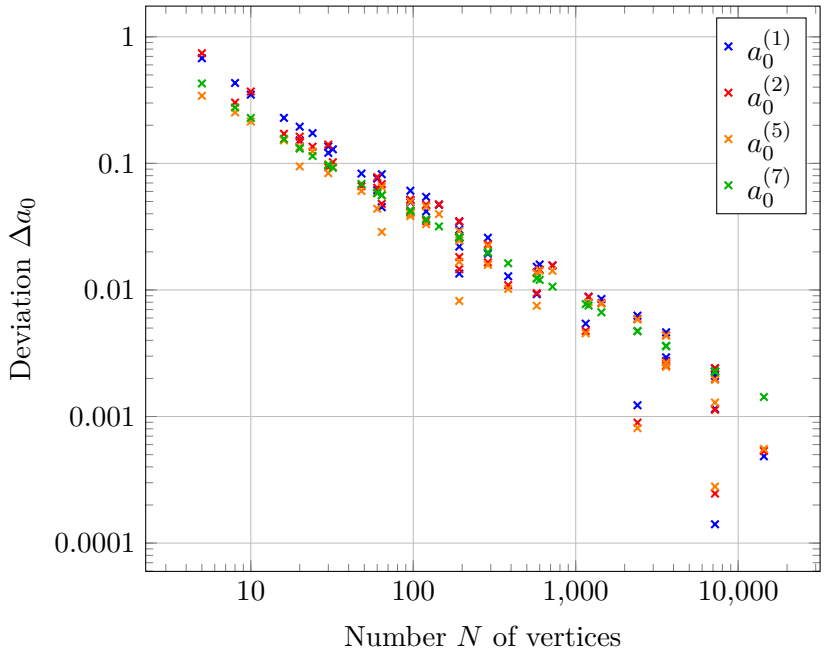


**Figure 8.3:** Comparison between the different candidates for the sizes: All candidates lead to similar results for the deviation $\Delta a_0 = |a_0 - a_0^{(4)}|$.

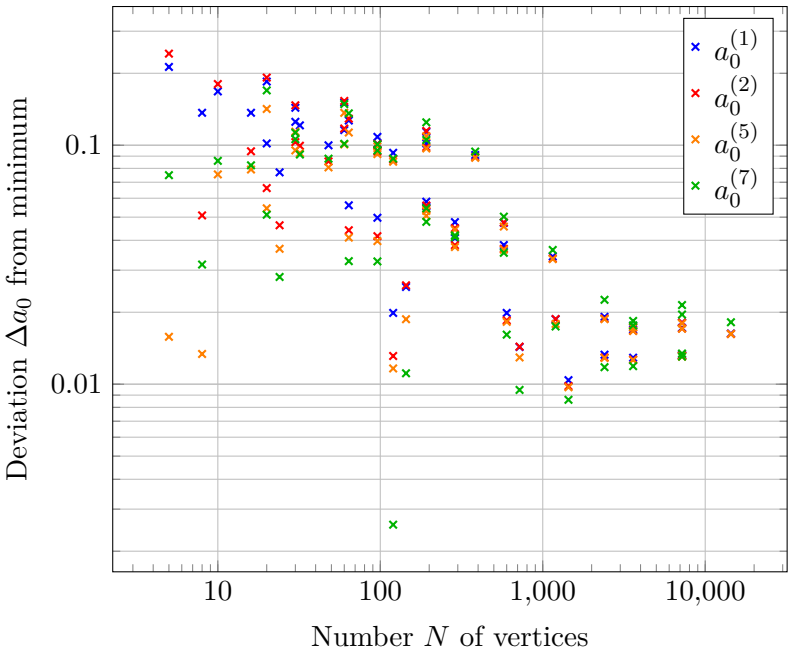


**Figure 8.4:** Deviation $\Delta a_0 = \frac{a_0 - \Psi^2_{\min}}{a_0}$ from the minima of the configurations: Although we observe a tendency that the deviation from the minimum decreases, there is a big variation in the deviation.

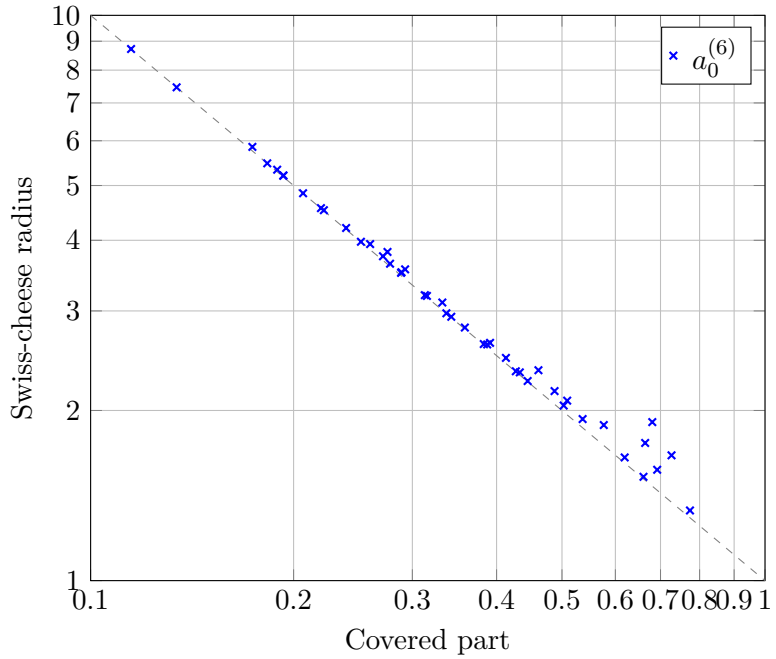


**Figure 8.5:** Radius $a_0^{(6)}$ from the Swiss-cheese models in dependence of the fraction of the hypersphere covered by the spherical caps.

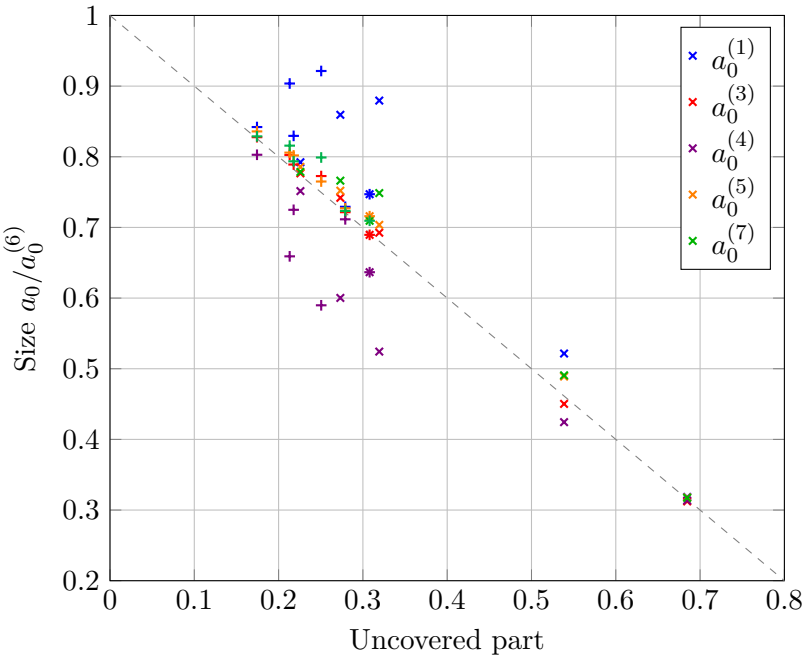


**Figure 8.6:** Regular polychorons (marked with $\times$) combined with their duals (marked with $+$) in units of the Swiss-cheese radius $a_0^{(6)}$

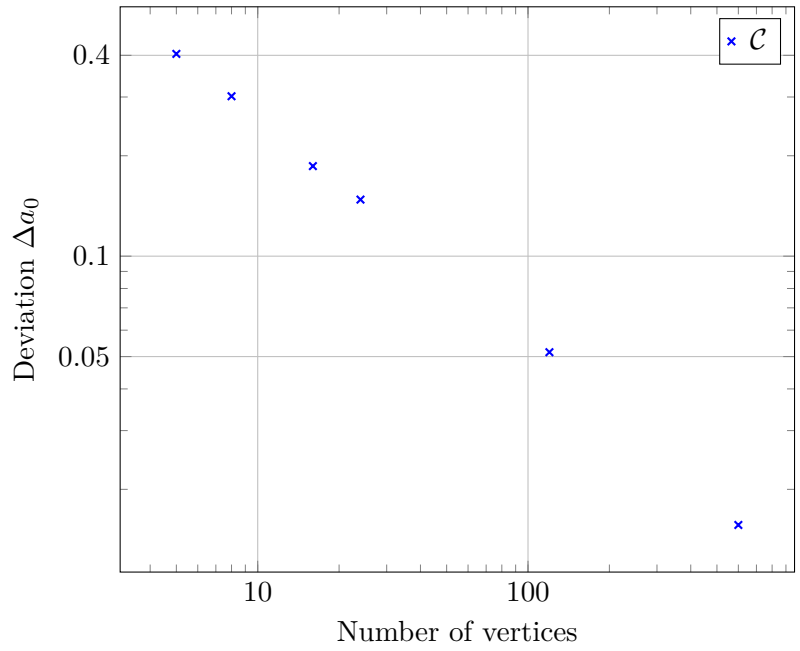


**Figure 8.7:** With an increasing number, the deviation $\Delta a_0 = |\mathcal{C} - a_0^{(4)}|$ of the central configuration constant from the expected size $a_0^{(4)}$ decreases.

the duals of the regular polychorons are also regular. Therefore we can combine the regular polychorons with their duals. The results for these configurations, shown in fig. 8.6, support our previous observations. In particular, $a_0^{(3)}, a_0^{(5)}$ and $a_0^{(7)}$ follow approximately the dashed line, whereas $a_0^{(1)} = \langle\Psi\rangle^2$ and $a_0^{(4)} = \frac{4M}{3\pi}$ deviate from the other candidates.

The idea to fill up the complete hypersphere by adding new spheres tangent to its neighbours is the foundation of the models based on Apollonian packings which we will discuss in section 8.3.

At last, we briefly discuss central configurations. It can easily be checked that the vertices regular polychorons form central configurations. For unifoamy central configurations, eq. (7.61) shows that the constant $\mathcal{C}$ equals the size, $\mathcal{C} = a_0$, if we use the masses instead of the parameters. Hence, the constant $\mathcal{C}$ is another candidate for the size. It is given by

$$\mathcal{C} = \frac{1}{2M} \sum_A \sum_{B \neq A} \frac{m_A m_B}{\|\boldsymbol{P}_A - \boldsymbol{P}_B\|}. \tag{8.10}$$

This can be obtained from eq. (7.61) by multiplying with $\boldsymbol{P}_A$, adding up all equations and using Euler's theorem on homogeneous functions, see also section 9.2. As shown in fig. 8.7, with an increasing number of black holes, the constant $\mathcal{C}$ approaches to the expected size $a_0^{(4)} = \frac{4}{3\pi} M$ obtained from the total mass.

## 8.2 Random Distributions

For the next example we simply distribute the locations of the black holes randomly on the hypersphere. In order to get a uniform probability distribution so that there are no regions where the points accumulate by construction, although such configurations may be also interesting, we have to be careful with the procedure. So it is not possible to use the generating vector of the hypersphere

$$\boldsymbol{E}_4(\chi, \vartheta, \varphi) = \begin{pmatrix} \sin\chi \sin\vartheta \sin\varphi \\ \sin\chi \sin\vartheta \cos\varphi \\ \sin\chi \cos\vartheta \\ \cos\chi \end{pmatrix} \tag{8.11}$$

and randomly choose the angles $\chi, \vartheta, \varphi$ from their intervals with a uniform probability. In this case we would have an increased number of points at the poles.

A correct distribution is given by the following method as shown by Marsaglia [Mar72]: From the interval $[-1, 1]$, we randomly take four numbers $x^1, x^2, x^3, x^4$ with uniform probability. These are ordered in two pairs $(x_1, x_2)$ and $(x_3, x_4)$. We only accept those pairs satisfying $x_1^2 + x_2^2 \leq 1$ and $x_3^2 + x_4^2 \leq 1$, else the pair is dropped and another one is chosen until we have found two pairs. From these pairs we get a point on the hypersphere via

$$\boldsymbol{X} = \begin{pmatrix} x_1 \\ x_2 \\ x_3 \sqrt{\frac{1-x_1^2-x_2^2}{x_3^2+x_4^2}} \\ x_4 \sqrt{\frac{1-x_1^2-x_2^2}{x_3^2+x_4^2}} \end{pmatrix} \tag{8.12}$$

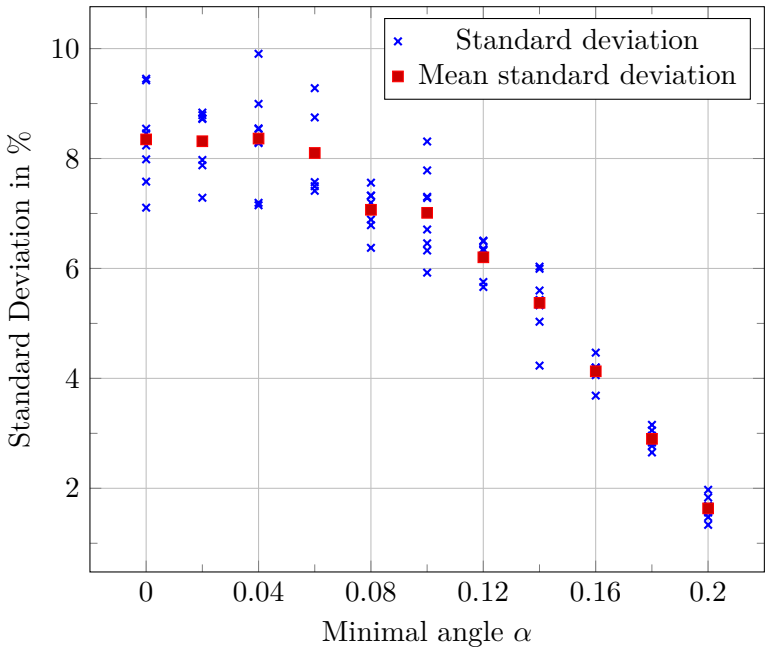


**Figure 8.8:** Standard deviation from the mean value of the mass in % in dependence of the minimal angle $\alpha$.

Selecting points this way leads to a uniform distribution on the hypersphere.

Since we are interested in configurations of black holes that are not too close to each other, we might add another parameter controlling the minimal distance between two points. For example, we can choose the scalar product of a new point with all other points, which is the cosine of the angle between those. Then we set a minimal distance. If the parameter falls below this limit, we drop this point and select a new one. Obviously, this procedure limits the number of points which we can select because to every point we associate a region forbidden for new points. This way we fill up the hypersphere until there is no space left for another point and the selection process has to stop. We could use the region to determine the mass, or the other way round, as we do in the Swiss-cheese models.

We set the mass parameters to $\mu = \frac{1}{N}$ for all black holes where $N$ is the number of black holes. Furthermore, we accept a new point $\boldsymbol{P}_{\text{new}}$ only if $\boldsymbol{P}_{\text{new}} \cdot \boldsymbol{P}_A < \cos\alpha$ for all previous points $\boldsymbol{P}_A$. All configurations of more or less evenly distributed points approximately satisfy the cumulated unifoamy condition

$$M = \sum_A \sum_{B\neq A} \frac{2\mu_A\mu_B}{\|\boldsymbol{P}_A - \boldsymbol{P}_B\|} = \frac{16}{3\pi} \sum_A \sum_{B\neq A} \mu_A\mu_B. \tag{8.13}$$

For this reason, it is not sufficient to consider just this condition but we have to check the unifoamy condition for each mass on its own. This means that we have to check if each mass holes satisfies

$$m_A = \sum_{B\neq A} \frac{2\mu_A\mu_B}{\|\boldsymbol{P}_A - \boldsymbol{P}_B\|} = \frac{16}{3\pi} \mu_A \sum_{B\neq A} \mu_B. \tag{8.14}$$

We have considered several configurations for different values of $\alpha$ and calculated the standard deviation from the mean value. Typical results are shown in fig. 8.8. The

configurations become more unifoamy the bigger the minimal angle $\alpha$ is set, that is the more evenly the black holes are distributed on the hypersphere. Furthermore, this goes along with the decreasing of the variation of the masses so that all black holes have about the same mass.

Although this model is an obvious procedure to generate a uniform configuration, it is quite inefficient. The reason is that the more points we have already marked on the hypersphere, it is more probable that the next generated point lies in a forbidden region. Therefore, it takes more and more time to add a new point. In the next section we provide another construction without this problem.

## 8.3 Apollonian Coverings

In section 3.5, we presented the Apollonian packings on the hypersphere with mutually tangent spherical caps. Apollonian packings allow us to easily construct a Swiss-cheese model where most of the dust is removed, that is an almost completely covered sphere. A big advantage is that we are able to calculate the exact centres $\boldsymbol{P}_A$ and opening angles $\beta_A$ for a huge number of spherical caps very fast.

The black holes are put at the centres of the caps. Their masses are determined by the size of the caps: If $\beta_A$ is the opening angle, we set $m_A = \frac{a_0}{2}\sin^3\beta_A$, as discussed in section 5.1. In this section we use the Swiss-cheese radius $a_0$ as the basic unit such that the mass of the black hole is

$$\tilde{m}_A = \frac{m_A}{a_0} = \frac{1}{2}\sin^3\beta_A. \tag{8.15}$$

If we consider to the corresponding initial data where the black holes are at the same positions and have the same masses, the mass parameters $\tilde{\mu}_A = \frac{\mu_A}{\sqrt{a_0}}$ are determined by the mass formula

$$\tilde{m}_A = \sum_{B\neq A} \frac{2\tilde{\mu}_A\tilde{\mu}_B}{\|\boldsymbol{P}_A - \boldsymbol{P}_B\|} \tag{8.16}$$

and the conformal factor becomes

$$\tilde{\Psi}^2 = \left(\sum_{A=1}^{N} \frac{\tilde{\mu}_A}{\|\boldsymbol{E}_4 - \boldsymbol{P}_A\|}\right)^2 = \frac{\Psi^2}{a_0}. \tag{8.17}$$

In order to determine the mass parameters, we have to solve the coupled system of quadratic equations (8.16). Unfortunately, this can only be done by numerical algorithms taking a lot of computation time. We used Newton's method to iteratively approximate the solution together with the Gauss-Seidel method, which is a modification of the famous Gauss algorithm, to solve systems of linear equations. The duration of this calculation is the biggest disadvantage of this model.

We concentrated on the tetrahedron- or pentatope-based packing. Its construction is explained in appendix A. Other packings can be obtained by applying a Lorentz transformation on this packing.

The results for all candidates $a_0$ from the pentatope-packing are shown in fig. 8.9. This time the different values for $a_0$ differ more than in the previous examples: So Korzyński's suggestion $a_0^{(1)} = \langle\Psi\rangle^2$ as well as $a_0^{(2)} = \langle\Psi^2\rangle$ are too big in all steps and seems to converge to another value than the minimum $a_0^{(3)} = \psi^2_{\min}$, the Lindquist-Wheeler radius $a_0^{(7)}$ or the

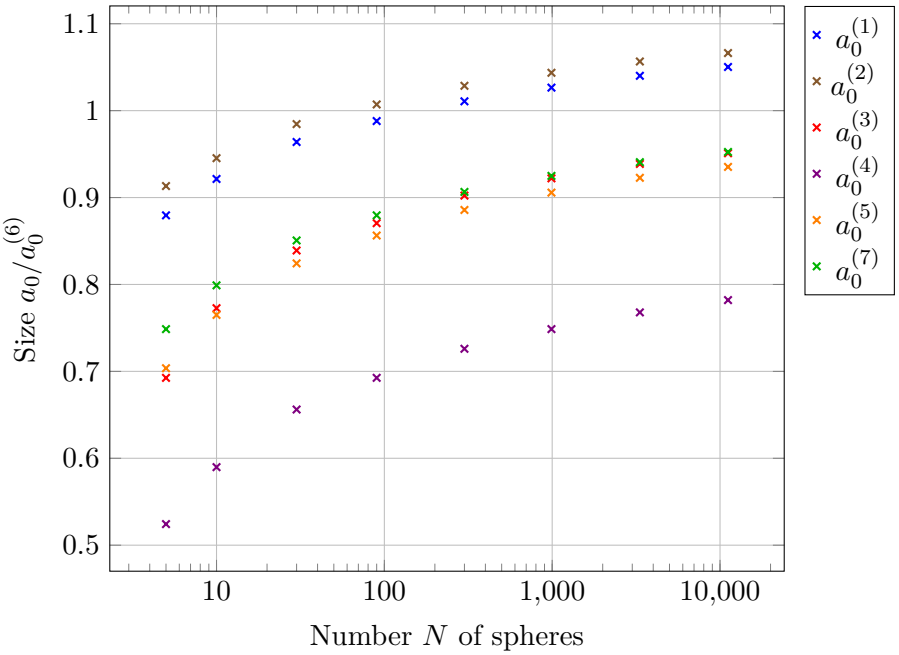


**Figure 8.9:** Comparison of the different candidates for the sizes $a_0$ for Apollonian packings.

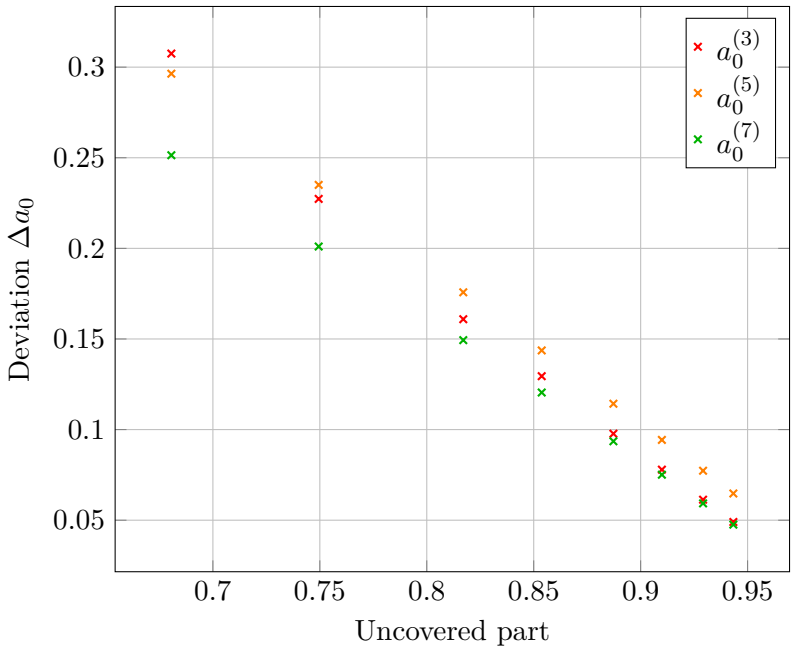


**Figure 8.10:** Deviation $\Delta a_0 = a_0 - a_0^{(6)}$ from the value $a_0^{(6)}$ of the Swiss-cheese model in dependence of the fraction of the hypersphere covered by the spherical caps.

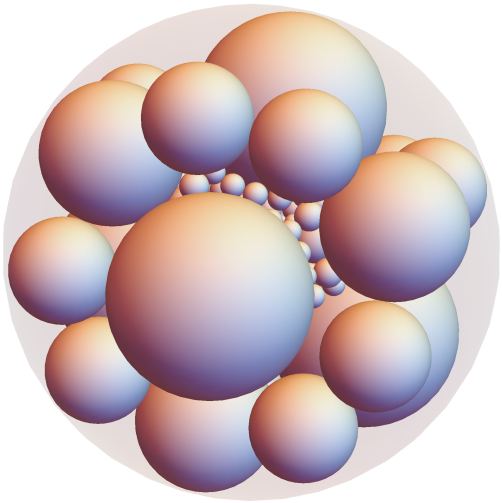

**Figure 8.11:** A nested Apollonian packing: The different sizes of the spheres are due to the projection. Actually, the projected spherical caps on the hypersphere are of about the same size.

unifoamy $a_0^{(5)}$. The values of the latter group are close to each other and seem to converge to approximately the same value.

If we consider the dependence of $a_0^{(3)}, a_0^{(5)}$ and $a_0^{(7)}$ on the covering of the hypersphere, shown in fig. 8.10, it seems that all three candidates $a_0^{(3,5,7)}$ approximately converge to $a_0^{(6)}$ if the whole hypersphere is covered. We are expecting that $a_0^{(6)}$ is the best fit if the black hole solution corresponds to a Swiss-cheese model with almost all dust removed, that is, the hypersphere is almost completely covered.

For this reason and since $a_0^{(5)}$ and $a_0^{(7)}$ are close to the squared minimum $a_0^{(3)} = \Psi_{\min}^2$, all three candidates are a good choice for the best fit to a dust universe. However, in all three cases we always have $a_0^{(3,5,7)} > a_0^{(4)} = \frac{4}{3\pi} \sum_A m_A$. Hence, we would not say that these configurations are Friedmann-like.

The reason for the deviation between $a_0^{(3,5,7)}$ and $a_0^{(4)}$ obtained from the total mass is the existence of very big spheres containing very massive black holes. For example, the five biggest spheres contain black holes possessing more than half of the total mass. As discussed in chapter 5, the masses should not be too big to obtain a good approximation. Furthermore, the biggest masses do not satisfy the unifoamy condition. Hence, we should not expect that these configurations are Friedmann-like.

In order to get rid of the biggest spheres, we consider a modification of the Apollonian packings: a nested version. This means that we take the biggest caps as starting points of new Apollonian packings. Therefore, we have to reverse the orientation of such a cap and put further four caps into the reversed cap such that they are mutually tangent. Then we construct the Apollonian packing as before. In the end, we remove the outer sphere. We can repeat this procedure several times until all spheres which are bigger than a certain limit size are removed. An example is shown in fig. 8.11. This way we obtain a more uniform configuration.

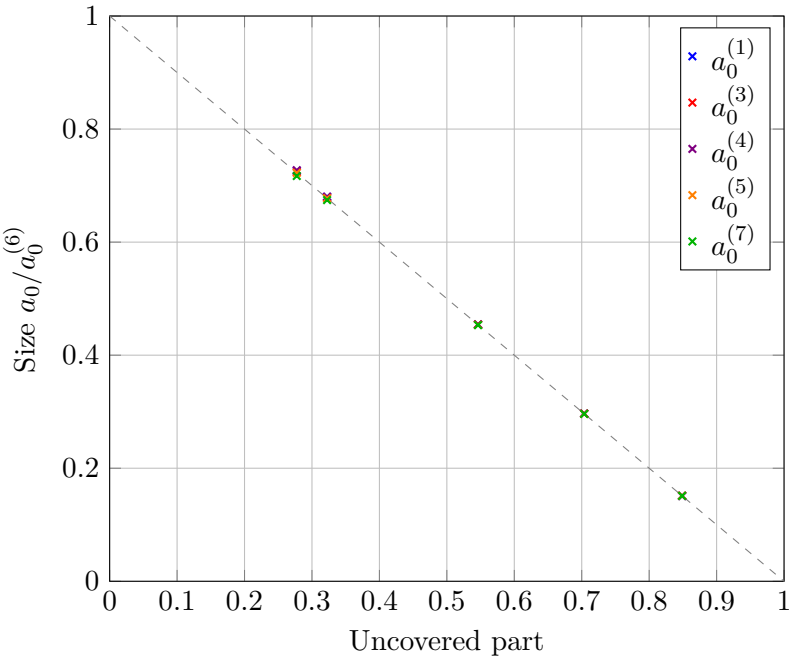


**Figure 8.12:** Comparison of the different candidates for the sizes $a_0$ for five nested Apollonian packings: We obtain approximately the same results for all candidates for each configuration.

The number of black holes becomes huge if we want to obtain a good covering of the hypersphere. For this reason, the computation time for the mass parameters grows drastically, as discussed above. However, since the nested packings are quite unifoamy, the mass parameters can be approximated by eq. (7.40)

$$\mu_A \approx m_A \sqrt{\frac{3\pi}{16M}}. \tag{8.18}$$

This has been verified for the considered example configurations.

This procedure allows us to construct a high variety of different configurations. As a simplification, we simply replace the spheres by a down-sized version of the original packing. In order to accelerate the computations of the mass parameters, we remove also the smallest spheres. As shown in fig. 8.12, the nested Apollonian packings are actually more unifoamy and all candidates for $a_0$ lead to approximately the same results. Again we can observe that the covering is good measure for the deviation from the Swiss-cheese radius $a_0^{(6)}$ since all values follow approximately the line $1 - x$, where $x$ is the uncovered part.

## 8.4 Tesseract Projection

This method is based on a procedure described by Korzyński [Kor14] and is illustrated in fig. 8.13 for the analogous three-dimensional case. The idea is to take a tesseract, the four-dimensional analogue of the cube, whose eight cells are cubes with an edge length of 2. Into the tesseract we inscribe the hypersphere with radius 1. The cells of the tesseract

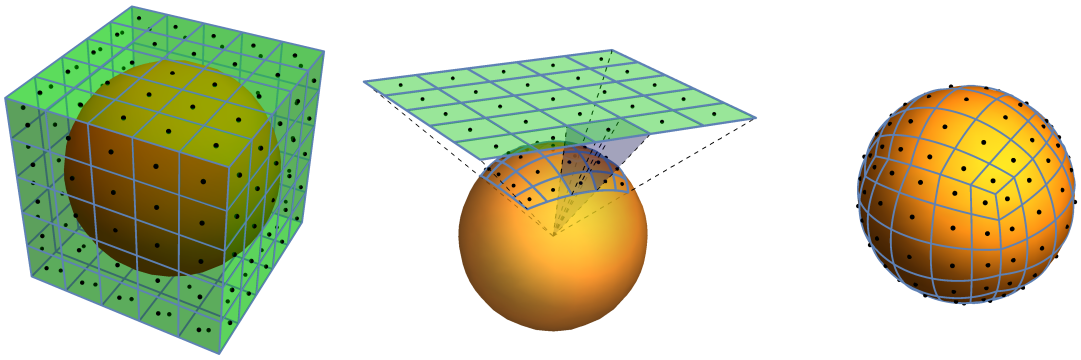

**(a)** Cube divided into sub-cells with black holes in their centres

**(b)** Central projection of the sub-cells onto the hypersphere

**(c)** Partition of the hypersphere after the projection

**Figure 8.13:** The two-dimensional analogue of the projection from the tesseract to the hypersphere: The sphere is put into a cube whose faces are divided into squares containing a black hole. The partition is projected onto the sphere by a central projection. The mass parameters are proportional to the volume of the projected sub-cells.

are subdivided into smaller equal cubes so that each cell contains in the end $n^3$ little cubes with an edge length of $\frac{2}{n}$. Altogether we have $N = 8n^3$ sub-cells. Into these sub-cells we put a black hole at an arbitrary position, usually at the centre. Finally, the black holes and also the boundaries of the sub-cells are projected onto the inscribed hypersphere by a radial projection from the origin. The mass parameters are taken to be proportional to the volume $V$ of its projected sub-cell given by

$$V_A = \int \frac{1}{(1 + x_1^2 + x_2^2 + x_3^2)^2} \, \mathrm{d}x_1 \, \mathrm{d}x_2 \, \mathrm{d}x_3, \tag{8.19}$$

where $\{x_1, x_2, x_3\}$ is the region of the sub-cell on the tesseract. This is easily proven if we use that the embedding of the hypersphere is

$$\boldsymbol{X} = \frac{1}{\sqrt{1 + x_1^2 + x_2^2 + x_3^2}} (x_1, x_2, x_3, 1). \tag{8.20}$$

We set $\mu_A = V_A$.

As discussed in section 7.3, the modified cap discrepancy $\mathcal{E}$ for such configurations is bounded from above by the diameter of the projected sub-cells. The latter are bounded by the diameter $\frac{2\sqrt{3}}{n}$ of the sub-cells on the tesseract. Hence, we get

$$\mathcal{E} \leq \frac{2\sqrt{3}}{n} = 4\frac{\sqrt{3}}{\sqrt[3]{N}}. \tag{8.21}$$

It follows [Kor14] that these configurations are Friedmann-like because the modified cap discrepancy vanishes for large numbers $N$. Hence, the space becomes rounder in most regions, except close to the black holes, the more masses we add. This is illustrated in fig. 8.14. Hence, we can use them in order to the unifoamity condition.

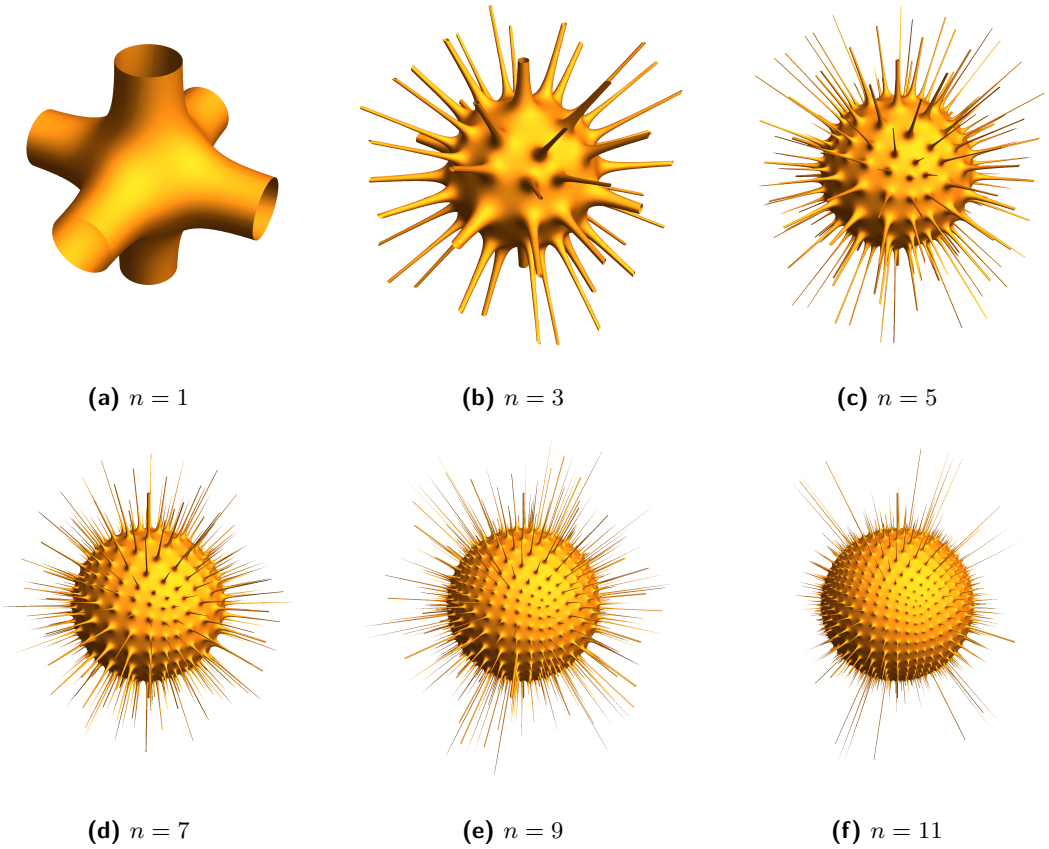

**(a)** $n = 1$ **(b)** $n = 3$ **(c)** $n = 5$

**(d)** $n = 7$ **(e)** $n = 9$ **(f)** $n = 11$

**Figure 8.14:** The spatial metric becomes rounder with an increasing number of black holes. This means that the conformal factor is approximately constant in most regions except close to the black holes where it diverges and a spike forms.

For these configurations, we find similar results for the different choices for size to the previous examples as shown in fig. 8.15. With an increasing number black holes the configurations become more unifoamy and the different possibilities for $a_0$ lead to similar results.

More interesting is the fact that, although the mean values of the mass parameters and masses decrease with the number of black holes, the relative standard deviation does not decrease as it can be seen in fig. 8.16. This means that there is still a high variation in the masses. However, this shows that it is not so important to have masses of the same order but not to have too big masses.

Another interesting observation is that, if we consider the corresponding Swiss-cheese model, the covered part of the hypersphere is approximately constant. The reason for this is that the configuration in each step is roughly a down-scaled version of the previous step with some additional black holes. In order to improve the covering of the 3-sphere, it is necessary to add new black holes between the previous ones so that we fill the gaps in the corresponding Lindquist-Wheeler model. Hence, the configurations of the tesseract projection model are not well approximated by the corresponding Swiss-cheese models even for big numbers of black holes, in contrast to the previous models. This raises the question whether the time evolution of this model differs from the previous ones.

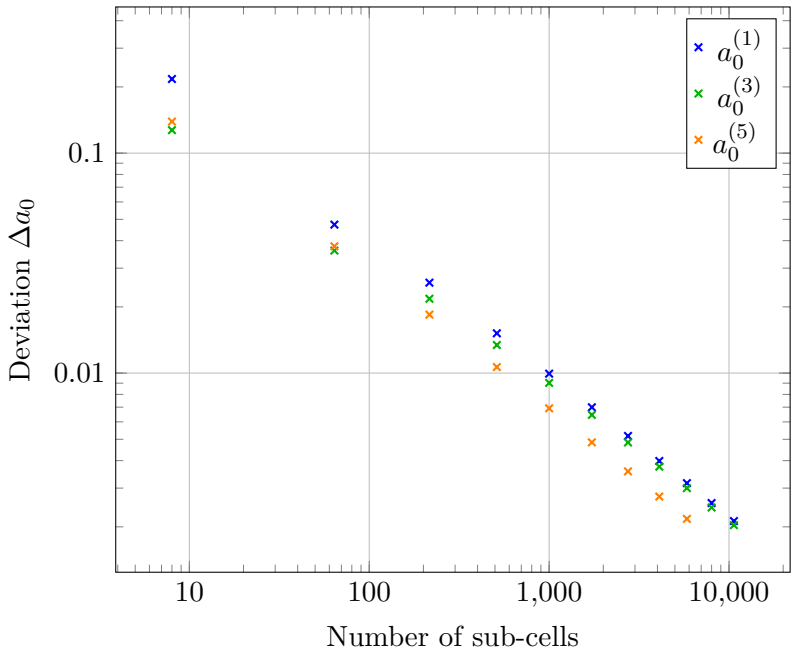


**Figure 8.15:** Comparison of the deviation $\Delta a_0 = |a_0 - a_0^{(4)}|$ between the different candidates for the sizes in the tesseract projection model.

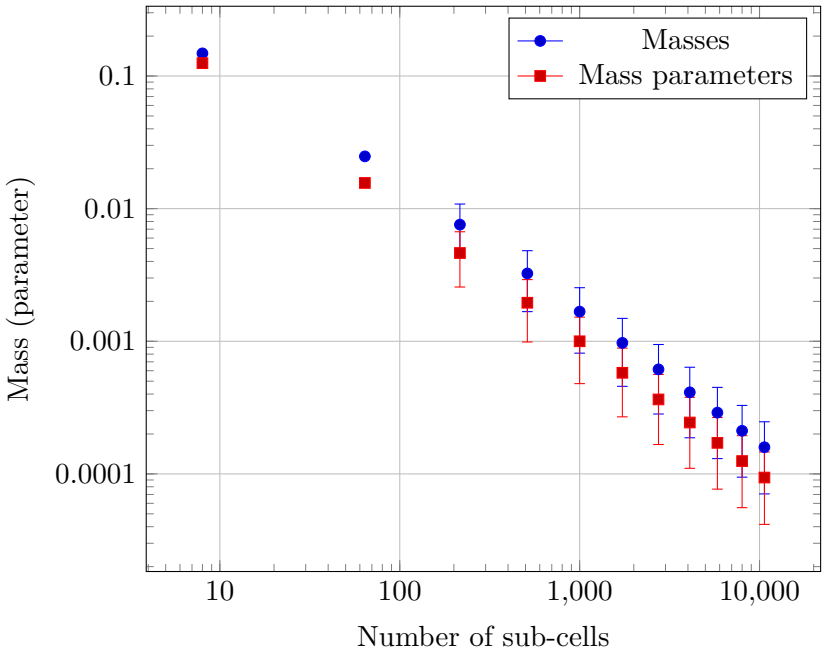


**Figure 8.16:** Mean and standard deviation for the masses

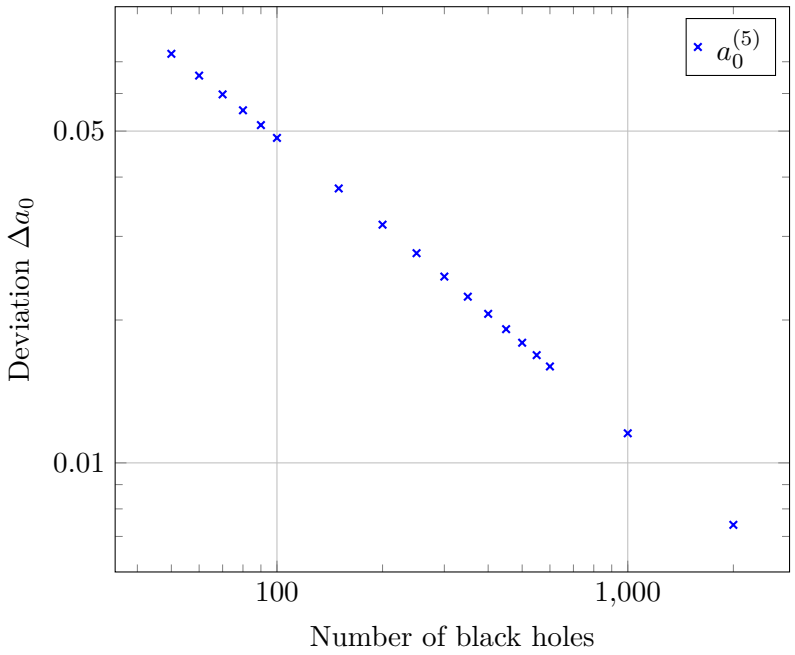


**Figure 8.17:** Unifoamity of minimum configurations: With an increasing number of black holes, the deviation $\Delta a_0 = |a_0 - a_0^{(4)}|$ for the unifoamy $a_0^{(5)}$ decreases.

## 8.5 Minimum of the Total Mass

In this last model, the black holes are distributed on the hypersphere in such a way that the total mass of black holes

$$\mathcal{M}(\boldsymbol{P}_1, \ldots, \boldsymbol{P}_{\boldsymbol{N}}) = \sum_A \sum_{B \neq A} \frac{2\mu_A \mu_B}{\|\boldsymbol{P}_A - \boldsymbol{P}_B\|} \tag{8.22}$$

is minimised for given $\{\mu_1, \ldots, \mu_N\}$, as discussed in the last chapter in section 7.3.

In order to make the construction more comprehensible, we interpret the total mass as a four-dimensional version of the Newtonian gravitational potential $V \equiv \mathcal{M}$, imaging the mass parameters as masses. Then we randomly put $N$ point particles with 'mass' $\mu_A$ on the hypersphere and let them move under the action of the 'gravitational' force $\boldsymbol{F}_A = -\nabla_{\boldsymbol{P}_A} V$. Furthermore, we include some friction so that the whole system settles down and comes to rest. Hence, a particle satisfies the equation of motion

$$\mu_A \ddot{\boldsymbol{P}}_A = -\nabla_{\boldsymbol{P}_A} V + \kappa \dot{\boldsymbol{P}}_A, \tag{8.23}$$

where $\kappa$ is a properly chosen friction constant. Note that, in view of the standard potential, we use the 'wrong' sign for $V$. For this reason the force is repulsive so that we actually find the minimum of $V$.

We have considered examples for up to 2000 black holes. In all cases we have set $\mu_A = \frac{1}{N}$ for all particles. As expected, fig. 8.17 shows that the minimum configurations become more unifoamy with an increasing number of black holes.

# 9 Time Evolution

In chapter 7, we constructed Friedmann-like initial configurations of black holes: Unifoamy distributions have a corresponding Friedmann dust universe such that the size and mass fit. However, this can only be the first step. The question is not if a single slice can be approximated by a Friedmann universe, but we are in the large-scale dynamics of the Universe. Hence, the more important step is the second one: the time evolution.

In this last chapter, we address the problem if these initial solutions may also have a Friedmann-like time evolution for at least a certain time interval. Here we briefly discuss some ideas if it si reasonable to assume that Friedmann-like initial data for unifoamy black hole configurations evolve like a Friedmann dust universe and how one could approach this problem.

Cosmological FLRW spacetimes are dynamically unstable in the sense that small perturbations from the FLRW-metric grow in time, that is, the matter collapses and forms structures. Similarly, we expect that interactions between black holes perturb the time evolution so that it differs from a dust universe. In particular, when black holes come close together and may merge, the black hole interaction is not negligible causing big perturbations, at least locally. Therefore, we expect that the time evolution is most probable Friedmann-like for unifoamy configurations.

Local perturbations, for example due to black hole interactions, probably propagate by gravitational waves through the whole spacetime causing global perturbations. These may be damped so that the global behaviour is barely influenced, but it may also be possible that they grow due to the non-linearity of Einstein's equations leading to big deviations from a Friedmann-like behaviour. In this latter case, we would say that backreaction effects occur. However, we are never expecting that the time evolution is Friedmann-like in the vicinity of the black holes which is why we should concentrate on the time evolution in the far regions.

## 9.1 Evolution Equations

There are several possibilities to tackle the problem of time evolution. Of course, the most satisfactory result would be an exact solution to the evolution equations (2.85). In the vacuum case $E \equiv 0$, $\boldsymbol{j} \equiv 0$ and $\boldsymbol{S} \equiv 0$, they are given by

$$\partial_t \bar{\boldsymbol{g}}_{ab} = \left(\boldsymbol{\mathcal{L}}_\beta \bar{\boldsymbol{g}}\right)_{ab} - 2\alpha\, \bar{K}_{ab}, \tag{9.1a}$$

$$\partial_t \bar{\boldsymbol{K}}_{ab} = \left(\boldsymbol{\mathcal{L}}_\beta \bar{\boldsymbol{K}}\right)_{ab} - \bar{\nabla}_b \bar{\nabla}_a \alpha + \alpha \left(\bar{R}_{ab} + \mathcal{K} \bar{K}_{ab} - 2\bar{K}_{ac} \bar{K}^c{}_b\right). \tag{9.1b}$$

We have to solve this system of coupled differential equations for our initial data

$$\bar{\boldsymbol{g}}(t, \boldsymbol{x})|_{t=0} = \Psi^4(\boldsymbol{x})\, \boldsymbol{h}(\boldsymbol{x}), \tag{9.2a}$$

$$\bar{\boldsymbol{K}}(t, \boldsymbol{x})|_{t=0} = 0. \tag{9.2b}$$

### Slicing Conditions

In view of the Friedmann solution, we would try a *normal geodesic slicing*[1] with $\alpha \equiv 1$ and $\boldsymbol{\beta} \equiv 0$ first. A natural ansatz for the spatial metric would be to assume that the conformal metric is constant in time and the time dependence is completely encoded in the conformal factor so that

$$\bar{\boldsymbol{g}}(t, \boldsymbol{x}) = \Psi^4(t, \boldsymbol{x})\, \boldsymbol{h}(\boldsymbol{x}). \tag{9.3}$$

In this case the first evolution equation (9.1a) reduces to $\partial_t \bar{\boldsymbol{g}} = -2\bar{\boldsymbol{K}}$ yielding $\bar{\boldsymbol{K}} = \frac{1}{3}\mathcal{K}\,\bar{\boldsymbol{g}}$, where $\mathcal{K} = -3\,\partial_t \ln \Psi^2$. The momentum constraint, which must be satisfied in every slice, implies for $\bar{\boldsymbol{K}} = \frac{1}{3}\mathcal{K}\,\bar{\boldsymbol{g}}$ that $\bar{\nabla}_a \mathcal{K} = 0$. It follows that the conformal factor must be spatially constant, $\bar{\nabla}_a \Psi \equiv 0$, and thus depends only on time, $\Psi = \Psi(t)$, in contradiction to our solution. For this reason, we need another ansatz for the metric or other slicing conditions for the lapse function and the shift vector field.

Perhaps, it may be possible to solve the system analytically for an appropriate choice of the lapse function $\alpha$ and the shift vector field $\boldsymbol{\beta}$. This could also avoid difficulties usually occurring in geodesic slicings[2]: After some time the evolution breaks down because we run into singularities; either the curvature singularities of the black holes or coordinate singularities due to intersecting $\boldsymbol{\partial}_t$-curves. The reason for this is the focussing property of gravity on vorticity-free geodesics. For example, the Schwarzschild singularity is hit after the time interval $m\pi$, where $m$ is the mass of the black hole.

An often used slicing with a singularity-avoidance property is the so-called *maximal slicing* where $\mathcal{K} \equiv 0$. In this case, all slices are maximal hypersurfaces in the spacetime[3] and the second evolution equation (9.1b) yields for the lapse function the differential equation

$$\Delta\alpha = \alpha\, \bar{K}_{ab} \bar{K}^{ab}. \tag{9.4}$$

For example, we used a maximal slicing for the Schwarzschild metric in section 6.1.

However, even if we find an slicing allowing us to solve the evolution equations, we are not able to decide if the time evolution is Friedmann-like without defining what this means. There is no obvious definition to arbitrary spacetimes and we can imagine several possibilities. For example, people have considered the evolution of the distance between two neighbouring black holes [BK12] or the evolution of the lengths of special curves [Cli+13]. It would also be possible to consider evolution of geodesic congruences in the far-region of the black holes. Of course, the most obvious idea is to fit a Friedmann dust universe to each slice and consider the evolution of its size. However, there are two problems: On the one hand, we do not know yet how to fit a Friedmann universe to a hypersurface with non-vanishing extrinsic curvature. On the other hand, even if would know how, deviations from a Friedmann-like behaviour in the time evolution may also arise to the fact that we have chosen an inappropriate slicing, that is, observers on the flow of the vector field $\boldsymbol{\partial}_t$ need not to be cosmic observers. The same problem occurs in Friedmann universes since the universe is not homogeneous and isotropic for non-comoving observers. This problems also concerns the evolution of distances: If we want to test a Friedmann-like behaviour, the curves should lie in constant-time slices of cosmic observers. Therefore, the next step must be definition of cosmic observers, that is, the appropriate choice of the lapse function

[1] This slicing is called *geodesic* because the curves generated by $\boldsymbol{\partial}_t$ are geodesics.
[2] See the textbook of Gourgoulhon [Gou12] for further details.
[3] In contrast, surfaces with $\mathcal{K} = 0$ in the Riemannian spaces are minimal surfaces, compare to section 6.4.

and shift vector field. Maybe it is possible to gain some insight from the condition that the total mass should be extremal in each slice.

Our conjecture is that a Friedmann-like time evolution most likely appears around the minima of the conformal factor in the initial slice. These should be the far-field regions of the black holes as discussed in the last chapter. A combination of both slicings, geodesic and maximal, seems to be most reasonable: Close to the inner ends like a maximal slicing in order to avoid running into singularities and in the far-field like a geodesic slicing as in the Friedmann solutions. It might be possible that a maximal slicing already provides this property. For two black holes, the lapse function can be determined exactly on the initial slice in the flat case [JS02]. If it is possible to generalise this to an arbitrary number of black holes in the spherical case, we could check if the maximal slicing approximately corresponds to a geodesic slicing in the far-field.

#### Perturbative Ansatz

First insight may also be gained from a perturbative ansatz. Close to the minima and in the beginning, the time evolution should be close to the real solution in first order if we consider a geodesic slicing with $\alpha \equiv 1$ and $\boldsymbol{\beta} \equiv 0$ everywhere. Further away or at later times, the perturbative solution probably deviates from the correct one.

First results in this direction were obtained by Clifton et al. [Cli+13]. Instead of the evolution of the spatial metric and the extrinsic curvature, they considered the evolution of the vector field $\boldsymbol{\partial}_t$, also known as *1+3 formulation*, see for example [EU97]. They claimed that, for the configurations based on the regular polychorons, the equations of motion in normal geodesic slicing reduce to ordinary differential equations at certain points designated by the symmetry of the polychorons. This means that spatial derivatives are not needed so that they should obtain exact results. They could show that the time evolution of the length of special curves is similar to a Friedmann dust universe for a certain time interval. Actually, it was shown later by [KHB15; CGR16] that the differential equations only decouple if the magnetic Weyl part can be neglected. Nevertheless, they could show that the evolution approximately follows a Friedmann universe.

In the same manner, numerical simulations may be used. For example, the tesseract configuration was simulated by Bentivegna and Korzyński [BK12] using the BSSN formalism. Here the lapse function and shift vector field are determined by some differential equations so that this is not a normal geodesic slicing. Interestingly, the time evolution is very close to the Friedmann dust universe for a long time: After 30% of the recollpase time of the dust universe the deviation is just about 1%.

## 9.2 Newtonian Approximations

As long as the black holes are far away from each other, as it is the case in the initial slice for Friedmann-like black hole configurations, it should be possible to neglect general relativistic effects. For this reason, we may apply a Newtonian approximation to our initial solution with point masses instead of black holes.

#### Standard (Post-)Newtonian Approximation

Since we can write the spatial metric in terms of flat conformal metric, it should be possible to perform a (post-)Newtonian approximation. A problem might be the mass at infinity which is probably fixed. This does not occur in the standard formalism. The question is

how this black hole interacts with the other masses? Naively, we would think of some kind of radial force attracting the masses to infinity. Perhaps it appears as a force due to a cosmological constant such that $\boldsymbol{F} = \Lambda\, \boldsymbol{x}$. However, this is purely speculative.

In order to avoid a black hole at infinity, it would be interesting if it is possible to develop some kind of post-Newtonian approximation on the hypersphere or even in the embedding space. There are already post-Newtonian approaches to cosmological perturbation theory on Friedmann backgrounds. Hence, such an approach seems feasible. In the case that such a formalism already exist, we are not aware of any.

**Central Configurations**

In this context, it is interesting to reconsider central configurations which have a Friedmann-like time evolution, see for example [EG14]. In Newtonian physics, central configurations are special solutions of gravitationally interacting point particles with masses $m_A$. Their equations of motion are given by Newton's law

$$m_A\, \ddot{\boldsymbol{x}}_A = \boldsymbol{F}_A, \tag{9.5}$$

where the force $\boldsymbol{F}_A = -\nabla_{\boldsymbol{x}_A} V$ is determined by the gravitational potential

$$V = -\frac{1}{2} \sum_{A=1}^{N} \sum_{B \neq A} \frac{m_A m_B}{\|\boldsymbol{x}_A - \boldsymbol{x}_B\|}. \tag{9.6}$$

If we demand that the configuration should have a homothetic motion, that is, we make the ansatz

$$\boldsymbol{x}_A = a(t)\, \boldsymbol{p}_A, \tag{9.7}$$

where $a(t)$ is the same for all particles and $\boldsymbol{p}_A$ is constant, $\dot{\boldsymbol{p}}_A = 0$, we obtain

$$a^2(t) \ddot{a}(t) m_A \boldsymbol{p}_A = -\sum_{B \neq A} m_A m_B\, \frac{\boldsymbol{p}_A - \boldsymbol{p}_B}{\|\boldsymbol{p}_A - \boldsymbol{p}_B\|^3}. \tag{9.8}$$

Since the right-hand side does not depend on time, the left-hand side must also be constant, hence we obtain

$$\ddot{a}(t) = -\frac{\mathcal{C}}{a^2(t)}, \tag{9.9a}$$

$$\mathcal{C} m_A \boldsymbol{p}_A = \sum_{B \neq A} m_A m_B\, \frac{\boldsymbol{p}_A - \boldsymbol{p}_B}{\|\boldsymbol{p}_A - \boldsymbol{p}_B\|^3}, \tag{9.9b}$$

where $\mathcal{C}$ is some constant. The latter eq. (9.9b) are the central configuration equations which have already appeared in section 7.3. They give constraints on the initial data. The constant $\mathcal{C}$ is determined by the condition

$$2\mathcal{C}\mathcal{I} = -V, \tag{9.10}$$

where $\mathcal{I} = \frac{1}{2} \sum_A m_A \boldsymbol{p}_A^2$. This is obtained from the central configuration equations by multiplying each one with $\boldsymbol{p}_A$, adding all up and using the Euler theorem on homogeneous

functions. The former eq. (9.9a) is the equation of motion for such configurations that can be integrated to

$$\left(\frac{\dot{a}(t)}{a(t)}\right)^2 = \frac{\mathcal{C}}{2a^3(t)} - \frac{k}{a^2(t)} \tag{9.11}$$

where $k$ is an integration constant. If we write $\mathcal{C} = 2a_0$, this equals the first Friedmann equation (4.27).

Now we return to unifoamy configurations on the hypersphere. We have seen that these are approximately central configurations in section 7.3. However, if we want to apply the above results, we have to assume that the gravitational law on the hypersphere is the same as in flat space but we have to use four-dimensional vectors of the embedding space instead of the three-dimensional ones, that is, we simply substitute $\boldsymbol{p}_A \mapsto \boldsymbol{P}_A$.

We want to stress that this is an ad hoc assumption, there is no reason to believe that there is an analogue of Newton's law on gravitation on the 3-sphere taking this form. We make this assumption only due to the observation that the ensemble of point masses follow the evolution of a hypersphere with a time-dependent radius $a(t)$ satisfying the first Friedmann equation corresponding to a spherical dust universe. However, we want to mention two severe counter-arguments: First, such a law contradicts Gauss's law because there exist only sources and no sinks of the gravitational field on a closed space. Second, eq. (7.61) indicates that the should have $\mathcal{C} = a_0$ for approximately unifoamy central configurations in contrast to $\mathcal{C} = 2a_0$ from the first Friedmann equation, as shown above. For this reason, our assumption is probably not correct or has to be modified.

This connection to central configurations is at least remarkable and should be studied in more detail in the future. A correct Newtonian-like approximation may modify the gravitational law on the hypersphere and remove the additional factor 2. However, is also possible that central configurations are good approximations of unifoamy configurations on the hypersphere and the time evolution is completely irrelevant.

## 9.3 Similarity to Swiss-cheese Models

At last, we come back to the Lindquist-Wheeler and Swiss-cheese models. For regular configurations, Lindquist and Wheeler could derive equations of motion and determine the global behaviour which is the same as for a Friedmann dust universe. In our case of more general configurations, the equation of motion of the comparison is still the first Friedmann equation since the construction is the same as for Swiss-cheese models as discussed in chapter 5. However, Lindquist-Wheeler models are still approximate solutions since the junction conditions between two cells are satisfied only at the intersection of the boundaries. In contrast, Swiss-cheese models are exact solutions to Einstein's equations. Therefore, we are expecting that the initial data for multi-black hole solutions should have a time evolution similar to a Friedmann dust universe if the initial are similar to a Swiss-cheese model where most of the dust is removed, that is, the Swiss-cheese model is almost a vacuum solution.

In the last chapter, we have seen that the values for $a_0$ of the Lindquist-Wheeler models seem to converge against the Swiss-cheese value if the hypersphere almost completely covered by the spherical caps. In this case, the difference between the Lindquist-Wheeler and Swiss-cheese model should be negligible so that the time evolution should be similar.

Hence, the fraction of the volume of the hypersphere covered by spherical caps in the Swiss-cheese model seems to be a good measure for the similarity of the Lindquist-Wheeler model to the Swiss-cheese model, and therefore, an indicator for the expected time evolution. We could observe a similar behaviour for approximately unifoamy initial data: The better the covering of the corresponding Swiss-cheese model, the smaller is the difference between the unifoamy size and the size of the Swiss-cheese dust universe. One could expect that, in order to obtain a good covering of the hypersphere, it should be sufficient if a configuration is unifoamy. However, the tesseract projection shows that this need not be the case so that we actually need the covering condition.

It seems likely to conclude that the time evolution for the initial data is similar to a Swiss-cheese model if the black hole configuration is Friedmann-like. The original motivation of Lindquist and Wheeler was the Wigner-Seitz approximation in solid state physics which is proven to be adequate. However, such an approach is not necessarily successful in general relativity. For example, it is known that a vacuum spacetime is only similar to the Minkowski spacetime if the spatial metric and the extrinsic curvature in the initial slice are close to the ones of the Minkowski spacetime with respect to a certain norm involving up to third derivatives in case of the spatial metric and second derivatives for the extrinsic curvature [CK14]. Hence, we expect that similar conditions have to be satisfied in the general case of arbitrary spacetimes. In our case, the extrinsic curvature vanishes for both solutions, the initial data and the Friedmann solution. The conformal metric in the spatial metric is in both cases the round metric. However, for the conformal factor, we only have similarity of the absolute value, that is the fit of the size, in the far-field of the black holes by Korzyński's first theorem, and similarity of the first derivatives around the minima of the conformal factor. Close to the inner ends, the spatial metric becomes so that we have Schwarzschild black holes in both models. In the intermediate region, both solutions probably differ, in particular, the initial data is smooth ($C^\infty$) everywhere whereas the Swiss-cheese model is only continuously differentiable ($C^1$) at the boundary. Hence, from the mathematical point of view, the similarity of the time evolution is not obvious.

# 10 Summary and Conclusions

The aim of this thesis was to improve the understanding of the fitting problem, that is, how to determine the Friedmann dust universe with a homogeneous mass density which best approximates a spacetime with an inhomogeneous matter distribution. We tackled the fitting problem from two sides: On the one hand, we constructed approximative solutions modelling the region around masses by a Schwarzschild spacetime. On the other hand, we have looked for exact vacuum solutions to Einstein's equations where matter is replaced by black holes.

**Approximative models**

In the first approach we assumed that the region around a mass is approximately spherically symmetric if the distance between the masses is big enough. In this case, the Schwarzschild spacetime should be a reasonable approximation for this region. In chapter 5, we discussed two possibilities to construct inhomogeneous cosmological models from this assumption: Swiss-cheese and Lindquist-Wheeler models.

In Swiss-cheese models, spherical regions are removed from a Friedmann dust universe and substituted by Schwarzschild spacetimes. Such a spacetime still behaves like a Friedmann universe on the largest scales by construction. Locally in the Schwarzschild regions, the spacetime is static. In order to be a regular solution to Einstein's equations, the Israel junction conditions had to be satisfied at the boundaries. In particular, they yielded a relation between the masses of the black holes and the removed dust. One can add arbitrarily many Schwarzschild regions to a dust universe as long as they do not overlap. In the limit that almost all dust is removed, we are expecting that a vacuum solution and the corresponding Swiss-cheese model have a similar time evolution.

Lindquist-Wheeler models are very similar to Swiss-cheese models but we needed not presuppose the existence of a dust universe. Instead, an auxiliary hypersphere, called comparison sphere, was used to formulate the junction conditions. The Schwarzschild regions are put onto the comparison sphere, tangent at their boundaries. In contrast to the Swiss-cheese models, the Schwarzschild regions are allowed to overlap. Hence, an additional condition is needed determining how much they are allowed to overlap. Lindquist and Wheeler considered only regular configurations of black holes on the comparison sphere such that all black holes are equal. The size of the Schwarzschild regions was determined by the condition that the sum of all volumes covered by the Schwarzschild regions equals the total volume of the comparison sphere. In this case, some regions of the comparison sphere are uncovered, whereas other regions are covered multiple times. Due to the symmetry of these configurations, the evolution of the boundaries has to be orthogonal to the comparison sphere. This yielded a Friedmann-like behaviour for the evolution of the boundaries. Furthermore, we obtained a relation for the masses of the black holes which is the same as in the Swiss-cheese models. In the limit of infinitely many black holes, the size of the comparison sphere converges to the corresponding value of a Friedmann dust universe.

Extensions of the Lindquist-Wheeler models usually consider regular lattices of black

holes in flat space. We provided a generalisation to non-regular configurations on the comparison sphere based on the observation that the construction of Lindquist and Wheeler is essentially the same as for Swiss-cheese models. Hence, the size of a Schwarzschild region, given by its opening angle, is determined by the mass of a black hole. Additionally, we still demanded that the sum of the volumes of all Schwarzschild cells equals the volume of the comparison sphere. For a given set of $N$ masses, these conditions yielded a system of $N + 1$ equations for the opening angles and the size $a_0$ of the comparison sphere. We suggested that the solution for $a_0$ is a good approximation to the size of a fitted dust universe. However, the mass condition could only be satisfied, as we showed, if the masses were small enough, or equivalently if the volume covered by each Schwarzschild region was not too big.

In the limit that the dust universe of a Swiss-cheese model was filled with Schwarzschild regions such that almost all dust was removed, the size of the corresponding Lindquist-Wheeler model converged to the value of the dust universe. For this reason, we concluded that the fraction of the volume covered by Schwarzschild cells is an good indicator of the reliability of the approximation, that is, a measure for the degree of uniformity. A good covering can be achieved only if the masses are distributed evenly on the hypersphere, that is, the Schwarzschild regions do not overlap much.

We provided a new and simple algorithm which efficiently generates a space-filling covering of the 3-sphere as a modification of the one given by Borkovec, De Paris and Peikert [BDP94]. Our algorithm is based on the Descartes theorem for mutually tangent spherical caps and the methods of Lie sphere geometry, discussed in chapter 3. Lie sphere geometry provided a unified description of points and sphere-like objects in Euclidean space as well as on the hypersphere and the hyperboloid. This allowed us to give a unified version of the Descartes theorem on these spaces. Furthermore, we were able to extend the hyperbolic Descartes theorem such that it includes horocycles and hypercycles.

Our algorithm starts with a set of mutually tangent spherical caps. The gaps between these caps are filled with additional caps tangent to their neighbours. The exact size and position of the new spheres are calculated by the methods of Lie sphere geometry and the Descartes theorem. In order to obtain a more uniform covering, big caps can be replaced by smaller Apollonian covering.

Space-filling Apollonian packings were used to construct Swiss-cheese models by putting a black hole at the centre of each sphere; the masses are determined by the volume. This provided a simple construction for various inhomogeneous configurations where the degree of uniformity can easily be determined.

We discussed Swiss-cheese models for all three shapes of dust universes. The construction is the same in all three cases, therefore it should be possible to extend our construction of non-regular Lindquist-Wheeler models on the hypersphere to flat space and the hyperboloid. As discussed, this has already been done for regular lattices of black holes. In the general case, we need to adapt the overlapping condition properly in another way since these spaces are not compact and their volume is infinite.

### Exact solutions

In the second approach, we considered exact solutions to Einstein's equations describing inhomogeneous matter distributions. Since it was too challenging to solve the full system of Einstein's equations analytically, we restricted ourselves to the initial value problem in order to give at least an exact solution on the initial slice. For this reason, we applied the

3+1 decomposition of Einstein's equations yielding constraint and evolution equations for the spatial metric and the extrinsic curvature.

In order to simplify the constraint equation, we replaced matter by black holes as done in Swiss-cheese models. This relied on the assumption that it is possible to approximate gravitationally bound systems like galaxies by a single object, neglecting the local dynamics. We did not motivate this assumption mathematically, nor did we tell how to determine the mass of the black hole. This step needs further investigation in order to justify the assumption, because it could be possible that we are excluding backreaction effects due to this approximation.

The second assumption is the existence of a time-symmetric hypersurface characterised by vanishing extrinsic curvature. This excludes many solutions for the sake of an exact one. For the same reason, we neglected the cosmological constant. In this case, the Lichnerowicz equation became linear, which allowed us to derive a solution for an arbitrary number of black holes. However, one should try to find solutions for non-vanishing extrinsic curvature and cosmological constant in order to treat the fitting problem for further cosmological spacetimes and, finally, to model our Universe. For example, the special case that the trace of the extrinsic curvature and a positive cosmological constant cancel was treated in [DC16], yielding the same spatial metric which we obtained.

In view of the FLRW metric, we derived solutions to the Lichnerowicz equation in chapter 6. These are conformally equivalent to a maximally symmetric space which is either flat, spherical or hyperbolic. The solutions in the flat and spherical case have already been known but the hyperbolic solution appears to be new. However, we showed that all three solutions can be transformed into each other by a stereographic projection. Hence, they describe the same initial data. This corresponds to the fact that only the spherical dust universe possesses a time-symmetric slice. For this reason, we concentrated on the spherical solution.

The spherical solution describes a time-symmetric space containing $N$ inner ends. Close to an inner end, the metric becomes Schwarzschild-like. If it is also enclosed by a minimal surface, we associate a black hole to this end. We assumed that each end is enclosed by a minimal surface, that is, we have $N$ black holes at rest. However, this need not always be the case. In particular, we raised the question how to construct a space with two black holes of different masses. In the case of two inner ends, we showed that the same mass is associated to both ends and, if the ends are antipodal, we obtained the Schwarzschild solution, that is, a single black hole.

We suggested that a dust universe can be fitted to a multi-black hole solution if the configuration is unifoamy, which is a condition on the masses of the black holes. In an arbitrary configuration, the mass of a black hole is determined by the inverse distances to all other black holes, weighted by their mass parameters. If the configuration is unifoamy, the mass of a black hole is basically determined by its mass parameter. In particular, this condition ensures that the black holes are not too close to each other. Furthermore, unifoamy configurations seem not to allow too big masses. Unfortunately, we could not prove all properties of unifoamy configurations rigorously yet. However, there is always evidence from numerical calculations or from plausibility checks. The next step would be to prove these statements.

In order to determine the fit, we demanded that the size $a_0$ is fixed by the mass condition. This ensures that the dust universe has the correct mass. We estimated the spherical cap discrepancy of a unifoamy configuration using the similarity of such configurations to

Lindquist-Wheeler models. Since our result for $a_0$ is approximately the same as the one of Korzyński, his first theorem allowed us to argue that the size also fits.

Korzyński used an averaging procedure. However, there is a lack of justification for the averaging procedure and Korzyński does not provide a criterion to decide which configurations are Friedmann-like. In contrast, our choice for the size is based on the configuration itself. Only if the configuration is approximately unifoamy, we would construct the fitting dust universe.

In chapter 7, we discussed several candidates for the size of the fitted dust universe which we compared in chapter 8 for some example configurations. As a result, we obtained that Korzyński's value, the unifoamy $a_0$, the value from the associated Lindquist-Wheeler model and the one obtained from the total mass $a_0 = \frac{4}{3\pi}\sum_A m_A$ lead to similar results if the black hole configurations is approximately unifoamy. If the associated Swiss-cheese model were almost completely covered, all these possibilities were close to the size of the dust universe.

**Conclusions and Outlook**

We mainly concentrated on models with discretely distributed masses $m_A$ on the 3-sphere at the moment of their maximal expansion. We were expecting that a spherical dust universe can be fitted to these spacetimes if the masses are almost uniformly distributed. This means the inhomogeneous spacetime is approximated well by a round sphere in most regions and the total mass satisfies the mass condition $\sum_A m_A = \frac{3\pi}{4}a_0$ where $a_0$ corresponds to the scale factor of the dust universe at the moment of its maximal expansion. We wanted to explain and clarify what is meant by 'almost uniformly distributed' as well as 'is approximated well by a round sphere' and when the mass condition is satisfied.

We answer this questions in the following way: Our multi-black hole solution can be approximated by a spherical dust universe if the black hole configuration is approximately unifoamy, that is, if the black hole masses are determined by the mass parameter. This should be the case when the black holes are not too close to each other such that their mutual interaction is negligible. The size of the best-fitting spherical dust universe to the multi-black hole solution is determined by the mass condition. If the Schwarzschild regions in the corresponding Swiss-cheese model cover almost the whole hypersphere, that is, almost all dust is removed, Korzyński's first theorem should be applicable. Hence, the deviation from the fit should be small in most regions except close to the black holes. Furthermore, the fitted size is close to the Swiss-cheese radius. Hence, we are expecting a similar time evolution.

Possible backreaction effects will become apparent only in the time evolution. For this reason, the time evolution is the next important step, as discussed in chapter 9. Numerical computations indicate a Friedmann-like behaviour for a certain time. However, a notion of cosmic observers in inhomogeneous spacetimes needs to be developed in order to exclude deviations due to the slicing. At the moment we can say that only the initial slice possesses an approximation by a Friedmann dust universe.

An interesting observation is that some unifoamy configurations seemingly minimise the total mass. It seems likely to assume that unifoamy configurations are good approximations to such minimal configurations in general. This would imply that the size determined from the minimal mass could be a the best fit and the unifoamy size $a_0$ would be a good approximation to this value. Therefore, we make the conjecture that black hole configurations with minimal total mass can be approximated by Friedmann dust universe

and its size is determined by the minimal mass. The advantage of this concept is that it can also be applied to more general solutions than ours, for example, if a cosmological constant is included as in the solution [DC16], mentioned above. It may also be useful for the time evolution in order to decide if we have chosen an appropriate slicing.

In this context, the methods of Lie sphere geometry, providing a more abstract view, may be a powerful tool which we only started to explore. We used Lie sphere geometry mainly as a simplifying tool for calculations, but the mathematical literature provides more advanced techniques. As we have shown, the spatial metric can be rewritten using Lie sphere vectors. This change of view on the spatial metric, using five-dimensional null vectors in order to describe a three-dimensional Riemannian manifold, shifts the problem to a (projective) Minkowski space which may yield new insights.

All our considerations concern only spherical dust universes, whereas our Universe is flat and contains also other matter components than dust. Therefore, our results have to be adapted to non-spherical solutions. Since these solutions are non-compact, it is not possible to use the total mass. Instead, we should reformulate our results with respect to the mass density. However, the adaptation to non-spherical universes is unclear due to the lack of exact solutions. In contrast, Lindquist-Wheeler models have already been extended to regular lattices and, in principle, we already know how to construct arbitrary configurations; we are only missing an appropriate overlapping condition. However, we hope that our contribution to inhomogeneous cosmological models is a useful step towards a better understanding of our Universe.

# A Pentatope-based Apollonian Covering

Here we describe the construction of an Apollonian covering of the 3-sphere based on an initial configuration of five equal, pairwise tangent spherical caps whose centres are located at the vertices of an inscribed pentatope, the four-dimensional analogue of the tetrahedron. Using a stereographic projection from the centre of a particular spherical cap, the initial configuration corresponds to a configuration of four equal spheres within a bigger sphere. All spheres are pairwise tangent and the centres of the inner spheres form a tetrahedron as shown in fig. A.1. Analogously, the Apollonian covering of the 3-sphere corresponds to a packing of mutually tangent spheres within the outer sphere. The details of this construction and the mathematical background are discussed in chapter 3.

We start with a set of five equal, pairwise tangent spherical caps on the 3-sphere, that is, the caps have the same opening angle and their centres are located at the vertices of an inscribed pentatope. The coordinates of the vertices are given by

$$\boldsymbol{P}_1 = (0, 0, 0, -1)\,, \tag{A.1a}$$

$$\boldsymbol{P}_2 = \left(\frac{\sqrt{5}}{4}, \frac{\sqrt{5}}{4}, \frac{\sqrt{5}}{4}, \frac{1}{4}\right), \tag{A.1b}$$

$$\boldsymbol{P}_3 = \left(\frac{\sqrt{5}}{4}, -\frac{\sqrt{5}}{4}, -\frac{\sqrt{5}}{4}, \frac{1}{4}\right), \tag{A.1c}$$

$$\boldsymbol{P}_4 = \left(-\frac{\sqrt{5}}{4}, \frac{\sqrt{5}}{4}, -\frac{\sqrt{5}}{4}, \frac{1}{4}\right), \tag{A.1d}$$

$$\boldsymbol{P}_5 = \left(-\frac{\sqrt{5}}{4}, -\frac{\sqrt{5}}{4}, \frac{\sqrt{5}}{4}, \frac{1}{4}\right). \tag{A.1e}$$

By construction, the opening angle $\alpha$ of all spheres is half the angle between two vertices.

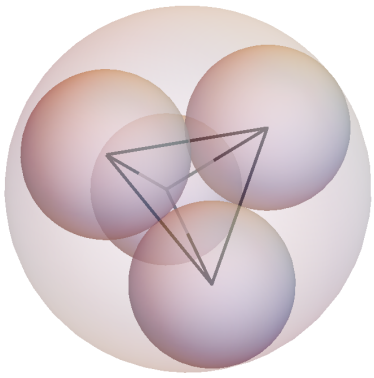

**Figure A.1:** Initial configuration

Hence, it is given by $\boldsymbol{P}_A \cdot \boldsymbol{P}_B = \cos(2\alpha)$ for any $A \neq B$, yielding

$$\alpha = \frac{1}{2} \arccos\left(-\frac{1}{4}\right) = \arcsin\sqrt{\frac{5}{8}}. \tag{A.2}$$

By a stereographic projection from the south pole, such a configuration is equivalent to four spheres in $\mathbb{R}^3$ with radius

$$r_{2,3,4,5} = \frac{\sqrt{10}}{1+\sqrt{6}} \tag{A.3}$$

and centres at the vertices of a tetrahedron

$$\boldsymbol{p}_2 = \left(\frac{\sqrt{5}}{1+\sqrt{6}}, \frac{\sqrt{5}}{1+\sqrt{6}}, \frac{\sqrt{5}}{1+\sqrt{6}}\right), \tag{A.4a}$$

$$\boldsymbol{p}_3 = \left(\frac{\sqrt{5}}{1+\sqrt{6}}, -\frac{\sqrt{5}}{1+\sqrt{6}}, -\frac{\sqrt{5}}{1+\sqrt{6}}\right), \tag{A.4b}$$

$$\boldsymbol{p}_4 = \left(-\frac{\sqrt{5}}{1+\sqrt{6}}, \frac{\sqrt{5}}{1+\sqrt{6}}, -\frac{\sqrt{5}}{1+\sqrt{6}}\right), \tag{A.4c}$$

$$\boldsymbol{p}_5 = \left(-\frac{\sqrt{5}}{1+\sqrt{6}}, -\frac{\sqrt{5}}{1+\sqrt{6}}, \frac{\sqrt{5}}{1+\sqrt{6}}\right), \tag{A.4d}$$

within a fifth sphere at the origin, $\boldsymbol{p}_1 = (0,0,0)$, with radius

$$r_1 = -\frac{\sqrt{10}}{4-\sqrt{6}} < 0. \tag{A.5}$$

The negative sign indicates that the inner points of the spherical cap at $\boldsymbol{P}_1$ is mapped to the exterior of the outer sphere. We say that the outer sphere is negatively oriented. This guarantees that new spheres are generated in the inside of the outer sphere. Note that all spherical caps have the same orientation. The Lie sphere vectors of a spherical cap are given by

$$\boldsymbol{\omega}_A = \left(\cot\alpha, \frac{\boldsymbol{P}_A}{\sin\alpha}\right) \tag{A.6}$$

such that

$$\boldsymbol{\omega}_1 = \left(\sqrt{\frac{3}{5}}, 0, 0, 0, -\frac{4}{\sqrt{10}}\right), \tag{A.7a}$$

$$\boldsymbol{\omega}_2 = \left(\sqrt{\frac{3}{5}}, \frac{1}{\sqrt{2}}, \frac{1}{\sqrt{2}}, \frac{1}{\sqrt{2}}, \frac{1}{\sqrt{10}}\right), \tag{A.7b}$$

$$\boldsymbol{\omega}_3 = \left(\sqrt{\frac{3}{5}}, \frac{1}{\sqrt{2}}, -\frac{1}{\sqrt{2}}, -\frac{1}{\sqrt{2}}, \frac{1}{\sqrt{10}}\right), \tag{A.7c}$$

$$\boldsymbol{\omega}_4 = \left(\sqrt{\frac{3}{5}}, -\frac{1}{\sqrt{2}}, \frac{1}{\sqrt{2}}, -\frac{1}{\sqrt{2}}, \frac{1}{\sqrt{10}}\right), \tag{A.7d}$$

$$\boldsymbol{\omega}_5 = \left(\sqrt{\frac{3}{5}}, -\frac{1}{\sqrt{2}}, -\frac{1}{\sqrt{2}}, \frac{1}{\sqrt{2}}, \frac{1}{\sqrt{10}}\right). \tag{A.7e}$$

The centres $\boldsymbol{x}_A$ and radii $r_A$ can be obtained from the circle representation of a Lie sphere vector

$$\boldsymbol{\omega}_A = \left( \frac{1 + \boldsymbol{p}_A^2 - r_A^2}{2r_A}, \frac{\boldsymbol{p}_A}{r_A}, \frac{1 - \boldsymbol{p}_A^2 + r_A^2}{2r_A} \right). \tag{A.8}$$

Hence, the radius is given by $r_A = \frac{1}{(\boldsymbol{\omega}_A)_0 + (\boldsymbol{\omega}_A)_4}$ and the centre by .

The inversion spheres are calculated by

$$\boldsymbol{\varpi}_A = \sqrt{3} \sum_{B=1}^{5} \mathcal{G}_{AB}^{-1} \boldsymbol{\omega}_B, \tag{A.9}$$

where $\mathcal{G}_{AB}^{-1} = \frac{1}{2} \left( \delta_{AB} - \frac{1}{3} \right)$. This yields

$$\boldsymbol{\varpi}_1 = \left( -\sqrt{\frac{1}{5}}, 0, 0, 0, -\sqrt{\frac{6}{5}} \right), \tag{A.10a}$$

$$\boldsymbol{\varpi}_2 = \left( -\sqrt{\frac{1}{5}}, \sqrt{\frac{3}{8}}, \sqrt{\frac{3}{8}}, \sqrt{\frac{3}{8}}, \sqrt{\frac{3}{40}} \right), \tag{A.10b}$$

$$\boldsymbol{\varpi}_3 = \left( -\sqrt{\frac{1}{5}}, \sqrt{\frac{3}{8}}, -\sqrt{\frac{3}{8}}, -\sqrt{\frac{3}{8}}, \sqrt{\frac{3}{40}} \right), \tag{A.10c}$$

$$\boldsymbol{\varpi}_4 = \left( -\sqrt{\frac{1}{5}}, -\sqrt{\frac{3}{8}}, \sqrt{\frac{3}{8}}, -\sqrt{\frac{3}{8}}, \sqrt{\frac{3}{40}} \right), \tag{A.10d}$$

$$\boldsymbol{\varpi}_5 = \left( -\sqrt{\frac{1}{5}}, -\sqrt{\frac{3}{8}}, -\sqrt{\frac{3}{8}}, \sqrt{\frac{3}{8}}, \sqrt{\frac{3}{40}} \right). \tag{A.10e}$$

The separation hyperplanes are calculated in the standard formalism by pairwise subtracting the sphere equations $(\boldsymbol{x} - \boldsymbol{p}_A)^2 = r_A^2$. This yields an equation for a hyperplane $\boldsymbol{x} \cdot \boldsymbol{n}_{AB} = d_{AB}$ whose Lie sphere vector is given by

$$\boldsymbol{\pi} = (d, \boldsymbol{n}, -d). \tag{A.11}$$

We obtain

$$\boldsymbol{\pi}_{12} = \left( -\frac{\sqrt{6}-1}{\sqrt{15}}, \sqrt{\frac{1}{3}}, \sqrt{\frac{1}{3}}, \sqrt{\frac{1}{3}}, \frac{\sqrt{6}-1}{\sqrt{15}} \right), \tag{A.12a}$$

$$\boldsymbol{\pi}_{13} = \left( -\frac{\sqrt{6}-1}{\sqrt{15}}, \sqrt{\frac{1}{3}}, -\sqrt{\frac{1}{3}}, -\sqrt{\frac{1}{3}}, \frac{\sqrt{6}-1}{\sqrt{15}} \right), \tag{A.12b}$$

$$\boldsymbol{\pi}_{14} = \left( -\frac{\sqrt{6}-1}{\sqrt{15}}, -\sqrt{\frac{1}{3}}, \sqrt{\frac{1}{3}}, -\sqrt{\frac{1}{3}}, \frac{\sqrt{6}-1}{\sqrt{15}} \right), \tag{A.12c}$$

$$\boldsymbol{\pi}_{15} = \left( -\frac{\sqrt{6}-1}{\sqrt{15}}, -\sqrt{\frac{1}{3}}, -\sqrt{\frac{1}{3}}, \sqrt{\frac{1}{3}}, \frac{\sqrt{6}-1}{\sqrt{15}} \right), \tag{A.12d}$$

$$\boldsymbol{\pi}_{23} = \left( 0, 0, -\frac{1}{\sqrt{2}}, -\frac{1}{\sqrt{2}}, 0 \right), \tag{A.12e}$$

$$\boldsymbol{\pi}_{24} = \left( 0, -\frac{1}{\sqrt{2}}, 0, -\frac{1}{\sqrt{2}}, 0 \right), \tag{A.12f}$$

$$\boldsymbol{\pi}_{25} = \left(0, -\frac{1}{\sqrt{2}}, -\frac{1}{\sqrt{2}}, 0, 0\right), \tag{A.12g}$$

$$\boldsymbol{\pi}_{34} = \left(0, -\frac{1}{\sqrt{2}}, \frac{1}{\sqrt{2}}, 0, 0\right), \tag{A.12h}$$

$$\boldsymbol{\pi}_{35} = \left(0, -\frac{1}{\sqrt{2}}, 0, \frac{1}{\sqrt{2}}, 0\right), \tag{A.12i}$$

$$\boldsymbol{\pi}_{45} = \left(0, 0, -\frac{1}{\sqrt{2}}, \frac{1}{\sqrt{2}}, 0\right). \tag{A.12j}$$

The inversion matrices are given by $\boldsymbol{\omega}' = \boldsymbol{\mathcal{I}}_{\boldsymbol{\varpi}}\boldsymbol{\omega} = \boldsymbol{\omega} - 2\langle\boldsymbol{\omega}, \boldsymbol{\varpi}\rangle\,\boldsymbol{\varpi}$. Written as a matrix equation, we get

$$\begin{pmatrix} \omega_0' \\ \omega_1' \\ \omega_2' \\ \omega_3' \\ \omega_4' \end{pmatrix} = \begin{pmatrix} 1+2\varpi_0^2 & -2\varpi_0\varpi_1 & -2\varpi_0\varpi_2 & -2\varpi_0\varpi_3 & -2\varpi_0\varpi_4 \\ 2\varpi_0\varpi_1 & 1-2\varpi_1^2 & -2\varpi_1\varpi_2 & -2\varpi_1\varpi_3 & -2\varpi_1\varpi_4 \\ 2\varpi_0\varpi_2 & -2\varpi_1\varpi_2 & 1-2\varpi_2^2 & -2\varpi_2\varpi_3 & -2\varpi_2\varpi_4 \\ 2\varpi_0\varpi_3 & -2\varpi_1\varpi_3 & -2\varpi_2\varpi_3 & 1-2\varpi_3^2 & -2\varpi_3\varpi_4 \\ 2\varpi_0\varpi_4 & -2\varpi_1\varpi_4 & -2\varpi_2\varpi_4 & -2\varpi_3\varpi_4 & 1-2\varpi_4^2 \end{pmatrix} \begin{pmatrix} \omega_0 \\ \omega_1 \\ \omega_2 \\ \omega_3 \\ \omega_4 \end{pmatrix}.$$

Now we can invert these spherical caps again and again and cover the whole 3-sphere. As described in section 3.5, we use the separation hyperplanes to decide if we accept a new sphere. In the limit of infinitely many caps, the remaining uncovered volume goes to zero. The residual set is a fractal of Hausdorff dimension 2.4739.

The number of new spheres grows roughly exponentially and the uncovered volume decreases also roughly exponentially. This means that we need a lot of spheres in order to reduce the uncovered volume. For example, the 3-sphere is covered by 1 424 790 tangent spherical caps after 11 iterations but 2.3 % of the volume of the 3-sphere is still uncovered. Alternatively, we can consider the stereographic projection of this configuration to the flat space which is shown on the cover. This packing consists of 1 424 789 mutually tangent spheres within the outer sphere. In this case, there is still about 5.8 % of the volume of the outer sphere unfilled. The difference to the first value is due to the change of volumes under a stereographic projection.

# B Uniform Polychora

Here we list all 68 spherical uniform polytopes on the 3-sphere. They are sorted with respect to the symmetry groups. The numbering follows the internet database of George Olshevsky [Ols]. For a more detailed discussion see section 3.4.

**Table B.1:** List of the 47 non-prismatic convex uniform polychorons

**(a)** Members of the $A_4$ family

| # | Name | Coxeter diagram | Vertices |
|---|---|---|---|
| 1 | 5-cell (pentatope) |  | 5 |
| 2 | rectified 5-cell |  | 10 |
| 3 | truncated 5-cell |  | 20 |
| 4 | cantellated 5-cell |  | 30 |
| 7 | cantitruncated 5-cell |  | 60 |
| 8 | runcitruncated 5-cell |  | 60 |
| 5 | runcinated 5-cell |  | 20 |
| 6 | bitruncated 5-cell |  | 30 |
| 9 | omnitruncated 5-cell |  | 120 |

**(b)** Members of the $B_4$ family

| # | Name | Coxeter diagram | Vertices |
|---|---|---|---|
| 10 | tesseract (8-cell) | 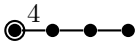 | 16 |
| 11 | Rectified tesseract | 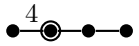 | 32 |
| 13 | Truncated tesseract | 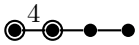 | 64 |
| 14 | Cantellated tesseract | 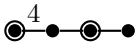 | 96 |
| 15 | Runcinated tesseract<br>runcinated 16-cell |  | 64 |
| 16 | Bitruncated tesseract<br>bitruncated 16-cell |  | 96 |
| 18 | Cantitruncated tesseract | 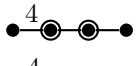 | 192 |
| 19 | Runcitruncated tesseract |  | 192 |
| 21 | Omnitruncated tesseract<br>omnitruncated 16-cell | 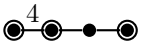 | 384 |
| 12 | 16-cell |  | 8 |
| 22 | rectified 16-cell<br>24-cell | 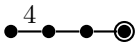 | 24 |
| 17 | truncated 16-cell | 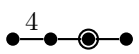 | 48 |
| 23 | cantellated 16-cell<br>rectified 24-cell |  | 96 |
| 24 | cantitruncated 16-cell<br>truncated 24-cell | 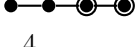 | 192 |
| 20 | runcitruncated 16-cell | 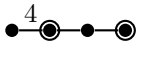 | 192 |

**(c)** Members of the $F_4$ family

| # | Name | Coxeter diagram | Vertices |
|---|---|---|---|
| 22 | 24-cell<br>rectified 16-cell | 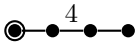 | 24 |
| 23 | rectified 24-cell<br>cantellated 16-cell | 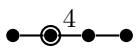 | 96 |
| 24 | truncated 24-cell<br>cantitruncated 16-cell |  | 192 |
| 25 | cantellated 24-cell | 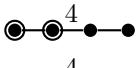 | 288 |
| 28 | cantitruncated 24-cell | 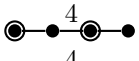 | 576 |
| 29 | runcitruncated 24-cell | 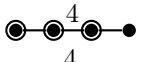 | 576 |
| 26 | runcinated 24-cell | 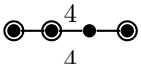 | 144 |
| 27 | bitruncated 24-cell | 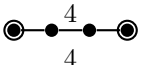 | 288 |
| 30 | omnitruncated 24-cell | 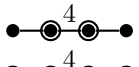 | 1152 |
| 31 | snub 24-cell | half $F_4$ | 96 |

**(d)** Members of the $H_4$ family

| # | Name | Coxeter diagram | Vertices |
|---|---|---|---|
| 32 | 120-cell | 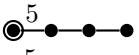 | 600 |
| 33 | rectified 120-cell |  | 1200 |
| 36 | truncated 120-cell | 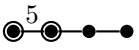 | 2400 |
| 37 | cantellated 120-cell | 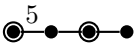 | 3600 |
| 38 | runcinated 120-cell<br>runcinated 600-cell | 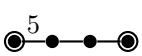 | 2400 |
| 39 | bitruncated 120-cell<br>bitruncated 600-cell | 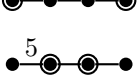 | 3600 |
| 42 | cantitruncated 120-cell |  | 7200 |
| 43 | runcitruncated 120-cell | 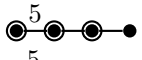 | 7200 |
| 46 | omnitruncated 120-cell<br>omnitruncated 600-cell | 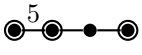 | 14400 |
| 35 | 600-cell |  | 120 |
| 34 | rectified 600-cell | 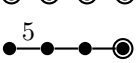 | 720 |
| 41 | truncated 600-cell |  | 1440 |
| 40 | cantellated 600-cell |  | 3600 |
| 45 | cantitruncated 600-cell |  | 7200 |
| 44 | runcitruncated 600-cell | 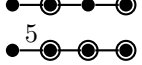 | 7200 |
| 47 | grand antiprism | diminished $H_4$ | 100 |

**(e)** Members of the $D_4$ family

| # | Name | Coxeter diagram | Vertices |
|---|---|---|---|
| 11 | Rectified tesseract |  | 32 |
| 16 | Bitruncated tesseract<br>bitruncated 16-cell |  | 96 |
| 12 | 16-cell |  | 8 |
| 17 | truncated 16-cell |  | 48 |
| 22 | 24-cell<br>rectified 16-cell |  | 24 |
| 23 | rectified 24-cell<br>cantellated 16-cell |  | 96 |
| 24 | truncated 24-cell<br>cantitruncated 16-cell |  | 192 |

**Table B.2:** 17 prismatic convex uniform polychorons

**(a)** Members of the $A_3 \times A_1$ family

| # | Name | Coxeter diagram | Vertices |
|---|---|---|---|
| 48 | Tetrahedral prism | 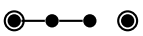 | 8 |
| 49 | Truncated tetrahedral prism | 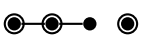 | 24 |
| 51 | Rectified tetrahedral prism<br>octahedral prism | 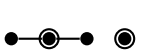 | 12 |
| 50 | Cantellated tetrahedral prism<br>cuboctahedral prism |  | 24 |
| 54 | Cantitruncated tetrahedral prism<br>truncated octahedral prism | 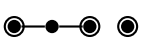 | 48 |

**(b)** Members of the $B_3 \times A_1$ family

| # | Name | Coxeter diagram | Vertices |
|---|---|---|---|
| 10 | Tesseract | 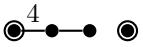 | 16 |
| 51 | Rectified tetrahedral prism<br>octahedral prism | 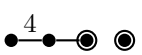 | 12 |
| 50 | Cantellated tetrahedral prism<br>cuboctahedral prism | 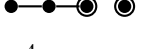 | 24 |
| 54 | Cantitruncated tetrahedral prism<br>truncated octahedral prism | 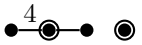 | 48 |
| 52 | Rhombicuboctahedral prism |  | 48 |
| 53 | Truncated cubic prism |  | 48 |
| 55 | Truncated cuboctahedral prism | 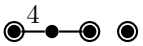 | 96 |
| 56 | Snub cubic prism | half $B_3$ | 48 |

**(c)** Members of the $H_3 \times A_1$ family

| # | Name | Coxeter diagram | Vertices |
|---|---|---|---|
| 57 | Dodecahedral prism | 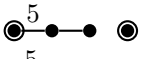 | 40 |
| 58 | Icosidodecahedral prism | 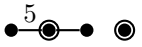 | 60 |
| 59 | Icosahedral prism | 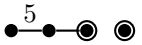 | 24 |
| 60 | Truncated dodecahedral prism | 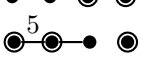 | 120 |
| 61 | Rhombicosidodecahedral prism | 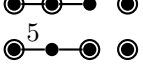 | 120 |
| 62 | Truncated icosahedral prism |  | 120 |
| 63 | Truncated icosidodecahedral<br>prism |  | 240 |
| 64 | Snub dodecahedral prism | half $H_3$ | 120 |

**Table B.3:** Comparison of the different possibilities for the size $a_0$.

| # | $\langle\Psi\rangle^2$ | unifoamy | $\langle\Psi^2\rangle$ | L-W model | $\psi^2_{\min}$ | S-c model | vertices | covered |
|---|---|---|---|---|---|---|---|---|
| 1 | 1.678 | 1.342 | 1.742 | 1.428 | 1.321 | 1.907 | 5 | 0.681 |
| 2 | 1.349 | 1.214 | 1.370 | 1.228 | 1.123 | 1.752 | 10 | 0.664 |
| 3 | 1.152 | 1.095 | 1.163 | 1.131 | 0.939 | 3.815 | 20 | 0.276 |
| 4 | 1.136 | 1.098 | 1.141 | 1.097 | 0.973 | 2.082 | 30 | 0.509 |
| 5 | 1.195 | 1.135 | 1.149 | 1.131 | 1.073 | 1.885 | 20 | 0.577 |
| 6 | 1.121 | 1.084 | 1.093 | 1.097 | 0.981 | 3.554 | 30 | 0.293 |
| 7 | 1.062 | 1.044 | 1.064 | 1.059 | 0.901 | 3.939 | 60 | 0.260 |
| 8 | 1.076 | 1.058 | 1.078 | 1.059 | 0.951 | 2.634 | 60 | 0.391 |
| 9 | 1.042 | 1.033 | 1.035 | 1.036 | 0.945 | 3.512 | 120 | 0.289 |
| 10 | 1.229 | 1.152 | 1.171 | 1.156 | 1.061 | 2.356 | 16 | 0.461 |
| 11 | 1.129 | 1.094 | 1.102 | 1.092 | 0.992 | 2.164 | 32 | 0.487 |
| 12 | 1.432 | 1.253 | 1.302 | 1.277 | 1.236 | 1.666 | 8 | 0.727 |
| 13 | 1.045 | 1.029 | 1.048 | 1.056 | 0.912 | 5.852 | 64 | 0.174 |
| 14 | 1.051 | 1.040 | 1.043 | 1.042 | 0.937 | 2.477 | 96 | 0.413 |
| 15 | 1.082 | 1.065 | 1.069 | 1.056 | 1.021 | 1.931 | 64 | 0.536 |
| 16 | 1.049 | 1.038 | 1.041 | 1.042 | 0.943 | 3.749 | 96 | 0.271 |
| 17 | 1.083 | 1.061 | 1.066 | 1.069 | 0.975 | 3.105 | 48 | 0.332 |
| 18 | 1.013 | 1.008 | 1.015 | 1.026 | 0.898 | 5.333 | 192 | 0.189 |
| 19 | 1.022 | 1.017 | 1.018 | 1.026 | 0.918 | 3.504 | 192 | 0.289 |
| 20 | 1.035 | 1.029 | 1.035 | 1.026 | 0.977 | 2.617 | 192 | 0.387 |
| 21 | 1.013 | 1.010 | 1.011 | 1.016 | 0.921 | 4.205 | 384 | 0.239 |
| 22 | 1.173 | 1.125 | 1.136 | 1.114 | 1.083 | 1.571 | 24 | 0.692 |
| 23 | 1.061 | 1.050 | 1.052 | 1.042 | 1.008 | 2.041 | 96 | 0.503 |
| 24 | 1.030 | 1.025 | 1.026 | 1.026 | 0.970 | 3.636 | 192 | 0.278 |
| 25 | 1.026 | 1.022 | 1.023 | 1.020 | 0.977 | 2.336 | 288 | 0.433 |
| 26 | 1.047 | 1.040 | 1.047 | 1.032 | 1.020 | 1.652 | 144 | 0.619 |
| 27 | 1.019 | 1.016 | 1.017 | 1.020 | 0.978 | 5.210 | 288 | 0.193 |
| 28 | 1.009 | 1.008 | 1.009 | 1.012 | 0.961 | 5.202 | 576 | 0.193 |
| 29 | 1.015 | 1.013 | 1.014 | 1.012 | 0.976 | 2.804 | 576 | 0.359 |
| 30 | 1.005 | 1.005 | 1.005 | 1.008 | 0.971 | 4.522 | 1152 | 0.222 |
| 32 | 1.016 | 1.014 | 1.014 | 1.012 | 0.996 | 3.189 | 600 | 0.315 |
| 33 | 1.009 | 1.008 | 1.009 | 1.008 | 0.990 | 2.929 | 1200 | 0.343 |
| 34 | 1.016 | 1.014 | 1.016 | 1.011 | 1.001 | 1.526 | 720 | 0.660 |
| 35 | 1.054 | 1.046 | 1.047 | 1.036 | 1.033 | 1.331 | 120 | 0.774 |
| 36 | 1.001 | 1.001 | 1.001 | 1.005 | 0.982 | 8.719 | 2400 | 0.115 |
| 37 | 1.003 | 1.002 | 1.003 | 1.004 | 0.985 | 3.199 | 3600 | 0.313 |
| 38 | 1.006 | 1.006 | 1.006 | 1.005 | 0.993 | 2.255 | 2400 | 0.445 |
| 39 | 1.003 | 1.003 | 1.003 | 1.004 | 0.986 | 4.560 | 3600 | 0.220 |
| 40 | 1.005 | 1.004 | 1.004 | 1.004 | 0.992 | 2.346 | 3600 | 0.427 |
| 41 | 1.008 | 1.008 | 1.008 | 1.007 | 0.998 | 2.621 | 1440 | 0.383 |
| 42 | 0.999 | 0.999 | 0.999 | 1.002 | 0.981 | 7.459 | 7200 | 0.134 |
| 43 | 1.000 | 1.000 | 1.000 | 1.002 | 0.983 | 4.845 | 7200 | 0.207 |
| 44 | 1.002 | 1.002 | 1.002 | 1.002 | 0.989 | 2.971 | 7200 | 0.337 |
| 45 | 1.002 | 1.002 | 1.002 | 1.002 | 0.989 | 3.977 | 7200 | 0.252 |
| 46 | 1.000 | 0.999 | 0.999 | 1.001 | 0.983 | 5.473 | 14 400 | 0.183 |

# Danksagung

Ich möchte mich bei allen bedanken, die mich auf meinem Weg zu dieser Doktorarbeit unterstützt haben. Alleine hätte ich dieses Ziel niemals erreicht. Der Weg war nicht immer leicht, teilweise sogar so beschwerlich, dass ich Zweifel hatte mein Ziel zu erreichen. Jedoch konnte ich mich immer auf meine Familie und meine Freunde verlassen, die mir immer zur Seite standen, auch wenn es nicht immer einfach mit mir war. Mein Dank gilt natürlich auch meinen Kollegen am ZARM und im Graduiertenkolleg „Models of Gravity“, die mich herzlich aufgenommen haben und mir fachlich kompetent stets weiterhelfen konnten. Ich hoffe, dass es umgekehrt auch der Fall ist. Ich möchte mich auch beim ZARM, der Universität Bremen und dem Graduiertenkolleg „Models of Gravity“ bedanken, die das Umfeld geschaffen haben, diese Arbeit zu erstellen. Mein Dank gilt auch der Universität Hannover, die es mir ermöglicht hat, die Arbeit in Ruhe zu beenden.

Ein paar Personen möchte ich dennoch hervorheben: Als erstes wäre das mein Doktorvater Domenico Giulini, ohne dessen Zuspruch, Rat, Wissen und Unterstützung diese Arbeit niemals entstanden wäre. Genauso wichtig sind Lukas Brunkhorst und Christian Pfeifer, mit denen ich jahrelang ein Büro geteilt habe und viele Gespräche und Diskussion, fachlich und privat, die ich nicht missen möchte und so auch ihren Teil beigesteuert haben, auch durch das Korrekturlesen einzelner Teile. Beide sind sehr gute Freunde von mir geworden. Lukas möchte ich noch einmal besonders hervorheben, der zusammen mit mir die Promotion begonnen hat und immer für mich da war, wenn ich jemanden brauchte, obwohl es wirklich nicht immer einfach mit mir ist. Selbst als er in Kopenhagen war, konnte ich auf ihn bauen. Vielen Dank, ohne ihn stände ich so jetzt sicherlich nicht hier. Auf ihn geht auch der Begriff „unifoamy“ zurück, von dem ich mir wünsche, dass er in der Wissenschaftscommunity erhalten bleibt. Ebenfalls gilt mein Dank meinen Freunden Marc Ruhmann und Daniel Schmidt, die große Teile meiner Doktorarbeit zur Korrektur gelesen und mir nützliche Kommentare gegeben haben, insbesondere Marc hat fast die gesamte Arbeit gelesen. Als weitere Korrekturleser möchte ich Vojtech Witzany und Andreas Schreiber nicht unerwähnt lassen, die auch ihren Teil beigetragen haben.

# Bibliography


[Abb+16a] B. P. Abbott et al. 'GW151226: Observation of Gravitational Waves from a 22-Solar-Mass Binary Black Hole Coalescence'. In: *Phys. Rev. Lett.* 116 (24 June 2016), p. 241103. DOI: 10.1103/PhysRevLett.116.241103. URL: http://link.aps.org/doi/10.1103/PhysRevLett.116.241103.

[Abb+16b] B. P. Abbott et al. 'Observation of Gravitational Waves from a Binary Black Hole Merger'. In: *Phys. Rev. Lett.* 116 (6 Feb. 2016), p. 061102. DOI: 10.1103/PhysRevLett.116.061102. URL: http://link.aps.org/doi/10.1103/PhysRevLett.116.061102.

[ADM08] R. Arnowitt, S. Deser and C. W. Misner. 'Republication of: The dynamics of general relativity'. In: *General Relativity and Gravitation* 40.9 (2008), pp. 1997–2027. ISSN: 1572-9532. DOI: 10.1007/s10714-008-0661-1. URL: http://dx.doi.org/10.1007/s10714-008-0661-1.

[ADM59] R. Arnowitt, S. Deser and C. W. Misner. 'Dynamical Structure and Definition of Energy in General Relativity'. In: *Phys. Rev.* 116 (5 Dec. 1959), pp. 1322–1330. DOI: 10.1103/PhysRev.116.1322. URL: http://link.aps.org/doi/10.1103/PhysRev.116.1322.

[AS03] M. Atiyah and P. Sutcliffe. 'Polyhedra in Physics, Chemistry and Geometry'. In: *Milan Journal of Mathematics* 71.1 (2003), pp. 33–58. ISSN: 1424-9294. DOI: 10.1007/s00032-003-0014-1. URL: http://dx.doi.org/10.1007/s00032-003-0014-1.

[BCK11] K. Bolejko, M.-N. Célérier and A. Krasiński. 'Inhomogeneous cosmological models: exact solutions and their applications'. In: *Classical and Quantum Gravity* 28.16 (2011), p. 164002. URL: http://stacks.iop.org/0264-9381/28/i=16/a=164002.

[BDP94] M. Borkovec, W. De Paris and R. Peikert. 'The Fractal Dimension Of The Apollonian Sphere Packing'. In: *Fractals* 02.04 (1994), pp. 521–526. DOI: 10.1142/S0218348X94000739. eprint: http://www.worldscientific.com/doi/pdf/10.1142/S0218348X94000739. URL: http://www.worldscientific.com/doi/abs/10.1142/S0218348X94000739.

[Ben+16] E. Bentivegna et al. 'Light propagation through black-hole lattices'. In: (2016). arXiv: 1611.09275.

[BGS03] R. A. Battye, G. W. Gibbons Paul and M. Sutcliffe. 'Central configurations in three dimensions'. In: *Proceedings of the Royal Society of London A: Mathematical, Physical and Engineering Sciences* 459.2032 (2003), pp. 911–943. ISSN: 1364-5021. DOI: 10.1098/rspa.2002.1061. eprint: http://rspa.royalsocietypublishing.org/content/459/2032/911.full.pdf. URL: http://rspa.royalsocietypublishing.org/content/459/2032/911.

[BI91] C. Barrabès and W. Israel. 'Thin shells in general relativity and cosmology: The lightlike limit'. In: *Phys. Rev. D* 43 (4 Feb. 1991), pp. 1129–1142. DOI: 10.1103/PhysRevD.43.1129. URL: http://link.aps.org/doi/10.1103/PhysRevD.43.1129.

[BK12] E. Bentivegna and M. Korzyński. 'Evolution of a periodic eight-black-hole lattice in numerical relativity'. In: *Classical and Quantum Gravity* 29.16 (2012), p. 165007. URL: http://stacks.iop.org/0264-9381/29/i=16/a=165007.

[BL12] J.-P. Bruneton and J. Larena. 'Dynamics of a lattice Universe: the dust approximation in cosmology'. In: *Classical and Quantum Gravity* 29.15 (2012), p. 155001. URL: http://stacks.iop.org/0264-9381/29/i=15/a=155001.

[BL13] J.-P. Bruneton and J. Larena. 'Observables in a lattice Universe: the cosmological fitting problem'. In: *Classical and Quantum Gravity* 30.2 (2013), p. 025002. URL: http://stacks.iop.org/0264-9381/30/i=2/a=025002.

[BL63] D. R. Brill and R. W. Lindquist. 'Interaction Energy in Geometrostatics'. In: *Phys. Rev.* 131 (1 July 1963), pp. 471–476. DOI: 10.1103/PhysRev.131.471. URL: http://link.aps.org/doi/10.1103/PhysRev.131.471.

[Bon47] H. Bondi. 'Spherically Symmetrical Models in General Relativity'. In: *Monthly Notices of the Royal Astronomical Society* 107.5-6 (1947), p. 410. DOI: 10.1093/mnras/107.5-6.410. eprint: /oup/backfile/Content_public/Journal/mnras/107/5-6/10.1093_mnras_107.5-6.410/2/mnras107-0410.pdf. URL: +%20http://dx.doi.org/10.1093/mnras/107.5-6.410.

[BS14] S. Bagheri and D. J. Schwarz. 'Light propagation in the averaged universe'. In: *Journal of Cosmology and Astroparticle Physics* 2014.10 (2014), p. 073. URL: http://stacks.iop.org/1475-7516/2014/i=10/a=073.

[BS98] T. W. Baumgarte and S. L. Shapiro. 'Numerical integration of Einstein's field equations'. In: *Phys. Rev. D* 59 (2 Dec. 1998), p. 024007. DOI: 10.1103/PhysRevD.59.024007. URL: http://link.aps.org/doi/10.1103/PhysRevD.59.024007.

[Buc+15] T. Buchert et al. 'Is there proof that backreaction of inhomogeneities is irrelevant in cosmology?' In: *Classical and Quantum Gravity* 32.21 (2015), p. 215021. URL: http://stacks.iop.org/0264-9381/32/i=21/a=215021.

[Buc+16] T. Buchert et al. 'Observational challenges for the standard FLRW model'. In: *International Journal of Modern Physics D* 25.03 (2016), p. 1630007. DOI: 10.1142/S021827181630007X. eprint: http://www.worldscientific.com/doi/pdf/10.1142/S021827181630007X. URL: http://www.worldscientific.com/doi/abs/10.1142/S021827181630007X.

[Buc00] T. Buchert. 'On Average Properties of Inhomogeneous Fluids in General Relativity: Dust Cosmologies'. In: *General Relativity and Gravitation* 32.1 (2000), pp. 105–125. ISSN: 1572-9532. DOI: 10.1023/A:1001800617177. URL: http://dx.doi.org/10.1023/A:1001800617177.

[Buc01] T. Buchert. 'On Average Properties of Inhomogeneous Fluids in General Relativity: Perfect Fluid Cosmologies'. In: *General Relativity and Gravitation* 33.8 (2001), pp. 1381–1405. ISSN: 1572-9532. DOI: 10.1023/A:1012061725841. URL: http://dx.doi.org/10.1023/A:1012061725841.

[Buc08] T. Buchert. 'Dark Energy from structure: a status report'. In: *General Relativity and Gravitation* 40.2 (2008), pp. 467–527. ISSN: 1572-9532. DOI: 10.1007/s10714-007-0554-8. URL: http://dx.doi.org/10.1007/s10714-007-0554-8.

[Buc11] T. Buchert. 'Toward physical cosmology: focus on inhomogeneous geometry and its non-perturbative effects'. In: *Classical and Quantum Gravity* 28.16 (2011), p. 164007. URL: http://stacks.iop.org/0264-9381/28/i=16/a=164007.

[Cec92] T. E. Cecil. 'Lie sphere geometry'. In: *Lie Sphere Geometry*. Springer, 1992, pp. 8–28.

[CF09a] T. Clifton and P. G. Ferreira. 'Archipelagian cosmology: Dynamics and observables in a universe with discretized matter content'. In: *Phys. Rev. D* 80 (10 Nov. 2009), p. 103503. DOI: 10.1103/PhysRevD.80.103503. URL: http://link.aps.org/doi/10.1103/PhysRevD.80.103503.

[CF09b] T. Clifton and P. G. Ferreira. 'Errors in estimating $\Omega_\Lambda$ due to the fluid approximation'. In: *Journal of Cosmology and Astroparticle Physics* 2009.10 (2009), p. 026. URL: http://stacks.iop.org/1475-7516/2009/i=10/a=026.

[CFO12] T. Clifton, P. G. Ferreira and K. O'Donnell. 'Improved treatment of optics in the Lindquist-Wheeler models'. In: *Phys. Rev. D* 85 (2 Jan. 2012), p. 023502. DOI: 10.1103/PhysRevD.85.023502. URL: http://link.aps.org/doi/10.1103/PhysRevD.85.023502.

[CG10] M. Carrera and D. Giulini. 'Influence of global cosmological expansion on local dynamics and kinematics'. In: *Rev. Mod. Phys.* 82 (1 Jan. 2010), pp. 169–208. DOI: 10.1103/RevModPhys.82.169. URL: http://link.aps.org/doi/10.1103/RevModPhys.82.169.

[CG69] Y. Choquet-Bruhat and R. Geroch. 'Global aspects of the Cauchy problem in general relativity'. In: *Communications in Mathematical Physics* 14.4 (1969), pp. 329–335. ISSN: 1432-0916. DOI: 10.1007/BF01645389. URL: http://dx.doi.org/10.1007/BF01645389.

[CGR16] T. Clifton, D. Gregoris and K. Rosquist. 'The Magnetic Part of the Weyl Tensor, and the Expansion of Discrete Universes'. In: (2016). arXiv: 1607.00775.

[CK14] D. Christodoulou and S. Klainerman. *The Global Nonlinear Stability of the Minkowski Space (PMS-41)*. Princeton Legacy Library. Princeton University Press, 2014. ISBN: 9781400863174. URL: https://books.google.de/books?id=-jsABAAAQBAJ.

[Cla+11] C. Clarkson et al. 'Does the growth of structure affect our dynamical models of the Universe? The averaging, backreaction, and fitting problems in cosmology'. In: *Reports on Progress in Physics* 74.11 (2011), p. 112901. URL: http://stacks.iop.org/0034-4885/74/i=11/a=112901.

[Cli+13] T. Clifton et al. 'Exact evolution of discrete relativistic cosmological models'. In: *Journal of Cosmology and Astroparticle Physics* 2013.11 (2013), p. 010. URL: http://stacks.iop.org/1475-7516/2013/i=11/a=010.

[Cli11] T. Clifton. 'Cosmology without averaging'. In: *Classical and Quantum Gravity* 28.16 (2011), p. 164011. URL: http://stacks.iop.org/0264-9381/28/i=16/a=164011.

[Cli14] T. Clifton. 'The method of images in cosmology'. In: *Classical and Quantum Gravity* 31.17 (2014), p. 175010. URL: http://stacks.iop.org/0264-9381/31/i=17/a=175010.

[Cox73] H. S. M. Coxeter. *Regular polytopes*. Courier Corporation, 1973.

[CRT12] T. Clifton, K. Rosquist and R. Tavakol. 'An exact quantification of backreaction in relativistic cosmology'. In: *Phys. Rev. D* 86 (4 Aug. 2012), p. 043506. DOI: 10.1103/PhysRevD.86.043506. URL: http://link.aps.org/doi/10.1103/PhysRevD.86.043506.

[Dar27] G. Darmois. 'Les équations de la gravitation einsteinienne'. In: *Mémorial des sciences mathématiques* 25 (1927), pp. 1–48.

[DC16] J. Durk and T. Clifton. 'Exact Initial Data for Black Hole Universes with a Cosmological Constant'. In: (2016). arXiv: 1610.05635.

[Des+91] R. Descartes et al. *The Philosophical Writings of Descartes: Volume 3, The Correspondence*. Vol. 3. Cambridge University Press, 1991.

[DS42] R. Descartes and J. Simon. *Oeuvres de Descartes*. Charpentier, 1842.

[EG14] G. F. R. Ellis and G. W. Gibbons. 'Discrete Newtonian cosmology'. In: *Classical and Quantum Gravity* 31.2 (2014), p. 025003. URL: http://stacks.iop.org/0264-9381/31/i=2/a=025003.

[Ein15] A. Einstein. 'Die Feldgleichungen der Gravitation'. In: *Sitzungsberichte der Königlich Preußischen Akademie der Wissenschaften (Berlin)* (Nov. 1915), pp. 844–847. URL: http://echo.mpiwg-berlin.mpg.de/MPIWG:ZZB2HK6W.

[Ein16] A. Einstein. 'Die Grundlage der allgemeinen Relativitätstheorie'. In: *Annalen der Physik* 354.7 (1916), pp. 769–822. ISSN: 1521-3889. DOI: 10.1002/andp.19163540702. URL: http://dx.doi.org/10.1002/andp.19163540702.

[Ell11] G. F. R. Ellis. 'Inhomogeneity effects in cosmology'. In: *Classical and Quantum Gravity* 28.16 (2011), p. 164001. URL: http://stacks.iop.org/0264-9381/28/i=16/a=164001.

[Ell84] G. F. R. Ellis. 'Relativistic Cosmology: Its Nature, Aims and Problems'. In: *General Relativity and Gravitation: Invited Papers and Discussion Reports of the 10th International Conference on General Relativity and Gravitation, Padua, July 3–8, 1983*. Ed. by B. Bertotti, F. de Felice and A. Pascolini. Dordrecht: Springer Netherlands, 1984, pp. 215–288. ISBN: 978-94-009-6469-3. DOI: 10.1007/978-94-009-6469-3_14. URL: http://dx.doi.org/10.1007/978-94-009-6469-3_14.

[ES16] D. Eisenstein and SDSS-III collaboration. *A slice through a map of our Universe*. 2016. URL: http://www.sdss.org/press-releases/astronomers-map-a-record-breaking-1-2-million-galaxies-to-study-the-properties-of-dark-energy/.

[ES45] A. Einstein and E. G. Straus. 'The Influence of the Expansion of Space on the Gravitation Fields Surrounding the Individual Stars'. In: *Rev. Mod. Phys.* 17 (2-3 Apr. 1945), pp. 120–124. DOI: 10.1103/RevModPhys.17.120. URL: http://link.aps.org/doi/10.1103/RevModPhys.17.120.

[ES87] G. F. R. Ellis and W. Stoeger. 'The 'fitting problem' in cosmology'. In: *Classical and Quantum Gravity* 4.6 (1987), p. 1697. URL: http://stacks.iop.org/0264-9381/4/i=6/a=025.

[EU97] H. van Elst and C. Uggla. 'General relativistic 1+3 orthonormal frame approach'. In: *Classical and Quantum Gravity* 14.9 (1997), p. 2673. URL: http://stacks.iop.org/0264-9381/14/i=9/a=021.

[FDU13] P. Fleury, H. Dupuy and J.-P. Uzan. 'Interpretation of the Hubble diagram in a nonhomogeneous universe'. In: *Phys. Rev. D* 87 (12 June 2013), p. 123526. DOI: 10.1103/PhysRevD.87.123526. URL: http://link.aps.org/doi/10.1103/PhysRevD.87.123526.

[Fou52] Y. Fourès-Bruhat. 'Théorème d'existence pour certains systèmes d'équations aux dérivées partielles non linéaires'. In: *Acta Mathematica* 88.1 (1952), pp. 141–225. ISSN: 1871-2509. DOI: 10.1007/BF02392131. URL: http://dx.doi.org/10.1007/BF02392131.

[Fou56] Y. Fourès-Bruhat. 'Sur l'intégration des équations de la relativité générale.' French. In: *Journal of Rational Mechanics and Analysis* 5 (1956), pp. 951–966. ISSN: 1943-5282.

[Fri22] A. Friedman. 'Über die Krümmung des Raumes'. In: *Zeitschrift für Physik* 10.1 (1922), pp. 377–386. ISSN: 0044-3328. DOI: 10.1007/BF01332580. URL: http://dx.doi.org/10.1007/BF01332580.

[Fri24] A. Friedmann. 'Über die Möglichkeit einer Welt mit konstanter negativer Krümmung des Raumes'. In: *Zeitschrift für Physik* 21.1 (1924), pp. 326–332. ISSN: 0044-3328. DOI: 10.1007/BF01328280. URL: http://dx.doi.org/10.1007/BF01328280.

[GB96] L. C. Grove and C. T. Benson. *Finite reflection groups*. Vol. 99. Springer Science & Business Media, 1996.

[Giu14] D. Giulini. 'Dynamical and Hamiltonian formulation of General Relativity'. In: *Springer Handbook of Spacetime*. Springer, 2014, pp. 323–362.

[Gos37] T. Gosset. 'The Hexlet'. In: *Nature* 139 (Feb. 1937), pp. 251–252. DOI: 10.1038/139251b0.

[Gou07] E. Gourgoulhon. '3+1 formalism and bases of numerical relativity'. In: (2007). gr-qc/0703035: arxiv.

[Gou12] É. Gourgoulhon. *3+1 Formalism in General Relativity: Bases of Numerical Relativity*. Lecture Notes in Physics. Springer Berlin Heidelberg, 2012. ISBN: 9783642245244. URL: https://books.google.de/books?id=XwB94Je8nnIC.

[Gra+05] R. L. Graham et al. 'Apollonian Circle Packings: Geometry and Group Theory I. The Apollonian Group'. In: *Discrete & Computational Geometry* 34.4 (2005), pp. 547–585. ISSN: 1432-0444. DOI: 10.1007/s00454-005-1196-9. URL: http://dx.doi.org/10.1007/s00454-005-1196-9.

[Gra+06a] R. L. Graham et al. 'Apollonian Circle Packings: Geometry and Group Theory II. Super-Apollonian Group and Integral Packings'. In: *Discrete & Computational Geometry* 35.1 (2006), pp. 1–36. ISSN: 1432-0444. DOI: 10.1007/s00454-005-1195-x. URL: http://dx.doi.org/10.1007/s00454-005-1195-x.

[Gra+06b] R. L. Graham et al. 'Apollonian Circle Packings: Geometry and Group Theory III. Higher Dimensions'. In: *Discrete & Computational Geometry* 35.1 (2006), pp. 37–72. ISSN: 1432-0444. DOI: 10.1007/s00454-005-1197-8. URL: http://dx.doi.org/10.1007/s00454-005-1197-8.

[GW14] S. R. Green and R. M. Wald. 'How well is our Universe described by an FLRW model?' In: *Classical and Quantum Gravity* 31.23 (2014), p. 234003. URL: http://stacks.iop.org/0264-9381/31/i=23/a=234003.

[GW15] S. R. Green and R. M. Wald. 'Comments on backreaction'. In: (2015). arXiv: 1506.06452.

[GW16] S. R. Green and R. M. Wald. 'A simple, heuristic derivation of our 'no backreaction' results'. In: *Classical and Quantum Gravity* 33.12 (2016), p. 125027. URL: http://stacks.iop.org/0264-9381/33/i=12/a=125027.

[HE73] S. Hawking and G. Ellis. *The Large Scale Structure of Space-Time*. Cambridge Monographs on Mathematical Physics. Cambridge University Press, 1973. ISBN: 9780521099066. URL: https://books.google.de/books?id=QagG%5C_KI7Ll8C.

[HHB14] Horváth, István, Hakkila, Jon and Bagoly, Zsolt. 'Possible structure in the GRB sky distribution at redshift two'. In: *Astronomy & Astrophysics* 561 (2014), p. L12. DOI: 10.1051/0004-6361/201323020. URL: http://dx.doi.org/10.1051/0004-6361/201323020.

[Hum92] J. E. Humphreys. *Reflection groups and Coxeter groups*. Vol. 29. Cambridge university press, 1992.

[Ise14] J. Isenberg. 'The Initial Value Problem in General Relativity'. In: *Springer Handbook of Spacetime*. Ed. by A. Ashtekar and V. Petkov. Berlin, Heidelberg: Springer Berlin Heidelberg, 2014, pp. 303–321. ISBN: 978-3-642-41992-8. DOI: 10.1007/978-3-642-41992-8_16. URL: http://dx.doi.org/10.1007/978-3-642-41992-8_16.

[Isr66] W. Israel. 'Singular hypersurfaces and thin shells in general relativity'. In: *Il Nuovo Cimento B (1965-1970)* 44.1 (1966), pp. 1–14. ISSN: 1826-9877. DOI: 10.1007/BF02710419. URL: http://dx.doi.org/10.1007/BF02710419.

[JS02] P. Jaranowski and G. Schäfer. 'Lapse function for maximally sliced Brill-Lindquist initial data'. In: *Phys. Rev. D* 65 (12 June 2002), p. 127501. DOI: 10.1103/PhysRevD.65.127501. URL: http://link.aps.org/doi/10.1103/PhysRevD.65.127501.

[KHB15] M. Korzyński, I. Hinder and E. Bentivegna. 'On the vacuum Einstein equations along curves with a discrete local rotation and reflection symmetry'. In: *Journal of Cosmology and Astroparticle Physics* 2015.08 (2015), p. 025. URL: http://stacks.iop.org/1475-7516/2015/i=08/a=025.

[Koc07] J. Kocik. 'A theorem on circle configurations'. In: (2007). arXiv: 0706.0372.

[Kol11] E. W. Kolb. 'Backreaction of inhomogeneities can mimic dark energy'. In: *Classical and Quantum Gravity* 28.16 (2011), p. 164009. URL: http://stacks.iop.org/0264-9381/28/i=16/a=164009.

[Kor14] M. Korzyński. 'Backreaction and continuum limit in a closed universe filled with black holes'. In: *Classical and Quantum Gravity* 31.8 (2014), p. 085002. URL: http://stacks.iop.org/0264-9381/31/i=8/a=085002.

[Kor15] M. Korzyński. 'Nonlinear effects of general relativity from multiscale structure'. In: *Classical and Quantum Gravity* 32.21 (2015), p. 215013. URL: http://stacks.iop.org/0264-9381/32/i=21/a=215013.

[Kra06] A. Krasiński. *Inhomogeneous Cosmological Models*. Nov. 2006.

[Lem27] G. Lemaître. 'Un Univers homogène de masse constante et de rayon croissant rendant compte de la vitesse radiale des nébuleuses extra-galactiques'. In: *Annales de la Société Scientifique de Bruxelles* 47 (1927), pp. 49–59.

[Lem33] G. Lemaître. 'L'Univers en expansion'. In: *Annales de la Société Scientifique de Bruxelles* 53 (1933).

[Lic39] A. Lichnerowicz. *Sur certains problèmes globaux relatifs au système des équations d'Einstein*. fre. 1939. URL: http://eudml.org/doc/192901.

[Lic44] A. Lichnerowicz. 'L'intégration des équations de la gravitation relativiste et le probleme des n corps'. In: *J. Math. Pures Appl* 23.37 (1944), p. 4.

[Lic52] A. Lichnerowicz. 'Sur les équations relativistes de la gravitation'. fre. In: *Bulletin de la Société Mathématique de France* 80 (1952), pp. 237–251. URL: http://eudml.org/doc/86860.

[Lie72] S. Lie. 'Ueber Complexe, insbesondere Linien- und Kugel-Complexe, mit Anwendung auf die Theorie partieller Differential-Gleichungen'. In: *Math. Ann.* 5.1 (1872), pp. 145–208. ISSN: 0025-5831. DOI: 10.1007/BF01446331. URL: http://dx.doi.org/10.1007/BF01446331.

[Liu15] R. G. Liu. 'Lindquist-Wheeler formulation of lattice universes'. In: *Phys. Rev. D* 92 (6 Sept. 2015), p. 063529. DOI: 10.1103/PhysRevD.92.063529. URL: http://link.aps.org/doi/10.1103/PhysRevD.92.063529.

[LMW02] J. C. Lagarias, C. L. Mallows and A. R. Wilks. 'Beyond the Descartes Circle Theorem'. In: *The American Mathematical Monthly* 109.4 (2002), pp. 338–361. ISSN: 00029890, 19300972. URL: http://www.jstor.org/stable/2695498.

[LR15] M. Lavinto and S. Räsänen. 'CMB seen through random Swiss Cheese'. In: *Journal of Cosmology and Astroparticle Physics* 2015.10 (2015), p. 057. URL: http://stacks.iop.org/1475-7516/2015/i=10/a=057.

[LRS13] M. Lavinto, S. Räsänen and S. J. Szybka. 'Average expansion rate and light propagation in a cosmological Tardis spacetime'. In: *Journal of Cosmology and Astroparticle Physics* 2013.12 (2013), p. 051. URL: http://stacks.iop.org/1475-7516/2013/i=12/a=051.

[LW16] R. G. Liu and R. M. Williams. 'Regge calculus models of closed lattice universes'. In: *Phys. Rev. D* 93 (2 Jan. 2016), p. 023502. DOI: 10.1103/PhysRevD.93.023502. URL: http://link.aps.org/doi/10.1103/PhysRevD.93.023502.

[LW57] R. W. Lindquist and J. A. Wheeler. 'Dynamics of a Lattice Universe by the Schwarzschild-Cell Method'. In: *Rev. Mod. Phys.* 29 (3 July 1957), pp. 432–443. DOI: 10.1103/RevModPhys.29.432. URL: http://link.aps.org/doi/10.1103/RevModPhys.29.432.

[Mar72] G. Marsaglia. 'Choosing a Point from the Surface of a Sphere'. In: *Ann. Math. Statist.* 43.2 (Apr. 1972), pp. 645–646. DOI: 10.1214/aoms/1177692644. URL: http://dx.doi.org/10.1214/aoms/1177692644.

[Mau62] J. G. Mauldon. 'Sets of equally inclined spheres'. In: *Canad. J. Math* 14 (1962), pp. 509–516. DOI: 10.4153/CJM-1962-042-6. URL: http://dx.doi.org/10.4153/CJM-1962-042-6.

[MS39] S. B. Myers and N. E. Steenrod. 'The Group of Isometries of a Riemannian Manifold'. In: *Annals of Mathematics* 40.2 (1939), pp. 400–416. ISSN: 0003486X. URL: http://www.jstor.org/stable/1968928.

[MTW73] C. W. Misner, K. S. Thorne and J. A. Wheeler. *Gravitation*. San Francisco: W. H. Freeman and Company, 1973.

[MW57] C. W. Misner and J. A. Wheeler. 'Classical physics as geometry'. In: *Annals of Physics* 2.6 (1957), pp. 525–603. ISSN: 0003-4916. DOI: http://dx.doi.org/10.1016/0003-4916(57)90049-0. URL: http://www.sciencedirect.com/science/article/pii/0003491657900490.

[MZ97] M. Mars and R. M. Zalaletdinov. 'Space–time averages in macroscopic gravity and volume-preserving coordinates'. In: *Journal of Mathematical Physics* 38.9 (1997), pp. 4741–4757. DOI: 10.1063/1.532119. eprint: http://dx.doi.org/10.1063/1.532119. URL: http://dx.doi.org/10.1063/1.532119.

[NAS] NASA / WMAP Science Team. *The Microwave Sky, c. 1965*. URL: https://map.gsfc.nasa.gov/media/030635/index.html.

[NAS13] NASA/JPL-Caltech/ESA. *PIA16874: The Universe Comes into Sharper Focus*. 2013. URL: http://photojournal.jpl.nasa.gov/catalog/PIA16874.

[NAS14] NASA, ESA, H. Teplitz and M. Rafelski (IPAC/Caltech), A. Koekemoer (STScI), R. Windhorst (Arizona State University), and Z. Levay (STScI). *Hubble Ultra Deep Field 2014*. 2014. URL: http://hubblesite.org/image/3380/news_release/2014-27.

[Ols] G. Olshevsky. *Uniform Polytopes in Four Dimensions*. URL: https://web.archive.org/web/20070204075028/members.aol.com/Polycell/uniform.html (visited on 04/02/2007).

[OV39] J. R. Oppenheimer and G. M. Volkoff. 'On Massive Neutron Cores'. In: *Phys. Rev.* 55 (4 Feb. 1939), pp. 374–381. DOI: 10.1103/PhysRev.55.374. URL: http://link.aps.org/doi/10.1103/PhysRev.55.374.

[ÓY73] N. Ó Murchadha and J. W. York Jr. 'Existence and uniqueness of solutions of the Hamiltonian constraint of general relativity on compact manifolds'. In: *Journal of Mathematical Physics* 14.11 (1973), pp. 1551–1557. DOI: 10.1063/1.1666225. eprint: http://dx.doi.org/10.1063/1.1666225. URL: http://dx.doi.org/10.1063/1.1666225.

[ÓY74a] N. Ó Murchadha and J. W. York. 'Initial - value problem of general relativity. I. General formulation and physical interpretation'. In: *Phys. Rev. D* 10 (2 July 1974), pp. 428–436. DOI: 10.1103/PhysRevD.10.428. URL: http://link.aps.org/doi/10.1103/PhysRevD.10.428.

[ÓY74b] N. Ó Murchadha and J. W. York. 'Initial-value problem of general relativity. II. Stability of solutions of the initial-value equations'. In: *Phys. Rev. D* 10 (2 July 1974), pp. 437–446. DOI: 10.1103/PhysRevD.10.437. URL: http://link.aps.org/doi/10.1103/PhysRevD.10.437.

[Ped67] D. Pedoe. 'On a Theorem in Geometry'. In: *The American Mathematical Monthly* 74.6 (1967), pp. 627–640. ISSN: 00029890, 19300972. URL: http://www.jstor.org/stable/2314247.

[Pen69] R. Penrose. 'Gravitational Collapse: the Role of General Relativity'. In: *Nuovo Cimento Rivista Serie* 1 (1969).

[Pla+16] Planck Collaboration et al. 'Planck 2015 results - I. Overview of products and scientific results'. In: *Astronomy & Astrophysics* 594 (2016), A1. DOI: 10.1051/0004-6361/201527101. URL: http://dx.doi.org/10.1051/0004-6361/201527101.

[Poi04] E. Poisson. *A relativist's toolkit: the mathematics of black-hole mechanics*. Cambridge university press, 2004.

[Räs11] S. Räsänen. 'Backreaction: directions of progress'. In: *Classical and Quantum Gravity* 28.16 (2011), p. 164008. URL: http://stacks.iop.org/0264-9381/28/i=16/a=164008.

[Rob35] H. P. Robertson. 'Kinematics and World-Structure'. In: *Astrophysical Journal* 82 (Nov. 1935), p. 284. DOI: 10.1086/143681.

[Rob36a] H. P. Robertson. 'Kinematics and World-Structure II.' In: *Astrophysical Journal* 83 (Apr. 1936), p. 187. DOI: 10.1086/143716.

[Rob36b] H. P. Robertson. 'Kinematics and World-Structure III.' In: *Astrophysical Journal* 83 (May 1936), p. 257. DOI: 10.1086/143726.

[Sch16] K. Schwarzschild. 'Über das Gravitationsfeld eines Massenpunktes nach der Einsteinschen Theorie'. In: *Sitzungsberichte der Königlich Preußischen Akademie der Wissenschaften (Berlin)* (1916), pp. 189–196.

[Sch54] E. Schücking. 'Das Schwarzschildsche Linienelement und die Expansion des Weltalls.' In: *Zeitschrift für Physik* 137.5 (1954), pp. 595–603. ISSN: 0044-3328. DOI: 10.1007/BF01375011. URL: http://dx.doi.org/10.1007/BF01375011.

[Slo13] Sloan Digital Sky Survey. *SDSS Galaxy Map*. 2013. URL: http://www.sdss.org/science/orangepie/.

[Sma98] S. Smale. 'Mathematical problems for the next century'. In: *The Mathematical Intelligencer* 20.2 (1998), pp. 7–15.

[SN95] M. Shibata and T. Nakamura. 'Evolution of three-dimensional gravitational waves: Harmonic slicing case'. In: *Phys. Rev. D* 52 (10 Nov. 1995), pp. 5428–5444. DOI: 10.1103/PhysRevD.52.5428. URL: http://link.aps.org/doi/10.1103/PhysRevD.52.5428.

[Sod36] F. Soddy. 'The Kiss Precise'. In: *Nature* 137 (June 1936), p. 1021. DOI: 10.1038/1371021a0.

[Söd92] B. Söderberg. 'Apollonian tiling, the Lorentz group, and regular trees'. In: *Phys. Rev. A* 46 (4 Aug. 1992), pp. 1859–1866. DOI: 10.1103/PhysRevA.46.1859. URL: http://link.aps.org/doi/10.1103/PhysRevA.46.1859.

[Spr+05] V. Springel et al. 'Simulations of the formation, evolution and clustering of galaxies and quasars'. In: *Nature* 435 (June 2005), pp. 629–636. DOI: 10.1038/nature03597. eprint: astro-ph/0504097.

[Str12] N. Straumann. *General relativity*. Springer Science & Business Media, 2012.

[Str74] N. Straumann. 'Minimal assumptions leading to a Robertson-Walker model of the universe'. In: *Helvetica Physica Acta* 47.3 (1974), pp. 379–383.

[Suz+12] N. Suzuki et al. 'The Hubble Space Telescope Cluster Supernova Survey. V. Improving the Dark-energy Constraints above z > 1 and Building an Early-type-hosted Supernova Sample'. In: *The Astrophysical Journal* 746.1 (2012), p. 85. URL: http://stacks.iop.org/0004-637X/746/i=1/a=85.

[SY79] R. Schoen and S.-T. Yau. 'On the proof of the positive mass conjecture in general relativity'. In: *Communications in Mathematical Physics* 65.1 (1979), pp. 45–76. ISSN: 1432-0916. DOI: 10.1007/BF01940959. URL: http://dx.doi.org/10.1007/BF01940959.

[SY81] R. Schoen and S.-T. Yau. 'Proof of the positive mass theorem. II'. In: *Communications in Mathematical Physics* 79.2 (1981), pp. 231–260. ISSN: 1432-0916. DOI: 10.1007/BF01942062. URL: http://dx.doi.org/10.1007/BF01942062.

[Sze75] P. Szekeres. 'A class of inhomogeneous cosmological models'. In: *Communications in Mathematical Physics* 41.1 (1975), pp. 55–64. ISSN: 1432-0916. DOI: 10.1007/BF01608547. URL: http://dx.doi.org/10.1007/BF01608547.

[Tol34] R. C. Tolman. 'Effect of Inhomogeneity on Cosmological Models'. In: *Proceedings of the National Academy of Sciences of the United States of America* 20.3 (1934), pp. 169–176. ISSN: 00278424. URL: http://www.jstor.org/stable/86706.

[Tol39] R. C. Tolman. 'Static Solutions of Einstein's Field Equations for Spheres of Fluid'. In: *Phys. Rev.* 55 (4 Feb. 1939), pp. 364–373. DOI: 10.1103/PhysRev.55.364. URL: http://link.aps.org/doi/10.1103/PhysRev.55.364.

[Urb08] H. Urbantke. *Gravitation und Kosmologie: Eine Einführung in die Allgemeine Relativitätstheorie*. Spektrum Akademischer Verlag, 2008.

[Wal37] A. G. Walker. 'On Milne's Theory of World-Structure*'. In: *Proceedings of the London Mathematical Society* s2-42.1 (1937), pp. 90–127. ISSN: 1460-244X. DOI: 10.1112/plms/s2-42.1.90. URL: http://dx.doi.org/10.1112/plms/s2-42.1.90.

[Wei08] S. Weinberg. *Cosmology*. Oxford University Press, 2008.

[Wei72] S. Weinberg. *Gravitation and cosmology: principles and applications of the general theory of relativity*. Vol. 1. 1972.

[WI91] R. M. Wald and V. Iyer. 'Trapped surfaces in the Schwarzschild geometry and cosmic censorship'. In: *Phys. Rev. D* 44 (12 Dec. 1991), R3719–R3722. DOI: 10.1103/PhysRevD.44.R3719. URL: http://link.aps.org/doi/10.1103/PhysRevD.44.R3719.

[Wit81] E. Witten. 'A new proof of the positive energy theorem'. In: *Communications in Mathematical Physics* 80.3 (1981), pp. 381–402. ISSN: 1432-0916. DOI: 10.1007/BF01208277. URL: http://dx.doi.org/10.1007/BF01208277.

[YBK10] J. K. Yadav, J. S. Bagla and N. Khandai. 'Fractal dimension as a measure of the scale of homogeneity'. In: *Monthly Notices of the Royal Astronomical Society* 405.3 (2010), p. 2009. DOI: 10.1111/j.1365-2966.2010.16612.x. eprint: /oup/backfile/Content_public/Journal/mnras/405/3/10.1111/j.1365-2966.2010.16612.x/2/mnras0405-2009.pdf. URL: +%20http://dx.doi.org/10.1111/j.1365-2966.2010.16612.x.

[YO14] C.-M. Yoo and H. Okawa. 'Black hole universe with a cosmological constant'. In: *Phys. Rev. D* 89 (12 June 2014), p. 123502. DOI: 10.1103/PhysRevD.89.123502. URL: http://link.aps.org/doi/10.1103/PhysRevD.89.123502.

[YON13] C.-M. Yoo, H. Okawa and K.-i. Nakao. 'Black-Hole Universe: Time Evolution'. In: *Phys. Rev. Lett.* 111 (16 Oct. 2013), p. 161102. DOI: 10.1103/PhysRevLett.111.161102. URL: http://link.aps.org/doi/10.1103/PhysRevLett.111.161102.

[Yoo+12] C.-M. Yoo et al. 'Black hole universe: Construction and analysis of initial data'. In: *Phys. Rev. D* 86 (4 Aug. 2012), p. 044027. DOI: 10.1103/PhysRevD.86.044027. URL: http://link.aps.org/doi/10.1103/PhysRevD.86.044027.

[Yor71] J. W. York. 'Gravitational Degrees of Freedom and the Initial-Value Problem'. In: *Phys. Rev. Lett.* 26 (26 June 1971), pp. 1656–1658. DOI: 10.1103/PhysRevLett.26.1656. URL: http://link.aps.org/doi/10.1103/PhysRevLett.26.1656.

[Yor72] J. W. York. 'Role of Conformal Three-Geometry in the Dynamics of Gravitation'. In: *Phys. Rev. Lett.* 28 (16 Apr. 1972), pp. 1082–1085. DOI: 10.1103/PhysRevLett.28.1082. URL: http://link.aps.org/doi/10.1103/PhysRevLett.28.1082.

[Yor73] J. W. York. 'Conformally invariant orthogonal decomposition of symmetric tensors on Riemannian manifolds and the initial-value problem of general relativity'. In: *Journal of Mathematical Physics* 14.4 (1973), pp. 456–464. DOI: http://dx.doi.org/10.1063/1.1666338. URL: http://scitation.aip.org/content/aip/journal/jmp/14/4/10.1063/1.1666338.

[Yor79] J. W. York Jr. 'Kinematics and dynamics of general relativity'. In: *Sources of gravitational radiation*. Vol. 1. Cambridge. 1979, pp. 83–126.

[Yor99] J. W. York. 'Conformal "Thin-Sandwich" Data for the Initial-Value Problem of General Relativity'. In: *Phys. Rev. Lett.* 82 (7 Feb. 1999), pp. 1350–1353. DOI: 10.1103/PhysRevLett.82.1350. URL: http://link.aps.org/doi/10.1103/PhysRevLett.82.1350.

[Zal08] R. Zalaletdinov. 'The Averaging Problem in Cosmology and Macroscopic Gravity'. In: *International Journal of Modern Physics A* 23.08 (2008), pp. 1173–1181. DOI: 10.1142/S0217751X08040032. eprint: http://www.worldscientific.com/doi/pdf/10.1142/S0217751X08040032. URL: http://www.worldscientific.com/doi/abs/10.1142/S0217751X08040032.

[Zal92] R. M. Zalaletdinov. 'Averaging out the Einstein equations'. In: *General Relativity and Gravitation* 24.10 (1992), pp. 1015–1031. ISSN: 1572-9532. DOI: 10.1007/BF00756944. URL: http://dx.doi.org/10.1007/BF00756944.

[Zal93] R. M. Zalaletdinov. 'Towards a theory of macroscopic gravity'. In: *General Relativity and Gravitation* 25.7 (1993), pp. 673–695. ISSN: 1572-9532. DOI: 10.1007/BF00756937. URL: http://dx.doi.org/10.1007/BF00756937.

# Picture Credits

[1] Figure 1.1 NASA / WMAP Science Team. *The Microwave Sky, c. 1965*. URL: https://map.gsfc.nasa.gov/media/030635/index.html

[2] Figure 1.2 D. Eisenstein and SDSS-III collaboration. *A slice through a map of our Universe*. 2016. URL: http://www.sdss.org/press-releases/astronomers-map-a-record-breaking-1-2-million-galaxies-to-study-the-properties-of-dark-energy/

[3] Figure 1.3 NASA, ESA, H. Teplitz and M. Rafelski (IPAC/Caltech), A. Koekemoer (STScI), R. Windhorst (Arizona State University), and Z. Levay (STScI). *Hubble Ultra Deep Field 2014*. 2014. URL: http://hubblesite.org/image/3380/news_release/2014-27

[4] Figure 1.4 Sloan Digital Sky Survey. *SDSS Galaxy Map*. 2013. URL: http://www.sdss.org/science/orangepie/

[5] Figure 1.5 NASA/JPL-Caltech/ESA. *PIA16874: The Universe Comes into Sharper Focus*. 2013. URL: http://photojournal.jpl.nasa.gov/catalog/PIA16874

[6] Figure 1.6 V. Springel et al. 'Simulations of the formation, evolution and clustering of galaxies and quasars'. In: *Nature* 435 (June 2005), pp. 629–636. DOI: 10.1038/nature03597. eprint: astro-ph/0504097

[7] Figure 4.1 N. Suzuki et al. 'The Hubble Space Telescope Cluster Supernova Survey. V. Improving the Dark-energy Constraints above z $>$ 1 and Building an Early-type-hosted Supernova Sample'. In: *The Astrophysical Journal* 746.1 (2012), p. 85. URL: http://stacks.iop.org/0004-637X/746/i=1/a=85

All other figures have been created by the author Michael Fennen.